Strategies for the nucleation, electric control and detection of magnetic skyrmions for memory and computing applications

Joseba Andoni Urrestarazu

THÈSE

Pour obtenir le grade de

DOCTEUR DE L'UNIVERSITÉ GRENOBLE ALPES

École doctorale : PHYS - Physique
Spécialité : Nanophysique
Unité de recherche : Spintronique et Technologie des Composants

Stratégies de nucléation, contrôle électrique et de détection des skyrmions magnétiques pour des applications calcul et mémoire

Strategies for the nucleation, electric control and detection of magnetic skyrmions for memory and computing applications

Présentée par :

Joseba Andoni URRESTARAZU

Direction de thèse :

Olivier BOULLE CHARGE DE RECHERCHE, CNRS DELEGATION ALPES	Directeur de thèse

Rapporteurs :

JOSE LUIS PRIETO MARTIN
PROFESSEUR, UNIVERSIDAD POLITECNICA DE MADRID
LIZA HERRERA DIEZ
CHARGEE DE RECHERCHE HDR, CNRS DELEGATION ILE-DE-FRANCE SUD

Thèse soutenue publiquement le **8 décembre 2023**, devant le jury composé de :

JOSE LUIS PRIETO MARTIN PROFESSEUR, UNIVERSIDAD POLITECNICA DE MADRID	Rapporteur
LIZA HERRERA DIEZ CHARGEE DE RECHERCHE HDR, CNRS DELEGATION ILE-DE-FRANCE SUD	Rapporteure
JEAN-PHILIPPE ATTANE PROFESSEUR DES UNIVERSITES, UNIVERSITE GRENOBLE ALPES	Président
STEFANIA PIZZINI DIRECTRICE DE RECHERCHE, CNRS DELEGATION ALPES	Examinatrice

Abstract

In the realm of microelectronics, the demand for data storage and rapid computing capabilities presents a formidable challenge. Meeting these exponentially growing requirements needs innovative approaches. Spintronics and nanomagnetism emerge as an alternative operating at the nanoscale, offering potential solutions. In this context, the magnetic skyrmion is as a promising candidate for information storage. This particle-like circular magnetic entity shows great potential, particularly in an energy-conscious future. However, early observations of magnetic skyrmions in ferromagnetic materials revealed certain limitations regarding their stabilization, electrical manipulation and detection that must be addressed to unlock their full potential in future applications. This thesis tackles these challenges proposing strategies to stabilize skyrmion structures using alternative material systems and achieve their electrical detection with larger readout signals. A first proposition involves the use of synthetic antiferromagnets. Here, we perform time-resolved observations of skyrmion nucleation, which offer insights into the processes that govern the nucleation of these magnetic entities. Furthermore, we study the influence of x-rays on an exchange-biased material system, a factor that plays a significant role in stabilizing skyrmions. This facet of the research expands our knowledge of the external factors that can be leveraged to optimize the stability and performance of skyrmions. Transitioning from fundamental investigations to practical applications, the second part of this thesis focuses on device realization. Magnetic tunnel junctions (MTJs) serve as the foundational elements for magnetic memories. We experimentally demonstrate the electrical detection, voltage-induced nucleation and annihilation of a single skyrmion in an MTJ via *operando* magnetic microscopy. We investigate the manipulation of skyrmions within MTJs using external excitations, including both magnetic and electric fields. This exploration allows the dynamical control of the skyrmion behaviour within functional devices. Lastly, to complement these experimental findings, micromagnetic simulations are conducted, employing parameters derived from experimental data. These simulations corroborate our observations, affirming the feasibility of the voltage-controlled writing operations—a significant stride towards realizing low-power skyrmion-based technologies. Through a multidisciplinary approach, bridging simulations and experiment, these results contribute to unlock the full potential of skyrmions in the landscape of modern spintronics.

Résumé

Dans le domaine de la microélectronique, la forte demande de stockage de données et de capacités de calcul rapide représente un formidable défi. Pour répondre à ces exigences, il est nécessaire d'adopter des approches innovantes. La spintronique et le nanomagnétisme, opérant à l'échelle nanométrique, apparaissent comme une alternative offrant des solutions potentielles. Dans ce contexte, le skyrmion magnétique est un candidat prometteur pour le stockage de l'information. Cette entité magnétique de forme circulaire, semblable à une particule, présente un grand potentiel. Cependant, les premières observations de skyrmions magnétiques dans des matériaux ferromagnétiques ont révélé certaines limitations concernant la stabilisation, la manipulation et la détection électrique qui doivent être résolues afin de libérer tout leur potentiel dans les applications futures. Cette thèse s'attaque à ces différents défis, en proposant des stratégies pour stabiliser les skyrmions en utilisant des systèmes de matériaux alternatifs. Une première proposition consiste à utiliser des antiferromagnétiques synthétiques. Ici, nous avons effectué des observations de l'évolution dans le temps de la nucléation des skyrmions, qui offrent des aperçus sur les processus qui gouvernent la nucléation de ces entités magnétiques. En outre, nous avons étudié l'influence des rayons X sur un système de matériaux à biais d'échange, un facteur qui joue un rôle important dans la stabilisation des skyrmions. Cette facette de la recherche élargit notre connaissance des facteurs externes qui peuvent être exploités pour optimiser la stabilité et la performance des structures skyrmioniques. La deuxième partie de cette thèse se concentre sur la réalisation de dispositifs, passant de la recherche fondamentale aux applications pratiques. Les jonctions tunnel magnétiques (MTJ) servent d'éléments fondamentaux pour les mémoires magnétiques. Nous avons démontré expérimentalement la détection électrique, la nucléation induite par la tension et l'annihilation d'un skyrmion unique dans une MTJ par des expériences de microscopie magnétique *operando*. Nous avons étudié la manipulation des skyrmions dans les MTJ à l'aide d'excitations externes, tels que des champs magnétiques et électriques. Cette exploration permet le contrôle du comportement dynamique des skyrmions dans des dispositifs fonctionnels. Enfin, pour compléter ces résultats expérimentaux, des simulations micromagnétiques sont réalisées en utilisant des paramètres issus des données expérimentales. Ces simulations corroborent nos observations, affirmant la faisabilité des opérations d'écriture contrôlées par la tension, un pas important vers la réalisation de technologies à base de skyrmion à faible consommation d'énergie. Grâce à une approche multidisciplinaire, associant simulation et expérimentation, ce travail contribue à démontrer tout le potentiel des skyrmions dans le paysage de la spintronique moderne.

Acknowledgements

The specific context surrounding this thesis has shaped the evolution I experienced personally and professionally. A kid who arrived in a foreign country with no expectations ended up locked down for six months, followed by a three-year thesis project. Behind such a journey, there are many people that I would like to acknowledge.

Thank you, Olivier Boulle. You were the first researcher who contacted me when I knocked on the doors of Spintec for an internship project. Coming from a fundamental physics background, believe me, I had no idea about skyrmions or nanofabrication, the archi-famous SiN membranes, or magnetic tunnel junctions. My thesis under your supervision has exceeded any kind of expectations, as I learned about topics I was not even aware of, and you educated me for research. Your knowledge and ambition characterize you. We also crossed Europe together many times, spent nights looking at 'random' black/white/grey pixels, and ate chickpeas and nuts. I deeply wish you the best during your already successful career, surrounded by exceptional researchers. Thank you, Gilles and Liliana; your infinite expertise made the perfect combo in our group.

The skyrmion team has considerably evolved during my PhD. I remember being a first-year-old student/kid in front of consolidated postdocs. The demanding DARPA project matched with the high skills of Naveen, Kaushik, Tuong, and Johan. Thank you all. Suddenly, everyone left, and I was the veteran who had to take care of the newcomers. I could not be happier, though; the arrivals of Ilaria (you are truly amazing!) and Rodrigo (Olivier chose well!) brought a fresh air that constantly pumped my batteries during the last year. I will not forget your help, particularly during my last months.

A big merci to my office mates Capucine and Hanna for the great vibes and infinite apple and cake supplies. You were always crystalline clear with me, and I appreciated it. Merci to Sergi, Andrea, Kamal, Mateo, Marco, and Fatima. It was fun there! Merci to the neighbors Ilaria, Louis, Rodri, Hasan, Georgy, Kuldeep, Subham, David, and the people in the dungeons, Javi, Paolo, Salvatore, Theo, Michael, and Maxime. Another giant merci to those who left before me, Michael, Aurélien, Charles, Miina, Marco, Nuno, Arijit, Samuel, Ruhey, Pedro...

The help with the administrative work resulted crucial, so a big-big merci to Catherine for optimizing every procedure (especially for beamtimes). Thank you to the directors Lucian and Olivier (you will be missed), and thank you to every researcher/staff member who helped and dedicated some time to me: Stéphane, Jérôme, Hélène, Kevin, Aurélien, Mair, Laurent, Ricardo, Florian...

I would like to dedicate this thesis to the old and new versions of the Spanish crew with the inseparable Zipi-Zape Álvaro and Dani, followed by the unbeatable duo Javi and Rodri. With different approaches, they all four taught me that life is not always rainbows and butterflies, but rather an ocean that sometimes goes through heavy storms and giant waves. Eskerrik asko, madridistas, for adopting a basque guy. Eskerrik asko, Javi, por pasarte mil veces por mi oficina con la excusa de tomarnos un café. Ya fuese para arreglar el mundo, dejarme las cosas claritas o tocarme los cataplines. Se te quiere. Special words for Laura, whose presence in the office made my cortisol levels drop. I was not aware of how much I needed you until you finally came back from Madrid. At least I kept your desk safe! Que sigamos cantando.

We must all be honest and admit that Spintec would not be Spintec without the views. Yes, the views of the mountains. An unbalanced balance of thesis work and mountain activities defined my years here. A big part of this was shared with Monsieur Libor, who was often the reason behind my heavy legs on Mondays. Matinales, long days, or sunsets; by foot, on skis, or by bike! Innumerable activities and experiences which would not have been the same without you. From the Pyrenees to the Alps, never let your memories be greater than your dreams, Monsieur! Thank you also, Johanna, for your endless excitement and infinite

patience with my terrible climbing skills. Without forgetting about your constant almond butter production. Wishing you a strong comeback!

Finally, thank you to the lovely people I met outside the lab, my important colocs Luisa and Line, and every cycling geek, trail-runner, and skier who I had the pleasure to share time with.

To my family and friends.

And to Aurélie, who I admire, for her unconditional support.

The best is yet to come.

Table of Contents

Abstract i

Résumé iii

Acknowledgements v

Table of Contents vii

List of Figures xi

List of Tables xiii

List of Abbreviations xv

List of Symbols xvii

Introduction 1

1 Basic notions on nanomagnetism and spintronics 5
- 1.1 Energies and interactions in micromagnetism . . . 6
  - 1.1.1 Exchange energy . . . 6
  - 1.1.2 Demagnetizing energy . . . 6
  - 1.1.3 Zeeman energy . . . 7
  - 1.1.4 Anisotropy energy . . . 8
    - 1.1.4.1 Interfacial magnetic anisotropy . . . 8
  - 1.1.5 Interlayer exchange coupling . . . 9
  - 1.1.6 Dzyaloshinskii-Moriya interaction . . . 10
- 1.2 Domain walls . . . 10
  - 1.2.1 Types and energies . . . 10
- 1.3 Domain wall dynamics . . . 14
  - 1.3.1 Field-driven dynamics . . . 14
  - 1.3.2 Current-driven dynamics . . . 17
    - 1.3.2.1 Spin transfer torque . . . 17
    - 1.3.2.2 Spin orbit torque . . . 18
- 1.4 Magnetic tunnel junctions and tunneling magnetoresistance . . . 20
- 1.5 Voltage controlled magnetic anisotropy (VCMA) . . . 21
- 1.6 Conclusions . . . 23

2 Magnetic skyrmions 25
- 2.1 Basics and properties about magnetic skyrmions . . . 26
- 2.2 Energies of skyrmion stabilization . . . 27
- 2.3 Observation of magnetic skyrmions . . . 30
- 2.4 Manipulation of magnetic skyrmions: current-induced motion . . . 32
  - 2.4.1 The skyrmion Hall effect . . . 33
- 2.5 Electrical detection of skyrmions . . . 36
- 2.6 Skyrmion-based applications . . . 37
- 2.7 Synthetic antiferromagnetic skyrmions: stability and dynamics . . . 38
- 2.8 Conclusions . . . 41

3 Experimental techniques: nanofabrication and characterization 43
3.1 Magnetron sputtering: deposition of magnetic stacks . . . 44
3.2 Characterization on thin films . . . 45
3.2.1 Magneto-optical Kerr effect (MOKE) . . . 45
3.2.2 Vibrating sample magnetometer (VSM) . . . 45
3.2.3 Superconducting quantum interference device (SQUID) . . . 46
3.3 Nanofabrication . . . 47
3.3.1 MRAM nanofabrication process on membranes . . . 47
3.3.1.1 MTJ patterning . . . 47
3.3.2 MTJ characterization . . . 50
3.4 X-ray microscopy techniques . . . 51
3.4.1 X-ray Magnetic Circular Dichroism (XMCD) . . . 51
3.4.2 Scanning Transmission X-ray Microscopy (STXM) . . . 52
3.4.3 Photo-emission electron microscopy (PEEM) . . . 53
3.4.4 STXM for time resolved magnetic imaging . . . 54

4 Nucleation and dynamics of magnetic skyrmions in synthetic antiferromagnets 57
4.1 Our SAF system . . . 59
4.2 STXM observations of current-induced nucleation and dynamics of SAF skyrmions . . . 60
4.2.1 Nucleation of AF skyrmion lattices at large current densities . . . 62
4.3 Simulations and modelling . . . 64
4.3.1 Electrical and thermal simulations . . . 64
4.3.2 Micromagnetic simulations . . . 64
4.3.3 Analytical model of the bubble expansion and relaxation . . . 65
4.4 Discussion and conclusions . . . 68

5 Magnetic skyrmions in exchange-biased synthetic antiferromagnets 69
5.1 The exchange bias . . . 70
5.2 Stabilization of magnetic skyrmions by exchange bias . . . 72
5.3 X-ray induced skyrmions in exchange biased stacks . . . 73
5.4 SAF skyrmions in exchange biased synthetic antiferromagnets . . . 74
5.4.1 Optimization of the magnetic stack . . . 74
5.4.2 X-ray induced reversing of the AF order . . . 76
5.4.3 Nucleation of SAF skyrmions exchanged biased to IrMn . . . 76
5.4.4 Skyrmion imprint using x-ray beam . . . 77
5.4.5 Current-induced dynamics of SAF skyrmions exchanged biased to IrMn . . . 78
5.5 Conclusions . . . 79

6 Magnetic skyrmions in magnetic tunnel junctions 81
6.1 Introduction . . . 82
6.2 Optimization of the magnetic tunnel junction thin film stack . . . 82
6.2.1 Transport characterization of MTJ fabricated on SiN membrane . . . 83
6.3 Operando STXM magnetic microscopy of MTJ . . . 84
6.4 Nucleation of skyrmions in 500 nm diameter MTJ using voltage . . . 85
6.4.1 Manipulation of the skyrmion by external magnetic field and gate voltage . . . 86
6.5 Nucleation of magnetic skyrmions in large pillars . . . 87
6.5.1 DC voltage dependence on large pillars . . . 88
6.5.2 Voltage pulse dependence on large pillars . . . 88
6.5.3 Time resolved STXM experiments . . . 89
6.6 Voltage control magnetic anisotropy experiments . . . 90
6.6.1 Hard axis magnetotransport measurements . . . 91
6.7 Characterization of the magnetic properties in thin film level . . . 92
6.7.1 Magnetic moment, saturation magnetization and magnetic anisotropy . . . 92
6.7.2 Measurement of the Dzyaloshinskii-Moriya interaction by Brillouin Light Scattering experiments . . . 93
6.7.3 Domain wall dynamics experiments . . . 94
6.7.4 Ferromagnetic resonance measurements . . . 95
6.8 Lorentz Transmission Electron Microscopy observations . . . 96
6.9 Micromagnetic simulations . . . 98
6.9.1 Simulations for 500 nm dots . . . 100

6.9.2 Simulations for 2 µm dots . . . 101
6.10 Conclusion . . . 102

7 Summary and perspectives **103**
7.1 Summary . . . 103
7.2 Perspectives . . . 104
7.2.1 Manipulation of the antiferromagnetic order using light . . . 104
7.2.2 Skyrmion racetrack memory . . . 104
7.2.3 Fast motion of SAF skyrmions . . . 104
7.2.4 Skyrmion-based logic gates . . . 105
7.2.5 Non-conventional computing based on magnetic skyrmions . . . 105

Appendix **107**
A.1 Skyrmion number . . . 108
A.1.1 From LLG to Thiele equation . . . 110
A.1.2 Thiele equation . . . 112
A.2 Thiele equation with the force due to the DL-SOT . . . 113

References **117**

List of Figures

1 Magnetic skyrmions 2

1.1 Demagnetizing field 7
1.2 Zeeman effect 7
1.3 Effective magnetic anisotropy 8
1.4 Ruderman-Kittel-Kasuya-Yosida interaction 9
1.5 Domain walls 11
1.6 Domain wall energies 12
1.7 Equilibrium domain wall configurations 13
1.8 Magnetization dynamics 14
1.9 Field driven Bloch DW dynamics 15
1.10 Domain wall motion 16
1.11 Field driven DW dynamics 17
1.12 Spin Hall effect (SHE) 19
1.13 Current driven dynamics with SOT 19
1.14 First room temperature Tunneling Magnetoresistance (TMR) experiments 21
1.15 Voltage control of magnetic anisotropy (VCMA) 22

2.1 Magnetic skyrmions 26
2.2 Magnetic antiskyrmion 27
2.3 Energies for a magnetic skyrmion 28
2.4 DMI, effective anisotropy and exchange dependencies on the magnetic skyrmion 29
2.5 Experimental observation of magnetic skyrmions 31
2.6 Observation of the current-driven skyrmion motion in ultrathin films at room temperature . . 32
2.7 Skyrmion Hall effect in thin films 33
2.8 Electrical detection of magnetic skyrmions 36
2.9 Towards non-conventional skyrmion-based applications 37
2.10 Antiferromagnetic and synthetic antiferromagnetic skyrmions 38
2.11 SAF skyrmions in synthetic antiferromagnets 39
2.12 Dynamics of SAF skyrmions in synthetic antiferromagnets 40

3.1 Magnetron sputtering 44
3.2 Schematics of the Kerr effect 45
3.3 Schematics of the VSM and the SQUID 46
3.4 Layout on the wafer for MTJ patterning 47
3.5 Definition of the MTJs 48
3.6 Bottom electrode definition 48
3.7 MTJ encapsulation and thinning with accuflo 49
3.8 Top contact definition 49
3.9 Process flow of the MTJ nanofabrication 50
3.10 X-ray Magnetic Circular Dichroism (XMCD) 51
3.11 Schematics of the STXM microscopy technique 52
3.12 Schematics of the X-PEEM microscopy technique 53
3.13 XMCD-PEEM image of Néel domain walls 54
3.14 Pump-probe mechanism 55

4.1 Current-induced nucleation/annihilation of SAF skyrmions 58
4.2 Optimization of the compensated SAF stack 59
4.3 Stack and nanofabrication for time resolved experiments 60

4.4 Time resolved STXM experiments . . . 60
4.5 Time evolution of the skyrmion dimension . . . 61
4.6 Time evolution of the skyrmion dimension for different current densities . . . 62
4.7 Current polarity dependence on the skyrmion dynamics . . . 62
4.8 Time evolution of the magnetization pattern at large current densities . . . 63
4.9 3D electrical simulations . . . 64
4.10 Micromagnetic simulations: Current-induced skyrmion nucleation/annihilation . . . 64
4.11 Skyrmion relaxation in the absence of current . . . 67
4.12 Comparison of the experimental, simulations and analytical data . . . 68

5.1 Exchange bias interaction . . . 70
5.2 Thickness dependence of the exchange bias interaction . . . 71
5.3 Room temperature skyrmions in exchange biased multilayers . . . 72
5.4 Magnetic Force Microscopy experiments . . . 72
5.5 STXM experiments for skyrmion nucleation . . . 73
5.6 X-ray illumination for room temperature skyrmions in multilayer stacks exchange biased to IrMn . . . 73
5.7 Optimization of the magnetic layers . . . 74
5.8 Optimization of compensated exchanged biased SAF multilayers . . . 75
5.9 Influence of the x-ray beam on the magnetization reversal . . . 76
5.10 Observation of SAF domain structure exchange biased to IrMn . . . 77
5.11 Observation of a SAF skyrmion exchange biased to IrMn . . . 77
5.12 Erasing and nucleating SAF skyrmions with x-rays . . . 78
5.13 Current-induced experiments in SAF exchange biased to IrMn . . . 79

6.1 Stack optimization of the MTJ . . . 83
6.2 Device level transport properties of 500 nm diameter MTJ on membrane . . . 83
6.3 MTJ nanopillar for operando STXM magnetic microscopy . . . 84
6.4 Electrical detection of a skyrmion in an MTJ and its nucleation/annihilation using voltage . . . 85
6.5 Observation of the SAF structure in the MTJ with a skyrmionic state . . . 86
6.6 Evolution of the magnetic skyrmion size in 500 nm dots in response to external magnetic field and applied DC voltage . . . 87
6.7 Magnetic field dependence of the skyrmion in a 2µm MTJ pillar . . . 87
6.8 DC voltage dependencies for different magnetic textures in a 2µm MTJ pillar . . . 88
6.9 Manipulation of a skyrmion by voltage pulse in a 2 µm dot . . . 89
6.10 Time resolved STXM observations of the MTJ . . . 89
6.11 Magnetotransport measurements of MTJ patterned on Si wafer . . . 90
6.12 Voltage control of magnetic anisotropy . . . 91
6.13 Voltage dependence measurements on the magnetoresistance hysteresis loops for an in-plane free layer configuration . . . 92
6.14 Thin film characterization of the magnetic properties . . . 93
6.15 Brillouin light scattering measurements . . . 93
6.16 Field-induced bubble expansion measurements for DMI measurements . . . 94
6.17 Ferromagnetic resonance measurements . . . 95
6.18 Magnetic field series observation in TEM . . . 96
6.19 Micromagnetic simulations for TEM analysis . . . 97
6.20 TEM observation with background subtraction . . . 98
6.21 Micromagnetic simulation of the skyrmion nucleation. . . . 99
6.22 Micromagnetic simulation of skyrmion manipulation by external magnetic field and DC voltage in a 500 nm diameter dot. . . . 100
6.23 Micromagnetic simulation of skyrmion manipulation by external magnetic field and DC voltage in a 2 µm diameter dot . . . 101

7.1 Dynamics of SAF skyrmions . . . 105
7.2 Magnetic skyrmion-based artificial synapses in MTJ . . . 106
A.3 Scheme of angles for skyrmion number calculation . . . 108

List of Tables

6.1 Summary of the parameters for the MTJ stack 99

List of Abbreviations

Al	Aluminium
B	Boron
Co	Co
Cr	Chromium
Cu	Copper
Fe	Iron
Ir	Iridium
MgO	Magnesium oxide
Mn	Manganese
Ni	Nickel
Ox	Oxide
Pd	Palladium
Pt	Platinum
Py	Permalloy
Ru	Ruthenium
Ta	Tantalum
W	Tungsten
AHE	Anomalous Hall effect
ANE	Anomalous Nernst effect
AP	Anti-parallel
bcc	Body centered cubic
BL	Bias(ing) layer
BLS	Brillouin light scattering
CMOS	Complementary metal oxide semiconductor
DMI	Dzyaloshinskii-Moriya interaction
DW	Domain wall
e-beam	Electron beam lithography
fcc	Face centered cubic
FL	Free layer
FM	Ferromagnet(ic)
FMR	Ferromagnetic resonance
FZP	Fresnel zone plate
GMR	Giant magnetoresistance
HDD	Hard disk drive
HM	Heavy metal
IBE	Ion beam etching
IP	In-plane
IPA	Isopropanol
MFM	Magnetic force microscopy
MIBK	Methyl isobutyl ketone
MOKE	Magneto-optical Kerr effect
MRAM	Magnetic random access memory
MTJ	Magnetic tunnel junction
NM	Non-magnet(ic)
NV	Nitrogen vacancy
OOP	Out-of-plane
P	Parallel
PMA	Perpendicular magnetic anisotropy

PSA	Perpendicular shape anisotropy
PVD	Physical vapor deposition
RC	Reservoir computing
RIE	Reactive ion etching
RKKY	Ruderman-Kittel-Kasuya-Yosida
RT	Room temperature
SAF	Synthetic antiferromagnet(ic)
SEM	Scanning electron microscopy
SHA	Spin Hall angle
SHE	Spin Hall effect
SNR	Signal to noise ratio
SOC	Spin-orbit coupling
SOT	Spin-orbit torque
SQUID	Superconducting quantum interference device
STT	Spin-transfer torque
STXM	Scanning transmission x-ray microscopy
TEM	Transmission electron microscopy
THE	Topological Hall effect
TMR	Tunnel(ing) magnetoresistance
VCDMI	Voltage-controlled DMI
VCMA	Voltage-controlled magnetic anisotropy
VSM	Vibrating sample magnetometry
XAS	X-ray absorption spectroscopy
XMCD	X-ray magnetic circular dichroism
X-PEEM	X-ray photo-emission electron microscopy

List of Symbols

A	Exchange constant	J m^{-1}
C	Magnetic field per unit current density	T A^{-1} m^2
D	Dzyaloshinskii-Moriya interaction constant	J m^{-2}
$\mathbf{D}$	Dissipation matrix	kg s^{-1}
e	Elementary charge	C
$\vec{F}$	Force	kg m s^{-2} (N)
$\vec{G}$	Gyrotropic vector	kg s^{-1}
G_X	Conductance of X state	Ω^{-1}
$\vec{H}$	Magnetic field	A m^{-1}
$\hbar$	Reduced Planck constant	J s
J	Current density	A m^{-2}
k	Wave vector	m^{-1}
K_1	Volume uniaxial anisotropy constant	J m^{-3}
K_d	Demagnetizing energy constant	J m^{-3}
K_{eff}	Effective anisotropy constant	J m^{-3}
K_s	Surface anisotropy constant	J m^{-2}
K_u	Uniaxial anisotropy constant	J m^{-3}
$\vec{m}$	Reduced magnetisation vector	
M_S	Saturation magnetisation	A m^{-1}
N_{Sk}	Topological charge or skyrmion number	
p	Skyrmion core polarity number	
R	Skyrmion radius	m
R_X	Resistance of X state	Ω
t_X	Thickness of material X	m
$\vec{T}_X$	X-like Torque	s^{-1}
v	Velocity	m s^{-1}
W	Winding number	
α	Magnetic damping	
γ	Gyromagnetic ratio	Hz T^{-1}
Δ	Domain wall width	m
ϵ	VCMA coefficient	J V^{-1} m^{-1}
ε_X	Energy density of X	
θ_{SkH}	Skyrmion Hall angle	
μ_0	Vacuum magnetic permeability	$4\pi \times 10^{-7}$ T A^{-1} m
μ_B	Bohr magneton	J T^{-1}
σ_{DW}	Domain wall energy	J m^{-2}
ξ	Domain wall helicity angle	

Introduction

The spin angular momentum is a fundamental quantum mechanical property intrinsic to every elementary particle among which our interest is focused on the electron. It quantifies (from a classical point of view) the degree of intrinsic self-rotation. The electron also carries an electrical charge, and when it is linked to the intrinsic spin rotation, it creates a magnetic moment. The research field that gathers both the electronic and spin degrees of freedom is called spintronics.

Technological applications such as magneto-resistive read heads of magnetic hard disk drives can benefit from the spin of the electron. This was demonstrated by Albert Fert and Peter Grünberg in 1988 based on their independent discovery of the giant magnetoresistance (GMR) [1,2]. When two ferromagnets are separated by a metallic spacer, the overall resistance of the device is dependent on the relative orientation of the magnetization of the ferromagnetic layers. The difference of resistance between both configurations is called the GMR. This physical mechanism has been used to sense the magnetic states of magnetic hard drives and led to a massive improvement of the storage capacity enabling the achievements of storage densities up to a few TB per inch square. The information is stored as bits. The tunnel magnetoresistance (TMR) effect [3,4] was found to be a one order of magnitude larger effect, improving the reading power consumption of HHDs using an insulator as the spacer between two ferromagnets. This device is known as a magnetic tunnel junction (MTJ). A few years later, the spin transfer torque magnetic random access memory (STT-MRAM) device emerged. It is based on the discovery of the spin transfer torque mechanism by Luc Berger and John Slonczewski in 1996 [5,6]. The magnetic state of a ferromagnet can be controlled via spin angular momentum transfer by sending a current though it (writing). This led to the development of the MRAM technology. The important property of this device is that it is non volatile, i.e there is no need to bring energy to the system in order to maintain the information. This technology is currently being pursued by semi-conductor industries like IBM, Intel or Samsung. In the decade of 2010, another mechanism to control the magnetization for memory applications was discovered, the spin orbit torque (SOT) [7]. It can be present in systems with large spin orbit coupling (SOC) and inversion symmetry such as heavy metal (HM)/ferromagnet structures. When a charge current flows through the HM, the SOC induces a spin current in the HM that generates a torque in the adjacent FM layer, enabling the reversal of its magnetization. An asymmetric exchange interaction is also present in systems with SOC and broken inversion symmetry, the Dzyaloshinskii-Moriya interaction (DMI). This interaction tends to favour the formation of non-collinear spin textures, where neighbouring magnetic moments do not align. Together with SOT, it allows to move domain walls (DW) with high speed using electrical current [8].

The current induced manipulation of domain walls is at the basis of a novel class of magnetic memory named magnetic racetrack memory [9]. It is built using magnetic nanotrack and the data is encoded by the orientation of the magnetic domains (either 'up' or 'down').

The DMI also leads to nm-scale topological spin textures, named magnetic skyrmions. The skyrmion is a particle-like circular magnetic texture stabilized by DMI that can be moved by electrical currents. Another approach to encode information in racetracks is the use of them. In this case, the binary information is encoded in the presence or absence of a skyrmion. Similarly to domain walls, they can also be moved along the racetrack using electrical current-induced spin-orbit torques. Compared to domain walls, they are smaller, highly stable, and can potentially be packed more densely.

Apart from memory applications, skyrmions have also attracted interest for their potential use in neuromorphic computing and other advanced computing paradigms. Instead of the usual setup where memory and processing happen separately, spintronics could be used to put them together in one unit in order to save energy using skyrmions. This field is called neuromorphic and holds the potential to emulate the brain functionality [10].

The popularity of magnetic skyrmions can be visualized in Figure 1 where the number of publications and the number of citations per year are displayed since the first experimental observation of skyrmions (2009). The exponential growth until the beginning of my thesis in December 2020 clearly demonstrates that skyrmionics became a well established field of research.

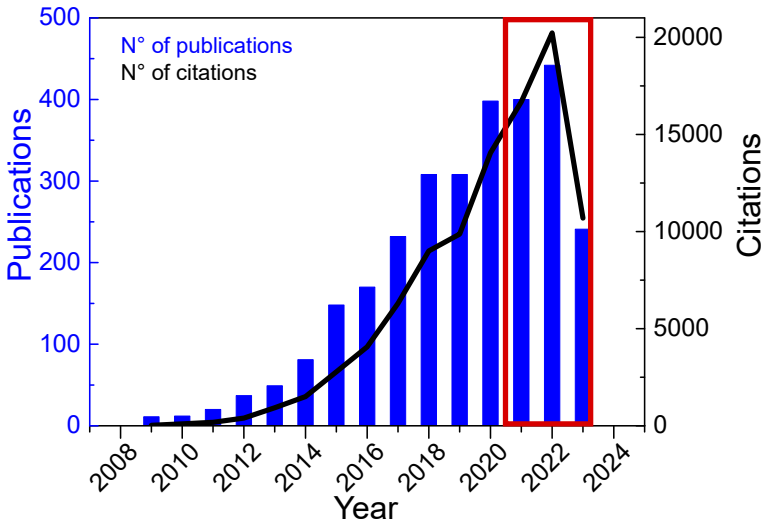

Figure 1: Magnetic skyrmions | Number of publications (blue) and number of citations (black) including the words 'magnetic' and 'skyrmion' since the first observations of magnetic skyrmions in 2009. In red, my thesis period that began in December 2020. Data from *Web of Science*.

When I started my thesis, important milestones for the use of skyrmion based applications had been fulfilled. This includes the stabilization of magnetic skyrmions at room temperature in ultrathin films and their manipulation using electrical current. However, challenges still remained to be addressed regarding the skyrmion manipulation, nucleation and electrical detection. In particular, the finite magnetic moment of the magnetic skyrmions limits their minimal size and leads to a deviation of the skyrmion motion towards the edge of the track where they can be annihilated. A way to solve this issue is to consider synthetic antiferromagnets (SAF), where two skyrmions are coupled antiferromagnetically, promising ultra-small and ultra-fast skyrmions. However, the vanishing magnetic moment in SAF makes the observation, stabilization and controlled nucleation of skyrmions very challenging. A first objective of my thesis has been to optimize SAF films to stabilize SAF skyrmions and explore different strategies to achieve their nucleation.

Another important milestone for skyrmion based applications is the electrical detection skyrmions. At the beginning of my thesis, the electrical detection of single skyrmions had been demonstrated in ultrathin films at room temperature using anomalous Hall effect, but the very low electrical signal prevents applications to devices. The second part of my thesis was dedicated to the integration of skyrmions in already existing memory elements named magnetic tunnel junctions, where a much larger electrical signal is expected. We optimized MTJ stacks to achieve the full electrical control of the nucleation of skyrmions in MTJs, with its unambiguous detection and operando observations.

In the following, we present the outline of this manuscript.

Outline This thesis is divided into six main chapters, a conclusion chapter and an appendix. Lists for all figures, tables, symbols and abbreviations are provided. The manuscript is organised as follows:

Chapter 1: Essential notions on interfacial magnetism and domain walls This chapter is meant to introduce in this chapter the basic concepts of nanomagnetism and spintronics which will be used in the manuscript, including energy terms and interactions, domain walls and magnetic tunnel junctions.

Chapter 2: Magnetic skyrmions and magnetic tunnel junctions This chapter will describe the basics of magnetic skyrmions. The requirements for nucleation, stability and dynamics are discussed as well as the means of detection. The existing literature is thoroughly examined, and any unresolved inquiries will be addressed. Applications to memory and logic devices are also introduced, going through their physics and development.

Chapter 3: Experimental techniques: nanofabrication and characterization In this chapter, we include the description of the diverse experimental techniques used throughout the thesis. Tools for deposition and characterization steps are explained, while we detail the x-ray microscopy techniques for the magnetic texture imaging. At the end of the chapter, the MTJ nanofabrication process on membranes is detailed.

Chapter 4: Nucleation and dynamics of magnetic skyrmions in synthetic antiferromagnets This chapter details the work carried out mainly in the first year of my PhD thesis. For this, we chose synthetic antiferromagnets. All the optimization process and the experimental results is explained.

Chapter 5: Magnetic skyrmions in exchange-biased synthetic antiferromagnets In this chapter, the material systems chosen were synthetic antiferromagnets exchange biased to an antiferromagnet. All the optimization process and the experimental results regarding the nucleation and observation of skyrmions is explained.

Chapter 6: Magnetic skyrmions in magnetic tunnel junctions This last chapter englobes the results obtained during the second half of my PhD research. Here, we demonstrate the electrical detection as well as the voltage induced nucleation and annihilation of a single skyrmion in a MTJ via the operando magnetic microscopy experiments. These results demonstrate the readout and voltage controlled writing operations for low power skyrmion-based technologies.

Chapter 7: Summary and perspectives Here, all the main results of this thesis are summarised, highlighting the future prospects and continuation of this work.

Chapter 1

Basic notions on nanomagnetism and spintronics

Contents

1.1 Energies and interactions in micromagnetism 6
1.1.1 Exchange energy 6
1.1.2 Demagnetizing energy 6
1.1.3 Zeeman energy 7
1.1.4 Anisotropy energy 8
1.1.4.1 Interfacial magnetic anisotropy 8
1.1.5 Interlayer exchange coupling 9
1.1.6 Dzyaloshinskii-Moriya interaction 10
1.2 Domain walls 10
1.2.1 Types and energies 10
1.3 Domain wall dynamics 14
1.3.1 Field-driven dynamics 14
1.3.2 Current-driven dynamics 17
1.3.2.1 Spin transfer torque 17
1.3.2.2 Spin orbit torque 18
1.4 Magnetic tunnel junctions and tunneling magnetoresistance 20
1.5 Voltage controlled magnetic anisotropy (VCMA) 21
1.6 Conclusions 23

I introduce in this chapter the basic concepts of nanomagnetism and spintronics which will be used in the manuscript, including energy terms and interactions (Section 1.1), domain walls (Sections 1.2 and 1.3) and magnetic tunnel junctions (Section 1.4).

1.1 Energies and interactions in micromagnetism

Solving the many-body electron problem for a spin ensemble is a tedious task. For this, a micromagnetic continuum theory was developed by Brown which is valid over length scales from few nm to µm [11]. The main assumption here is to consider a continuous magnetization and describe it as a vector field. In the following, the vector $\vec{m}(\vec{r}) = \vec{M}(\vec{r})/M_S$ denotes the normalized magnetization vector at a given position $\vec{r}$. In the following section I will describe the main energy terms that rule the micromagnetic order. More detailed description can be found in the literature (Ref. [12–15] and others).

1.1.1 Exchange energy

The exchange energy, also known as exchange interaction or Heisenberg interaction, arises from the Pauli exclusion principle, which states that two identical fermions (such as electrons) cannot occupy the same quantum state simultaneously. In ferromagnetic materials, the exchange interaction favours a parallel alignment of neighboring spins, resulting in a net magnetic moment, while on antiferromagnetic materials, it favours an antiparallel alignment. It is a short range interaction. For two spins ($\vec{S}_i$ and $\vec{S}_j$) of neighbouring atoms i and j, it reads:

$$\vec{H}_{ex} = -\sum_{i<j} J_{ij}\vec{S}_i \cdot \vec{S}_j, \tag{1.1}$$

where the J_{ij} is the exchange energy constant. In particular, if we consider only neighbouring atoms with identical interaction strength $J_{ij} = J$, it favours the parallel (antiparallel) alignment of neighbouring spins, resulting in ferromagnetic (antiferromagnetic) ordering when the sign is positive (negative). In micromagnetism, in the continuum approximation, the energy density of this interaction is given by:

$$\varepsilon_{ex} = A\left(\left(\vec{\nabla}m_x\right)^2 + \left(\vec{\nabla}m_y\right)^2 + \left(\vec{\nabla}m_z\right)^2\right), \tag{1.2}$$

where $A \sim JS^2n/a$ is the exchange stiffness constant (J/m). Here, n is the number of atoms per unit cell, S is the electron spin and a is the lattice parameter. A typically ranges between 5-30 pJ/m for 3d transition metal ferromagnets (depending on the temperature).

1.1.2 Demagnetizing energy

Magnetic moments in a ferromagnet create magnetic fields, called dipolar (or magnetostatic) field. The stray field refers to the dipolar field outside the sample while the demagnetizing field refers to the dipolar field inside the sample. The energy density associated with the interaction of the magnetic moments with the demagnetizing field is called the demagnetizing energy. It is a long range, Zeeman like energy term and it is given by:

$$\varepsilon_d = -\frac{\mu_0 M_S}{2}\vec{m} \cdot \vec{H}_d, \tag{1.3}$$

where the factor 1/2 avoids counting twice the interaction of two magnetic moments. Given that the stray field energy is a long range with a $1/r^3$ spatial dependency, there is an alternative approach for its calculation using a magnetic scalar potential. Surface ($\sigma = \vec{M} \cdot \vec{n}$) and volume charges ($\rho_m = -\vec{\nabla} \cdot \vec{M}$) are introduced and similar to Gauss electrostatic law, we get the following expression:

$$\varepsilon_d = \frac{1}{2}\mu_0\left(\int_V \rho_m\phi_d dV + \int_{\partial V}\sigma\phi_d dS\right), \tag{1.4}$$

where ϕ_d is the scalar magnetic potential. This approach was introduced by LaBonte [16] and Schabes and Aharoni [17] and it briefly means that the stronger the magnetic charges, the stronger the demagnetizing field that these charges create. As a consequence, the magnetization will preferably lie in the direction along which the magnetic charges are minimized, bringing us to a new concept: the shape anisotropy. The shape of the magnetic object plays a role determining the direction of magnetization. For a homogeneous magnetization the demagnetizing field is given by:

$$H_{d,i} = -N_i M_i \tag{1.5}$$

where repeated indices mean summation along the three spatial directions with $N_x + N_y + N_z = 1$. N_i are called the demagnetizing coefficients and are always positive. This field therefore is aligned in a direction

opposite to the magnetization. For clarification, Figure 1.1 illustrates how the demagnetizing field behaves with the magnetic charges in a thin film where the thickness t_{FM} is many orders of magnitude smaller than the plane dimensions.

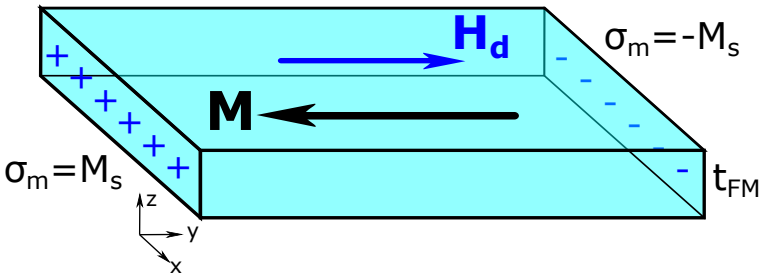

Fig. 1.1: Demagnetizing field | In a thin film geometry, the magnetization tends to align along the plane in order to minimize the magnetic charges it creates. These charges are responsible of creating the demagnetizing field inside the sample which is oriented against the magnetization direction.

For the thin film in Figure 1.1, the demagnetizing coefficients in the plane can be neglected, as $N_x \approx N_y \approx 0; N_z \approx 1$ [18]. So this energy term tends to align the magnetization in the film plane. The corresponding demagnetizing field writes $\vec{H}_d = -M_S\vec{m}$ and with an energy density:

$$\varepsilon_d = -\frac{\mu_0 M_S^2}{2}\sin^2\theta. \tag{1.6}$$

1.1.3 Zeeman energy

In the presence of an external magnetic field $\vec{H}_{ext}$, the Zeeman interaction of the magnetization $\vec{m}$ with the external magnetic field leads to the energy density ε_Z:

$$\varepsilon_Z = -\mu_0 M_S \vec{m}\cdot\vec{H}_{ext}. \tag{1.7}$$

In a non-uniform configuration, the magnetic domains with a magnetization aligned along the magnetic field will be energetically favoured compared to the ones with a magnetization aligned opposite to the field. This is illustrated in Figure 1.2.

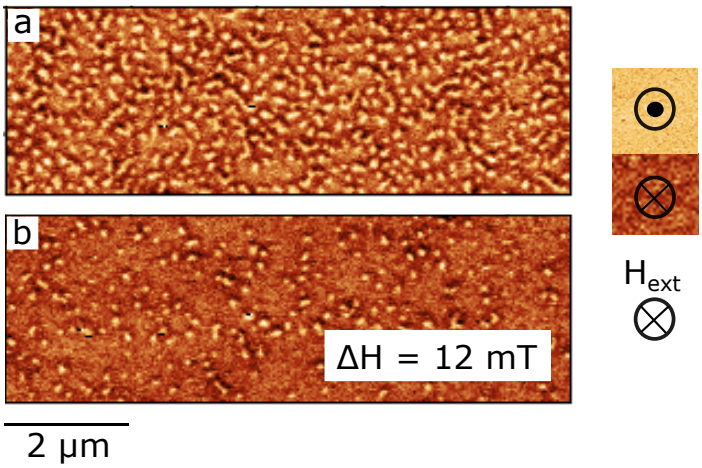

Fig. 1.2: Zeeman effect | **a** A non uniform domain structure measured by magnetic force microscopy in Pt/Co/Py. The white contrast domains have their magnetization oriented perpendicular to the film plane, upward, while the dark contrast domains have their magnetization oriented downward. **b** The same domain measured after applying a magnetic field perpendicular to the film plane downward. The Zeeman interaction leads to larger dark domains and smaller white domains.

1.1.4 Anisotropy energy

The properties of magnetic materials are often direction dependent. Magnetic anisotropy refers to the different magnetic response of magnetic materials depending on the direction of the excitation. The preferred direction of the magnetization is set by the magnetic anisotropy and finds its origin in various factors. One of this is the *shape anisotropy* which is induced by the shape of the material as we introduced before. Another factor that has an impact is the crystal symmetry of the material, which results in the so-called magnetocrystalline anisotropy. For instance, in the case of an uniaxial magnetic anisotropy, the energy is minimized when the magnetization lies along the magnetic easy axis. In a second order approximation, the energy cost associated to a magnetization angle θ away from this easy magnetic anisotropy axis is:

$$\varepsilon_{MC} = K_1 \sin^2 \theta, \tag{1.8}$$

where K_1 is the volume uniaxial anisotropy (J/m^3).

1.1.4.1 Interfacial magnetic anisotropy

Additional anisotropy energy contributions which are relevant in thin films were predicted by Néel [19]. The asymmetric environment related to the interfaces of a ferromagnet breaks its inversion symmetry. This leads to an interfacial magnetic anisotropy which can become predominant over the volume contributions (magnetocrystalline and shape anisotropies) when the magnetic object gets confined in two dimensions, i.e. thin films. Similar to 1.8, it reads:

$$\varepsilon_S = \frac{K_s}{t} \sin^2 \theta, \tag{1.9}$$

where K_s is the surface anisotropy constant (J/m^2), t is the magnetic thin film thickness and θ is the angle from the direction out of the plane.

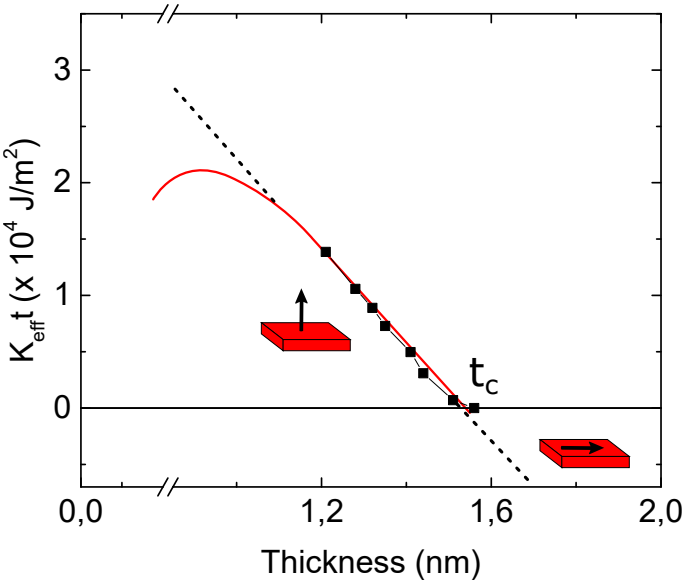

Fig. 1.3: Effective magnetic anisotropy | Thickness dependence of the anisotropy for a Pt/Co(t)/Ru based sample. The critical Co thickness corresponding to the in-plane/out-of-plane spin reorientation transition is around 1.6 nm. The slope represents the shape anisotropy constant $\frac{\mu_0}{2} M_S^2$ and the intercept at zero thickness would give the surface anisotropy constant K_S. The red curve is a guide for the eye that represents the drop of $K_{eff}t$ before it gets paramagnetic.

This interface-induced anisotropy contribution leads to a perpendicular magnetic anisotropy (PMA) with an easy axis direction perpendicular to the plane, directly competing with the shape anisotropy. Gathering all the anisotropy contributions we can define the effective anisotropy for a thin film with uniaxial anisotropy:

$$\varepsilon_{Keff} = \varepsilon_{MC} + \varepsilon_S + \varepsilon_d = K_1 \sin^2 \theta + \frac{K_s}{t} \sin^2 \theta - \frac{\mu_0}{2} M_S^2 \sin^2 \theta = K_{eff} \sin^2 \theta, \tag{1.10}$$

where $K_{eff} = K_1 + \frac{K_s}{t} - \frac{\mu_0}{2}M_S^2$. In ultrathin films the volume contribution from the crystallographic anisotropy is often small compared to the volume anisotropy, so the global anisotropy is the balance between the interfacial and the shape anisotropy, meaning $K_{eff} = \frac{K_s}{t} - \frac{\mu_0}{2}M_S^2 = K_u - \frac{\mu_0}{2}M_S^2$. If $K_{eff} > 0$, the preferable axis will be in the out-of-plane direction. We also see a direct dependence of the anisotropy on the film thickness: the anisotropy can be decreased (increased) by increasing (decreasing) the film thickness respectively. The spin reorientation transition i.e. between out-of-plane and in-plane anisotropies is obtained for a critical thickness value t_C for which $K_{eff} = 0$.

A part of my thesis was dedicated to the optimization of the magnetic properties of Pt/Co/Ru heterostructures. I show in Figure 1.3 some experimental values of $K_{eff}t$ as a function of the Co thickness. The thicker the ferromagnet, the lower the effective anisotropy due to the drop of the interfacial anisotropy. After the critical thickness t_C, the shape anisotropy brings the magnetization into the plane. For lower thicknesses, there is a point below which the material loses its magnetic properties and it becomes paramagnetic. This thickness is called *dead layer* and it has to be taken into account to calculate the surface anisotropy constant K_S, which is the intercept of the plot.

1.1.5 Interlayer exchange coupling

When magnetic films are separated by a thin metallic non-magnetic spacer layer, the magnetizations of these layers interact through an exchange mechanism involving the conduction electrons in the spacer layer named the RKKY (Ruderman-Kittel-Kasuya-Yosida) interaction [20–22]. It is analogous to the interaction observed between magnetic impurities within a non-magnetic host. This exchange mechanism can be either ferromagnetic or antiferromagnetic by varying the thickness of the spacer layer. The oscillatory dependence on the spacer layer thickness of the RKKY interaction was studied in particular during the investigation of giant magnetoresistance (GMR) with different transition metals [23]. The RKKY energy density is given by an exchange constant and the product of the magnetization direction of the layers: $\varepsilon_{RKKY} = J_{12}\vec{m}_1 \cdot \vec{m}_2$ where J_{12} represents the interlayer exchange constant. The dependence on the film thickness of the RKKY interaction can be described by the relation:

$$J_{12} \propto \frac{1}{t_{NM}^2} \sin\left(2k_F t_{NM} + \Theta\right), \tag{1.11}$$

where t_{NM} is the spacer thickness, k_F is the Fermi wave vector and Θ is a phase.

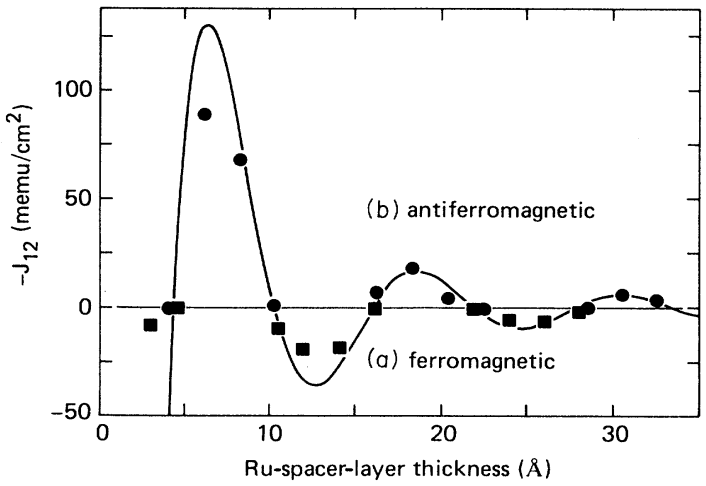

Fig. 1.4: Ruderman-Kittel-Kasuya-Yosida interaction | RKKY exchange constant measured in a CoNi/Ru/CoNi film as a function of the Ru thickness. The solid line is a fit. Adapted from [24].

Figure 1.4 shows the damped oscillatory behaviour of this interaction demonstrated by Parkin *et al.* in 1991 [24]. During my thesis in particular, I studied Co/Ru systems, characterized by a large RKKY interaction and we will take advantage of this interaction in order to build artificial antiferromagnetic ordering, i.e. the synthetic antiferromagnets in Chapters 4 and 5 for SAF skyrmions and in Chapter 6 for perpendicular MTJ structures.

1.1.6 Dzyaloshinskii-Moriya interaction

In the 60s Dzyaloshinskii made a significant contribution to the scientific community by exploring the interpretation of weak ferromagnetism measured in antiferromagnets [25]. Louis Néel initially referred to it as a 'parasitic' moment, attributing it to defects. However, Dzyaloshinskii proposed that this effect was real establishing a systematic framework for the directional behaviour of antiferromagnetic samples. He identified specific crystal lattices that could account for the observed phenomena in well-known samples such as αFe_2O_3, $MnCO_3$, $CoCO_3$. He proposed the existence of an additional exchange mechanism, distinct from the already established exchange energy terms. In his words, this would manifest in situations where inversion symmetry was lacking, resulting from relativistic spin-lattice interactions. However, it was Moriya who first proposed a microscopic explanation for the origins of this interaction [26,27]. He worked with a generalized form of the exchange interaction (repeated indices mean summation):

$$\varepsilon_{ij} = \vec{S}_i \cdot \left(\bar{\bar{J}}_{ij}\vec{S}_j\right), \qquad \bar{\bar{J}}_{ij} = \bar{\bar{J}}_{ij}^{symm} + \bar{\bar{J}}_{ij}^{antisymm}. \tag{1.12}$$

Here, it is possible to decompose the generalized exchange tensor in its symmetric and antisymmetric parts. It also means that the energy term will have both contributions:

$$\varepsilon_{ij} = \varepsilon_{ij}^{symm} + \varepsilon_{ij}^{antisymm} = \vec{S}_i \cdot \left(\bar{\bar{J}}_{ij}^{symm}\vec{S}_j\right) + \vec{S}_i \cdot \left(\bar{\bar{J}}_{ij}^{antisymm}\vec{S}_j\right). \tag{1.13}$$

The symmetric part can be diagonalized resulting in the symmetric exchange interaction (see Equation 1.1). The antisymmetric matrix can be written as:

$$\bar{\bar{J}}_{ij}^{antisymm}\vec{S} = -\vec{D}_{ij} \times \vec{S}. \tag{1.14}$$

This leads to the following expression for the Dzyaloshinskii-Moriya interaction:

$$\varepsilon_{ij}^{antisymm} = \vec{S}_i \cdot \left(\bar{\bar{J}}_{ij}^{antisymm}\vec{S}_j\right) = \vec{S}_i \cdot \left(-\vec{D}_{ij} \times \vec{S}_j\right) = \vec{D}_{ij} \cdot \left(\vec{S}_i \times \vec{S}_j\right). \tag{1.15}$$

The $\vec{D}_{ij}$ is the DMI vector whose direction is fixed by the symmetry of the crystal and its magnitude depends on the SOC. This interaction is known as Dzyaloshinskii-Moriya interaction. This interaction tends to favour a 90° alignment between neighbouring spins with a given sense of rotation, named *chirality*. The sense of rotation is fixed by the direction of the DMI vector. This asymmetric exchange interaction hence competes with the symmetric exchange interaction in the short range lengths opening the possibility to create non-collinear spin textures.

The origin of this interaction varies depending on how the inversion symmetry breaking is created. First, bulk DMI is present in some material systems such as FeGe B20 cubic phase and in MnSi where helical arrangements of spins were observed [28,29] at low temperatures and high magnetic fields. The common feature between these materials is the inversion symmetry breaking of their crystallinity structure. Bak *et al.* [30] associated those spin arrangements to the presence of "ferromagnetic Dzyaloshinskii instability". This bulk DMI favours Bloch like spin rotation. On the other hand, it was proposed that the DMI does not only exist in bulk systems, but also at the interfaces between magnetic materials and heavy metals [31,32]. This so called interfacial Dzyaloshinskii-Moriya interaction results from the breaking of the symmetry inversion at the interface, combined with the large spin orbit coupling in the heavy metal. In ultrathin films, the D vector lies in the film plane and it is perpendicular to the direction which links the two interacting spins. It tends thus to favour Néel like spin rotation, creating homochiral spin structures. As we have seen before, these interfaces play a major role in ultrathin films and the inversion symmetry comes from the stacking order using different materials [33].

1.2 Domain walls

1.2.1 Types and energies

In magnetic materials, the emergence of domains arises directly from the minimization of the free energy. Typically, within each domain, magnetization uniformly aligns along the sample magnetic easy axis due to the strong exchange interaction among neighboring spins and the magnetic anisotropy. On the other hand, the stray field energy tends to favour antiparallel alignment of the magnetization in neighboring domains. The transitional regions that separate these domains are known as domain walls. The characteristic width of domains is determined by the competition between the domain wall energy (minimizing the number of walls)

and the magnetostatic energy (maximizing the number of magnetic domains).

The specific internal structure of these domain walls, depends on the interplay and competition of various magnetic energies. Figure 1.5 illustrates different domain wall structures that help in understanding the energies at play in the domain wall formation. Figure 1.5a depicts an instantaneous reversal of the magnetic moments without a gradual transition between the antiparallel domains. This configuration is energetically favoured for the anisotropy term, as all spins align along the easy axis. However, it is the least favourable for exchange energy. Conversely, Figure 1.5b and 1.5c present the opposite scenario: a very wide domain wall with an extensive transition region between domains. Here, the angle variation between neighboring spins is minimal, optimizing exchange energy. However, a large number of spins deviate from the easy axis orientation, leading to a substantial cost in anisotropy energy. Therefore, the equilibrium domain wall width is determined by minimizing both energy contributions and by the relative strength of A and K.

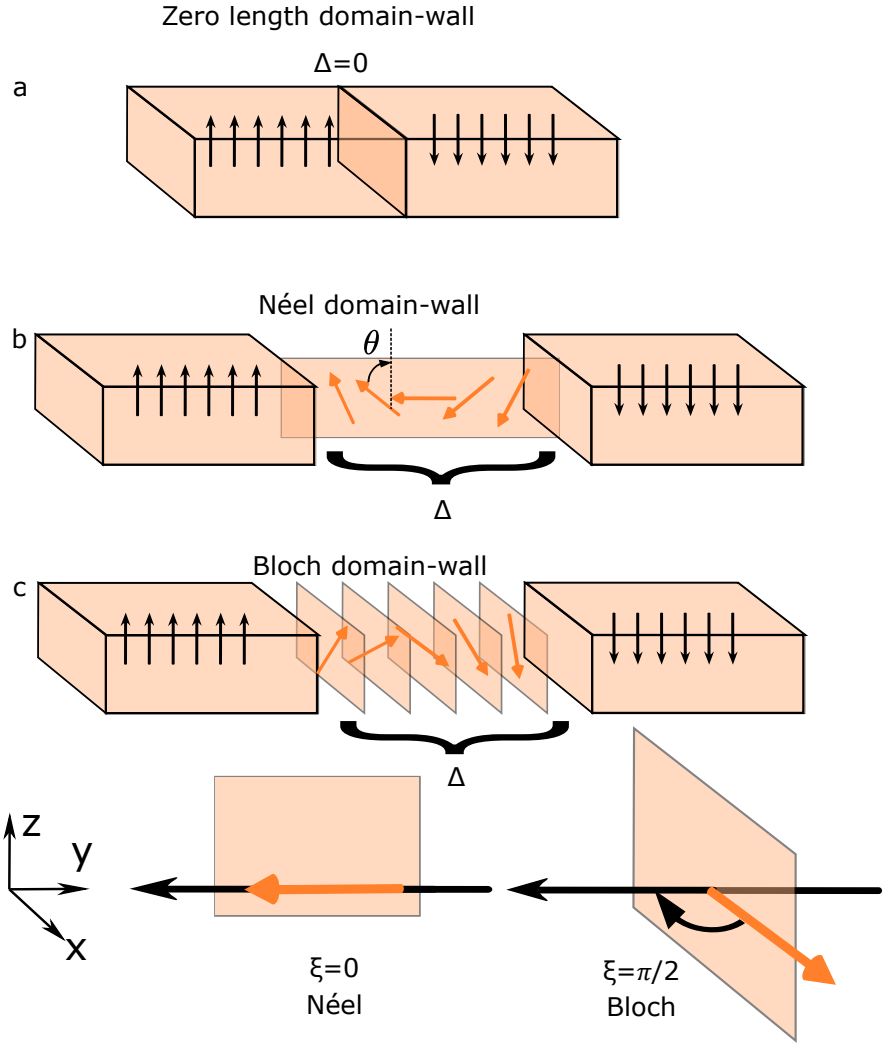

Fig. 1.5: Domain walls | **a** Domain wall of zero width. **b** Néel domain wall with finite width Δ. **c** Néel domain wall with finite width Δ. The type of domain wall is given by the helicity angle ξ. The tilt angle is represented as θ and varies as a function of the position y.

Let us consider a one dimensional scenario with PMA in which a domain wall is dividing two domains that are pointing in $\vec{z}$ and $-\vec{z}$. Here, considering only the exchange and anisotropy energies, we have the following energy density:

$$\varepsilon_{DW} = \varepsilon_{DW}^{ex} + \varepsilon_{DW}^{K}. \tag{1.16}$$

Developing the expressions for both energy densities using the equations 1.2 and 1.10, we have:

$$\varepsilon_{DW} = A\left(\left(\vec{\nabla}m_x\right)^2 + \left(\vec{\nabla}m_y\right)^2 + \left(\vec{\nabla}m_z\right)^2\right) + K_{eff}\sin^2\theta. \tag{1.17}$$

In the one dimensional approximation and using the polar (ϕ, θ) coordinate system defined relative to the z axis, we can express the local exchange and anisotropy energies in terms of these angle rotations:

$$\varepsilon_{DW} = A\left[\left(\frac{\partial\theta}{\partial y}\right)^2 + \sin^2\theta\left(\frac{\partial\phi}{\partial y}\right)^2\right] + K_{eff}\sin^2\theta. \tag{1.18}$$

It means that the domain wall structure will be such that it minimizes this energy. Note that θ and ϕ are only rotating as a function of the y position and θ gets values of π and 0 in the domain wall boundaries. Variations of the functions $\theta(y)$ and $\phi(y)$ should not have any effect in the energy functional, which means that[1] $\delta\varepsilon/\delta\phi = \delta\varepsilon/\delta\theta = 0$. Using Euler's equations for the functional derivatives to get the minimization of the energy density:

$$\frac{\partial\varepsilon_{DW}}{\partial\theta} - \frac{\partial}{\partial y}\left(\frac{\partial\varepsilon_{DW}}{\partial\left(\frac{\partial\theta}{\partial y}\right)}\right) = 0, \tag{1.19}$$

$$2A\left(\frac{\partial^2\theta}{\partial y^2}\right) = \left(A\left(\frac{\partial\phi}{\partial y}\right)^2 + K_{eff}\right)\sin 2\theta. \tag{1.20}$$

Similarly for ϕ:

$$\frac{\partial\varepsilon_{DW}}{\partial\phi} - \frac{\partial}{\partial y}\left(\frac{\partial\varepsilon_{DW}}{\partial\left(\frac{\partial\phi}{\partial y}\right)}\right) = 0, \tag{1.21}$$

$$\sin 2\theta\left(\frac{\partial\theta}{\partial y}\right)\left(\frac{\partial\phi}{\partial y}\right) + \sin^2\theta\left(\frac{\partial^2\phi}{\partial y^2}\right) = 0. \tag{1.22}$$

A domain wall profile that solves this equation is well known: $\theta(y) = 2\arctan(\exp(y/\Delta))$ and $\phi(y) = \xi$ (a constant value), where $\Delta = \sqrt{A/K_{eff}}$ is the domain wall width. Plugging this domain wall profile in the energy density and integrating over y gives the domain wall energy:

$$\sigma_{DW} = \int(\varepsilon_{ex} + \varepsilon_K)\,dy = (A/\Delta^2 + K_{eff})\int_{-\infty}^{\infty}\mathrm{sech}^2(y/\Delta)\,dy = (A/\Delta^2 + K_{eff})2\Delta$$
$$= 4\sqrt{AK_{eff}}. \tag{1.23}$$

All ξ values of the domain wall angle magnetization are solutions of the equations. This is due to the fact that we did not consider other energy terms.

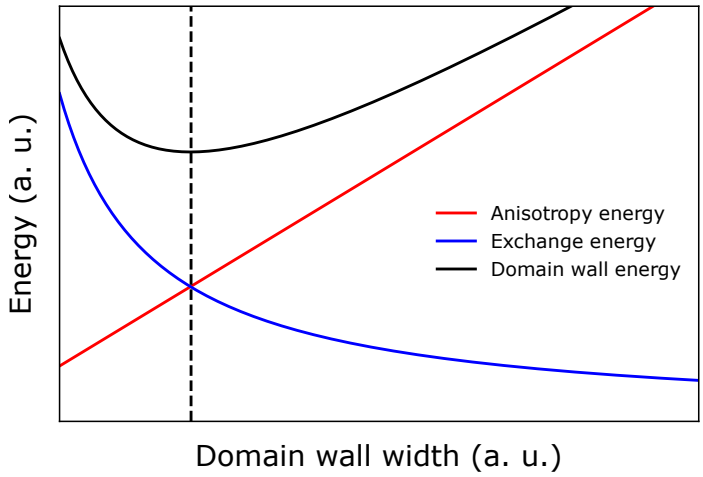

Fig. 1.6: Domain wall energies | Domain wall energy (black) and both exchange (blue) and anisotropy (red) energy contributions as a function of the domain wall width. As the vertical dotted line shows, the minimum in the domain wall energy is the point at which the exchange energy and the anisotropy energy are equal.

It is notable to mention that both energies contribute equally to the DW energy. This is represented in Figure 1.6 where the intersection of the exchange and anisotropy energies corresponds to the minimum

[1] The functional derivatives are defined as: $\delta\varepsilon/\delta\theta = \partial\varepsilon/\partial\theta - \vec{\nabla}\cdot\partial\varepsilon/\partial\vec{\nabla}\theta$.

DW energy. So far we have only considered the case with anisotropy and symmetric exchange energies in 1D. However, we can implement a further analysis including the DW demagnetizing energy. In thin films, another factor influencing the DW type is the interfacial DMI. For instance, when magnetic thin films exhibit perpendicular magnetic anisotropy (PMA) and lack interfacial DMI, the minimization of the DW volume magnetic charges favours the stabilization of Bloch-type DWs (see Figure 1.5c). Conversely, the introduction of interfacial DMI into such systems promotes the stabilization of Néel-type DWs (see Figure 1.5b).

Generalizing hence and including the DMI and the DW demagnetizing energy terms to the system we analyzed before, a similar computation brings us to the energy density. We introduce K_d as the DW demagnetizing energy constant:

$$\varepsilon_{DW} = \varepsilon_{DW}^0 + K_d \cos^2\phi \sin^2\theta - D\left(\frac{\partial\theta}{\partial y}\right)\cos\phi, \tag{1.24}$$

where ε_{DW}^0 stands for Equation 1.18. Here, if D is small compared to the other energy terms, Equation 1.24 looks like Equation 1.18. Thus, we may assume $\phi = \xi$ and the DW satisfies again the equation $\theta(y) = 2\arctan(\exp(y/\Delta))$. We consider also that Δ does not change in the first approximation. Inserting these solutions in energy:

$$\begin{aligned}\sigma_{DW} &= \int (\varepsilon_{ex} + \varepsilon_K + \varepsilon_{DMI} + \varepsilon_d) \\ &= 4\sqrt{AK_{eff}} - D\Delta\cos\xi \int_{-\infty}^{\infty} \operatorname{sech}(y/\Delta)\, dy - \frac{\mu_0}{2} 2\Delta M_S^2 \cos^2\xi \\ &= 4\sqrt{AK_{eff}} - D\pi\cos\xi + 2\Delta K_d \cos^2\xi.\end{aligned} \tag{1.25}$$

The DMI acts on the DW similarly to an effective field which is perpendicular to the DW surface, favouring a Néel domain wall. In the absence of DMI, the wall is in a Bloch configuration ($\xi = \pi/2$) as dictated by the dipolar energy (see Figure 1.7). Upon increasing the DMI, the magnetization in the wall progressively tilts away from the transverse direction and gets oriented perpendicular to the DW surface. In such configurations the helicity angle ξ is solvable and reads:

$$\xi = \arccos\frac{\pi D}{4\Delta K_d}, \qquad D < D_C. \tag{1.26}$$

If the magnitude of the interfacial DMI is insufficient, a competition with the volume magnetic charges can lead to the stabilization of domain walls with a structure between the Néel and Bloch configuration.

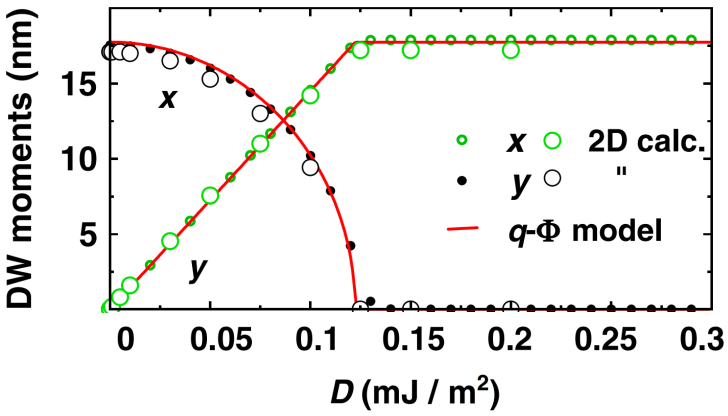

Fig. 1.7: Equilibrium domain wall configurations | DMI strength dependence for a domain wall showing a transition from Bloch at $D = 0$ to a Néel wall. From [34].

Finally, when the DMI is large enough, the wall is in a Néel configuration. The critical DMI value at which this transition occurs is given by:

$$D_C = \frac{4}{\pi}\sqrt{AK_d}. \tag{1.27}$$

It determines the boundary between intermediate and purely Néel wall configurations. To conclude, in a magnetic material with large DMI, given the energetically favoured sense of domain wall rotation, we arrive to the concept of *homochirality*. Every domain wall will have the same favoured chirality. In case there is no DMI, Bloch walls will be favoured without any fixed sense of rotation.

1.3 Domain wall dynamics

The magnetization dynamics and particularly the domain wall dynamics is ruled by the Landau-Lifshitz-Gilbert (LLG) [35,36] equation:

$$\frac{\partial \vec{m}}{\partial t} = -\gamma_0 \left(\vec{m} \times \vec{H}_{eff} \right) + \alpha \left(\vec{m} \times \frac{\partial \vec{m}}{\partial t} \right), \tag{1.28}$$

where $\vec{H}_{eff}$ includes all the respective fields that each energy term creates through $\mu_0 \vec{H}_i = -\frac{1}{M_S} \frac{\delta E_i}{\delta \vec{m}}$, namely the anisotropy, exchange, dipolar, Zeeman and the external field. $\vec{m}$ is the reduced magnetization and $\gamma_0 = \mu_0 \gamma$ where γ (GHz/T) is the gyromagnetic ratio given by $\gamma = g\,|e|\,/2m$. g represents the Landé factor, while e and m are the charge and mass of the electron. α is the Gilbert damping parameter. This equation describes how magnetization responds to an effective field, generating torques that can induce precession or switching, among other effects. When the magnetization is not aligned with the effective magnetic field, two torques are generated. Both are orthogonal to each-other and to the magnetization, as illustrated in Figure 1.8.

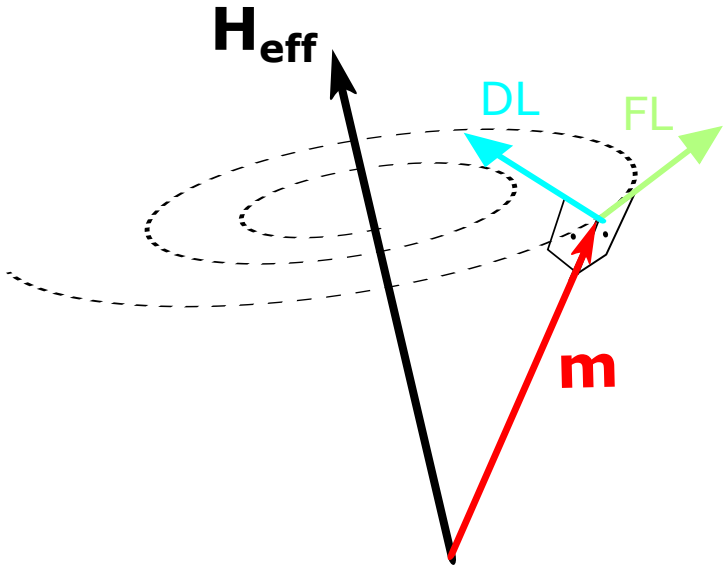

Fig. 1.8: Magnetization dynamics | Trajectory of the magnetization under an effective field. DL and FL are the 'damping like' and 'field like' torques generated by the LLG equation acting on the magnetization vector due to $\vec{H}_{eff}$.

These torques have different character: on the one hand, we have a torque (green in Figure 1.8) that drives the magnetization in a precessional way around the direction of the effective magnetic field $\vec{H}_{eff}$. This term is energy conservative, meaning that in the absence of dissipation, the precessional motion would last forever. In the presence of this term only, the magnetization would precess at the Larmor angular velocity $\omega = \gamma_0 H_{eff}$ around the direction of the effective field. The second torque (blue in Figure 1.8) is the Gilbert damping torque. It tends to bring the magnetization vector towards the direction of $\vec{H}_{eff}$. It is a dissipative term and describes how the systems loses its energy [37]. The combination of both torques results in a damped precession of the magnetization until it aligns with the effective external field. The parameter α represents the strength of this damping and varies from material to material. In case other energy terms are also taken into account to describe the magnetization (or DW) dynamics, one can add them in the LLG equation as if they would represent an additional effective magnetic field. This way, the torques that will be associated with that energy term will also have both a 'field like' (FL) or 'damping like' (DL) character.

1.3.1 Field-driven dynamics

In order to understand better how the magnetization in a magnetic material is affected by an external field it is more convenient to rewrite the equation 1.28 in an equivalent way:

$$\frac{\partial \vec{m}}{\partial t} = -\frac{\gamma_0}{1+\alpha^2} \left(\vec{m} \times \vec{H}_{eff} \right) - \frac{\alpha \gamma_0}{1+\alpha^2} \vec{m} \times \left(\vec{m} \times \vec{H}_{eff} \right) \tag{1.29}$$

$$= \vec{T}_{FL} + \vec{T}_{DL}, \tag{1.30}$$

where it is easier to identify the orthogonal direction of both torques. Figure 1.9 represents an example of how the external field applied in the $+\vec{z}$ affects a magnetic material with PMA with two domains (up/down) and a Bloch DW.

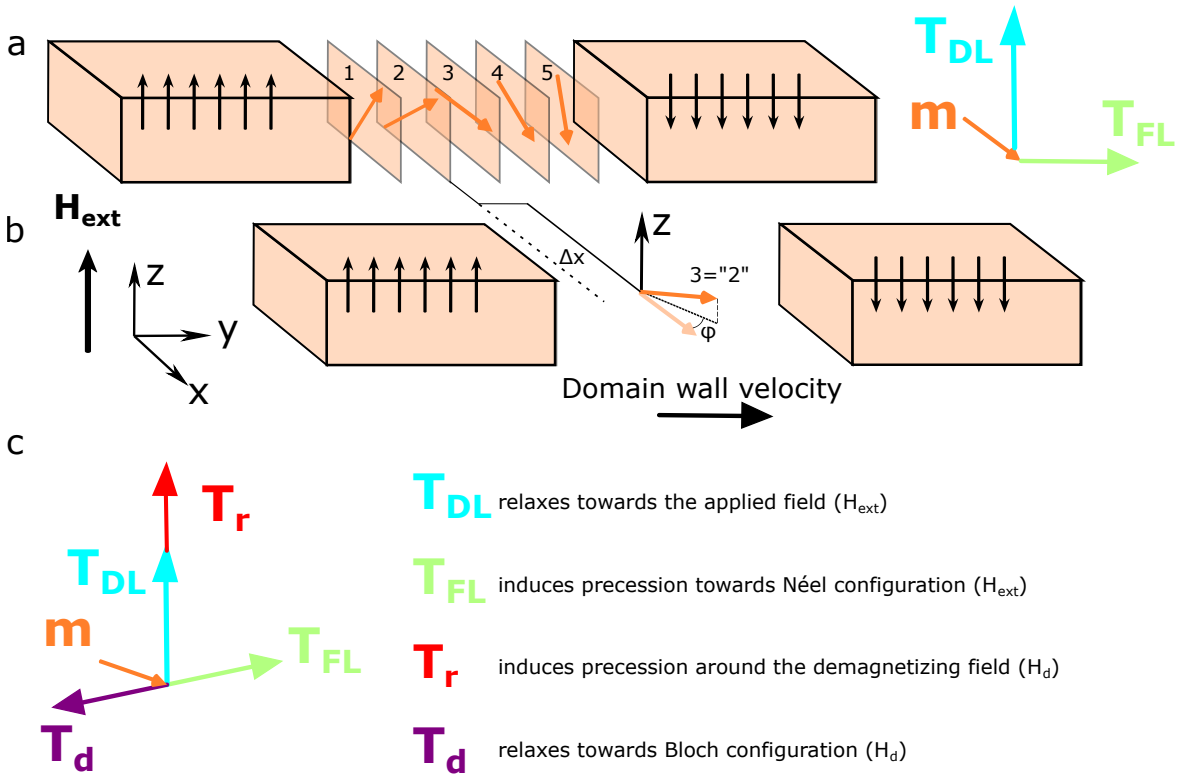

Fig. 1.9: Field driven Bloch DW dynamics | **a** Schematics of the torques in the center of the domain wall. **b** Effect of the torques on the magnetization vector Nr.3 that becomes like Nr.2 with a tilt during the motion. This represents an effective translation Δx of the wall towards the $\vec{y}$ direction due to the external field. **c** Direction of the generated torques on the magnetization (Nr.3) in **b** when it goes away from the equilibrium. In parenthesis, the field that originates those torques for clarity.

It is straightforward to see that no torque is applied in the perpendicular domains parallel to the field. It means that all the dynamics in this geometry will be related to the domain wall. If we focus on the magnetization vector at the center of the domain wall (Nr.3) pointing towards the x direction, the torques that it will feel due to the external field are:

$$\vec{T}_{FL} = -\frac{\gamma_0}{1+\alpha^2}\left(\vec{m}\times\vec{H}_{ext}\right) = \frac{\gamma_0}{1+\alpha^2}H_{ext}\vec{y}, \tag{1.31}$$

$$\vec{T}_{DL} = -\frac{\alpha\gamma_0}{1+\alpha^2}\vec{m}\times\left(\vec{m}\times\vec{H}_{ext}\right) = \frac{\alpha\gamma_0}{1+\alpha^2}H_{ext}\vec{z}. \tag{1.32}$$

As a result, the magnetization tilts both towards $+\vec{y}$ and $+\vec{z}$ away from the xy plane. This represents an effective translation of the domain wall center together with a tilt on the xy plane of the wall during the dynamics. The tilt of the magnetic moment leads to an accumulation of magnetic charges. In this new position, the magnetic moment experiences two additional torques due to the demagnetizing field: first, an additive reacting torque ($\vec{T}_r$, red torque in Figure 1.9c) in the direction of the damping-like torque, and second, a dissipative torque ($\vec{T}_d$, purple) that competes directly with the field-like torque. While the field torque tries to take the magnetic moments away from its Bloch configuration, the damping torque due to the demagnetizing field tries to put it back. Therefore, as long as these two torque compensate each-other, the tilting angle of the magnetic moment is fixed and determined by the balance between these two torques. The resulting wall is in an intermediate configuration between Bloch and Néel and the domain wall is in steady motion, only driven by the torques along the external field direction. To sum up, the DW is moving with a steady-state angle φ along the $+\vec{y}$ direction in this case. This flow regime has a high domain wall mobility and it was first proposed by Walker in 1974 [38]. If the external field is creating a torque larger than the damping torque of demagnetizing field, the magnetic moment precesses around the external field. This threshold field is known as the Walker field $\vec{H}_W$, and as a result, the azimuthal angle is not constant anymore and the domain wall enters in a precessional regime. There is a sharp drop in the velocity of the domain wall and the mobility is lower [39] (see Figure 1.10).

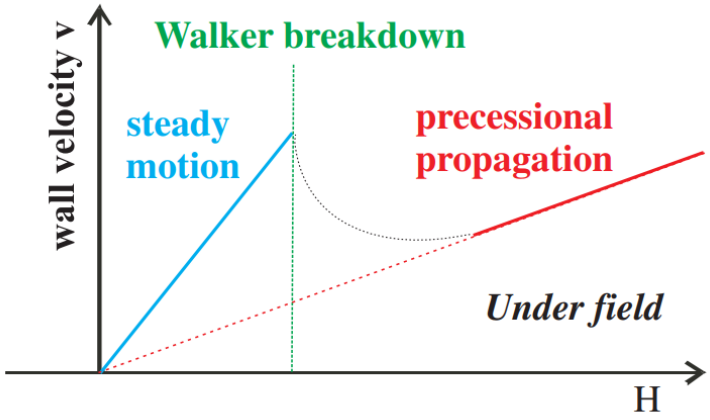

Fig. 1.10: Domain wall motion | Sketch of a domain wall velocity as a function of an external magnetic field. From [39].

The equations of motion of the azimuthal angle and velocity driven by an external field can be derived [38] and they read as:

$$\frac{d\xi}{dt} + \frac{\alpha v}{\Delta} = \gamma_0 H, \tag{1.33}$$

$$\left(1+\alpha^2\right)\frac{d\xi}{dt} = \gamma_0 H - \alpha\gamma_0 \frac{2K_d}{M_S}\sin\xi\cos\xi. \tag{1.34}$$

For a steady motion, $\frac{d\xi}{dt} = 0$ and the azimuthal angle is constant for a given field. Together with the steady state velocity, they are given by:

$$\sin 2\xi = \frac{M_S}{\alpha K_d} H, \tag{1.35}$$

$$v = \frac{\gamma_0 \Delta}{\alpha} H. \tag{1.36}$$

A characteristic feature of the steady motion is that the velocity is inversely proportional to the magnetic damping. If we consider now the case when the applied field exceeds the critical Walker field $H > H_W = \frac{\alpha K_d}{M_S}$, the time derivative of the azimuthal angle does not vanish anymore and the domain wall enters the precessional regime as stated before. In this precessional regime, the azimuthal angle has a complex time dependence but one can assume that the time average of the $\cos\xi\sin\xi$ is zero. Taking the time average of the velocity:

$$< v > = \alpha\Delta\frac{d\xi}{dt} + \gamma_0\Delta\frac{2K_d}{M_S} < \cos\xi\sin\xi >, \tag{1.37}$$

$$v = \frac{\gamma_0\alpha\Delta}{1+\alpha^2} H. \tag{1.38}$$

The mobility of the domain wall is much smaller in the precessional regime compared to the steady state regime as we see in Figure 1.10.

This model is considering perfect samples without defects that may lead to local variations of magnetic properties, creating stable local sites called pinning sites. This brings us to define the depinning field, which is the required field in order to see motion of the domain wall. In real systems at room temperature, even if the applied magnetic field is lower than the depinning field, the DW can move via thermally activated jumps or deformations. This regime is called the creep/thermally activated regime and velocities are still low (typically below 10 m/s). Here, the domain wall velocity loses its linearity, as can be seen in Figure 1.11 compared to Figure 1.9c. Increasing the magnetic field would lead the system to a flow regime in which the pinning sites are no longer relevant. However, in order to identify the steady or precessional regimes, the analysis has to be done with care because it can be difficult to distinguish between both regimes. This is important, for instance, when field-driven domain wall dynamics experiments are performed to characterize the magnetic damping.

The analysis of field-driven DW motion in presence of interfacial DMI was done by Thiaville *et al.* [34] where it was reported that the effective field created by the DMI energy opposes to the tilt of the magnetization. As a consequence, the Walker breakdown comes at higher external fields and larger DW velocities were reported in ultrathin HM/FM/NM asymmetric trilayers compared to the HM/FM/HM symmetric ones. Pham *et al.* compared Pt/Co/Pt and Pt/Co/AlOx trilayers (see Figure 1.11) reporting that the DMI allowed to reach very large field-driven DW velocities [40]. The authors argue that in symmetric Pt/Co/Pt stacks the Walker field is expected to be low, 12 mT, having as a result a precessional regime with low mobility. On the contrary, in Pt/Co/AlOx, the DMI stabilizes the flow regime up to large magnetic field, explaining the large mobility observed.

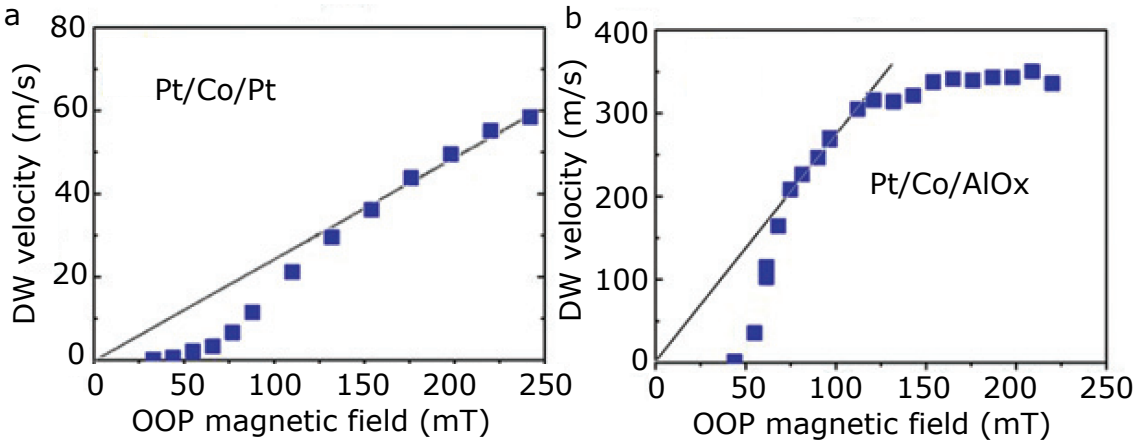

Fig. 1.11: Field driven DW dynamics | Comparison of DW velocities vs external out-of-plane magnetic field in **a** symmetric Pt/Co/Pt and **b** asymmetric Pt/Co/AlOx trilayers. From [40], labels in have been rewritten for better visualization.

In this scenario, following Equation 1.29 and minimizing for ξ gives $\sin\xi\,(D\pi - 4\Delta K_d \cos\xi) = 0$, meaning that Néel DWs ($\xi = 0$) are favoured when $D > D_C = 4\pi K_d/\pi$. When applying an external field and using Slonczewski equations [34], the model is also analytically solvable in the stationary regime $d\xi/dt = 0$. The stability condition for ξ requires $2K_d/(\mu_0 M_S)\cos 2\xi - \pi D/(2\mu_0 M_S \Delta)\cos\xi < 0$. From this, we can solve for $\cos\xi$:

$$\cos\xi_W = \frac{1}{4}\left(\frac{\pi D}{4\Delta K_d} - \sqrt{\left(\frac{\pi D}{4\Delta K_d}\right)^2 + 8}\right), \tag{1.39}$$

where ξ_W is the angle at the Walker field. The Walker field is given by:

$$H_W = \alpha \frac{\pi D}{2\mu_0 M_S \Delta} \sin\xi_W \left(1 - \frac{4\Delta K_d}{\pi D}\cos\xi_W\right). \tag{1.40}$$

The DW becomes a Néel type wall at large D with $H_W = \alpha\pi D/(2\mu_0 M_S\Delta)$. We therefore see directly how the Walker field depends on the DMI. In absence of DMI, note that we recover the same ξ value in Equation 1.39 as in Equation 1.35.

1.3.2 Current-driven dynamics

Other means to manipulate the magnetization and in particular the domain walls are electrical currents. Large current-induced DW velocities, up to 400 m/s, were reported by Miron *et al.* in ultrathin Pt/Co/AlO_x films showing similar dynamical trends between field and current-driven motions [8].

There are two main mechanisms for current-induced magnetization dynamics: the spin transfer torque (STT) [41] and the spin orbit torque (SOT) [7]. Both can be present in magnetic materials, but for DW dynamics the SOT driven motions have more advantages [42,43]. I will briefly mention them.

1.3.2.1 Spin transfer torque

It was initially proposed by Berger [44] and Slonczewski [5] in 1996. The key advantage of STT lies in its ability to manipulate magnetization without the need for an external magnetic field. For instance, in

magnetic random-access memories (MRAM), STT is employed for writing information in magnetic tunnel junctions. The STT refers to a transport phenomenon where the angular momentum is transferred from the spins of conduction electrons to the local magnetic moments. The impact of the spin current on the magnetization can be characterized by two additional torque terms in the Landau-Lifshitz-Gilbert (LLG) equation: the adiabatic and non-adiabatic torques:

$$\frac{\partial \vec{m}}{\partial t} = -\gamma_0 \left(\vec{m} \times \vec{H}_{eff}\right) + \alpha \left(\vec{m} \times \frac{\partial \vec{m}}{\partial t}\right) + \vec{T}_{ad} + \vec{T}_{non-ad}, \tag{1.41}$$

$$\vec{T}_{ad} = -\left(\vec{u} \cdot \vec{\nabla}\right) \vec{m}, \tag{1.42}$$

$$\vec{T}_{non-ad} = \beta \vec{m} \times \left(\left(\vec{u} \cdot \vec{\nabla}\right) \vec{m}\right). \tag{1.43}$$

The adiabatic torque tends to align the magnetic moments with the spin direction of the conduction electrons. $\vec{u} = (g\mu_B P/2eM_S)\,\vec{J}$ with P the spin polarization of the current and $\vec{J}$ is the current density [45]. When an electron current is injected into a FM, it is spin polarized in the direction of the magnetization $\vec{m} = \pm\vec{z}$. This means that the current spin polarization rotates by 180° when traversing a 180° domain wall. This change of spin angular moment is transferred to the domain wall magnetization, leading to a torque, named adiabatic torque, along $\vec{z}$. This torque results in a net translation of the DW. For any kind of domain wall (configuration or helicity) the current-induced domain wall dynamics via STT leads to a motion of the domain wall along the electron flow, assuming a positive polarization. The non-adiabatic torque had to be introduced in order to explain the lower threshold current observed experimentally as compared to predictions and acts as a dissipative torque [46–49]. The dimensionless β coefficient is related to the strength of the non-adiabatic term.

1.3.2.2 Spin orbit torque

Another mechanism to manipulate magnetization and particularly domain walls by electrical currents is the spin orbit torque (SOT). While the spin current generation in STT results from the electron spin dependent scattering in metallic ferromagnets, for SOT in HM/FM/NM trilayer systems the spin current is generated due to the interaction between the spin of electrons and their orbital moment, known as spin-orbit coupling (SOC). The two predominant effect originating the SOT are the spin Hall effect (SHE) [50–52] and the Rashba-Edelstein effect [53,54]. When SOT is considered, additional terms are introduced in the LLG equation to account for the torque exerted on the magnetization. The LLG equation with the inclusion of SOT terms is as follows:

$$\frac{\partial \vec{m}}{\partial t} = -\gamma_0 \left(\vec{m} \times \vec{H}_{eff}\right) + \alpha \left(\vec{m} \times \frac{\partial \vec{m}}{\partial t}\right) + \vec{T}_{SOT}, \tag{1.44}$$

$$\vec{T}_{SOT} = -\gamma_0 \left(\vec{m} \times \vec{H}_{DL}\right) - \gamma_0 \left(\vec{m} \times \vec{H}_{FL}\right). \tag{1.45}$$

where we decomposed the SOT into two orthogonal torques, the damping-like (DL) and field-like (FL) SOT. They are also orthogonal to the magnetization vector and effective fields are used to express them. I will present now the two physical mechanisms through which the SOC acts in systems with broken inversion symmetry, such as HM/FM/NM.

Spin Hall effect When a current is injected into a HM, the SOC in the HM induces a pure spin current, leading to a spin accumulation in the boundaries as shown in Figure 1.12. This phenomenon is known as the spin Hall effect. At a HM/FM interface, this spin accumulation creates a torque on the FM magnetization via the transfer of the angular momentum to the magnetic moments close to the interface. The direction of spin current is transverse to the current density and is given by $\vec{J}_S \propto \vec{s} \times \vec{J}$. Considering that the SHE effect only generates DL torques, the damping like effective field associated to this torque is given by:

$$\vec{H}_{DL} = H^0_{DL} \left(\left(\vec{z} \times \vec{j}\right) \times \vec{m}\right), \tag{1.46}$$

where $\vec{j}$ is the normalized current density unit vector and $H^0_{DL} = \hbar\theta_{SH} J/(2|e|M_S t)$ gathers the current density value as well as θ_{SH}, the spin Hall angle (SHA) [55]. The SHA is the efficiency of the charge to spin conversion and its amplitude and signs are material dependent. The use of the HM to generate large spin accumulations is due to the larger SOC in large atomic number atoms, as it scales as Z^4 [56]. Regarding the sign of the SHA, it can be positive (Pt [57–59], Pd, Ti, Au) or negative (Ta [59,60], W [61], Hf) having therefore opposite spin polarization at the interfaces and directly influencing in the torque direction.

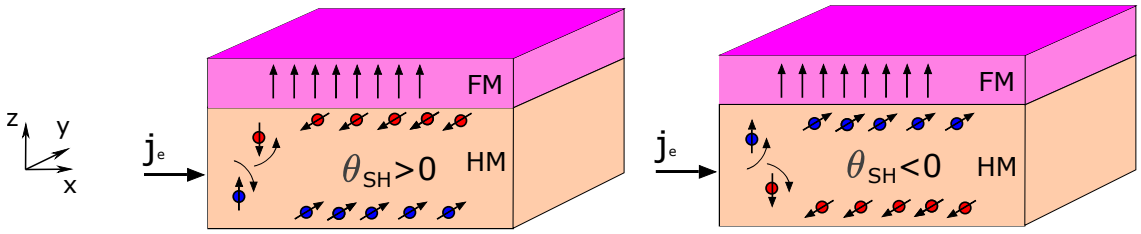

Fig. 1.12: Spin Hall effect (SHE) | Schematic figure of the spin Hall effect where a current goes through a heavy metal and the different spins accumulate in the opposite interfaces. The direction of the spin polarization of the accumulated spins depends on the nature of the HM.

SOT driven DW motion To better understand how the SOT acts on a spin texture such as a homochiral Néel domain wall stabilized by DMI, we follow the work of Thiaville *et al.* [34] where the Thiele force equation approach is used. The effect of the SOT on the domain wall can be considered as an equivalent field along the easy axis:

$$H = \frac{\pi\hbar\theta_{SH}}{4e\mu_0 M_S t} J\cos\xi. \tag{1.47}$$

Thus, the largest effective field is expected for Néel walls, while there would not be any effect for Bloch walls. Let us consider now the configuration shown in Figure 1.13 where two homochiral Néel domain walls are stabilized by DMI. We choose the Pt as a HM with a positive SHA and the current density injected along the x direction. The direction of the spin accumulation at the HM/FM interface is along -$\vec{y}$. As a result, following Equation 1.46, the damping like field associated to the SOT is $\vec{H}_{DL} = H^0_{DL}\,(\vec{m}\times\vec{y})$. This means that the damping like field is opposite in both domain walls (see Figure 1.13) and they move in the same direction. Furthermore, the field is maximum for the homochiral Néel wall configuration we chose, as stated before in Equation 1.47. This effect is highly useful for domain wall based applications such as racetrack memories.

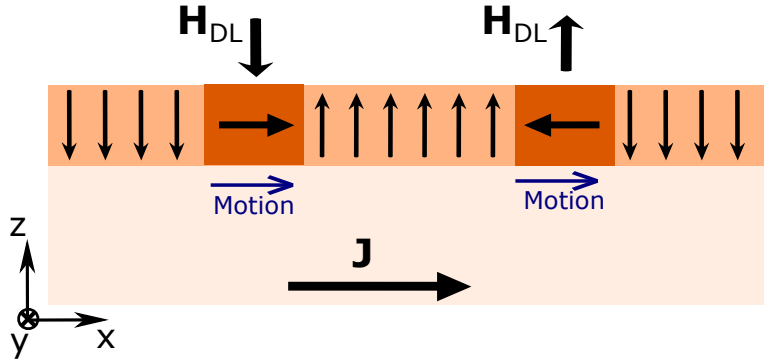

Fig. 1.13: Current driven dynamics with SOT | Schematic figure of the motion of two domain walls. An electric current is injected through the HM, generating an effective damping like torque that moves both domain walls along the same direction.

With large DMI values the current-induced DW velocity at the steady state is [34]:

$$v = \frac{\gamma_0\pi D}{2\mu_0 M_S}\frac{1}{\sqrt{1+\left(\frac{2\alpha teD}{\hbar\theta_H\Delta J}\right)^2}}. \tag{1.48}$$

Here, larger DMI values give larger velocities and at large current densities the velocity saturates.

1.4 Magnetic tunnel junctions and tunneling magnetoresistance

The magnetic tunnel junction (MTJ) serves as a fundamental unit for magnetoresistive random access memory cells (MRAM) [62]. MTJs are composed of two ferromagnetic layers separated by a thin insulating layer. Here, electrons can tunnel through the barrier when a bias voltage is applied between the two metal electrodes on either side of the insulator. The crucial characteristic of an MTJ is that the relative orientation of the magnetizations in the two ferromagnetic layers results in different tunneling currents. This alignment can be altered by an applied magnetic field. This phenomenon is known as tunneling magnetoresistance (TMR). The concept of MTJ and TMR was first demonstrated by Jullière in 1975 [3], using a Fe/GeO/Co trilayer at low temperatures (4.2 K). To explain this observation, Jullière developed a simple model based on the different tunneling probabilities of majority and minority spin-polarized currents when the electrode's magnetizations are aligned parallel or antiparallel.

The model is based on two assumptions. Firstly, that the electron spin is conserved during the tunneling event. As a result, the tunneling of up and down spins are two independent processes, such that one can define two independent conducting spin channels. As a result, when both FM are in a parallel configuration, the transport will be dominated by the path of the majority spin up electrons from FM1 that freely tunnel to the majority spin states of FM2. Same for the minority spin down electrons. In contrast, when the layers are in anti-parallel configuration, majority spin electrons from FM1 can only tunnel into minority states of FM2, and vice versa. A second assumption is that the electron tunneling probability is proportional to the density of states. Here, Jullière postulated that the conductance for a specific spin alignment is directly related to the combined effective density of states (pertaining to tunneling) of the two ferromagnetic electrodes. Based on these postulates, the conductance for parallel (G_P) and antiparallel (G_{AP}) configurations can be expressed as follows:

$$G_P \propto \rho_1^{up}\rho_2^{up} + \rho_1^{down}\rho_2^{down}, \tag{1.49}$$

$$G_{AP} \propto \rho_1^{up}\rho_2^{down} + \rho_1^{down}\rho_2^{up}. \tag{1.50}$$

Here, ρ_i^{up} and ρ_i^{down} represent the tunneling density of states (DOS) of the ferromagnetic electrodes (indexed as i = 1, 2) for electrons with majority and minority spins. The parallel and anti-parallel conductances are therefore different and there is a net TMR effect which can be expressed as the difference of the conductances normalized by the AP conductance [3]:

$$TMR = \frac{G_P - G_{AP}}{G_{AP}} = \frac{R_{AP} - R_P}{R_P}, \tag{1.51}$$

where the R_{AP} and R_P represent the respective resistances. Applying equation 1.50, we arrive to Jullière's formula where the magnetoresistance ratio of a MTJ can be expressed as a function of the spin polarizations of the ferromagnets:

$$TMR = \frac{2P_1P_2}{1 - P_1P_2}, \tag{1.52}$$

by defining the ferromagnet polarizations:

$$P = \frac{\rho^{up} - \rho^{down}}{\rho^{up} + \rho^{down}}. \tag{1.53}$$

Initially, the tunnel magnetoresistance (TMR) effect did not receive much attention. However, with the subsequent discovery of giant magnetoresistance (GMR) and its potential applications, researchers became more interested in developing MTJ structures that exhibit TMR at room temperature. Interface quality and crystallinity are crucial in order to enhance the TMR. The breakthrough came with the work of Miyazaki *et al.* and Moodera *et al.* [4,63], who achieved TMR at room temperature using insulating barriers based on amorphous aluminum oxides (AlOx) (see Figure 1.14). In addition to the studies regarding the bias [3] and the relative angle between the layers [4], temperature [64], crystalline orientation [65] and barrier type [66] dependencies of the TMR quickly arrived. With further optimizations in the composition of ferromagnetic electrodes and the crystal quality of the entire MTJ structure, the TMR ratios continued to increase. It became evident that not only the ferromagnetic electrodes played a crucial role in determining the spin polarization efficiency, but also the crystallographic structure and epitaxial growth of the entire trilayer contributed significantly. In 2001, more advanced model calculations by Butler and Mathon took into account the impact of the different density of states (DOS) for each type of electron in the trilayer band structure. These calculations predicted a large TMR of up to 1600% for Fe and Co epitaxially grown on MgO.

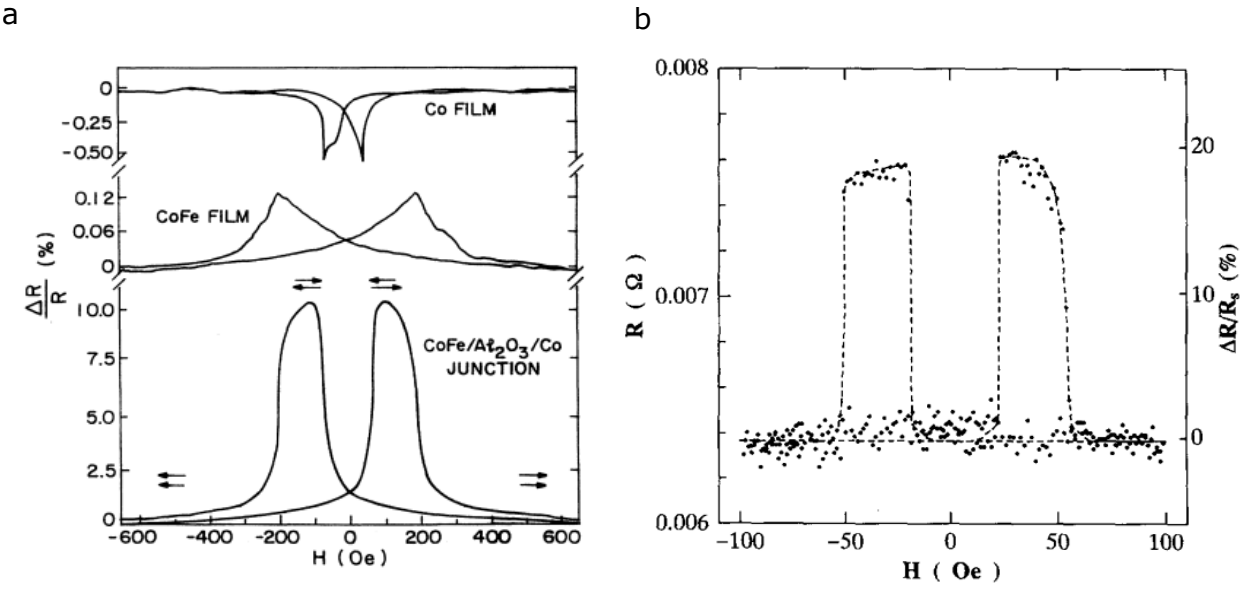

Fig. 1.14: First room temperature Tunneling Magnetoresistance (TMR) experiments | **a** Resistance of $CoFe/Al_2O_3/Co$ junction vs magnetic field in the film plane, at 295 K. Variations in the CoFe and Co film resistances are shown. The arrows indicate the direction of the magnetization in the two films. **b** Resistance as a function of the magnetic field for a $Fe/Al_2O_3/Fe$ junction. Both adapted from [4,63].

However, the epitaxial growth of MgO-based MTJs is challenging and not compatible with industrial constrains due to the slow growth process with Molecular-beam epitaxy (MBE). This can be overcome by considering a novel MTJ structure: CoFeB/MgO/CoFeB [67]. Here a (001) MgO barrier layer could be grown on an amorphous CoFeB layer through sputtering deposition at room temperature. Subsequent annealing of the CoFeB/MgO/CoFeB MTJs above 250°C causes the amorphous CoFeB electrode layers to crystallize into the bcc (001) structure. The excellent lattice matching between MgO (001) and bcc CoFeB (001) allows the MgO to act as a template for crystallizing CoFeB. This fully (001) textured configuration explains the large TMR observed in this stack with %604 at 300 K measured by Ikeda *et al.* in 2008 [68].

A benefit of employing an insulating barrier in this setup is the resulting increased impedance compared to spin valves relying on giant magnetoresistance (GMR). This higher resistance, typically measuring a few kΩ, simplifies the integration of magnetic tunnel junctions with transistors, a necessity for MRAM applications. Other advantages of MTJs is their high sensitivity and low power consumption combined with non-volatility, having as a result a significant gain in attention. These devices can retain their data even when the power is turned off. The cost of production of MTJs varies depending on the specific materials and processes used. However, the use of advanced manufacturing technologies has made it possible to produce MTJs on a large scale, which has reduced their overall cost and increased their availability.

Chapter 6 describes the MTJ stack we optimized during my thesis. X-ray microscopy measurements and observations will be shown as well as the characterization of its magnetic properties.

1.5 Voltage controlled magnetic anisotropy (VCMA)

Voltage control of magnetic anisotropy (VCMA) is a phenomenon that allows for the manipulation of the preferred orientation of the magnetization using an applied voltage. This effect is of great interest in spintronics, as it offers a mean to control magnetic properties without the need for a magnetic field. When a voltage is applied across a typical FM/MOx structure, an accumulation or a depletion of electrons is induced at the FM/MOx interface [69], depending on its polarity. The limited penetration of the electric field into the FM layer localizes this effect at the interface. The electron density distribution is therefore altered, having as a result a direct impact on the magnetic properties related to the interfaces, such as the interfacial magnetic anisotropy or the interfacial DMI [70,71]. The VCMA effect can be associated with several mechanisms, such as the electronic distribution or oxygen migration from the oxide towards the MOx/FM interface [72–75]. The change in magnetic anisotropy can be detected using various techniques, such as magnetoresistance measurements or magnetic imaging methods.

In 2006, Duan *et al.* [76] made a significant theoretical progress with the prediction of the existence of the VCMA effect in an $Fe/BaTiO_3$ composite multiferroic sandwich. Through *ab-initio* calculations, they discovered that electric fields in the $BaTiO_3$ could modulate the magnetic moment of interfacial Fe atoms by inducing orbital modifications, such as changes in bonding at the $Fe/BaTiO_3$ interface. This effect had nothing to do with the strain from $BaTiO_3$ and the findings paved the way for future electric field control of magnetism. Rondinelli *et al.* [77] extended those theoretical predictions showing that the VCMA effect could apply to any interface between a dielectric and a spin-polarized metal, interpreting their calculations as a direct magnetic response of the system to an applied electric field.

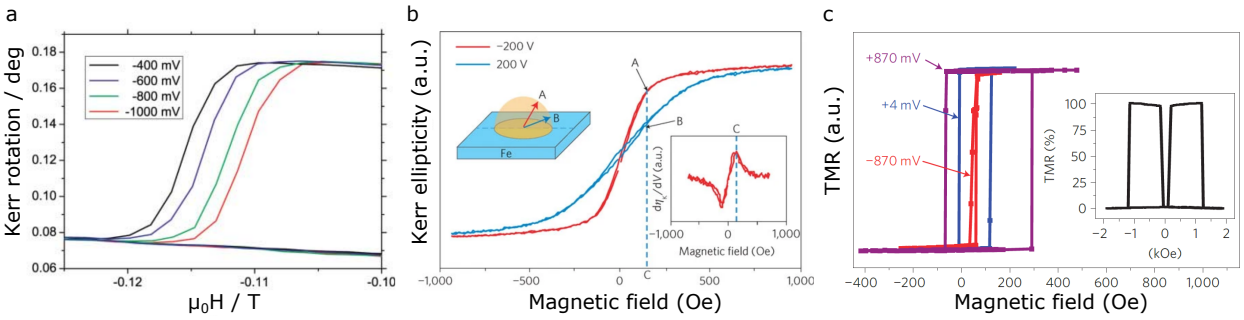

Fig. 1.15: Voltage control of magnetic anisotropy (VCMA) | **a** Magnetization switching of the 2 nm-thick FePt film for different voltage values. From [78]. **b** A significant change in the hysteresis curve indicates a large change in perpendicular anisotropy following application of the bias voltage. From [79]. **c** TMR loops for different voltages showing the anisotropy modulation. From [80]. Labels have been rewritten for better visualization.

Experiments did not take long to arrive: Weisheit *et al.*, in 2007, demonstrated the VCMA effect by observing a maximum 4.5% change in the coercivity of FePt and FePd thin-films immersed in an electrolyte solution that allowed charges to accumulate at the film surface due to an electric field (Figure 1.15a). "The modification of the magnetic parameters was attributed to a change in the number of unpaired d electrons in response to the applied electric field", claimed the authors [78]. In the field, an important step forward was then achieved by Maruyama *et al.* in 2009 [79], setting the stage for exploiting the VCMA effect in MTJs (Figure 1.15b). They observed a significant VCMA effect using a Fe/MgO sandwich, a highly relevant material combination in spintronics. A couple of years later, the first electric field induced switching of MTJ devices was reported by Wang *et al.* [80] and Shiota *et al.* [81], as illustrated in Figure 1.15c.

The change in magnetic anisotropy of the free layer is a key input for electric-field-induced switching. In a FM film, the effective magnetic anisotropy reads as:

$$K_{eff}(V) = \frac{\mu_0 H_{Keff} M_S}{2} \approx \frac{K_s(V)}{t} - 2\pi M_S^2, \tag{1.54}$$

where $K_s(V)$ is the voltage dependent surface anisotropy and t is the thickness of the FM layer. The external electric field is given by $E_{ext} = V/d$, where V represents the applied voltage, and d is the thickness of the MgO barrier. The function $K_s(V)$ may not have a linear dependence but in most experiments the results led to the following expression:

$$K_s(V) = K_s(V = 0) - \epsilon V/d, \tag{1.55}$$

where ϵ is the VCMA coefficient used to characterize this effect. It is highly dependent on the material stack and on the interfacial properties and it ranges in values around 30-50 fJ/V·m [80,82]. Chapter 6 details more on these VCMA measurements on our MTJ samples.

1.6 Conclusions

In this chapter, we have first provided an overview of the different energetic contributions that determine the stable magnetic configuration in ultrathin film systems with PMA. In particular, we have studied the crucial role of the DMI in the stabilization of chiral Néel DWs. We have also presented the main mechanism that governs the current-induced dynamics of Néel DW, particularly the SOTs originated from the SHE. Finally, we have introduced the MTJ memory element and the concept of TMR, as well as the VCMA phenomenon, which is responsible for modulating the anisotropy of a system with an electric field. These effects will be present in magnetic skyrmions both in thin films and MTJs.

Chapter 2

Magnetic skyrmions

Contents

2.1 Basics and properties about magnetic skyrmions 26
2.2 Energies of skyrmion stabilization 27
2.3 Observation of magnetic skyrmions 30
2.4 Manipulation of magnetic skyrmions: current-induced motion 32
2.4.1 The skyrmion Hall effect 33
2.5 Electrical detection of skyrmions 36
2.6 Skyrmion-based applications 37
2.7 Synthetic antiferromagnetic skyrmions: stability and dynamics 38
2.8 Conclusions 41

This chapter will describe the basics of magnetic skyrmions. The requirements for nucleation, stability and dynamics will be discussed as well as the means of detection. The existing literature will be thoroughly examined, and any unresolved inquiries will be addressed. Applications to memory and logic devices are also introduced, going through their physics and development.

2.1 Basics and properties about magnetic skyrmions

Initially proposed by T. Skyrme to describe hadrons in particle physics [83], skyrmions are known in magnetism as bi-dimensional, axis-symmetric, localized, non-collinear spin textures in a ferromagnetic background. These textures are enclosed by a chiral domain wall with a given sense of rotation, defining the opposite magnetization direction in the core and outside the core of these entities.

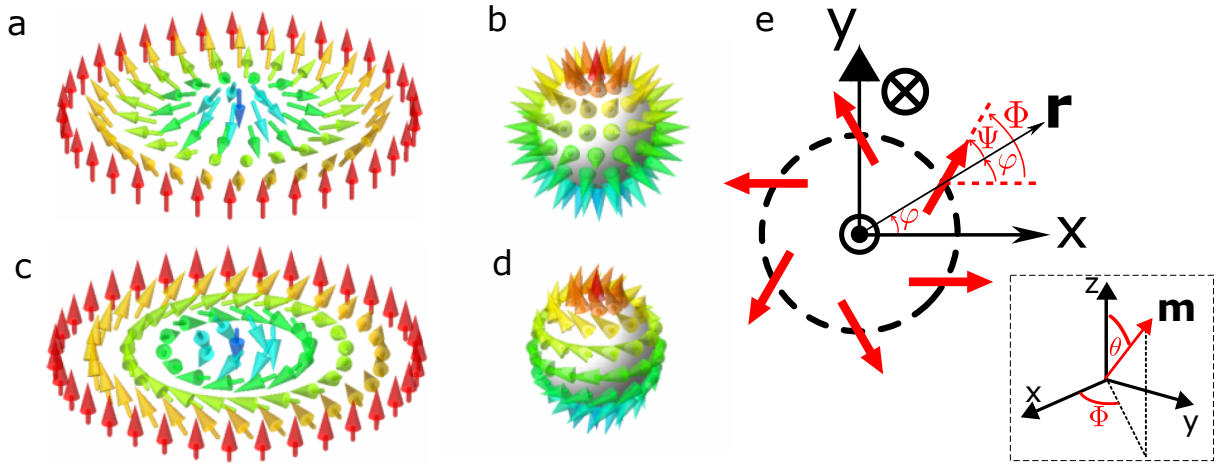

Fig. 2.1: Magnetic skyrmions | **a** A Néel skyrmion with its core pointing down (blue arrow) and a gradual radial-plane rotation of the spins until the periphery (red arrows). **b** Mapping of the spins from the configuration in **a** to the unit sphere, showing a full radial direction of the spins. The stereographic projection of **b** leads to the skyrmion in **a**. **c** A Bloch skyrmion with its core pointing again down (blue arrow) and the spins rotating in the tangential planes, perpendicular to the radial directions, when moving from the core to the periphery. **d** Same as in **b** but for a Bloch skyrmion, with the characteristic tilt of the spins. Adapted from [84]. **e** Top view of a skyrmion for the definition of magnetization angles with respect to the radial direction. The inset in dashed rectangle represents the spherical polar angles for the calculation of the skyrmion number.

Magnetic skyrmions were first proposed in the 90s by Bogdanov *et al.* [85,86]. We introduce in Figure 2.1 schematic representations of these whirling textures. The way the magnetization is twisted from the center to the edge is defining two types of magnetic skyrmions, named Néel and Bloch where the magnetization rotates in the radial or in the tangential plane. This angle between the magnetization and the radial direction is called the helicity angle, Ψ (see Figure 2.1e). It has a value of 0 (or π) for Néel skyrmions and $\pi/2$ (or -$\pi/2$) for Bloch skyrmions (Figure 2.1a and 2.1c respectively), but there can be also be some intermediate helicity angles. Both Bloch and Néel skyrmions can be stabilized in magnetic materials. The skyrmion topology is described by the skyrmion number N_{Sk} (or topological index, topological charge):

$$N_{Sk} = \frac{1}{4\pi} \iint \vec{m} \cdot \left(\frac{\partial \vec{m}}{\partial x} \times \frac{\partial \vec{m}}{\partial y} \right) dxdy. \tag{2.1}$$

To better understand this mathematical notion, let us consider the case of a uniform ferromagnetic thin film with the magnetization oriented in the $+\vec{z}$ direction: here, the reduced magnetization texture would simply be $\vec{m}(\vec{r}) = +\vec{z}$ without any spatial dependence in the infinite film. This means the derivatives in the integral are trivially cancelled and we end up with $N_{Sk} = 0$. When the magnetization $\vec{m}$ with spherical coordinates (θ, Φ) has a dependence on the position vector $\vec{r}$, the cylindrical symmetry (r, φ) (see Figure 2.1e) allows us to write the integral in the following way:

$$\begin{aligned} N_{Sk} &= \frac{1}{4\pi} \int_0^{2\pi} \int_0^{\infty} \frac{\partial \theta}{\partial r} \frac{\partial \Phi}{\partial \varphi} \sin\theta dr d\varphi \\ &= \frac{1}{4\pi} \int_0^{2\pi} d\varphi \frac{\partial \Phi}{\partial \varphi} \int_0^{\infty} \sin\theta \frac{\partial \theta}{\partial r} dr \\ &= \frac{1}{4\pi} \left[\Phi(\varphi)\right]_0^{2\pi} \left[-\cos\theta(r)\right]_0^{\infty} = W \cdot p, \end{aligned} \tag{2.2}$$

with p the skyrmion core polarity number and W the winding number. Note that $m_z = \cos\theta(r)$. So the

definition of these two numbers is given by:

$$p = \frac{1}{2}\left[-\cos\theta(r)\right]_0^{\infty} = \frac{1}{2}\left[m_z(0) - m_z(\infty)\right] = \pm 1, \tag{2.3}$$

$$W = \frac{1}{2\pi}\left[\Phi(\varphi)\right]_0^{2\pi}, \tag{2.4}$$

which classifies them depending on the direction of their core polarity p and the number of times the spin configuration covers the whole sphere, denoted by W. If one integrates all the spin configuration containing a skyrmion along the infinite bi-dimensional plane, the result for skyrmions is a winding number of $W = 1$, and thus skyrmion numbers of -1 or +1, while antiskyrmions [87] have a winding number of $W = -1$ (see Figure 2.2). This integral is a way to count the number of times the spin configuration can wrap a sphere [87,88]. Further development of this calculation to classify skyrmion is performed in the Appendix A.1, but having a look to the Figure 2.1, we can see that both skyrmions have a negative core orientation in z ($p = -1$) and wrap the sphere only once ($W = 1$), giving as a result a skyrmion number of $N_{Sk} = -1$. Changing the ferromagnetic background and twisting the core of these skyrmions would lead to $N_{Sk} = 1$. Owing to its topological properties, the skyrmion cannot be continuously transformed toward a ferromagnetic state or any other states with a different skyrmion number. However, one can show that the resulting energy barrier in a continuous model is around $8\pi Ad$ with A the exchange constant and d the film thickness [89–91]. This provides a large stability to the skyrmion.

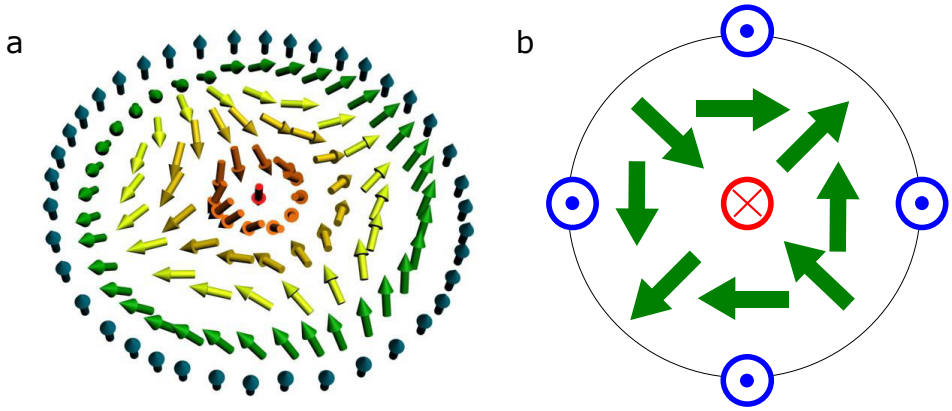

Fig. 2.2: Magnetic antiskyrmion | **a** Adapted illustration from [87] for an antiskyrmion whose magnetization rotates both as a cycloid and a transverse helix, shown as top view in **b**.

Since the experimental demonstration of skyrmions (see Section 2.3), other (topological) magnetic textures have been also introduced and observed, namely the antiskyrmion (see Figure 2.2), the skyrmionium [92,93] or the in-plane skyrmion [94–96]. They are beyond the scope of this thesis but these entities are characterized with the different number of times they wrap the sphere.

2.2 Energies of skyrmion stabilization

All the energy terms we described in Chapter 1 contribute in different ways on the skyrmions. A fine balance between them is necessary for the skyrmion stabilization. The topological soliton energy functional that contains the exchange, anisotropy, DMI, demagnetizing and Zeeman energy terms can be written as [85,97–100]:

$$E_\sigma\left[\theta(r)\right] = \\ = 2\pi t \int_0^{\infty} \left[A\left[\left(\frac{d\theta}{dr}\right)^2 + \frac{\sin^2\theta}{r^2}\right] - K_u\cos^2\theta - D\left[\frac{d\theta}{dr} + \frac{\cos\theta\sin\theta}{r}\right] - \mu_0 M_S H\cos\theta + E_d \right] r dr, \tag{2.5}$$

where the demagnetizing energy can be written as the sum of volume and surface magnetic charges $E_d = E_d^{vol} + E_d^{surf}$. The long range nature of the demagnetizing effects prevents us from having an analytical expression of $\theta(r)$ that minimizes the energy functional. In order to solve this, we follow the analysis of the energy terms in magnetic skyrmions with the model proposed by Bernard-Mantel *et al.* [97] where isolated skyrmions and bubble spin textures are described in an infinite ferromagnetic thin film. In this model, the skyrmion energy with respect to the uniforms state is:

$$E_{sk} = E_{exch} + E_{anis} + E_{DMI} + E_Z + E_d. \tag{2.6}$$

When the skyrmion radious is much larger than the DW width, the analytical expressions for those energy terms can be written as:

$$E_{exch} = \frac{E_0}{\frac{2R}{\pi\Delta}+1} + 2\sqrt{AK_{eff}} \cdot 2\pi Rt, \tag{2.7}$$

$$E_{anis} = 2\sqrt{AK_{eff}} \cdot 2\pi Rt, \tag{2.8}$$

$$E_{DMI} = -\pi D \cdot 2\pi Rt, \tag{2.9}$$

$$E_Z = \mu_0 M_S H_{ext} \cdot \pi R^2 t, \tag{2.10}$$

$$E_d = -\mu_0 M_S^2 I(2R/t) \cdot 2\pi Rt^2, \tag{2.11}$$

where R is the skyrmion radious, Δ is the domain wall width, A is the exchange constant, K_{eff} is the effective anisotropy, D is the DM constant ($D > 0$ and considering the DM reduces the energy), t is the thin film thickness, M_S the saturation magnetization, $\mu_0 H_{ext}$ the external magnetic field and $I(2R/t)$ is a formula to obtain the surface demagnetising energy for large radius and is composed of complete first and second kind elliptical integrals [101]. Finally, $E_0 = E_{sk}(R = 0) = 8\pi At$ is the zero radious limit finite energy value. So the skyrmion energy is:

$$E_{sk} = \frac{E_0}{\frac{2R}{\pi\Delta}+1} + 4\sqrt{AK_{eff}} \cdot 2\pi Rt - \pi D \cdot 2\pi Rt + \mu_0 M_S H \cdot \pi R^2 t - \mu_0 M_S^2 I(d) \cdot 2\pi Rt^2. \tag{2.12}$$

Note that these are already integrated energy contributions, not energy densities. This is why we can now extract the different energy dependencies on several sets of parameters to get the corresponding skyrmion radious, if any. If the skyrmion is stable it means that the skyrmion energy will have a minima for those set of material parameters. We choose the following standard parameters making sure that the radious is always large compared to the DW width: $A = 16$ pJ/m, $t = 1$ nm, $\mu_0 H_K = 100$ mT, $D = 1$ mJ/m^2 and $M_S = 1.4$ MA/m. The plots in Figure 2.3 show the total skyrmion energy and the different individual energy contributions with respect to the radius and for different external fields.

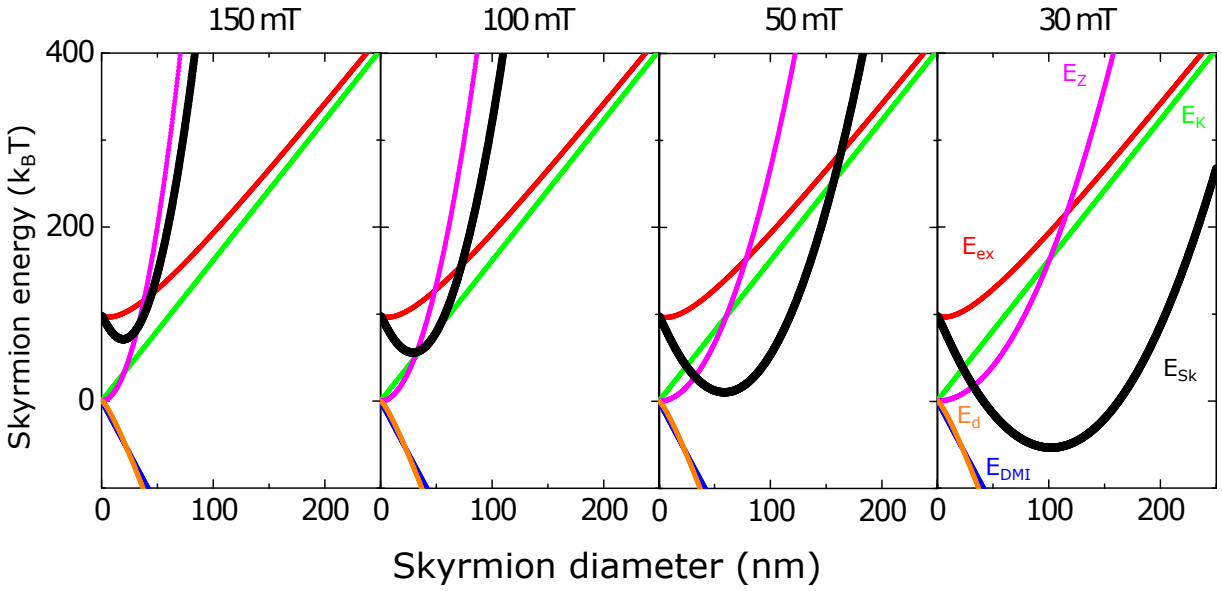

Fig. 2.3: Energies for a magnetic skyrmion | **a** Different energy contributions for a magnetic skyrmion in a homogeneous infinite FM thin film vs the radious of the skyrmion. Skyrmion energy (E_{sk}) in black, exchange (E_{ex}), anisotropy (E_{Keff}), DMI (E_{DMI}), Zeeman (E_Z) and dipolar (E_d) energies are plotted for the following magnetic parameters: $A = 16$ pJ/m, $t = 1$ nm, $\mu_0 H_K = 100$ mT, $D = 1$ mJ/m^2, $M_S = 1.4$ MA/m.

First of all, the anisotropy and exchange energies are monotonously increasing with the size of the skyrmion. At high diameter values compared to the domain wall width, their contribution to the skyrmion energy is identical and the exchange energy converges to the anisotropy energy. Secondly, the DMI and

long-range dipolar terms are monotonously decreasing the skyrmion energy with the skyrmion size. These terms tend to stabilize the skyrmion. Lastly, there is the Zeeman energy which has a quadratic growth (proportional to the skyrmion area) with the diameter. The larger the external field, the sharper growth of the Zeeman energy, which would lead to a decrease of the skyrmion size.

To further study the dependencies on tunable parameters, we choose a range of external magnetic fields in which the skyrmion is stable and vary the anisotropy and the DMI around common values of HM/FM structures. Figure 2.4 shows the corresponding behaviours of the skyrmion size and the associated energy in each case. Larger DMI in Figure 2.4a,c leads to larger and more stable skyrmions, while larger anisotropy (Figure 2.4b,d) tends to decrease the size and reduce the stability due to the increase of the skyrmion energy.

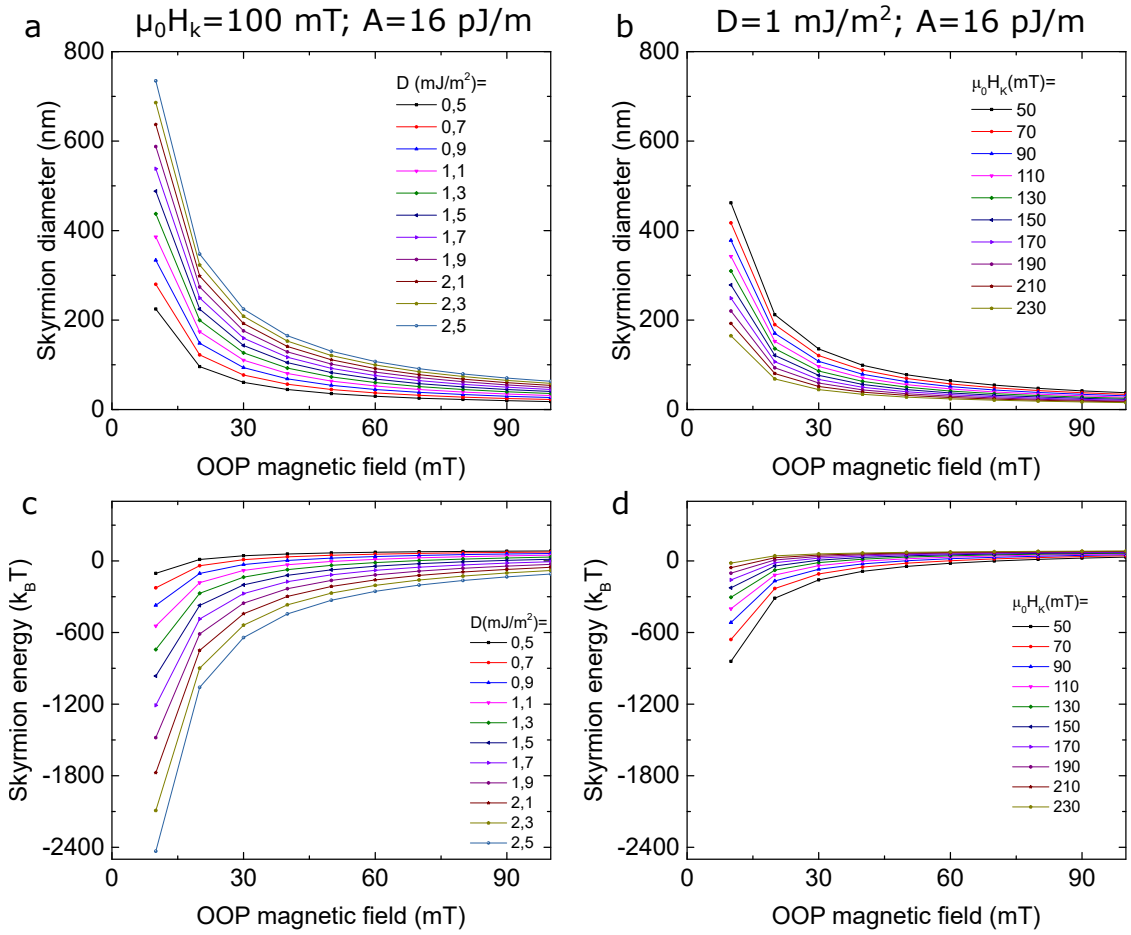

Fig. 2.4: DMI, effective anisotropy and exchange dependencies on the magnetic skyrmion | **a** Skyrmion diameter as a function of the external out-of-plane magnetic field for different DMI values with $\mu_0 H_K = 100$ mT and $A = 16$ pJ/m. **b** Skyrmion diameter as a function of the external out-of-plane magnetic field for different anisotropy values with $D = 1$ mJ/m^2 and $A = 16$ pJ/m. **c-d** Same as **a-b** but for the skyrmion energy. The other parameters are kept constant: $t = 1$ nm and $M_S = 1.4$ MA/m.

This means, convenient properties of materials to host thermally stable skyrmions are large DMI and small anisotropy. Lastly, when one wants to start to find materials to host skyrmions and the DMI strength of the interfaces is uncertain, it is interesting to target low anisotropies by increasing the thickness of the FM material. This way, even if their size will be large, the long range dipolar contributions will help to stabilize the skyrmions. As an example, in Chapter 6, we host skyrmions in an environment which is known not to have large DMI. This is why we targeted a low anisotropy stack composition by increasing the material thickness. With our experimental parameters ($\mu_0 H_K = 35$ mT, $A = 12$ pJ/m, $M_S = 1.63$ MA/m, $t = 1.08$ nm and $D = 0.14$ mJ/m^2), the model predicts a skyrmion around 253 nm diameter with an external field of 16 mT.

2.3 Observation of magnetic skyrmions

The first experimental observation of magnetic skyrmions was in 2009 by Mühlbauer *et al.* The authors reported the evidence of skyrmion lattices in MnSi with a B20 crystalline structure, utilizing small angle neutron scattering [110]. The study showed that at temperatures around 27 K and external out-of-plane magnetic field of 0.16 T, magnetic materials without inversion symmetry can create new kinds of stable spin arrangements. Skyrmion lattices were later observed using real space Lorentz transmission electron microscopy in $Fe_{1-x}Co_xSi$, another B20 chiral magnet [102] (Figure 2.5a) as well as in FeGe [111] by Yu *et al.* Here Bloch skyrmions with a well defined chirality are observed. Their stabilization is explained by the presence of a bulk like DMI due to the non-centrosymmetric structure of B20 crystals. First chiral spin textures were observed in ultrathin films in 2007, with the demonstration of spin spirals in Mn(1ML) on W(110) at cryogenic temperatures [112] and in nanowires in 2010 [113]. In 2011, skyrmion lattices were observed in monolayers of Fe on Ir(111) by Heinze *et al.* [114] using spin-polarized scanning tunnelling microscopy, demonstrating these textures in real space. The short-range four-spin interaction and large DMI in the interface between the Fe and Ir(111) led to atomic scale Néel skyrmion sizes. However, strong magnetic fields and low temperatures were required for their stabilization. Other works by Romming *et al.* followed in thin film systems [105] on PdFe bilayers epitaxially grown on Ir(111). Non collinear spin textures such as spin spirals were detected in the absence of magnetic fields, while a transition to a saturated state was observed at fields around 1 T, through an emergence of individual skyrmions.

The first observations and stabilization of skyrmions both in bulk and thin film systems were performed at low temperature. The potential use of magnetic skyrmions to encode information in memory and logic devices led to a search for materials which allow the stabilization of skyrmions at RT. This requires a fine tuning of the different energies, namely the DMI, the stray field, the anisotropy energy and the exchange energies. For this, the attention has shifted to ultrathin heavy metal (HM)/ferromagnetic (FM) films, such as Pt/Co multilayers. Indeed, the different energies can be easily tuned by playing on the nature and thickness of the multilayer structure. In particular, these materials feature large perpendicular magnetic anisotropy at the ferromagnetic/heavy metal interfaces as well as a large interfacial DMI owing to the large spin orbit coupling and structure inversion asymmetry at the interface. Furthermore, these asymmetrical heterostructures can be efficiently deposited on Si substrates using magnetron sputtering, a technique compatible with industry requirements.

After 2014, several groups demonstrated RT skyrmions in sputtered HM/FM/non magnetic stacks (FM $\sim$ 1 nm), having either a single or many repetitions of the trilayer system such as Pt/Co/MgO (Figure 2.5b) [103], Ta/FeCoB/TaOx (Figure 2.5e) [106], $(Pt/CoFeB/MgO)_{15}$ (Figure 2.5h) or $(Pt/Co/Ta)_{15}$ [109]. In particular, in 2016, Moreau-Luchaire *et al.* reported in sputtered multilayers the addition of interfacial DM interaction to achieve the stabilization of individual skyrmions at RT. The Co layer was sandwiched between two different heavy metals (Pt and Ir) forming an asymmetric environment for the ferromagnet. The reason behind stacking ten repetitions was to overcome the temperature fluctuations. This combination resulted in an enhancement of the DM interaction, reaching values close to 2 mJ/m^2 in the case of the Ir/Co/Pt asymmetric multilayers. The sizes of the skyrmions were about 30–90 nm as observed by STXM (see Figure 2.5g). Another example is the work of Boulle *et al.* from SPINTEC [103]. They demonstrated RT skyrmion in ultrathin Pt/Co/MgO and observed their internal chiral Néel structure. They used the XMCD-PEEM magnetic microscopy combining a high spatial resolution as well as a sensitivity to the in-plane components of the magnetization, which include the information on the chirality. They also measured a large DMI using BLS experiments which can be explained by an additional contribution at the Co/MgO interface as suggested by ab-initio calculations. Soumyanarayanan *et al.* demonstrated the control of the skyrmion stability, density and size in Ir/Fe/Co/Pt multilayer (20 repetitions) stacks [115]. For this, they continuously tuned the interactions governing the skyrmion formation, namely the DM interaction, the anisotropy and the exchange stiffness A, via the modification of the FM layer composition and thickness.

Beyond RT skyrmion stabilization, the prediction of the current-induced control of skyrmions in nanotracks in 2013 by Sampaio *et al.* [42] gave rise to an important effort of research on the manipulation of skyrmions using electrical current. This research was motivated by promising applications in the field of memory and logics where skyrmions in tracks are encoding the information and manipulated using electrical current. This is described in the following section.

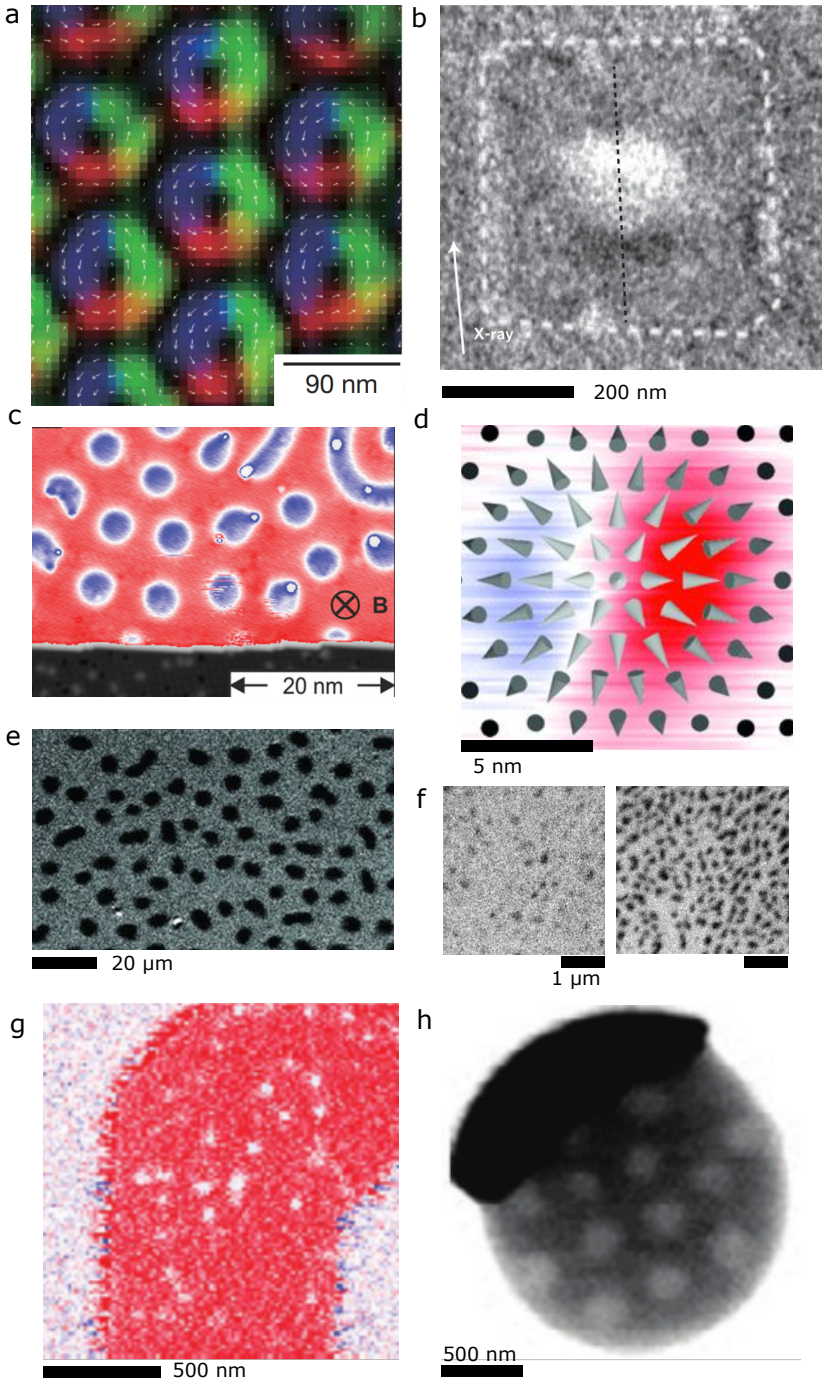

Fig. 2.5: Experimental observation of magnetic skyrmions | **a** Skyrmion-crystal texture observed by Lorentz transmission electron microscopy (LTEM) in $Fe_{0.5}Co_{0.5}Si$ under an out-of-plane field of 50 mT and $T = 40$ K. From [102]. **b** X-ray photo-emission electron microscopy (X-PEEM) image of a confined skyrmion without any external magnetic field in a Pt/Co/MgO ultrathin film at room temperature. From [103]. **c** Lattice of skyrmions and stripe domain structure observed by spin polarized scanning tunnelling microscopy on PdFe/Ir(111) under an out-of-plane magnetic field of 1.5 T and $T = 2.2$ K. From [104]. **d** Spin polarized scanning tunnelling microscopy of a skyrmion in Ir(111)/PdFe with its expected spin configuration shown schematically (arrows) under an out-of-plane magnetic field of 3.25 T and $T = 4.2$ K. From [105]. **e** Polar magneto-optical Kerr effect microscope images of skyrmions in Ta/FeCoB/TaOx thin films under an out-of-plane magnetic field of 0.5 mT at RT. From [106]. **f** Spin polarized low-energy electron microscopy image showing different densities of skyrmions depending on the Cu spacer in Fe/Ni/Cu/Ni/Cu(001) films without magnetic field and at RT. From [107]. **g** Scanning transmission x-ray microscopy (STXM) images showing the z component of magnetization on a $(Ir/Co/Pt)_{10}$ multilayer structure under an out-of-plane magnetic field of 68 mT at RT. From [108]. **h** STXM image of isolated skyrmions in $(Pt/Co/Ta)_{15}$ with an external out-of-plane magnetic field around 10 mT at RT. From [109].

2.4 Manipulation of magnetic skyrmions: current-induced motion

The first demonstration of the current-induced skyrmion motion was performed in 2010 by Jonietz *et al.* [116] who reported the current-induced rotation of a skyrmion lattice in MnSi crystal at low temperature. Later, Iwasaki *et al.* [117] showed a robust current-velocity relation of skyrmion motion in chiral magnets, validating their results with Thiele's equation[1]. Yu *et al* [118] in 2012, performed current-induced motion of skyrmions in the FeGe helimagnet with in-situ LTEM observations utilizing low current densities (< 100 A/cm^2, $3-6$ orders of magnitude lower) compared to the ones used for DW motion in FM nanostructures. Here the current-induced motion was explained by the spin transfer torque mechanism. These demonstrations of very low current density motion of skyrmions in bulk chiral magnets were very promising for the low power manipulation of skyrmions in devices. However, these experiments suffer from several limitations: firstly, only skyrmion crystals were stabilized and manipulated by electrical currents and at low temperature, while devices require the manipulation of isolated skyrmions at room temperature. Secondly, the skyrmion motion was very slow, below 10^4 nm/s, which explains the low current density required to move them. Thirdly, these materials are quite thick, several tens of nm up to hundreds of nm, such that large current was needed to move the skyrmion. This leads to a prohibitory large power consumption for skyrmion-based devices.

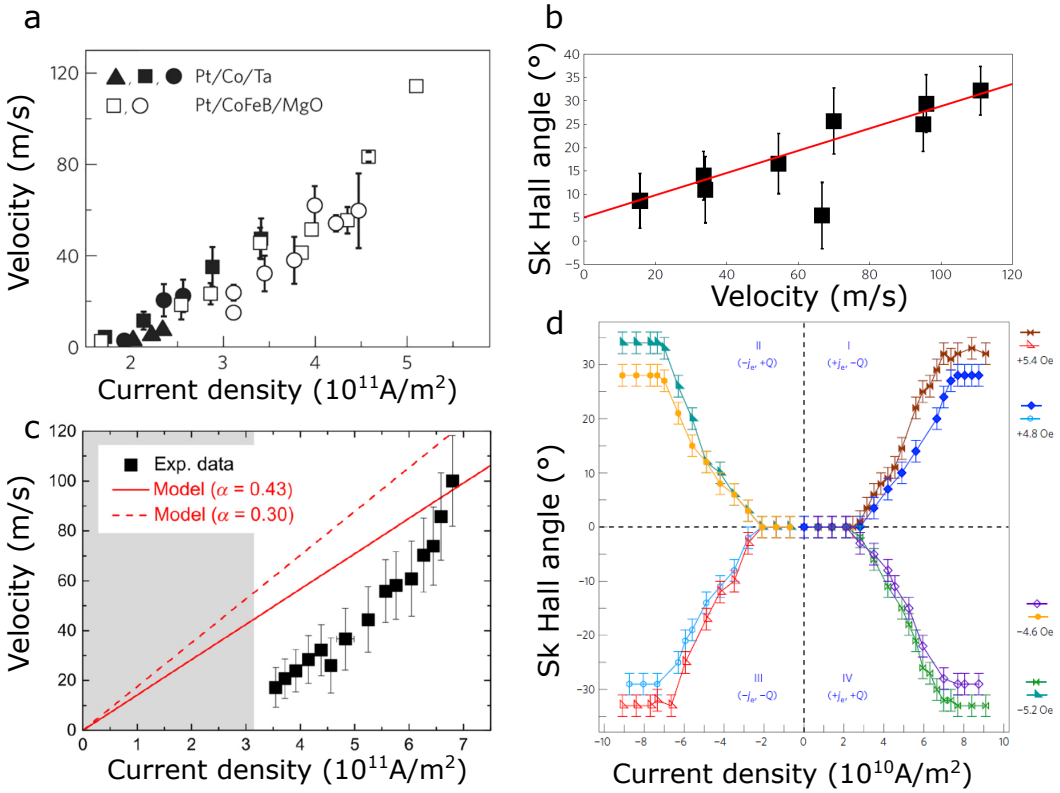

Fig. 2.6: Observation of the current-driven skyrmion motion in ultrathin films at room temperature | **a** Velocity vs the applied current density in Pt/Co/Ta and Pt/CoFeB/MgO multilayers. From [109]. **b** Skyrmion Hall angle dependence on velocity in Pt/CoFeB/MgO multilayers. From [119] **c** Skyrmion velocity dependence on the current density in a Pt/Co/MgO ultrathin trilayer. From [120]. **d** Skyrmion Hall angle as a function of the current density for both topological numbers and current polarities in a Ta/CoFeB/TaOx trilayer. From [121]. Labels have been rewritten for proper visualization.

To address these limitations, ultrathin HM/FM films combine several advantages: on the one hand, the stabilization of isolated skyrmions at room temperature and on the other hand, the possibility to manipulate the skyrmions efficiently via spin orbit torque. For this, the spin Hall effect in the heavy metal is exploited, allowing the decrease of the power consumption for current-induced motion. The potential of this class of materials was supported by Sampaio *et al.* in 2013 [42], who demonstrated numerically that an isolated skyrmion can be stabilized in a sub-micronic track and be moved efficiently by spin orbit torque.

[1] More about Thiele equation in the Appendix A.1.2.

Later, several groups demonstrated the current-induced motion of skyrmion in ultrathin HM/FM at room temperature (see Figure 2.6) [106,109,119,121–123]. They measured the dependence of the velocity and skyrmion trajectory on the current density [119,121]. Maximum values up to 100 m/s were reported by Woo *et al.* in 15 repetition Ta/CoFeB/MgO multilayered systems (see Figure 2.6a). Later, current-induced motion in Pt/Co/MgO single-layered system was observed at room temperature with the demonstration of skyrmion motion above 100 m/s [120] (see Figure 2.6c). In these experiments, the skyrmion trajectory deviates from the current direction. This effect was first observed by Jiang et al. in Ta/FeCoB/TaOx [121] and it is known as the skyrmion Hall effect. Figure 2.7a shows the sketch of this phenomenon as well as some real imaging of this effect (see Figure 2.7b-d).

2.4.1 The skyrmion Hall effect

The skyrmion Hall effect is a consequence of the current-induced dynamics of skyrmions. Considering a HM/FM/NM trilayer structure, spin orbit torques are expected on a skyrmion when the current flows through the HM (see Figure 2.7).

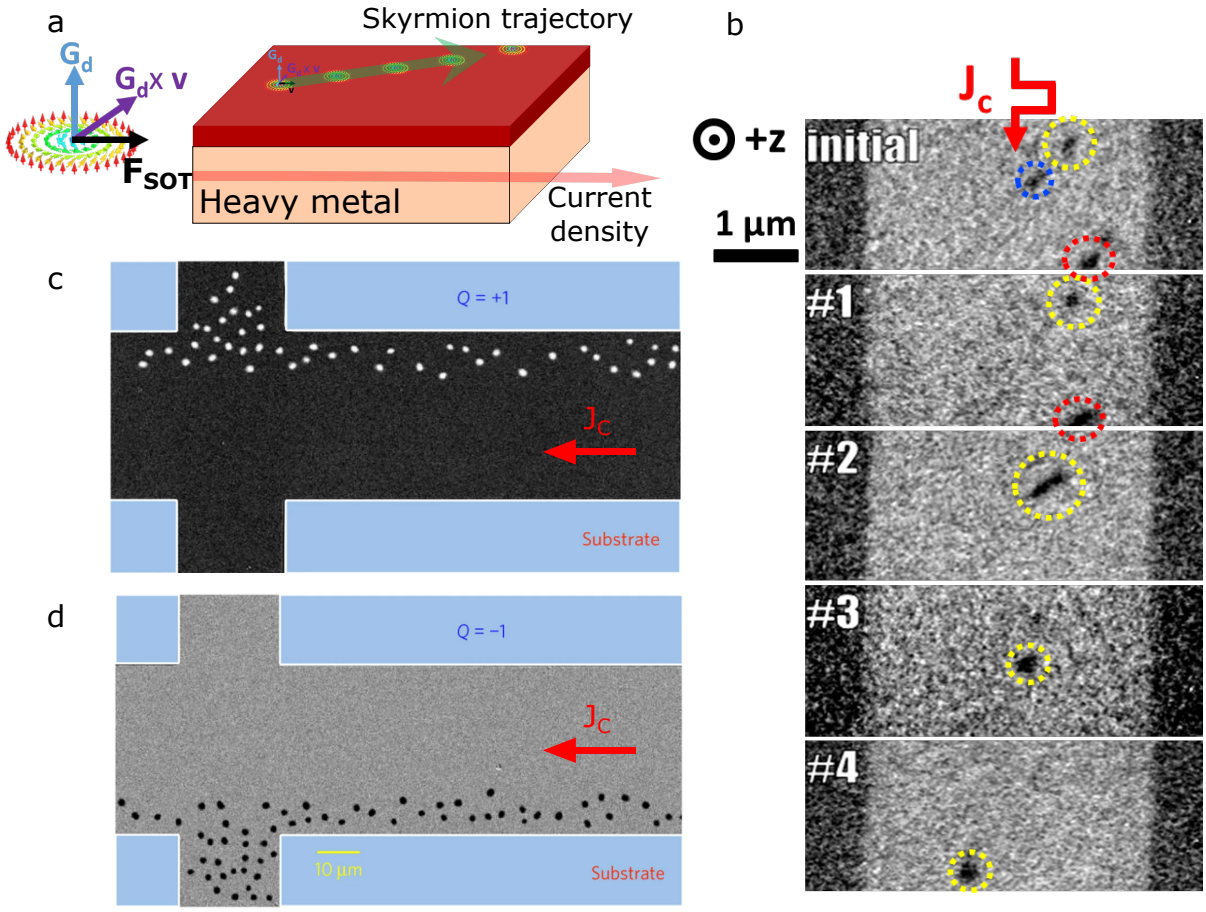

Fig. 2.7: Skyrmion Hall effect in thin films | **a** Sketch of the skyrmion Hall effect. A SOT driven force acts on a skyrmion which deviates due to the gyrotropic vector. **b** XMCD-PEEM images acquired after the successive injection of 10 ns current pulses in the track. The yellow skyrmion is moving in a transverse direction with respect to the current direction. From [120]. **c** MOKE microscope image showing skyrmion accumulation in edges of the nanotrack as a consequence of the skyrmion Hall effect. **d** Same as **c** but reversing the magnetic field. This leads to an accumulation of skyrmions with opposite topological charge at the other edge. Both from [121].

Limiting ourselves to the case with only damping like SOT term, this is the LLG equation that rules the magnetization dynamics:

$$\frac{\partial \vec{m}}{\partial t} = -\gamma_0 \left(\vec{m} \times \vec{H}_{eff}\right) + \alpha \left(\vec{m} \times \frac{\partial \vec{m}}{\partial t}\right) - \gamma_0 \left(\vec{m} \times \vec{H}_{DL}\right), \tag{2.13}$$

where the effective field due to the damping like SOT term is included in $\vec{H}_{DL} = H^0_{DL}\left(\vec{m}\times\left(\vec{j}\times\vec{z}\right)\right)$. If the current density flows in $+x$, so that $\vec{J} = J\vec{j} = J\vec{x}$, and considering that the positive spin Hall angle of Pt gives the sign to H_{DL}, we have $\vec{H}_{DL} = H^0_{DL}\,(\vec{y}\times\vec{m})$. All the other energy terms (exchange, anisotropy, dipolar, DMI and external fields) that contribute to create an effective field are included in $\vec{H}_{eff}$. From here, the derivation of the equation of motion can be described using the method proposed by Thiele [124] and its subsequent extension [49,125,126]. The model is based on the assumption that the spin texture is rigid during its motion. More is developed in the Appendix A.1.2:

$$\vec{F}_{ext} + \vec{G}\times\vec{v} - \alpha\mathbf{D}\cdot\vec{v} = 0. \tag{2.14}$$

One can notice that a force contribution in Equation 2.14 is perpendicular to the velocity vector ($\vec{G}\times\vec{v}$), similar to the behaviour of a charged particle in a magnetic field. This transverse force leads to the manifestation of the skyrmion Hall effect. This equation represents a balance of forces acting on a (moving) skyrmion, where $\vec{F}_{ext}$ is the external driving force on the skyrmion (from a damping like SOT in our case) and $\mathbf{D}$ is a dissipative tensor which depends on the material properties. The term $\vec{G}$, named gyrotropic vector, naturally arrives from the derivation, and is intrinsically related to the skyrmion number dependency, N_{Sk}. The FM thickness and saturation magnetization are relevant for its amplitude. These are the derived expressions for those terms:

$$\vec{F}_{DL} = \begin{pmatrix} F_{DL,x} \\ F_{DL,y} \\ 0 \end{pmatrix}, F_{DL,i} = -\mu_0 M_S t H^0_{DL} \iint dxdy \left(m_x \frac{\partial m_z}{\partial i} - m_z \frac{\partial m_x}{\partial i} \right), \tag{2.15}$$

$$\vec{G} = \begin{pmatrix} 0 \\ 0 \\ G \end{pmatrix}, G = -\frac{M_S t}{\gamma} \iint dxdy \vec{m}\cdot\left(\frac{\partial \vec{m}}{\partial x} \times \frac{\partial \vec{m}}{\partial y} \right), \tag{2.16}$$

$$\mathbf{D} = \begin{pmatrix} D_{xx} & D_{xy} \\ D_{yx} & D_{yy} \end{pmatrix}, D_{ij} = \frac{M_S t}{\gamma} \iint dxdy \left(\frac{\partial \vec{m}}{\partial i} \cdot \frac{\partial \vec{m}}{\partial j} \right), \tag{2.17}$$

where i and j denote the spatial x, y coordinates and t is the film thickness that appears after a previous integration of the z component. The SOT contribution is included in the SOT effective field that the torque creates, given by H^0_{DL}. With the assumption of rotational symmetry in the (x,y) plane, the terms outside the diagonal in $\mathbf{D}$ are orthogonal and they cancel out: $(\partial\vec{m}/\partial x)\cdot(\partial\vec{m}/\partial y) = (\partial\vec{m}/\partial y)\cdot(\partial\vec{m}/\partial x) = 0$. In addition, due to rotational symmetry, the terms in the diagonal are identical with $D_{xx} = D_{yy} = D$. This way, the equations read as:

$$\vec{F}_{DL} = \begin{pmatrix} F_{DL,x} \\ F_{DL,y} \\ 0 \end{pmatrix}, F_{DL,i} = -\mu_0 M_S t H^0_{DL} \iint dxdy \left(m_x \frac{\partial m_z}{\partial i} - m_z \frac{\partial m_x}{\partial i} \right), \tag{2.18}$$

$$\vec{G} = \begin{pmatrix} 0 \\ 0 \\ G \end{pmatrix}, G = -4\pi \frac{M_S t}{\gamma} N_{Sk}, \tag{2.19}$$

$$\mathbf{D} = \begin{pmatrix} D & 0 \\ 0 & D \end{pmatrix}, D = \frac{M_S t}{\gamma} \iint dxdy \left(\frac{\partial \vec{m}}{\partial x} \right)^2. \tag{2.20}$$

Going back to the Thiele equation of motion (see Equation 2.14) and plugging in these terms, we arrive to the following expression considering there is no velocity component along z:

$$\begin{pmatrix} F_{DL,x} \\ F_{DL,y} \\ 0 \end{pmatrix} + G \begin{pmatrix} -v_y \\ v_x \\ 0 \end{pmatrix} - \alpha D \begin{pmatrix} v_x \\ v_y \\ 0 \end{pmatrix} = 0. \tag{2.21}$$

Solving for both x and y velocity components leads us to their explicit expressions:

$$\begin{aligned} v_x &= \frac{\alpha D F_{DL,x} - G F_{DL,y}}{G^2 + \alpha^2 D^2}, \\ v_y &= \frac{\alpha D F_{DL,y} + G F_{DL,x}}{G^2 + \alpha^2 D^2}. \end{aligned} \tag{2.22}$$

For Néel skyrmions the SOT driven force only has a component in the current direction. Therefore $F_{DL,x} =$

F_{DL} and $F_{DL,y} = 0$, and it leads to:

$$v_x = \frac{\alpha D F_{DL}}{G^2 + \alpha^2 D^2}, \tag{2.23}$$

$$v_y = \frac{G F_{DL}}{G^2 + \alpha^2 D^2}. \tag{2.24}$$

Equation 2.24 shows that the gyrotropic vector, that is the topological charge of the skyrmions, leads to a velocity component perpendicular to the driving force. This effect is known as the skyrmion Hall effect and is a direct consequence of the skyrmion non-trivial topology. In experiments (see Figure 2.7), the measured quantity is the skyrmion Hall angle θ_{SkH}, i.e. the angle between $\vec{F}_{DL}$ and $\vec{v}$, and can be calculated by taking the tangent of the angle and both velocity components:

$$\tan\theta_{SkH} = \frac{G}{\alpha D}. \tag{2.25}$$

This expression is not dependent on current density or the velocity even if there have been observations with such dependencies (see Figure 2.6). The origin of the observed dependence of the SkHE in the current is associated to the pinning [120], especially at low velocities where still the flow regime is not reached. For larger speeds, the reported values are in better agreement with the model prediction.

Continuing with Néel skyrmions, we will finish this section by computing the force, dissipative tensor and the gyrotropic terms. The force parallel to the current direction reads:

$$F_{DL,x} = F_{DL} = -\mu_0 M_S t H^0_{DL} \iint dxdy \left(m_x \frac{\partial m_z}{\partial x} - m_z \frac{\partial m_x}{\partial x} \right). \tag{2.26}$$

Using the spherical coordinates from Figure 2.1e, this expression develops to:

$$F_{DL} = -\mu_0 M_S t H^0_{DL} \pi \int_0^\infty r dr \frac{d\theta}{dr}. \tag{2.27}$$

We continue evaluating the integral with the assumption of the skyrmion 180° domain wall profile, given by $\theta(r) = -2\arctan\left(\exp\left(\frac{r-R}{\Delta}\right)\right)$, and its direct relation $\sin\theta = \Delta\frac{d\theta}{dr}$. Also, if the skyrmion radius is large compared to the domain wall width ($R >> \Delta$), we can substitute in the integral $r = R$ and then perform the integration of the $\sin\theta$ [127], having as a result:

$$F_{DL} \approx -\mu_0 M_S t H^0_{DL} \pi \int_0^\infty dr \frac{R}{\Delta} \sin\theta \approx \mu_0 M_S t H^0_{DL} \pi^2 R. \tag{2.28}$$

For the dissipative tensor, a similar procedure follows with $D \approx \frac{M_S t}{\gamma} 2\pi \frac{R}{\Delta}$. Lastly, the gyrotropic vector is trivially $G = -4\pi \frac{M_S t}{\gamma} p$ for Néel skyrmions. Finally, the velocity and skyrmion Hall angle expressions in this model would read as:

$$v = \frac{\gamma\pi R}{4\sqrt{1 + \left(\frac{\alpha R}{2\Delta}\right)^2}} \mu_0 H^0_{DL} = \frac{\gamma\pi R}{4\sqrt{1 + \left(\frac{\alpha R}{2\Delta}\right)^2}} C_{DL} J, \tag{2.29}$$

$$\tan\theta_{SkH} = \frac{G}{\alpha D} = -p\frac{2\Delta}{\alpha R}, \tag{2.30}$$

where we wrote the velocity extracting the current density and the associated damping like SOT constant from the effective damping like SOT field using $\mu_0 H^0_{DL} = C_{DL} J$. The velocity scales linearly with the current density and the deviation direction depends on the polarity of the skyrmion.

The skyrmion Hall effect would have important drawbacks for devices based on the motion of skyrmions in tracks. Indeed, it drives skyrmions toward the edges of patterned devices, where they might either bounce back or annihilate, which would result in a loss of information. It was proposed that the skyrmion Hall effect could be mitigated by considering coupled skyrmions with opposite topological charges, such that both gyrotropic forces cancel out. This equilibrium can be achieved in scenarios such as synthetic antiferromagnets (SAF) [128] or in skyrmions within antiferromagnetic materials [129]. A part of my thesis, specially the first and second year, was focused on the optimization of SAF stacks in order to stabilize SAF skyrmions. This will be introduced in the following sections and the results are discussed in Chapters 4 and 5.

2.5 Electrical detection of skyrmions

Electrical transport measurements have been used in the early 2010 decade to investigate skyrmions [87] in bulk systems [130], single crystals [131–133], thin films [134,135] and nanostructures [136–138]. However, the evidence had been limited to below room temperature [114,139]. Regarding thin films, current-induced motion of skyrmions was so far characterized by imaging methods. However, applications need to be able to electrically readout the skyrmions with sufficiently high signal.

Various techniques have emerged, each leveraging distinct electronic properties. The most reliable ones are the anomalous Hall effect and the anomalous Nernst effect. When a non-ferromagnetic metallic sample is subjected to a perpendicular external magnetic field, the Lorentz force acting on the current carriers induces a transverse potential difference (the Hall voltage) within the sample plane. The measured quantity is the transverse resistivity (ρ_{xy}) and it linearly depends on the external field $\rho_{xy} = R_0 \mu_0 H_{ext}$. R_0 is used to characterize conducting materials. In ferromagnetic materials, the Hall resistivity has an additional contribution, known as the anomalous Hall effect. It is independent of the magnetic field and it only requires magnetization. When a current flows in a magnetic material, electrons are primarily deflected in one direction and leads to an additional transverse voltage which depends on magnetization. As far as the Nernst effect is concerned, it occurs in certain materials when they are subjected to both a temperature gradient and an external magnetic field. The anomalous Nernst effect arises when the transverse voltage is not solely proportional to the temperature gradient, but also exhibits a contribution dependent on the magnetization of the material without the need of an applied external field. In both effects, these additional terms can be used to electrically detect magnetic textures.

In 2018, single skyrmions were detected at room temperature by Maccariello *et al.* [140] using transverse Hall resistivity combined with in-situ MFM measurements (see Figure 2.8a). This transverse Hall resistivity includes the contributions from the ordinary, the anomalous and the topological Hall effects. They measured that each skyrmion was contributing equally to the transverse resistivity and concluded that the anomalous Hall effect contribution was the predominant term among the other contributions for sizes around 80-100 nm diameter. Individual skyrmions were also detected giving typical resistance values of the order of mΩ per skyrmion, which means that the reported sensitivity of the electrical detection of skyrmions is still relatively low.

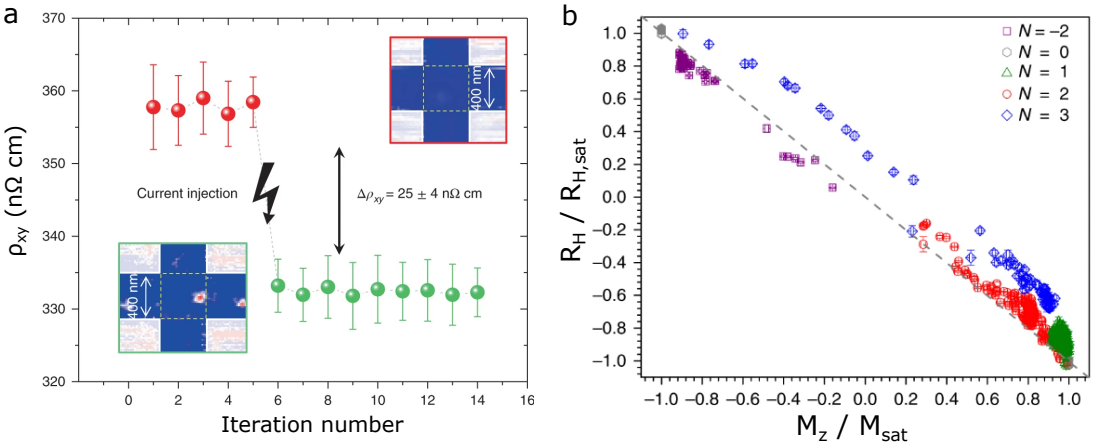

Fig. 2.8: Electrical detection of magnetic skyrmions | **a** Detection of a single skyrmion related to the change in anomalous Hall resistivity at RT. From [140]. **b** Hall resistance signals vs M_Z/M_S for different number of skyrmions, showing a difference from the anomalous contribution, dashed line. From [141]. Labels have been rewritten for better visualization.

Later, Zeissler *et al* [141] studied the in situ Hall measurements of skyrmions in a nanodisk at room temperature with operando STXM microscopy (see Figure 2.8b), showing that it scales with the skyrmion number and area, which is explained by a dominant contribution from the anomalous Hall effect. Additionally, a small contribution independent from the skyrmion size was measured which is proportional to the number of skyrmions. The anomalous Nernst effect due to the presence of skyrmions was also measured by Wang *et al* [142] and Fernandez *et al* [143], but low electrical signals per skyrmion were reported (90 ± 10 nV and 4.6 ± 0.2 nV respectively).

In Chapter 6, I will show the results with a magnetic tunnel junction that can host skyrmions offering a several orders of magnitude larger reading signal.

2.6 Skyrmion-based applications

The particle-like behaviour of solitons was already introduced by Skyrme himself when he developed the theory for hadrons [83], meaning that magnetic skyrmions are expected to have this same property. Together with their topological stability, they were proposed as information carriers for future memory [126] and logic devices [144]. In the decade of 2010, skyrmion racetrack memory was the most predominant proposed application, where the information bits were the skyrmions themselves. The presence or absence of these entities would correspond to the bit encoding of 1 or 0 [42,43,126,145,146]. Another examples of in memory devices are three-terminal MRAM devices, where electrical currents would manipulate large number of skyrmions giving the possibility to build dense multilevel memories [147]. Bogdanov *et al.* in 1994 [98] stated that particles with the same skyrmion number repel each other due to their topology, while particles with opposite topological charges would attract each other, and eventually annihilate[2]. It is straightforward to notice that for a given ferromagnetic background, all the skyrmions would have the same skyrmion number, such that they repulse each other on short distance due to their topology. Furthermore, the longer range stray field interaction leads to an additional repulsive force between magnetic skyrmions. This repulsive interaction can be exploited for logic applications [144] to perform Boolean [148,149] operations. More recently, non-conventional computing applications of skyrmions have emerged. Non-conventional computing refers to approaches and technologies that diverge from the traditional binary digital computing methods we have in modern electronic devices.

Among them, skyrmion-based neuromorphic computing is a rapidly advancing field that aims to replicate the structure and function of neurons and synapses using skyrmions [150,151]. The goal is to create devices that can mimic the behaviour of biological neural networks, enabling brain-like information processing. Figure 2.9a shows the results of the study of an artificial synapse for neuromorphic computing based on the nucleation/annihilation of skyrmions by current pulses in a track. The electrical manipulation of magnetic skyrmions in ferrimagnetic Pt/GdFeCo/MgO multilayers at room temperature allowed the authors to accumulate and dissipate them, mimicking the synaptic weights depending on the pulse polarity.

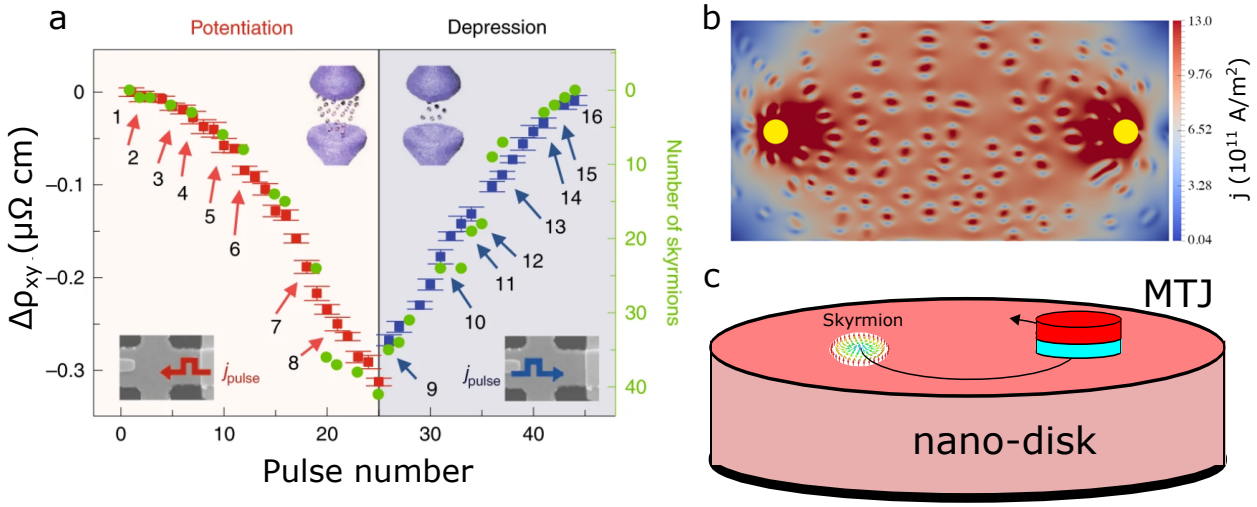

Fig. 2.9: Towards for non-conventional skyrmion-based applications | **a** Correlation between Hall resistivity measurements (left axis) with the number of skyrmions (right axis) while different polarity pulses are applied. It shows potentiation (red) and depression (blue) depending on the pulse polarity. From [150]. **b** Distribution of the current in the skyrmionic magnetic texture. The yellow dots are nanocontacts and a voltage (110 mV) is going across them. From [152]. **c** Schematic of a skyrmionic nano-oscillator where a skyrmion would oscillate and be detected by a MTJ. Some labels have been rewritten for better visualization.

Reservoir computing (RC) [153] is another attractive type of non-conventional application for researchers. It is a machine learning approach that simplifies complex computations. It employs a fixed, randomly interconnected network known as the "reservoir" to process data (for instance an ensemble of skyrmions that

[2]For example, when a skyrmion and an antiskyrmion meet.

interact with each other [152]). This reservoir, often a recurrent neural network, processes input information (an input electrical signal), generating rich, dynamic patterns due to internal connections in the reservoir. These patterns are then read by a trainable output layer to produce desired results. Unlike traditional neural networks, only the output layer is trained, making reservoir computing computationally efficient. Pattern recognition and making predictions from dynamic data are excellent tasks that RC can perform. Figure 2.9b displays a setup of such computations in which we have an input, the computing reservoir and an output.

We now briefly present the skyrmion nano-oscillator as another potential application [154]. Skyrmions are placed in a magnetic disk and driven into a circular motion via a spin torque generated by an injected spin current into the disk. For the electrical detection, a compact MTJ is placed on the disk. This MTJ probes the skyrmion's state during each rotation around the disk's center (see Figure 2.9c). The injected spin polarized current affects the oscillation frequency and the size of the skyrmion. For the detection, a jump in the resistance is measured when the skyrmion moves below the MTJ, which leads to an oscillatory output voltage [154]. The oscillation frequency of these devices is easily adjustable through the current, so they are an excellent choice for compact frequency generators. Note the possibility to integrate not only one or more skyrmions, but also one or more junctions, opening a path to diverse circuitry.

2.7 Synthetic antiferromagnetic skyrmions: stability and dynamics

The finite magnetic moment of ferromagnetic skyrmions has an important impact on the skyrmion stability, size and dynamics. However, it can limit the device functionality. Firstly, an external magnetic field is needed to stabilize ferromagnetic skyrmions [89,97,108,109], which can be hardly implemented in a device. In addition, while stray fields resulting from the finite magnetic moment helps to stabilize the skyrmions, it limits its minimum size to several tens of nm diameter (depending on material parameters) [89]. Finally, the topological charge of magnetic skyrmions leads to the skyrmion Hall effect presented above, deviating the skyrmion trajectory away from the current direction.

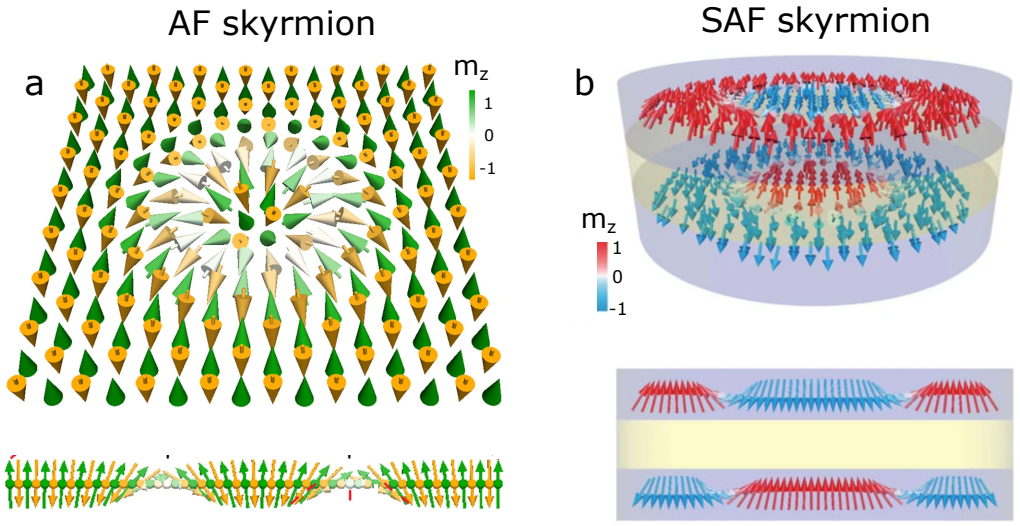

Fig. 2.10: Antiferromagnetic and synthetic antiferromagnetic skyrmions | **a** Schematic drawing of an AF skyrmion, where two sublattices with a skyrmion are AF coupled, therefore having an AF skyrmion. From [155]. **b** Schematic drawing of a SAF skyrmion where two layers are AF coupled through a non magnetic spacer. From [128].

Antiferromagnetic (AF) skyrmions allow to address these issues (see Figure 2.10a). AF skyrmions are composed of skyrmions in antiferromagnetically coupled sublattices (orange and green in the figure). Owing to their vanishing magnetic moments and stray field, small AF skyrmions (tens of nm in diameter) and RT stability at zero magnetic fields are expected [89,156]. In addition, their zero effective topological charge leads to a cancellation of the gyrotropic forces resulting in a motion along the current direction without skyrmion Hall effect. Models predict that this can lead to an enhancement of the current-induced velocity which can exceed 1 km/s [155,157,158].

A particularly attracting material system to stabilize AF skyrmions are *synthetic* antiferromagnets (SAF). SAFs are composed of two (or an even number of) ferromagnetic layers which are AF coupled through an intermediate non magnetic layer due to the RKKY interaction [159]. Figure 2.10b shows a schematic representation of a SAF skyrmion, where two skyrmions are stabilized in their respective ferromagnets and coupled antiferromagnetically. The two skyrmions have an opposite topological charge but the same chirality. Multilayers with more repetitions are also allowed in this system, offering a variety of possibilities. Moreover, magnetic and transport properties, namely the SOT efficiency, PMA or DMI, can be tuned by adjusting the thickness and the nature of the individual layers. Normally, the interlayer exchange coupling is adjusted to its maximum value, such as a Ru interlayer whose coupling strength has a damped oscillatory (FM/AFM) behaviour with the film thickness.

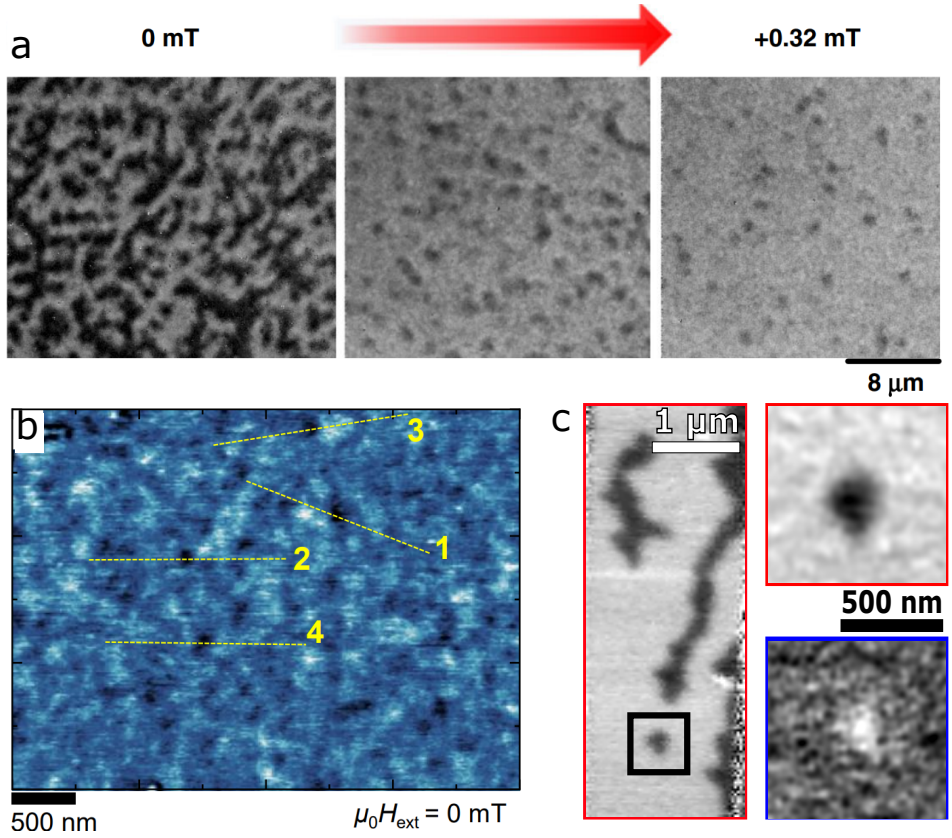

Fig. 2.11: SAF skyrmions in synthetic antiferromagnets | **a** Different magnetic domain patterns observed by MOKE in a non compensated SAF stack (FM_1 = Co(0.2)/$Co_{0.19}Fe_{0.56}B_{0.25}$(0.925) and FM_2 = Co(0.375)/$Co_{0.19}Fe_{0.56}B_{0.25}$(0.6)) depending on the external field applied. From [160]. **b** MFM images of the SAF + bias layer system at zero external magnetic field showing skyrmions. From [161]. **c** XMCD-STXM image acquired at the Co edge (red) showing an isolated skyrmion at zero field. Ptychography reconstructions of the skyrmion in the black box acquired at the Co (red) and Fe (blue) edges. From [162].

The stabilization of SAF skyrmions at room temperature was reported recently in different sputtered thin films stacks, a relevant requirement for future compatibility with CMOS [160–162]. Legrand *et al.* built a Pt/Co/Ru-based multilayer SAF stack coupled to a thick perpendicularly magnetized bias FM layer and used MFM to image the skyrmions (see Figure 2.11b). The thickness of the ferromagnetic layers was adjusted to be close to the in-plane to out-of-plane spin reorientation transition. As a result, without a bias layer, stripe domains are observed. The bias layer allows the application of an effective perpendicular magnetic field on one of the layers by interfacial exchange, which turns the stripe domains into isolated skyrmionic state. However, one drawback of this bias layer is that it would shunt the current used for current-induced manipulation of the skyrmions. Later, Dohi *et al.* considered an uncompensated SAF Pt/FM1/Ir/FM2/W, such that isolated non–compensated SAF skyrmions could be nucleated by applying external magnetic fields (see Figure 2.11a). This allowed them to perform MOKE observations and current-induced experiments (not shown in plots). They reported an enhancement of the speed as well as a reduction of the skyrmion Hall effect in SAF as compared to their ferromagnetic counterpart. However, this could be related to the (still) low velocities measured and therefore the resulting creep dynamical regime of the skyrmions.

Juge *et al.* in Spintec considered a fully compensated SAF system [162]. They demonstrated compensated SAF skyrmions at room temperature and zero external magnetic field using synchrotron based experimental observations. The multilayered stack grown by sputtering was fully compensated but the two ferromagnetic layers composing the SAF structure were different, one being composed of a thin Co layer and the other of a NiFe layer. This allowed them to confirm the antiferromagnetic alignment by probing each element (Co and Fe from NiFe alloy) with STXM (see Figure 2.11c) microscopy. For the skyrmion nucleation, different strategies to overcome the poor sensitivity nature of SAF systems to external magnetic field perturbations were chosen. Firstly, low anisotropy stacks were grown, where the ferromagnet thickness was adjusted to be close to the out-of-plane/in-plane spin reorientation transition. With this, the domain wall energy was minimized and spontaneous nucleation was favoured. However, the little control on the nucleation could be a potential issue for applications. That is why secondly, local current injection using nanofabricated local current injectors were considered to induce the nucleation and annihilation of skyrmions by current. Lastly, ultrafast laser stimulation was also carried out to nucleate individual SAF skyrmions from a uniformly magnetized state without any external field.

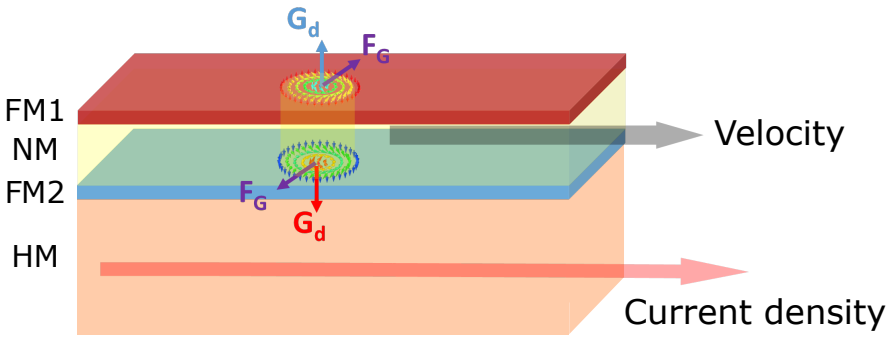

Fig. 2.12: Dynamics of SAF skyrmions in synthetic antiferromagnets | **a** A schematic representation of the dynamics in SAF stacks. FM_1 and FM_2 are AF coupled via the NM. The skyrmions in the individual ferromagnets have opposite polarity but same chirality and are coupled through RKKY interaction. Their respective gyromagnetic forces cancel each other out, resulting in zero transverse displacement. The current goes through the HM and the resulting velocity is parallel to it.

Having a look to the equations that rule the dynamics in SAF systems, we can follow a similar procedure as in Section 2.4. In a very simple way, we can consider that both gyrotropic vectors cancel out. In a steady state, a point-like SAF skyrmion would have the same equation of motion as the FM skyrmion without the gyrotropic vector:

$$\vec{F}_{ext} - 2\alpha \mathbf{D} \cdot \vec{v} = 0. \tag{2.31}$$

Compared to Equation 2.14, there is a factor two in front of the dissipative tensor due to the presence of two skyrmions in the SAF, so that $\mathbf{D}$ keeps representing the parameters for one FM. Here, the velocity vector is parallel to the SOT driven force (see also Figure 2.12), meaning that the trajectory is along the current direction and the skyrmion Hall angle trivially cancels. Considering the same assumptions we did with the ferromagnetic skyrmions, we take the force and dissipative expressions developed above. So the velocity reads:

$$v = \frac{F_{ext}}{2\alpha D} = \frac{\Delta \pi \gamma}{2\alpha} \mu_0 H^0_{DL} = \frac{\Delta \pi \gamma}{2\alpha} C_{DL} J. \tag{2.32}$$

This equation already predicts higher velocities than for FM skyrmions. Using typical parameters for Pt/Co based materials such as $\Delta \approx 25$ nm, $\gamma/2\pi = 31$ GHz/T, $\alpha = 0.3$ and $C_{DL} = 1 \cdot 10^{-14}$ Tm^2/A we already reach speeds over 250 m/s at high current densities. Some material engineering to reduce the damping given its strong dependency would lead quickly to even faster skyrmion motions. The SOT efficiency could also be tuned for velocity enhancement. With all the assumptions, the velocity does not have a skyrmion radious or DM interaction dependence, which may not be completely true. Also, both FM layers will never have identical material parameters such as anisotropy or DMI. Finally, we implicitly considered an infinite RKKY coupling between the skyrmions. All this means that there may be other material parameters playing a key role in the complex SAF dynamics.

2.8 Conclusions

It is truly impressive to witness all the advancements the skyrmionic community has made in recent years. Predictions that looked ambitious at the beginning were realized within months and even the dynamical understanding of these entities was matured by many groups, with the consequent discovery of a vast range of different material systems hosting skyrmions. However, the objective to reach high speed still remains pending while a direct, unambiguous detection with larger signal is necessary for technological applications. In addition, the mechanisms behind the skyrmion nucleation by currents have to be studied and lastly alternative options for skyrmion nucleation avoiding multilayers would be desirable.

These questions and objectives marked the path I took during my thesis. Chapters 4, 5 and 6 are dedicated to answer them, but first we need to present the experimental tools used to grow and characterize the samples for these studies.

Chapter 3

Experimental techniques: nanofabrication and characterization

Contents

3.1 Magnetron sputtering: deposition of magnetic stacks 44
3.2 Characterization on thin films 45
3.2.1 Magneto-optical Kerr effect (MOKE) 45
3.2.2 Vibrating sample magnetometer (VSM) 45
3.2.3 Superconducting quantum interference device (SQUID) 46
3.3 Nanofabrication 47
3.3.1 MRAM nanofabrication process on membranes 47
3.3.1.1 MTJ patterning 47
3.3.2 MTJ characterization 50
3.4 X-ray microscopy techniques 51
3.4.1 X-ray Magnetic Circular Dichroism (XMCD) 51
3.4.2 Scanning Transmission X-ray Microscopy (STXM) 52
3.4.3 Photo-emission electron microscopy (PEEM) 53
3.4.4 STXM for time resolved magnetic imaging 54

In this chapter, we include the description of the diverse experimental techniques used throughout the thesis. Tools for deposition and characterization steps are explained, while we detail the x-ray microscopy techniques for the magnetic texture imaging. At the end of the chapter, the MTJ nanofabrication process on membranes is detailed, since additional care was taken for the process.

3.1 Magnetron sputtering: deposition of magnetic stacks

Magnetron sputtering is a vapour deposition technique used in Spintec for thin films and particularly during my thesis. This process takes place at room temperature within a highly reduced vacuum environment, at 10^{-8} mbar. The sputter deposition involves utilizing a gaseous argon (Ar) plasma, where high-energy Ar ions are directed toward the target surface, causing atoms to be removed. The Ar ions transfer physical momentum and kinetic energy to the target atoms, resulting in sufficient force to break bonds and dislodge the atoms. These atoms then condense on the surface of the substrate, forming a thin film (see Figure 3.1a). Concerning oxidation, the deposition tool is also designed for this step. In our case, the MgO we use for tunnel barrier is created through the natural oxidation of metallic Mg within the treatment chamber. The magnetic stack is prepared without interrupting the vacuum environment to avoid oxidation. Wedge deposition which allows to vary the thickness along the wafer is achieved by translating the substrate from the axis of deposition by 100 mm (Figure 3.1b). This allows us to deposit continuous gradients of thicknesses. Note that there is no rotation of the substrate in wedge depositions. A combination of two orthogonal gradients is also possible. For this, the substrate has to be rotated by 90° before the deposition of the following material. It is a powerful way of optimizing all the stack engineering steps, since it allows a proper fine-tuning of the material parameters. Regarding the substrates, the magnetron sputtering is compatible with all those (Si, SiO_2, Si_3N_4) we used during the thesis.

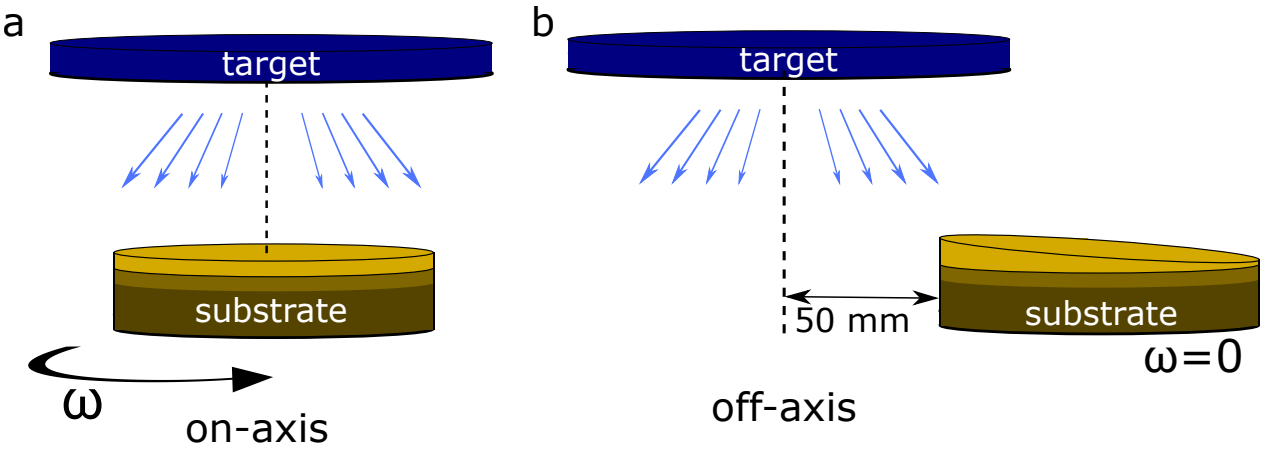

Fig. 3.1: Magnetron sputtering | Geometries of the sputtering machine showing **a** on axis (uniform deposition) where the substrate is rotating and **b** off-axis (wedge deposition) configuration where the wafers are displaced by 100 mm from the deposition axis.

All the samples were deposited by Stéphane Auffret and Jérôme Faure-Vincent at Spintec.

3.2 Characterization on thin films

The different techniques for magnetic characterization of thin films are described in this section, namely, the Magneto-Optical Kerr Effect (MOKE), Vibrating Sample Magnetometer (VSM) and the Superconducting QUantum Interference Device (SQUID).

3.2.1 Magneto-optical Kerr effect (MOKE)

We name magneto-optics all the phenomena that happen when the properties of an electromagnetic wave are altered due to the presence of magnetic fields and magnetization. The magneto-optical Kerr effects (MOKE) are related to the reflected light which experienced a change either in polarization or intensity after the interaction with a magnetic sample [163].

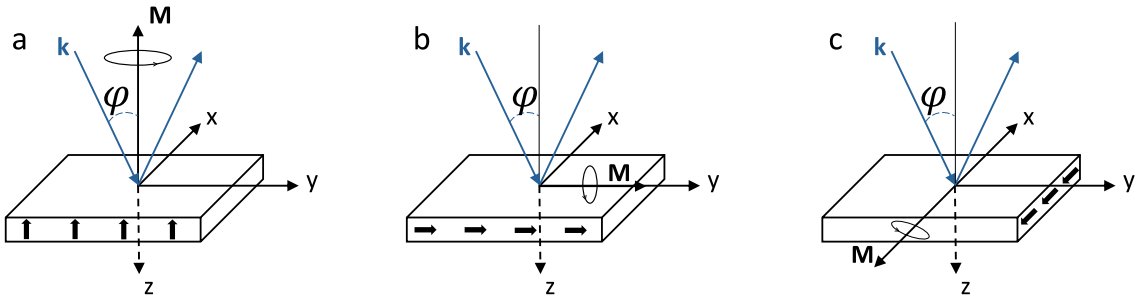

Fig. 3.2: Schematics of the Kerr effect | **a** Polar, **b** longitudinal and **c** transverse configurations of Kerr effects. **k** (in blue) represents the electromagnetic wave vector which has an incidence angle of φ from the normal direction of the sample. **M** represents the magnetization direction of the sample.

When a linearly polarized light beam from a laser is reflected from a magnetic sample, as in Figure 3.2, several effects can take place on its polarization that are related to the magnetic properties of the sample: the direction of polarization of the sample can rotate, a certain ellipticity can be introduced in the beam or the intensity of the beam can be changed. The Kerr rotation angle, θ_K, and the Kerr ellipticity, ϵ_K, are linearly dependent on the magnetization which can be measured by controlling the change in the polarization of the reflected light.

Figure 3.2 shows the three geometries that can be used depending on the direction of the magnetization with respect to the plane of incidence and the sample surface: polar, longitudinal, and transverse. In the polar configuration the magnetization is normal to the sample surface but in the laser incidence plane. The longitudinal configuration has the magnetization both in the sample and laser incidence plane. Lastly, in the transverse configuration the magnetization is in the surface plane but orthogonal to the incidence laser.

For fast measurements of magnetic properties, a nanoMoke tool was used. The nanoMOKE uses a focused laser on the sample which allows the fast measurement of the perpendicular magnetization (polar Kerr effect) of a specific region of the sample, providing a rapid mapping of deposited wafers with material wedges. In this configuration, the rotation of the polarization is proportional to the component of the magnetization perpendicular to the thin film. A laser (or LED) emits visible light with a wavelength of 660 nm which results in a 300 µm spot that is first linearly polarized with a polarizer. After the reflection, the light passes through an analyzer which is nearly crossed with the incident light polarizer. Only the component generated through the Kerr effect is thus allowed to pass to the detector. The magnetization of the magnetic thin film can also be changed thanks to an electromagnet creating a magnetic field either perpendicular or into the film plane. This way we change between the configurations in Figure 3.2, for instance to measure hysteresis loops. In our setup, the fact that the maximum field is limited to 400 mT makes the study of some SAF properties in the following chapters not possible with this tool, due to their larger reversal fields in many cases.

3.2.2 Vibrating sample magnetometer (VSM)

The vibrating sample magnetometry measurements are based on the Faraday's law of induction, which tells us that a magnetic field that is changing in time will create an electric field. Then, the electric field can be measured and the information about the magnetic field is obtained. For this, a sample is introduced into an external magnetic field and it starts to vibrate at a certain frequency, as shown in Figure 3.3. When the sample is magnetic, the external field will align the magnetization of the sample along its direction. This will

create the so called stray field around the sample. Due to the oscillatory movement of the sample, the stray field is changing in time provoking small perturbations on the external field. Then, following Faraday's law of induction, the electric field can be sensed by a set of pick-up coils. The current detected is proportional to the magnetization of the sample. The VSM offers a measurement of the magnetization depending on the orientation of the external magnetic field. We cannot change the external magnetic field direction, but the holder can be adjusted in such a way that one can measure the hysteresis loop at any desired angle between the sample and the field (in-plane and out-of-plane, for instance). During the thesis, several VSM measurements were performed, all at room temperature, even if VSM offers also temperature dependence measurements. We are able to apply an external magnetic field up to 1.8 T, and the magnetometer from MicroSense reaches a sensitivity of 10^{-6} emu. Overall, the VSM offers a relatively fast way to measure hysteresis loops of ultra-thin films with large saturation fields. In thin films, which have low magnetic moment, the diamagnetic effect coming generally from the Si substrate must be subtracted from the whole signal. However, there is a large dependence of the VSM measurements on the shape and size of the samples. As a result, we have not trusted for instance the saturation magnetization values given by VSM during the thesis. For such purposes and more precise measurements, another magnetometry technique is more reliable, the SQUID, which is described in the following subsection.

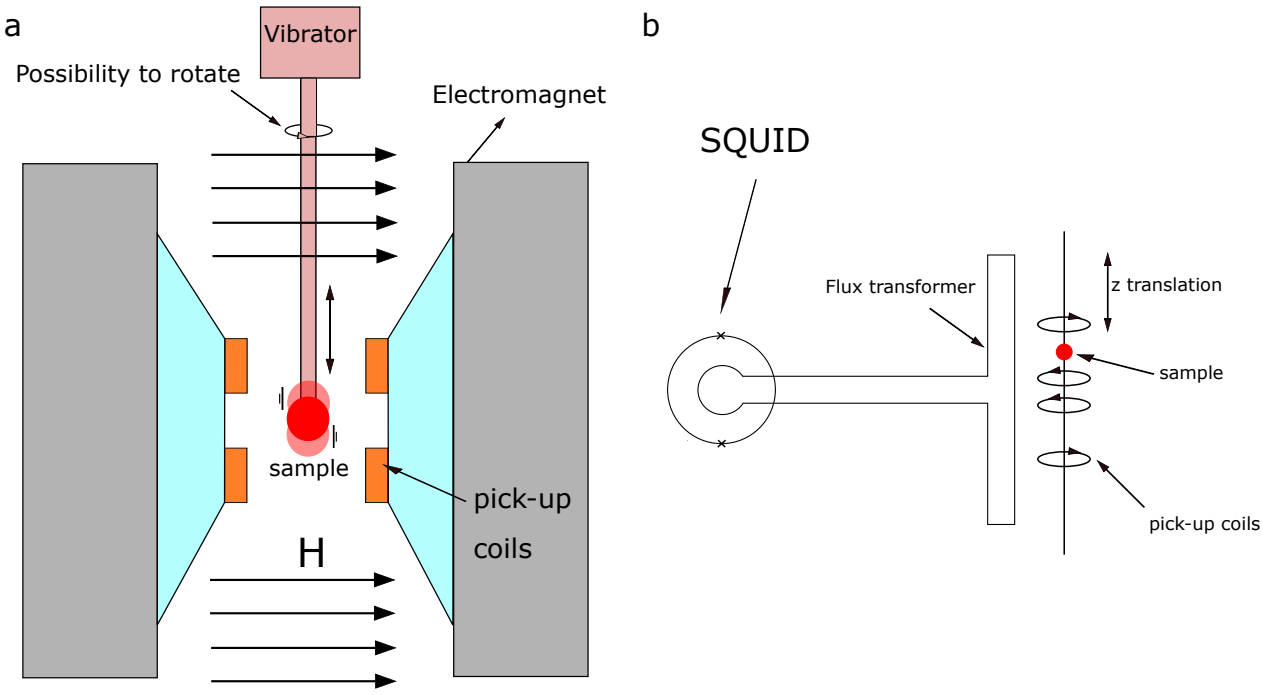

Fig. 3.3: Schematics of the VSM and the SQUID | **a** Schematics of the VSM magnetometer showing a sample (in red) attached to a vibrator that can rotate. The magnetic field (arrows shown in black) is generated by the electromagnet (grey) and the signal is detected by the pick-up coils (in orange). **b** Schematics of the SQUID magnetometer.

3.2.3 Superconducting quantum interference device (SQUID)

The SQUID is a magnetometry technique used for measuring very small magnetizations. Figure 3.3b shows a schematic of the SQUID magnetometer. As a magnetic sample moves along the z direction through the coils, it generates currents in the coil due to a change in the magnetic flux. Then, similar levels of currents are induced in the Flux transformer and the current flow is generating a magnetic field in the coil inside the SQUID. Then, the SQUID detects the resulting magnetic flux and allows the measurement of the current. This SQUID sensor is isolated from the sample, only coupled via the current we mentioned. These features permit the application of external magnetic fields and perform M-H loops, for instance. The SQUID allows us to measure the magnetization of the sample at any cryogenic temperature and up to external fields of more than 5 T. The sensitivity is 100 times larger than the VSM (10^{-8} emu) and has been the tool used to measure several hysteresis loops of samples during the thesis for material characterization.

3.3 Nanofabrication

For every STXM image we show in the manuscript, samples have been grown on Si_3N_4 in order to allow the x-ray go through it. Overall, the nanofabrication process I carried out to pattern MTJ pillars on Si_3N_4 membrane was similar to the standard "MRAM" process, which is well established in our laboratory. This process allows us to fabricate magnetic pillars with diameter down to typically 50 nm which are contacted electrically by top and bottom electrodes to measure their electronic transport properties. However, there were a few important differences. Firstly, membranes were defined at the beginning of the process such that the whole MRAM process was performed on a substrate with a network of 50 µm wide 70 nm thick SiN membranes. The fragility of the Si_3N_4 membranes made us modify several steps of the process and leads to extreme care in handling the wafer in the different steps of the fabrication process. Secondly, to increase the soft x-ray transmission, the Ta 150 nm etching mask used to define the magnetic pillar by ion beam etching was replaced by a 100 nm Ti mask deposited by lift-off. Indeed, Ti has a higher transmission coefficient at the x-ray energy used for the observation compared to Ta (0.55 for Ti(100 nm) instead of 0.17 for Ta(150 nm) around 700 eV [164]). Similarly, a 225 nm Al electrode was used to limit the x-ray absorption. In the following lines, I will quickly go through the nanofabrication steps.

3.3.1 MRAM nanofabrication process on membranes

The first step of the process was to define thin (tens of nm) SiN membranes in the 100 mm substrate. The substrate was composed of a SiO_2 (150 nm) and Si_3N_4 (70 nm) layers on the surface of Si (500 µm) (see Figure 3.4a). The SiO_2 layer allows us to decrease the stress on the Si_3N_4 membrane. Given the thickness of the membranes and the technical difficulties of the MRAM nanofabrication process, we designed a layout with localized Si_3N_4 windows spread all over the wafer. The density of the Si_3N_4 windows was chosen in order to maximize the number of pillars but at the same time to not compromise the wafer's fragility. For x-ray microscopy observation purposes, Si_3N_4 windows are opened by etching the Si and creating a cavity as we observe in Figure 3.4b. This etching is done from the backside with KOH and is a well documented anisotropic process. It relies on the different etching rates depending on the crystallographic planes. The diagonal sidewalls of the Si are defined by the (111) plane, whose etch rate is low compared to the (100) direction. Due to the nature of this etching step, careful considerations must be taken when designing the layout as well as ensuring the proper alignment during lithography. Figure 3.4c shows the layout with the four Si_3N_4 windows in every square. A match with the optical MRAM mask is crucial to follow the standard lithography processes. This first step was done by Bruno Fernandez in Institute Néel.

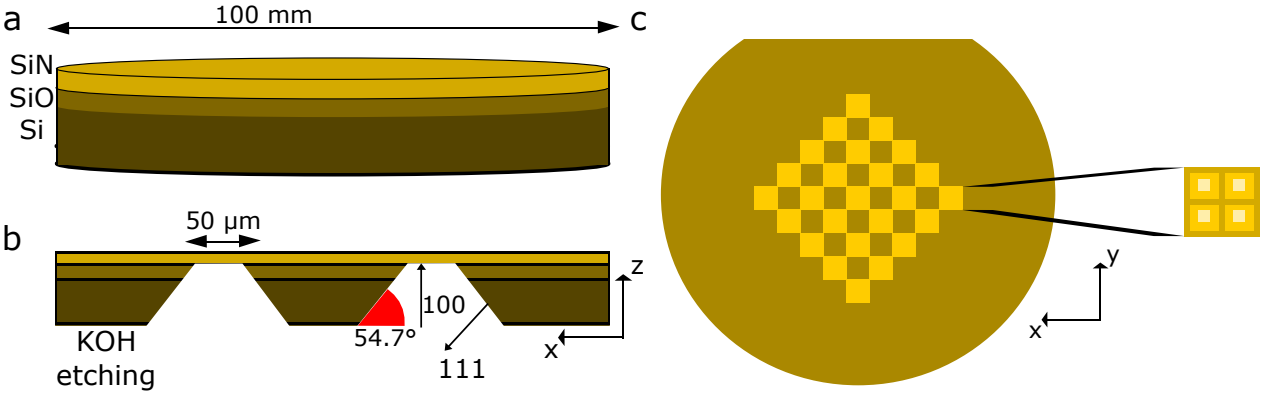

Fig. 3.4: Layout on the wafer for MTJ patterning | **a** A sketch of a 100 mm wafer representing a thick Si, followed by an oxidized SiO_2 layer and a thin Si_3N_4 (thickness not in scale). **b** Side view of the wafer after the etching process with KOH that creates the cavity in silicon and opens a Si_3N_4 window of 50 µm. **c** Top view of the wafer with the 'chessboard' layout and zoomed section with the the four Si_3N_4 windows we designed per die.

3.3.1.1 MTJ patterning

To define circular holes with a variety of diameters, ranging from 50 nm to 5 µm, electron beam lithography (e-beam) is used. A polymer is spin-coated onto the wafer (Figure 3.5a), baked and exposed by electron beam lithography (Figure 3.5b). The locations of some Si_3N_4 windows were used to align the e-beam pattern. After the development step, holes are created in the resist. The holes in the PMMA resin are filled with the 120 nm

Ti (0.5 nm/s rate), which is acting as a hard mask and serves as a guide for the stack etching. Ti deposition is performed in a physical vapor deposition (PVD) tool at 0.5 nm/s rate. During the lift-off process, PMMA is removed and the Ti remains only on top of the stack (Figure 3.5c) where the e-beam defined the dots. In the standard MRAM process used in Spintec, Reactive Ion Etching (RIE) of a 150 nm Ta pillar is preferred instead of lift-off to define the hard mask of the pillar[1].

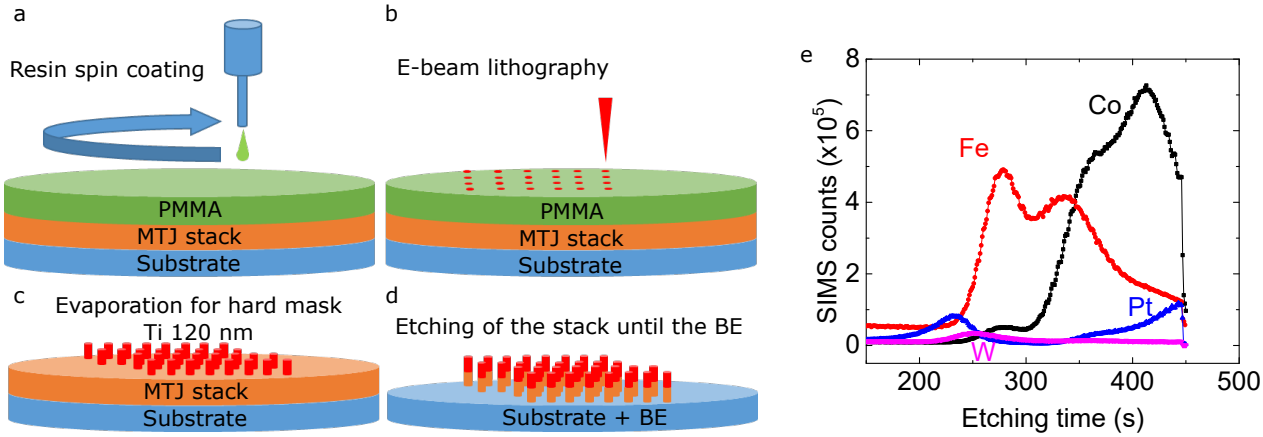

Fig. 3.5: Definition of the MTJs | Schematic representations of **a** PMMA spin coating, **b** e-beam writing **c** the Ti hard mask deposition and the lift-off and **d** the etching of the stack. **e** SIMS signal of the MTJ stack during the IBE etching process showing the detection of different materials. The drop in the signal represents the closure of the shutter at the right time.

The magnetic stack is then etched by ion beam etching (IBE) at a certain tilted angle (55°) which prevents the etched atoms from redepositing on the conductive sidewalls, but vertically enough to ensure that the diameter does not become too large resulting in a cone shape. After etching the magnetic stack (Figure 3.5d), a second grazing incidence (10°) etching is performed to remove the potential conductive redeposited atoms from the sidewalls in the tunneling barrier which could lead to short circuits. This same step can also be used in order to reduce the diameter of the pillars. In our case, the diameter precision step is not as crucial as for our colleagues in Spintec working on perpendicular shape anisotropy (PSA), for instance, since our pillars are relatively large (>100 nm). Regarding the etched materials, an in-situ secondary ion mass spectrometer (SIMS) in the ion beam etching tool is used during the etching process (see Figure 3.5e), which allows us to follow the etched species in real time during the etching process. In this particular example, we were etching the standard MTJ stack used in Chapter 6, with Pt/W which are etched at the beginning, followed by two Fe peaks and later the Co from the SAF. If one looks more closely, there is also some Co being etched at the same moment as the Fe. At the end of the etching process, the Pt starts to increase (both from the SAF repetitions and from the metallic bottom contact when it is reached). This is when the IBE tool has to be stopped. It is essential to note this was a highly challenging step given the thin bottom electrode in our stack. There was a trade-off between the etching rate to slow it down without affecting the pillar shape. Some of the Ti of the hard mask also gets etched, a point to keep in mind for the future top contact.

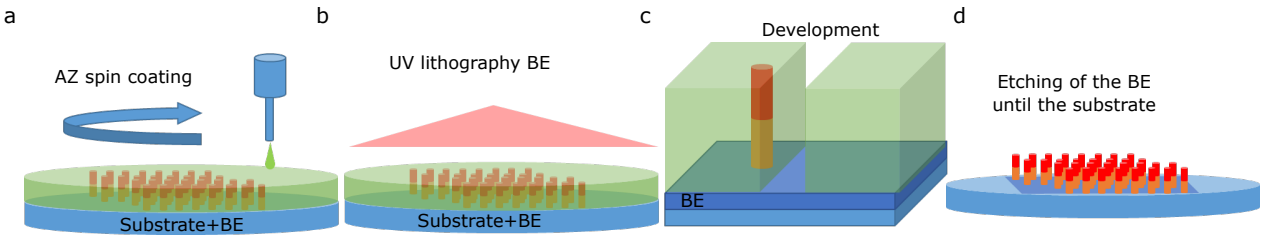

Fig. 3.6: Bottom electrode definition | Schematic representation of the **a** coating step, **b** UV illumination, **c** development of the resist and **d** isolated pads on the wafer. BE stands for bottom electrode.

[1]For this, a 150 nm-thick metallic hard mask of tantalum (Ta) is deposited by magnetron sputtering in standard MRAM processes, together with a 3 nm ruthenium (Ru) layer, which will serve as an etching stop layer during a future the hard mask etching process.

Bottom contact definition The definition of the bottom electrode is achieved in the next step by etching the remaining part of the stack in the desired areas of the wafer. Positive resist (AZ1512HS) is coated and baked to be then exposed to UV to define the regions between the devices. After the development, the resist remains in the areas where our bottom electrode is defined (see Figure 3.9a) All the rest is etched again by IBE and controlled by the SIMS. To note also the care taken during this step, the substrate below our bottom electrode is Si_3N_4 and physical etching is dangerous for such thin membranes. At the same time it is imperative to remove all the Pt and Ta of our stack to avoid short circuits. Once the bottom pads are isolated from one to the other, we deposited an insulating polymer to encapsulate the pillar and separate the bottom and the future top contacts.

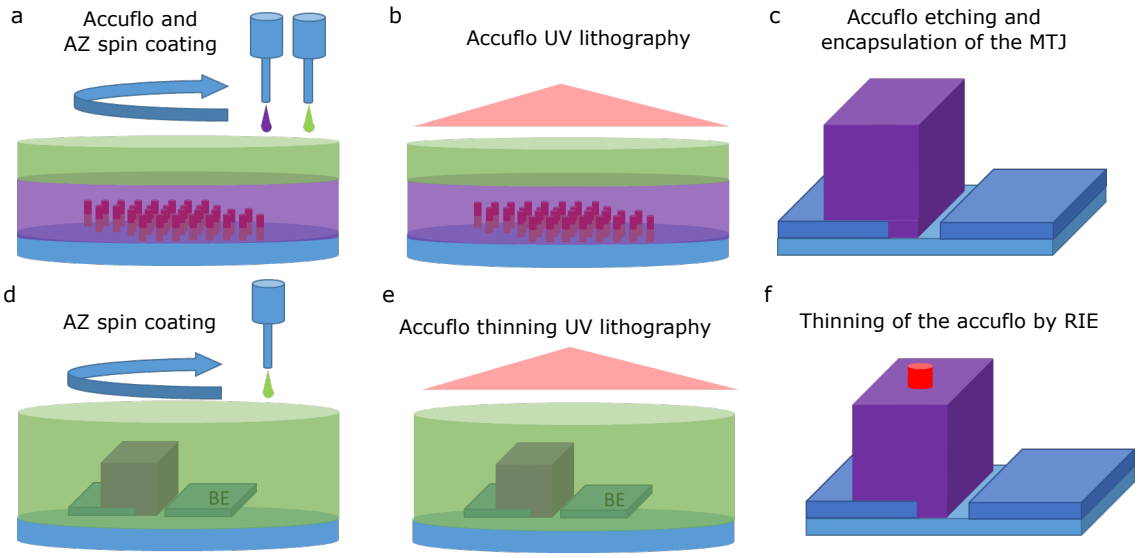

Fig. 3.7: MTJ encapsulation with accuflo | Schematics of the **a** deposition of accuflo and the AZ resist for coating, **b** UV lithography step, **c** accuflo reactive ion etching all over the wafer except around the pillar, **d**, coating for the thinning, **e** lithography step of the hole opening for the thinning and **e** result of the etching step with the pillar emerging from the polymer.

MTJ encapsulating Accuflo organic polymer is used for pillar encapsulation (Figure 3.7a). An AZ resin is then coated and baked to define the regions where accuflo is etched (Figure 3.7b). All of the accuflo is etched except in the region around the pillars, which separates both electrodes (Figure 3.7c). The initial height of the accuflo is measured by profilometry (typically 500 nm) and then the etching rate is obtained. This rate is crucial in order to let the pillar come out from the polymer as we see in the sketch of Figure 3.9f. For this thinning step, another positive resist coating and UV lithography are required (Figure 3.9d,e). The holes should be deep enough to reach the hard Ti mask, but not too deep to avoid short circuits. For this, since the height of the accuflo hole can be measured with the profilometer, the half of the hard mask height is targeted to get a proper electrical contact.

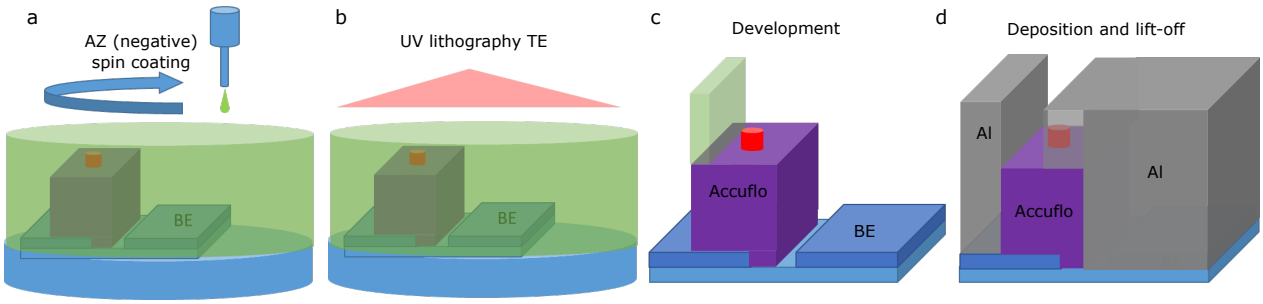

Fig. 3.8: Top contact definition | Schematics of **a** coating step with a reversible resist, **b** UV exposure, **c** development and the remaining resist to avoid short circuits and **d** result of the MTJ nanofabrication after the evaporation of the Al layer and the lift-off.

Top contact definition The last lithography step (with a reversible AZ resist and double UV exposure shown in Figure 3.8a,b) defines the top electrodes by depositing the Al metallic layer on the holes to contact the pillar. A last lift-off process ends the nanofabrication (Figure 3.8d).

Given the fragility of the wafer with SiN membranes, some precautions while handling the wafer, spin coating and introducing the sample in vacuum chambers must be taken. In standard nanofabrication processes, every liftoff process is performed with the help of ultrasounds. In our case, this has to be imperatively avoided to prevent the membrane from ripping up. Secondly, for every coating step we stick the wafer onto another one with PMMA by placing a few drops in the periphery of the wafer, away from the membrane pattern. Here, kapton can help to sandwich both wafers for further safety. Same thing for steps that require vacuum (RIE, IBE, evaporation). The pressures of both sides of the membrane equalize, avoiding its collapse. In addition, note that the height of the wafer is now double, so one should also be cautious in the MJB4 lithography tool. Lastly, every lift-off step must release both wafers as soon as the acetone goes through them.

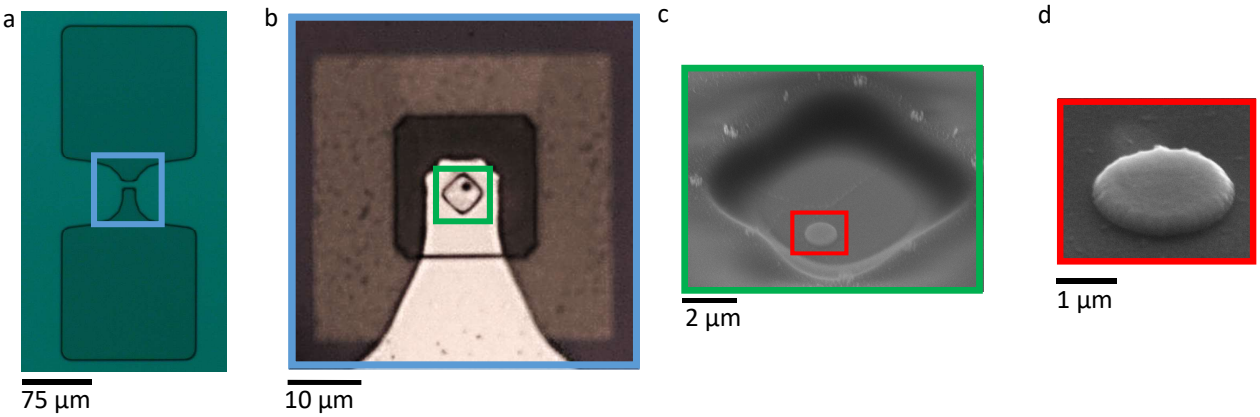

Fig. 3.9: Process flow of the MTJ nanofabrication | **a** Optical microscope image of the wafer state after the bottom electrode lithography process. The membrane is not visible here due to the lack of contrast, caused by the stack. **b** Optical microscope image after the lithography step for the accuflo thinning showing the membrane and both accuflo lithographies. The dark dot is a pillar. **c** SEM image of the accuflo opening showing how the pillar comes out. **d** SEM image zoom of the pillar ready to be contacted. The color code is added to follow the zooming.

In addition to the sketches shown above, I add in Figure 3.9 images obtained by optical microscope and SEM of a few steps during the nanofabrication process on membranes, namely, the bottom contact definition in Figure 3.9a, the accuflo thinning in 3.9b and the SEM images of the pillar coming out from the polymer in 3.9c,d before the deposition of the electrode. The color code on the contour of the images is added to help the visualization of the process and the zooming.

3.3.2 MTJ characterization

In addition to pillars on SiN, we also patterned nanopillars following the standard process additional MTJs on 100 mm Si substrates for the MTJ characterization. For this, an automated prober station evaluates the first properties of the patterned devices. Resistance vs perpendicular magnetic field hysteresis loops are obtained in order to determine the basic behaviours of the junctions all over the wafer. This allows us to quickly identify the desired areas for further analysis and see the dependencies of the magnetic properties on wedge deposition along a wafer axis direction, if any. Applying a low bias voltage by a source-meter, the device resistance is measured. To assess wafer yield[2], defective devices with short or open circuits are filtered out, which could be caused by manufacturing flaws. This step is crucial for identifying issues related to specific steps during the nanofabrication process. Short circuit devices may arise from excessive polymer window etching prior to top electrode deposition, while open circuit devices can result from pillar losses/falls during patterning or, more commonly, insufficient polymer window etching before contacting.

[2]The percentage of the pillars that are working after the nanofabrication process.

3.4 X-ray microscopy techniques

3.4.1 X-ray Magnetic Circular Dichroism (XMCD)

X-ray magnetic imaging utilizes physical effect named XMCD (X-ray Magnetic Circular Dichroism) which relies on the interaction between circularly polarized light and magnetic material.

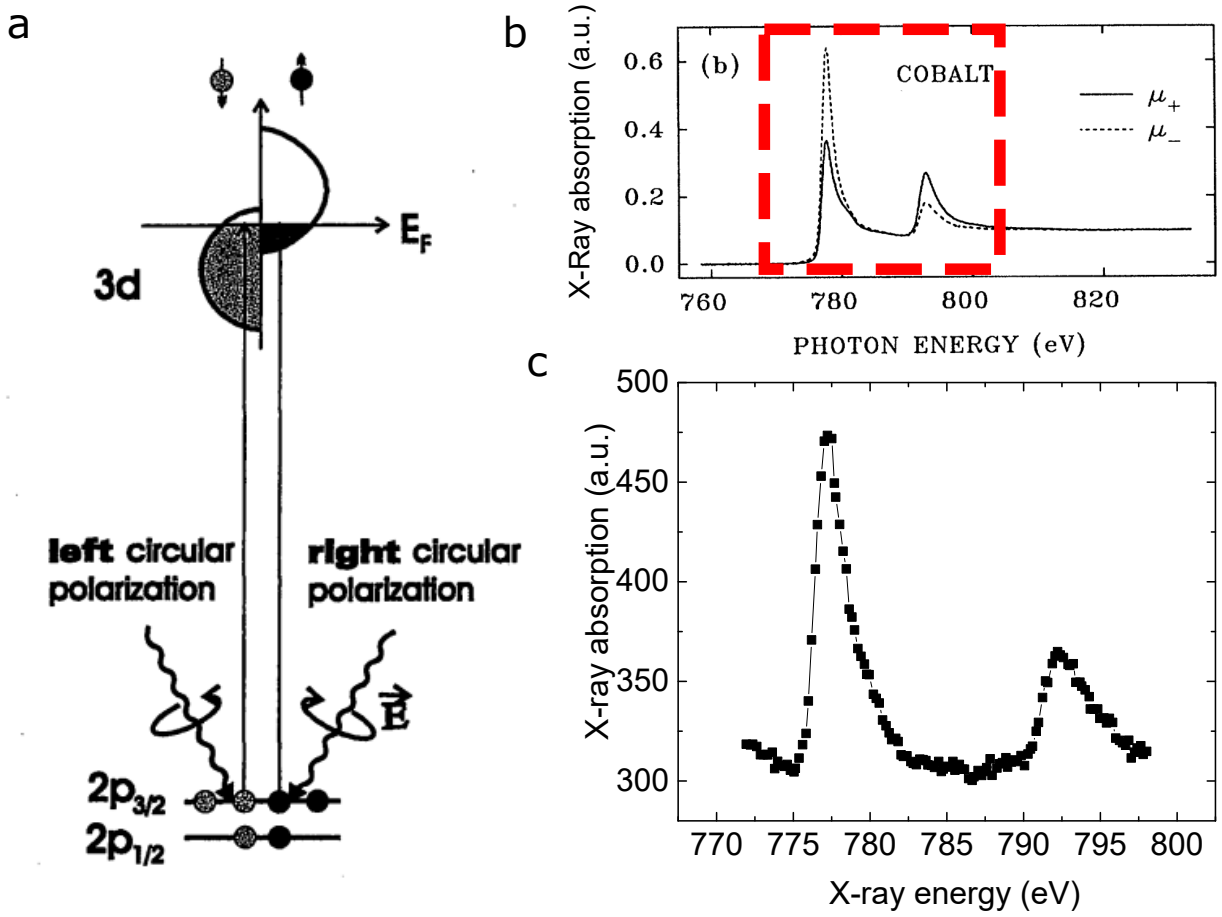

Fig. 3.10: X-ray Magnetic Circular Dichroism (XMCD) | **a** Absorption of circularly polarized x-rays inducing the electronic transitions in a 3d transition material. Adapted from [165]. **b** Absorption vs energy of x-rays for Co of both left and right circularly polarized x-rays. Adapted from [166]. **c** Zoom and example of one of our samples showing the two typical L_3 and L_2 peaks in Co, measured in Elettra synchrotron.

Dichroism is a property found in certain materials, referring to their ability to selectively absorb or transmit light waves of specific polarizations. XMCD is the different absorption of left and right circularly polarized light in a magnetic material. For a given helicity, the x-ray absorption depends on the relative orientation of the x-ray beam direction and the magnetic moment orientation. More specifically, it is proportional to the projection of the magnetic moment on the x-ray beam direction. The principles of x-ray magnetic circular dichroism spectroscopy are shown in Figure 3.10a for the case of L-edge absorption in a 3d band transition metal. In a magnetic transition, metal the 3d valence band is split into spin-up and spin-down states with different occupation. The absorption of right (left) circularly polarized light mainly excites spin-up (spin-down) photo-electrons respectively. Due to the spin-orbit coupling (SOC), the 2p band in these materials splits into two sub-bands: $2p_{1/2}(L-S)$ and $2p_{3/2}(L+S)$, corresponding to L_2 and L_3 absorption edges as we can see in Figure 3.10. When a photon's energy matches one of these absorption edges, an electron gets excited from the 2p to the 3d band. In the 3d band, there is an asymmetric distribution of energy states, leading to a higher number of holes of one spin type at the Fermi level. Additionally, the orbital momentum of electrons in the $2p_{1/2}$ band is opposite to their spin orbital momentum (unlike the $2p_{3/2}$ band, where they are aligned). When a photon with a fixed angular momentum interacts with the 2p band, the probability of exciting a specific spin direction depends on the conservation of total angular momentum [165]. Consequently, different transition probabilities result in an asymmetrical absorption spectrum for photons with right and left circular helicity. The x-ray energy to which each material is sensitive to should be tuned to maximize

the absorption. X-ray absorption spectroscopy (XAS) employs the energy-dependent absorption of x-rays for different materials (the case of Co is illustrated in Figure 3.10b). This technique is mainly used in order to gather details about the element composition of a sample. Given the difference in the absorption of left and right circularly polarized x-rays, subtracting them leads us to a net signal named XMCD. In our case, XAS energy scans help us to tune the x-ray energy to identify the different peaks of absorption. Figure 3.10c shows one of our XAS measurement performed in order to find the peaks of absorption of the Co edges for a circularly left polarized x-ray. The energy value corresponding to the largest peak is the one chosen for imaging. Little deviations in the energy from the absorption edge of the material can lead to a significant decrease of the contrast, especially when the thickness values of the thin films are ranging around 1 nm, like in our case.

In the upcoming sections, we will introduce two imaging techniques that take advantage of this effect to visualize magnetic textures. In both cases, the images were obtained using the L_3 absorption edge of the ferromagnetic material (Co or Fe), as it demonstrates the highest absorption.

3.4.2 Scanning Transmission X-ray Microscopy (STXM)

A STXM (Scanning Transmission X-ray Microscope) is a type of microscope that uses x-ray radiation to create high-resolution images of samples. It operates based on the following principle: A monochromatic x-ray beam is focused onto an illumination spot of just a few nanometers using a Fresnel zone plate (FZP). These FZPs typically have an outer zone width of 25 or 50 nm, resulting in beam spot sizes of 31 to 62 nm, respectively, and this determines the spatial resolution of the STXM. An order separating aperture (OSA), acting as a pinhole, is positioned between the sample and the FZP. It blocks the non-diffracted light, commonly known as zero order light, transmitted through the FZP. Circularly polarized light, either left or right, can be selected for XMCD measurements using a bending magnet or undulators. To create images, the sample is scanned pixel by pixel using piezo-positioners. Here, the beam is stationary and it is the sample which moves. The transmitted photons are collected by a point integrating photo-detector. To achieve proper focus, a focus scan is performed, moving the sample with respect to the FZP.

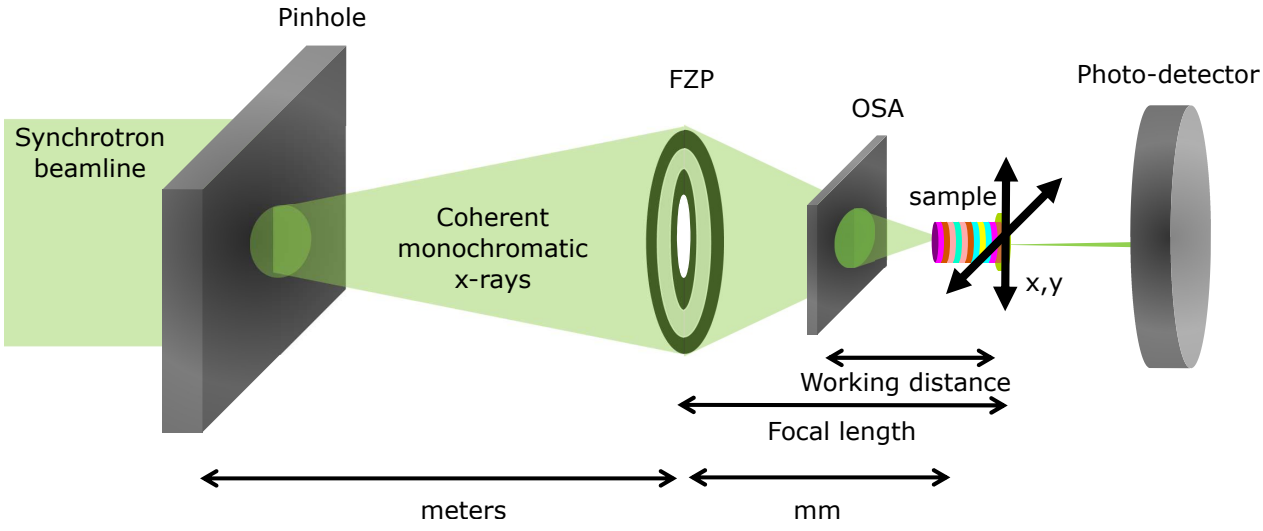

Fig. 3.11: Schematics of the STXM microscopy technique | A FZP is illuminated by synchrotron emitted x-ray light. The OSA focuses the light onto the sample. The transmitted photons are recorded by a x-ray detector. The distances between the microscopy elements are not in scale.

These experiments were realised with the support of Sebastian Wintz and Markus Weigand at the MAXYMUS beamline, Bessy synchrotron, Berlin, Germany and Rachid Belkhou and Nicolas Mille at the HERMES beamline, Soleil synchrotron, Saint-Aubin, France.

3.4.3 Photo-emission electron microscopy (PEEM)

X-PEEM imaging technique operates by inducing the emission of a cascade of photo-emitted secondary electrons through x-ray absorption in a thin layer at the sample surface. A circularly polarized beam with an incident angle of 16° degrees relatively to the surface plane is employed (see Figure 3.12). To accelerate the emitted electrons, a voltage (typically around 15-20 kV) is applied. The accelerated electrons are then processed by all the electro-optical components of the microscope and then impact on a screen sensitive to the electrons. Among some of these components, there is the contrast aperture which is manually adjusted to prevent image aberrations that can arise from high emission angle electrons. Since the electrons' escape depth is low, the secondary emitted electrons originate from a surface depth of only a few nanometers, making this technique highly surface sensitive. Therefore, it is crucial to consider the capping layer thicknesses of the samples for PEEM observations. One drawback of this technique is that the x-ray beam illuminates a large area of the sample (typically 100×100 µm^2), resulting in only a little fraction of photons contributing to the high magnification image.

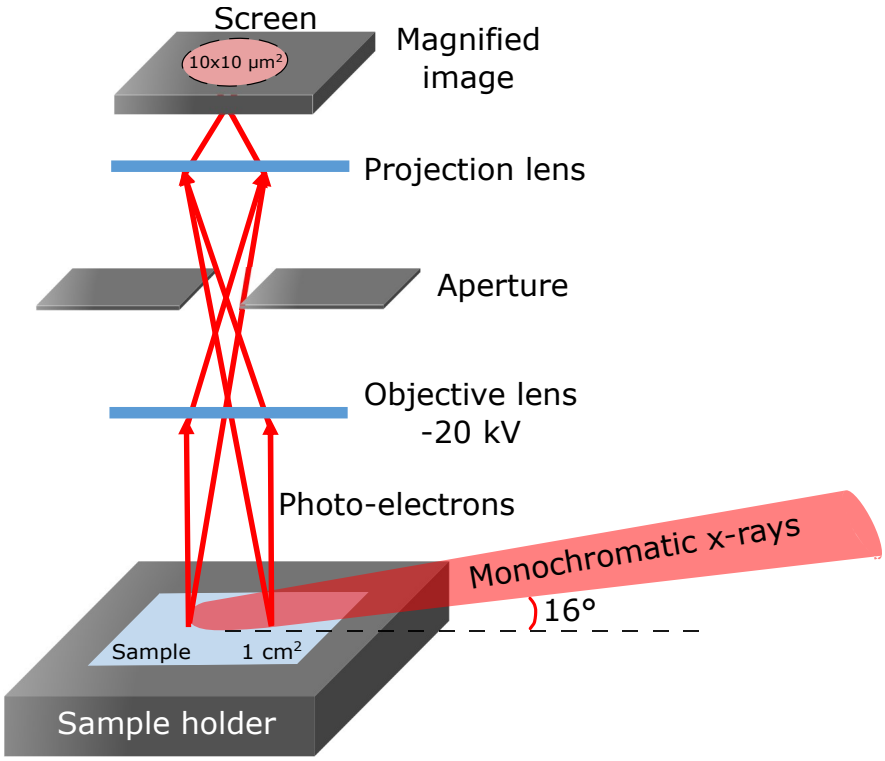

Fig. 3.12: Schematics of the X-PEEM microscopy technique | The X-PEEM setup. X-rays illuminate the sample at a grazing angle. The electrons are accelerated with high voltage through the electro-optical components and the acquired image is magnified. The distances are not in scale.

Figure 3.13a displays an image obtained through XMCD-PEEM at the L3 Co edge, revealing the domain arrangement within a Pt/Co/Ru based SAF sample with PMA at room temperature. The white and black contrasts in the domain correspond to the down and up component of the magnetization. A magnetic contrast is observed even though the SAF is fully compensated. This is possible due to the surface sensitivity of the PEEM. Given the incidence angle of the beam, for domain walls that are oriented perpendicular to the x-ray beam, the in-plane contrast is approximately three times larger compared to the out-of-plane. Indeed, in the image, distinct black and white lines emerge, indicating alignment (along or against) of magnetization with the x-ray beam direction. The line scan that follows the white dots is plotted in Figure 3.13b, which represents the measured XMCD contrast along the direction of the beam, showing the typical up and down trend of the signal [103]. This is related to a rotation of the magnetization that corresponds to a left-handed Néel DW. This tool therefore allows us to observe the internal structure of domain walls or skyrmions.

The X-PEEM experiments were done with the support of Michael Foerster and Miguel Ángel Niño at the CIRCE beamline, Alba synchrotron, Cerdanyolla del Vallès (Barcelona), Spain and Andrea Locatelli and Tevfik Onur Mentes at the Nanospectroscopy beamline in Elettra synchrotron, Basovizza (Trieste), Italy.

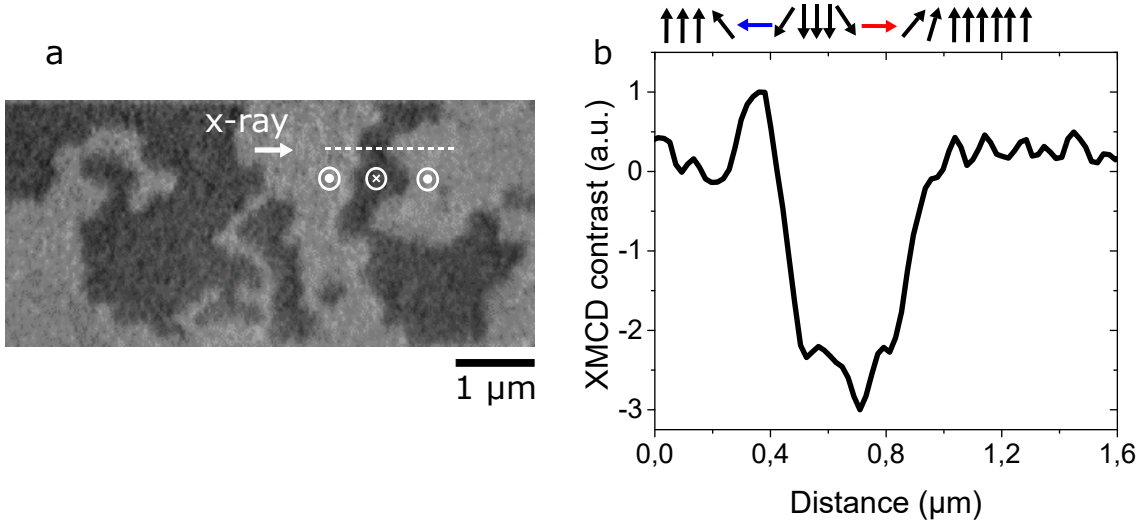

Fig. 3.13: XMCD-PEEM image of Néel domain walls | **a** XMCD-PEEM image of the domain configuration in an ultra-thin Pt/Co/Ru film at RT acquired at the Co L_3 absorption edge. **b** XMCD contrast along the dashed white line in **a**. The XMCD contrast is proportional to the projection of the incident x-ray beam on the magnetization direction. Hence, the brightest and darkest contrasts in the direction of the beam are represented in the typical peaks and dips we see in the graph, indicating a Néel configuration with a left-handed chirality (see arrows). This measurement was performed in ELETTRA synchrotron during my thesis in order to confirm the left handed chirality of the Néel domain walls, which agrees with the sign of the DMI expected in Pt/Co/Ru interfaces.

3.4.4 STXM for time resolved magnetic imaging

In conventional x-ray imaging, static mode techniques are used, which provide snapshots before and after an external stimulus is applied. However, to gain insight into real-time magnetization dynamics, imaging during the stimulus is crucial [167–172]. In the next lines, we will briefly go through the pump-probe approach, using the synchrotron-generated x-rays, to achieve time-resolved imaging. Specifically, the STXM technique is employed, coupled with an external excitation period, to capture images of the sample's response during the stimulus. This is the technique we used in order to get the time resolved skyrmion nucleation via localized electrical current pulses in Chapter 4.

The x-rays emitted from the synchrotron source with bunches around 50 ps width permit the combination of high space and time resolutions for periodic operations. Inside the synchrotron ring, electrons are emitted in bunches with a discrete period, and consequently the arriving x-rays have a periodic pulse character. For soft x-rays, the arrival period is around 2 ns (500 MHz) (see Figure 3.14). In our case, pump refers to the external excitation we apply. We induce periodic excitations on our sample and probe the excitation with the synchrotron source.

Using a straightforward stroboscopic illumination with a pump period synchronized to the probe period will only allow the sample to be probed every 2 ns. In order to get a finer temporal probing than the 2 ns, an acquisition scheme for pump-probe imaging was implemented at Bessy synchrotron that uses all bunches of electrons [173]. This system's main components are a quick detector for finding single x-ray photons and a connected FPGA board. The FPGA board sorts photon events into a maximum of 2048 channels based on when they arrive after the sample is excited. If one can distinguish signals from two neighboring x-ray pulses, the sample does not need to recover its initial state between them and one can organize the data from each pulse into a suitable channel synchronized with the external stimulus. Here, the pumping period is chosen to introduce a time shift τ in relation to the synchrotron clock after each pumping event. When the photon count from a bunch is assigned to a channel, it keeps track of the corresponding phase shift. This results in a consistent temporal sampling of the excitation period, with the time step τ serving as the interval between time channels. When this τ represents an integer fraction (M) of the period between synchrotron flashes ($\tau = 2/M$ ns), the original time relationship is restored after M pumping cycles. For this to be true, the following rule must be fulfilled:

$$T_P = T_S \frac{N}{M}, \tag{3.1}$$

where T_P is the pump period, T_S is the synchrotron period (2 ns), N is the number of channels (an integer) and M is the fraction of the synchrotron period. Consequently, the phase shift between the excitation and the bunch is different for every bunch.

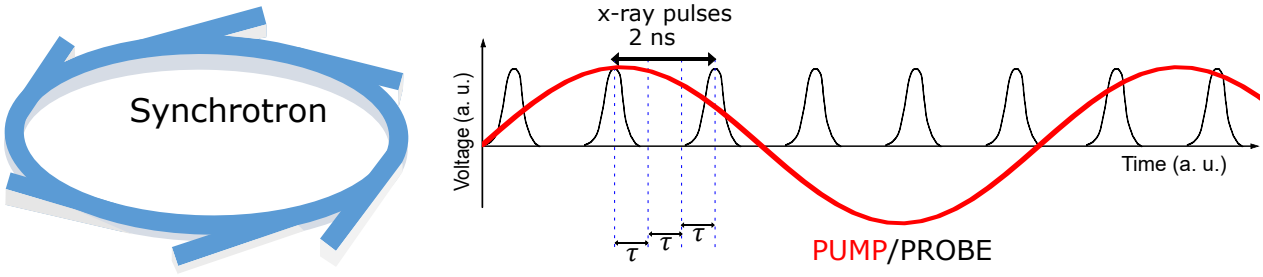

Fig. 3.14: Pump-probe mechanism | Schematics of the pump-probe setup. The photons from the synchrotron arrive every 2 ns (500 MHz). The pump period is a fractional multiple of the probe period and this creates a shift of τ after each pump cycle between pump and probe. This adds up to the full 2 ns probe period after an integer number M of pump cycles, resulting in a time resolution of τ for the acquisition. In this example: $N = 17$, $M = 3$, $T_P = 11.33$ ns, $\tau = 0.667$ ns.

When the measurement is running and the STXM is focused on a pixel, the different channels accumulate data throughout the entire duration of the excitation period. The acquisition time per pixel was optimized to obtain a high quality time-resolved series within approximately 100 ms. Note that this approach required extreme reproducibility of the magnetization dynamics. This setup allows for a time resolutions below 100 ps and spatial resolutions around 30 nm.

The time resolved experiments were carried out at the MAXYMUS beamline, in Bessy synchrotron, Berlin, Germany. These experiments were realised with the support of Sebastian Wintz and Markus Weigand.

Chapter 4

Nucleation and dynamics of magnetic skyrmions in synthetic antiferromagnets

Contents

4.1 Our SAF system 59
4.2 STXM observations of current-induced nucleation and dynamics of SAF skyrmions 60
4.2.1 Nucleation of AF skyrmion lattices at large current densities 62
4.3 Simulations and modelling 64
4.3.1 Electrical and thermal simulations 64
4.3.2 Micromagnetic simulations 64
4.3.3 Analytical model of the bubble expansion and relaxation 65
4.4 Discussion and conclusions 68

This chapter details the work carried out mainly in the first and second year of my PhD thesis. The material systems chosen were synthetic antiferromagnets. All the optimization process and the experimental results regarding the nucleation, dynamics and observation of skyrmions will be explained in the following pages.

Due to their zero magnetic moment, the observation and nucleation of SAF skyrmions is highly challenging. The magnetic compensation makes them insensitive to the external magnetic fields, so other nucleation means have to be addressed. Juge *et al.* [162] successfully nucleated SAF skyrmions in SAF multilayers using low anisotropy stacks to reduce the domain wall energy and favour the spontaneous nucleation of skyrmions. Not only they demonstrated the AF alignment of the FM layers but also the controlled nucleation of the skyrmions using electrical current. For this, x-ray magnetic microscopy techniques were utilized to probe the individual FM layers.

The optimized multilayer stack was $[\mathrm{Pt}(0.5)/\mathrm{FM1}/\mathrm{Ru}(0.85)/\mathrm{Pt}(0.5)/\mathrm{FM2}/\mathrm{Ru}(0.85)]_2$, where FM1 = $\mathrm{Co}(0.3)/\mathrm{Ni_{80}Fe_{20}}(1.45)/\mathrm{Co}(0.3)$ and FM2 = $\mathrm{Co}(1.35)$ (thicknesses in nanometer). In order to determine the chirality of these SAF skyrmions, micromagnetic simulations and analytical modeling were performed. Experimentally measured magnetic parameters were used for simulations, confirming the same left-handed chirality in all the FM layers.

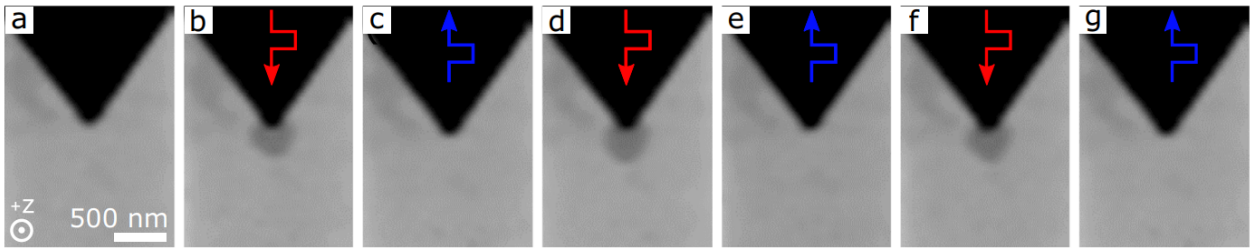

Fig. 4.1: Current-induced nucleation/annihilation of SAF skyrmions | **a-g** Zero field sequence of STXM images at the L_3 Co edge after applying successive positive and negative 5 ns current pulses for each image. The triangular-shaped gold (100 nm) injector triggers the nucleation of the skyrmions. From [162].

Other means of nucleation were also chosen, via localized current injection and laser excitation. The objective here was to control the nucleation site, overcoming the problem of the uncontrolled stochastic nucleation in the track for applications. In particular, the nucleation of a single SAF skyrmion was demonstrated via the local injection of a current in the track using a thick metallic tip with a triangular shape (see Figure 4.1). Starting from a monodomain state, the injection of a positive 5 ns current led to the creation of the skyrmion (Figure 4.1b). The skyrmion was then annihilated by injecting a second current pulse with an opposite current polarity (Figure 4.1c). This process was found to be very reproducible. Regarding laser excitations, several isolated skyrmions and skyrmion lattices were also observed with XMCD-PEEM due to the laser-induced heating. The fs laser pulse leads to a fast temperature rise, overcoming the nucleation energy barrier.

However, open questions such as the mechanism behind the current-induced nucleation and the nucleation dynamics were still to be answered. For this, time resolved magnetic imaging is required. In the following sections I will describe the steps for the optimization of the magnetic stack for these objectives.

4.1 Our SAF system

The stack composition for the microscopy observations is Ta(3)/Pt(2.5)/[Pt(0.5)/FM_1/Ru(0.85)/Pt(0.5)/ FM_2/ Ru(0.85)]$_{12}$/Ta(2) (thickness in nm), where FM_1 = Co(0.2)/NiFe(t)/Co(0.2) and FM_1 = Co(0.9). The Co/NiFe/Co structure is acting as a single FM due to the exchange coupling. The reason to add the ultrathin Co is in order to maintain the same interface in both FM. The thickness of 0.9 nm of Co gives a strong PMA and the Py is deposited as a wedge in order to find the compensation point. This can be seen in Figure 4.2, which shows magnetization hysteresis loops for different thickness of Py layers. While a non zero magnetization is measured at remanence for t_{Py} = 1.1 nm and t_{Py} = 1.0 nm (see Figure 4.2a and 4.2b), a zero magnetization is obtained for t_{Py} = 0.95 nm. The sharp reversals of the layers confirm the large anisotropy expected.

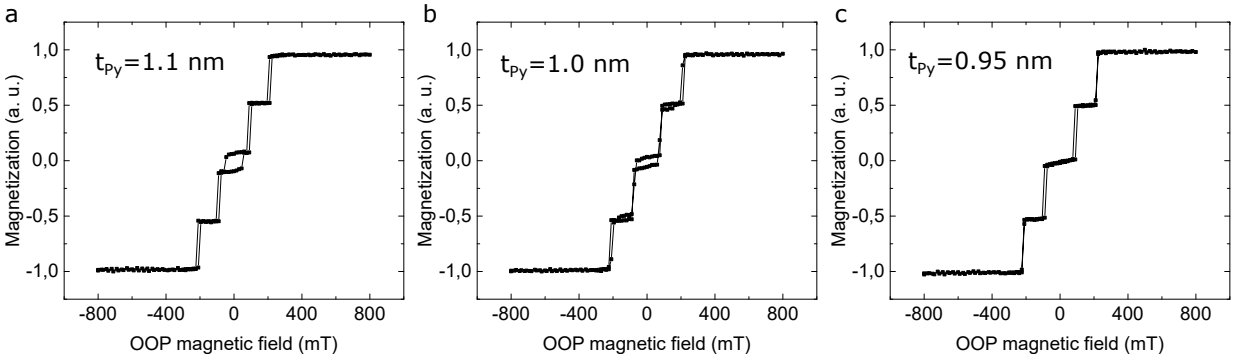

Fig. 4.2: Optimization of the compensated SAF stack | VSM hysteresis loops for different Py thickness values to get the compensation for SAF on a two repetition stack. **a** t = 1.1 nm, **b** t = 1.0 nm and **c** t = 0.95 nm. The study for the optimization of the stack was performed in the same stack composition but with two repetitions in order to facilitate the sputtering process.

One of the problems for time resolved STXM experiments can be the lack of magnetic contrast in the samples. A way to address this issue is to sputter multilayer structures to increase the magnetic volume and therefore the contrast. In particular for SAF, it means that there is an even number of FM layers coupled each-other antiferromagnetically to the neighbouring layers. The first and last FM layers have only one neighbouring FM, while the rest of the layers have an AF coupling to both neighbours. In addition to the strong AF coupling, these multilayers need to fulfill relevant requirements in each FM such as PMA and a strong DMI in order to promote homochiral spin textures. The designed multilayer was inspired from the work of Roméo Juge [174] using a Pt/Co/Ru based structure. The Pt/Co interface gives rise to the PMA and interfacial DMI, while the optimized Ru thickness of 0.85 nm provides the maximum AF coupling. Moreover, the Co/Ru interface leads to an enhancement of PMA and DMI [175,176].

Different FM materials, namely Co and $Ni_{80}Fe_{20}$, are used for the magnetic layers composing the SAF. This allows the observation of the spin textures in the different AF coupled sub-lattices by adjusting the x-ray energy at the L_3 Co or Fe edges. Note that no magnetic contrast would be obtained in fully compensated SAF composed of the same FM layers.

4.2 STXM observations of current-induced nucleation and dynamics of SAF skyrmions

The geometry used to nucleate the SAF skyrmions was the same as the one as Juge *et al.* chose [162] (see Figure 4.3). It is composed of a 2 µm wide track patterned in the SAF stack on which a 200 nm thick Cu electrode with a triangular shape was patterned for the local current injection (see Figure 4.3b). The stack was deposited on a 300 nm Si_3N_4 membrane for the STXM observations. As expected, a homogeneous magnetization is observed in the XMCD-STXM images, in line with the large PMA (see Figure 4.3c, measured at the Co L_3 edge).

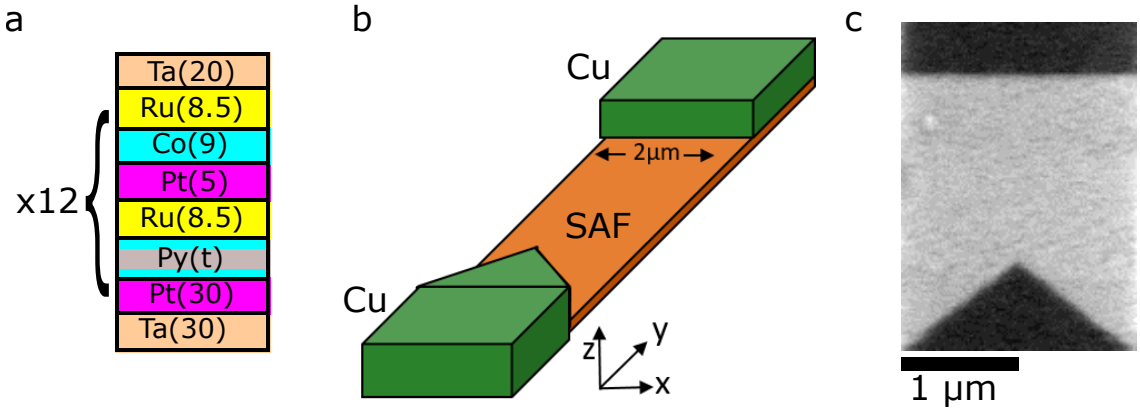

Fig. 4.3: Stack and nanofabrication for time resolved experiments | **a** Stack of 12 repetitions SAF. **b** A sketch of the geometry used for SAF skyrmion current-induced nucleation. **c** XMCD-STXM image in the L_3 Co edge showing a homogeneous magnetization (white) and the Cu electrodes (black).

To study the dynamics of the current-induced nucleation, time resolved pump-probe scanning transmission x-ray microscopy experiments were performed at the Maxymus beamline in Bessy synchrotron. As mentioned in Chapter 3, the multichannel time acquisition capacity of the beamline allows us to achieve very high time resolution image acquisition, down to 125 ps. For such pump-probe experiments, highly reproducible nucleation of SAF skyrmions is required, which was demonstrated from the static experiments described in the previous section.

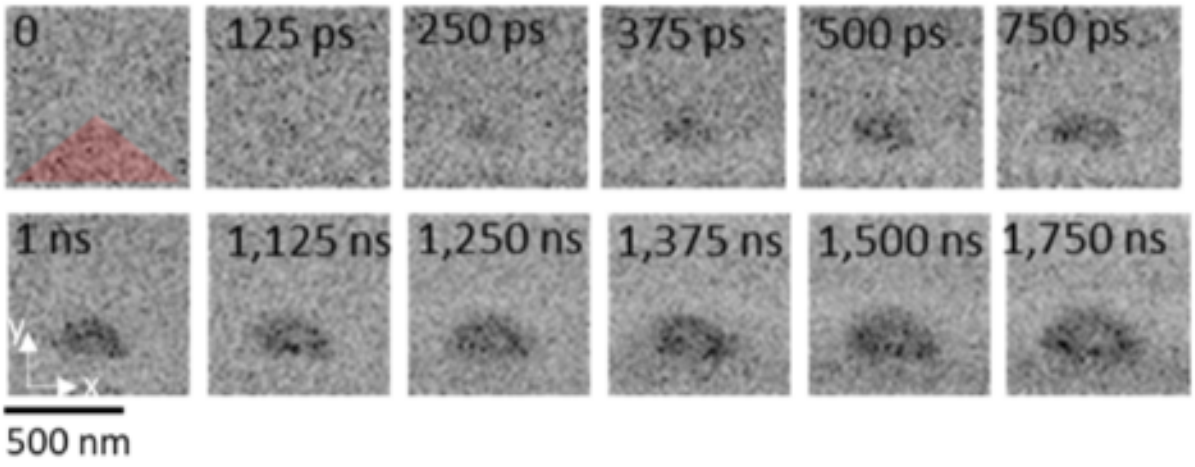

Fig. 4.4: Time resolved STXM experiments | Sequence of images obtained at the Co L_3 edge of time resolved pump-probe STXM magnetic microscopy images measured at different time after the injection of a 3 ns width current pulse. The red triangle indicates the location of the Cu tip.

For these experiments, 3 ns width current pulses were injected at a 4 MHz repetition rate and the pulse trigger was synchronized to the x-ray bunch of the synchrotron with a 500 MHz repetition. The high repetition rate led to different nucleation and annihilation density thresholds, as compared to the single pulse injection. The average nucleation threshold current density value was about $7.5 \cdot 10^{11}$ A/m^2 in the 2 µm

wide track. For these parameters, the nucleated SAF skyrmion was found to be unstable and it annihilated after typically ten ns (see experiments below). Since the period of the current pulse injection was 250 ns, the skyrmion was annihilated when each new pulse was applied.

Figure 4.4 shows the time evolution of the skyrmion nucleation acquired at the Co L_3 edge without any external magnetic field with a time resolution of 125 ps. The background image was subtracted so that only differences from the initial monodomain state are observed. We observed that the nucleation proceeds by the nucleation of an initial very small domain at the apex of the tip, which then grows rapidly. An elliptical shape of the SAF skyrmion is noticed along the transverse direction of the track.

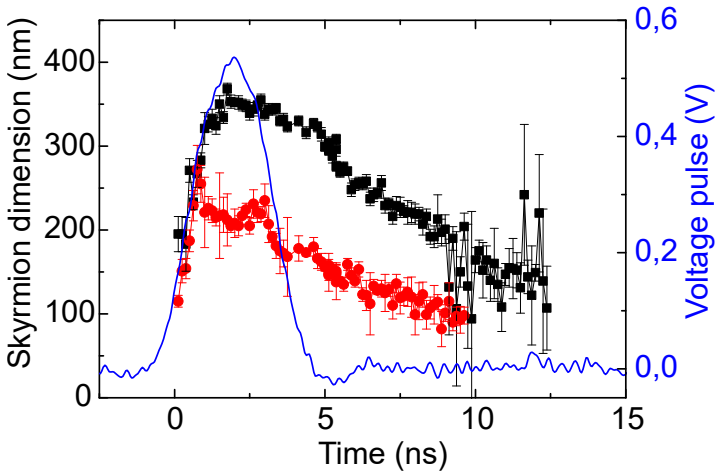

Fig. 4.5: Time evolution of the skyrmion dimension | Diameter values along both x (black) and y (red) directions vs time for the SAF skyrmion. The applied voltage of the pulse is in blue. We induced 3 ns width current pulses with an average current density of about $8.2 \cdot 10^{11}$ A/m^2 in this case.

These experiments allowed us to measure the time dependence of the SAF skyrmion size along both elliptical axes. To this end, we fitted the normalized STXM signal, which corresponds to the perpendicular magnetization $m_z = \cos\theta$ direction to a 360° skyrmion profile in both x and y directions:

$$\theta = 2\arctan\left(\exp\frac{r - d/2}{\Delta}\right) + 2\arctan\left(\exp\frac{r + d/2}{\Delta}\right), \tag{4.1}$$

where the diameter is given by d. Figure 4.5 shows the evolution of both diameters of the SAF skyrmion as a function of time. In blue, we plotted the pulse amplitude. Note here that we were not able to clearly identify the time correspondence between the STXM images and the electrical pulse injection signal, such that the $t = 0$ of the electrical pulse might be offset. We observed that the pulse injection leads to a fast increase of the skyrmion size over the first ns followed by a plateau and a slow relaxation when the pulse is turned off. After typically 10 to 15 ns, the XMCD contrasts from the SAF skyrmion vanishes demonstrating a gradual collapse of the skyrmion when the pulse is off.

Similar experiments were performed for current densities ranging between $7.5 \cdot 10^{11}$ A/m^2 and $9 \cdot 10^{11}$ A/m^2. For lower current density values we do not see any nucleation, obtaining a bottom threshold current density. In Figure 4.6a we represented the size evolution of different SAF skyrmions as a function of time for many current density values. A similar trend is observed for all current densities with a fast increase of the skyrmion diameter followed by a plateau and a slower decrease of the skyrmion diameter when the pulse is off.

An interesting parameter regarding the dynamics of the skyrmion is to see how fast the current-induced expansion occurs. For this, we analyzed the dependence of the skyrmion expansion velocity on the current density as represented in Figure 4.6b. The initial expansion velocity values are extracted from linear fits considering a steady expansion. In addition, we plotted the maximum effective diameter value which increases with the current density. The expansion velocity grows from the lowest to the highest current values and ranges between 175 and 250 m/s, but some irregularities are present. Considering the skyrmion radial expansion as domain wall motion, these irregularities could be associated to a saturation of the velocity predicted for SOT driven Néel domain walls stabilized by DMI [34] due to the high injected current densities.

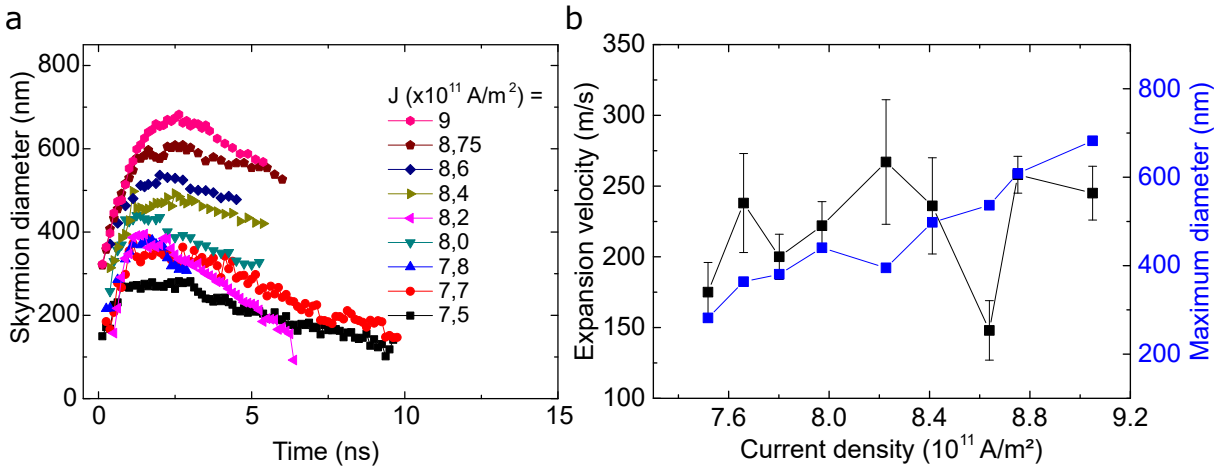

Fig. 4.6: Time evolution of the skyrmion dimension for different current densities | **a** Effective diameter vs time for the SAF skyrmions nucleated at different current densities. The effective diameter was extracted from the area of the ellipse after performing the fits for in both x and y directions. **b** Expansion velocity and maximum area of the SAF skyrmion depending on the current density.

We also noted that the nucleation process almost does not depend on the current polarity. For this, we plot in Figure 4.7 the diameter evolution for both polarities, observing little difference between them. This suggests that Joule heating plays an important role in the nucleation process due to the large injected currents, although spin orbit torque may also lead to similar features [177,178]. The corresponding nucleation energy due to the Joule heating and can be written as $E = RI^2 t_{pulse}$, where $R \approx 40\ \Omega$ is the resistance of the track, I is the injected current and t_{pulse} it the injected pulse width. In our case, an estimated energy ranges around 30 pJ. In our experiments, the track was very long (10 µm) resulting in a large resistance and thus power dissipation. A way to decrease the sample resistance is to decrease the length of the magnetic track. Tracks with lower length would facilitate the nucleation due to the decrease in the power dissipation. A simple calculation shows that sub-100 fJ nucleation energy can be achieved for lengths below 200 nm.

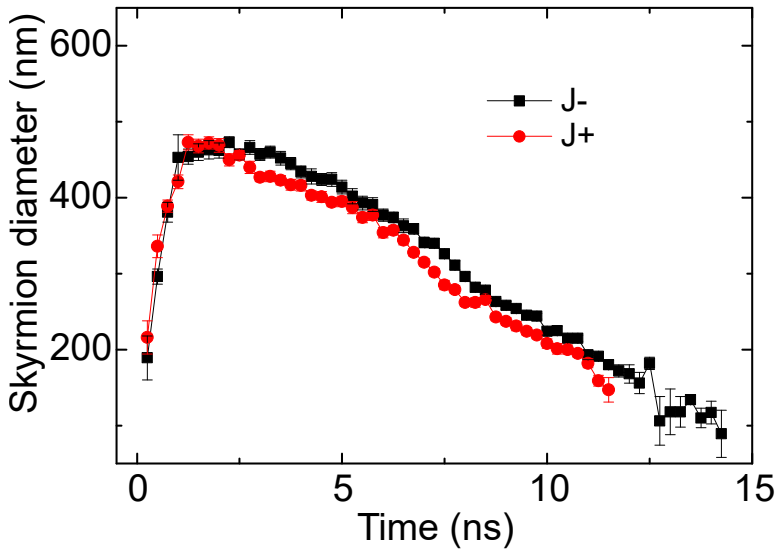

Fig. 4.7: Current polarity dependence on the skyrmion dynamics | Nucleation and relaxation of a SAF skyrmion for both positive (red) and negative (black) injected currents.

4.2.1 Nucleation of AF skyrmion lattices at large current densities

For low current densities, the influence of the current on the magnetization is localized around the area of the Cu apex. However, for current densities larger than the ones shown in Figure 4.6a ($J > 9{\cdot}10^{11}$ A/m^2), the

large current can affect the magnetization in the entire track and lead to unexpected magnetization patterns. Figure 4.8 displays the magnetization pattern at different time frames after the injection of a 3 ns current pulse of average density $J = 9.45 \cdot 10^{11}$ A/m^2. In the first ns, a skyrmion nucleates under the apex of the tip but at $t = 2$ ns, the magnetization starts to reverse within the whole tracks, leading to a "mushroom" reversal pattern in the track which remains up to 40 ns after the end of the pulse. This new pattern may be attributed to heating of the track leading to a transient multidomain or demagnetized state. Indeed, it is expected that the sample temperature is maximum in the center of the track, away from the metallic contacts where most of the heat dissipation occurs [177].

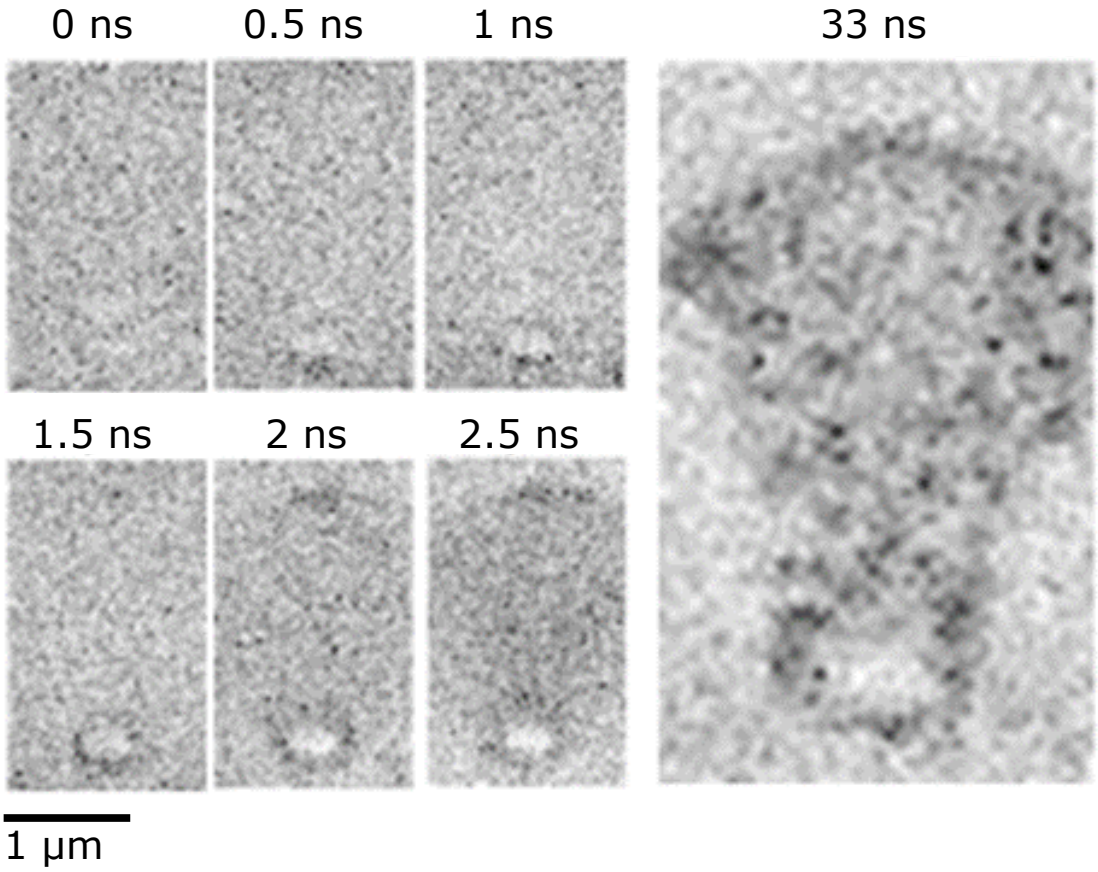

Fig. 4.8: Time evolution of the magnetization pattern at large current densities | Starting from a skyrmion nucleation, a reversal of the magnetization on the full track and a "mushroom" shaped magnetization pattern is obtained after 2.5 ns. The pulse parameters are 3 ns and $J = 9.45 \cdot 10^{11}$ A/m^2.

Interestingly, some ordered spin textures are observed during the pulse injection. We show in Figure 4.8 the observation of transient AF skyrmion lattices observed a few tens of ns after the pulse injection. These skyrmions lattices are stable for several tens of ns and then collapse. Similar transient skyrmion lattices and topological spin texture were predicted during relaxation after laser induced demagnetization [179,180].

4.3 Simulations and modelling

4.3.1 Electrical and thermal simulations

In order to gain a deeper understanding of the experimental findings, we performed 3D electrical and thermal simulations of the AF skyrmions in SAF. For the 3D FEM electrical simulations, we employed GMSH174 and GETDP175, which are free software tools for geometry construction, mesh generation, and solving. We assume here that the SAF has a uniform resistivity. As anticipated, the simulations revealed a higher current density at the apex of the tip (Figure 4.9a). The power distribution analysis (Figure 4.9b and 4.9c) displayed a concentration of dissipated power in the center of the track, exhibiting a pattern resembling the experimentally observed "mushroom" contour (see Figure 4.8).

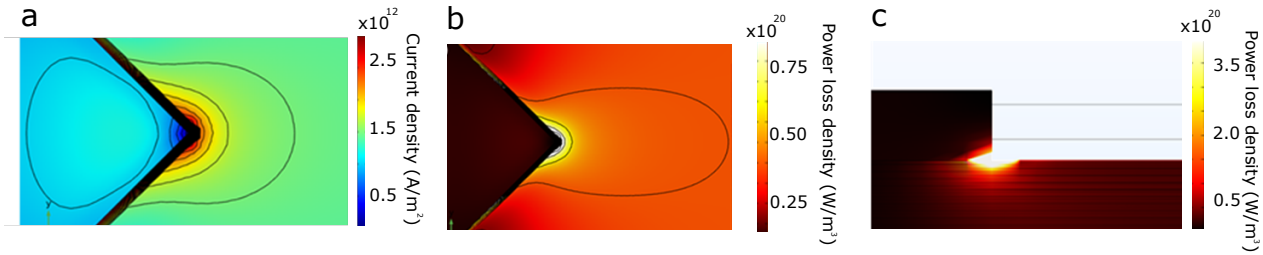

Fig. 4.9: 3D electrical simulations | **a** Current density distribution in the xy plane. **b** Power density distribution during the current pulse injection in the xy plane. **c** Same as **b** in the xz plane.

This part of the work was done by Van Tuong Pham, who worked as a post-doc in our team.

4.3.2 Micromagnetic simulations

Micromagnetic simulations were performed by Naveen Sisodia in the group in order to reproduce the experimental current-induced nucleation and annihilation of SAF skyrmions (see Figure 4.1). The simulations took into account the non homogeneous current distribution. Typical values of spin orbit torque were used. First relaxation simulations show that SAF skyrmions were not stable using the experimental parameters, which can be explained by the large perpendicular magnetic anisotropy. To stabilize the skyrmions, local pinning was introduced by adding randomly distributed grain with Gaussian variations in both the magnetic anisotropy and DMI (full width at half maximum 5%). The simulations are performed at $T = 0$ K using magnetic parameters measured at room temperature.

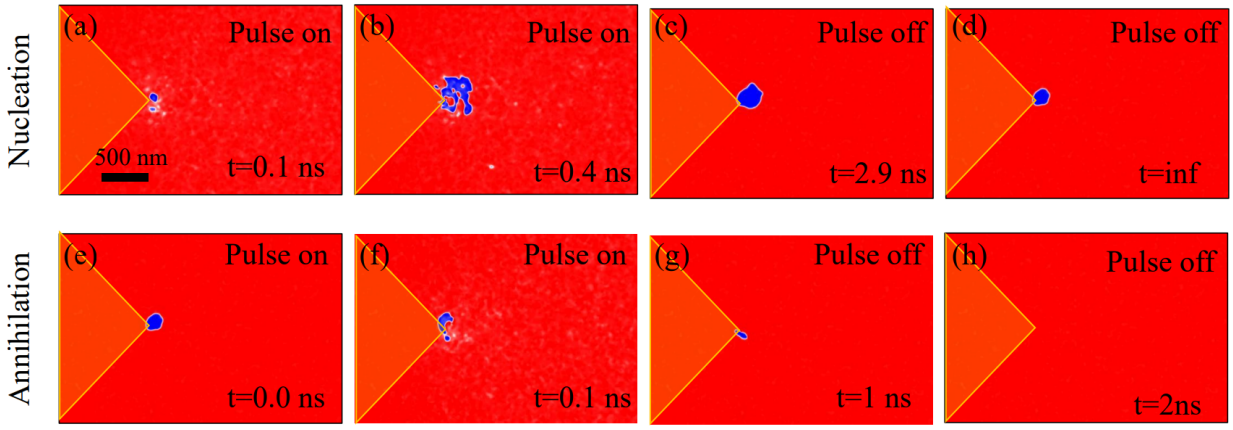

Fig. 4.10: Micromagnetic simulations: Current-induced skyrmion nucleation/annihilation | **a-d** Evolution of the SAF skyrmion nucleation process after applying a 0.4 ns width and $15 \cdot 10^{12}$ A/m^2 current pulse. **e-h** Same but for negative polarity and a width of 0.15 ns. From [162].

The micromagnetic simulations qualitatively reproduce the nucleation and annihilation of skyrmions at the apex of the tip above certain threshold current density. Figure 4.10a-d show the nucleation and the stabilization of the skyrmion. Applying a current pulse with opposite polarity leads to its annihilation (see Figure 4.10e-h). This shows that the inhomogeneous spin orbit torque at the apex of the tip can explain the observed nucleation/annihilation of the skyrmions. However, a current density 20x higher ($15 \cdot 10^{12}$ A/m^2) is

required to nucleate the skyrmions in the simulation as well as a lower pulse width (0.4 ns). This discrepancy may be explained by a local heating during the current injection, which is not taken into account in the simulations and may play a significant role in the skyrmion nucleation.

To understand the results from time-resolved STXM experiments, we also performed micromagnetic simulations focusing on the relaxation dynamics of the SAF. For this, we introduced similar SAF skyrmion sizes guided by the observed values in the STXM experiments, ranging from 300 nm to 700 nm. Anisotropy grains were not included in the simulations. We used the following magnetic parameters, extracted experimentally. For the Co layers we have $M_S = 1.43$ MA/m, $t_{\mathrm{Co}} = 0.9$ nm, $\mu_0 H_K = 540$ mT, $\alpha = 0.3$, $D = 1$ mJ/m^2 and $A = 16$ pJ/m. For the Co/Py/Co layer we have $M_S = 0.946$ MA/m, $t_{\mathrm{Py}} = 1.3$ nm, $\mu_0 H_K = 68$ mT, $\alpha = 0.3$, $D = 0.38$ mJ/m^2 and $A = 6$ pJ/m. Indeed, similarly to experiments, the simulations showed that the skyrmion is not stable and it collapses until the remanence magnetization is reached.

In order to perform these simulations, I used a Mumax code provided by Naveen Sisodia, who worked in our group as a post-doc.

4.3.3 Analytical model of the bubble expansion and relaxation

To better understand these experimental and numerical results, we develop an analytical model of the SAF skyrmions expansion dynamics. The LLG equation in the θ and ϕ coordinates can be written as [181]:

$$\frac{\partial \theta}{\partial t} = -\frac{\gamma}{M_S}\left(\frac{\delta \varepsilon}{\delta \phi}\right)\sin\theta - \alpha \frac{\partial \phi}{\partial t}\sin\theta, \tag{4.2}$$

$$\frac{\partial \phi}{\partial t}\sin\theta = \frac{\gamma}{M_S}\left(\frac{\delta \varepsilon}{\delta \theta}\right) + \alpha \frac{\partial \theta}{\partial t}. \tag{4.3}$$

ε represents the magnetic energy density, which includes the Zeeman, magnetic anisotropy and DMI energies. $\left(\frac{\delta \varepsilon}{\delta \theta}\right)$ and $\left(\frac{\delta \varepsilon}{\delta \phi}\right)$ are functional derivatives. To deduce DW dynamics equations, we follow the collective coordinate model proposed by J. Slonczewski [181]. We first assume an infinite planar DW, such that the DW is parallel to the xz plane and the DW magnetization depends only on y and the time t. We also assume that the DW is described by two variables, its position q and the DW angle ϕ with a Bloch DW profile:

$$\theta(y,t) = 2\arctan\left(\exp\left(\frac{y-q(t)}{\Delta}\right)\right), \tag{4.4}$$

$$\phi(y,t) = \xi. \tag{4.5}$$

Here, θ and ϕ are the azimuthal and polar angle respectively and Δ is the DW width. We can take advantage of the following useful expressions, derived through the DW solution:

$$\sin\theta = \mathrm{sech}\left(\frac{y-q(t)}{\Delta}\right), \tag{4.6}$$

$$\frac{d\theta}{dt} = -\frac{1}{\Delta}\frac{dq}{dt}\sin\theta, \tag{4.7}$$

$$\frac{\partial \theta}{\partial y} = \frac{1}{\Delta}\sin\theta. \tag{4.8}$$

The integration along y gives the equations of motion. Note $\int_{-\infty}^{\infty}\sin\theta dy = \Delta\pi$ and $\int_{-\infty}^{\infty}\sin^2\theta dy = \Delta$. This way, the equations of motion write:

$$\frac{dq}{dt} = \frac{\gamma}{M_S}\left(-\frac{K_d}{\Delta}\sin 2\xi + \frac{1}{2}D\pi\sin\xi\right) + \alpha\Delta\frac{d\xi}{dt}, \tag{4.9}$$

$$\frac{d\xi}{dt} = \gamma H_z - \frac{\alpha}{\Delta}\frac{dq}{dt}. \tag{4.10}$$

These equations were generalized to 3 dimensions by Slonczewski as, where q is now the wall normal magnetization displacement and ξ is the wall-magnetization orientation angle [181]:

$$\frac{\delta \sigma}{\delta \xi} = \frac{2M_S}{\gamma}\left(\frac{dq}{dt} - \alpha\Delta\frac{d\xi}{dt}\right), \tag{4.11}$$

$$\frac{\delta \sigma}{\delta q} = -\frac{2M_S}{\gamma}\left(\frac{d\xi}{dt} + \frac{\alpha}{\Delta}\frac{dq}{dt}\right), \tag{4.12}$$

where $\delta\sigma/\delta\xi$ and $\delta\sigma/\delta q$ are functional derivatives of the domain wall energy density σ. We now assume that the domain wall is nearly parallel to the xz plane and that its position $q(x,z,t)$ and angle $\xi(x,z,t)$ depend on x and z and vary slowly in the lateral direction, that is over distances larger than the DW width. Under this assumption, one can write [181]:

$$\frac{\delta\sigma}{\delta\xi} = K_d\Delta\sin 2\xi + \pi D\Delta\sin\xi - 4\Delta A\nabla^2\xi, \tag{4.13}$$

$$\frac{\delta\sigma}{\delta q} = -2\mu_0 MsH_z - \sigma_0\nabla^2 q - K_d\Delta\frac{\partial\sin^2\xi}{\partial x}, \tag{4.14}$$

where $\sigma_0 = 4\sqrt{AK_eff}$ and $\Delta = \sqrt{A/K_eff}$. Assuming a circular bubble with homogeneous magnetization along the film thickness and constant domain wall angle, one can write:

$$\frac{\delta\sigma}{\delta\xi} = K_d\Delta\sin 2\xi + \pi D\Delta\sin\xi, \tag{4.15}$$

$$\frac{\delta\sigma}{\delta q} = -2\mu_0 MsH_z - 4\sigma_0/q \tag{4.16}$$

Given the radial expansion, we can consider the DW position parameter $q(t)$ as the size of the the bubble. Substituting $q(t)$ with $R(t)$, representing the radial expansion, the equations of motion for a magnetic bubble read:

$$\frac{dR}{dt} = \frac{\gamma}{M_S}\left(-\frac{K_d}{\Delta}\sin 2\xi + \frac{1}{2}D\pi\sin\xi\right) + \alpha\Delta\frac{d\xi}{dt}, \tag{4.17}$$

$$\frac{d\xi}{dt} = \gamma H_z - \frac{\alpha}{\Delta}\frac{dR}{dt} - \frac{2K_{eff}\gamma\Delta}{M_S}\frac{1}{R}. \tag{4.18}$$

These equations hold for a bubble in a ferromagnetic material. Haltz *et al.* [182] demonstrated that the dynamics of domain walls in ferrimagnets and synthetic aniferromagnets can be obtained from the ferromagnetic equations by replacing the magnetic and transport parameters by effective ones. In the case of SAF with rigid AF coupling between both SAF layers, namely, infinitely large RKKY interaction, one obtains:

$$\alpha \to \alpha^{eff} \to \infty, \tag{4.19}$$

$$M_S \to M_S^{eff} = 0, \tag{4.20}$$

$$M_S\alpha \to M_S^{eff}\alpha^{eff} = 2\alpha M_S. \tag{4.21}$$

Making the corresponding substitutions, the equations of motion for a SAF bubble read:

$$\frac{2M_S\alpha}{\gamma\Delta}\frac{dR}{dt} = -\frac{2K_{eff}\Delta}{R} + (\pi/2)\,\chi J\cos\xi, \tag{4.22}$$

$$\frac{d\xi}{dt} = -\frac{\gamma}{2\Delta\alpha M_S}\left(-\frac{K_d}{\Delta}\sin 2\xi + \frac{D\pi}{2}\sin\xi\right). \tag{4.23}$$

Here, the effect of the spin orbit torque can be included in an effective out-of-plane magnetic field. We assumed that the current flows perpendicular to the DW surface, i.e, along the radial direction of the bubble. In this case, one can write the effective field as $H_z = (\pi/2)\,\chi J$, where χ corresponds to the SOT efficiency [183].

We note that, in our experiments, this assumption does not hold since the current goes only into a part of the bubble. For this reason, we focus on the relaxation regime, that is when the pulse is turned off. Here, the term with the current density is zero and the equation of motions are decoupled. The expression for the evolution of the radius becomes analytically solvable and is given by:

$$R(t) = \sqrt{R_{init}^2 - \frac{2A\gamma}{\alpha M_S}t}, \tag{4.24}$$

where we define R_{init} as the radius when the pulse goes off. Remember that t here represents time, not thickness.

To better understand these results, we performed micromagnetic simulations of the skyrmion process using experimental parameters. We start the simulations with a skyrmion of diameter 700 nm and then integrate the LLG to see the evolution of the skyrmion size as a function of time. We repeat the same process

for different initial skyrmion sizes and plot the diameter vs time for each case in Figure 4.11a. In Figure 4.11b, we plot the rate of change of the skyrmion diameter as a function of the diameter itself (instantaneous value). We observe that all curves for different cases collapse together. From this we can infer that the dynamics shown here do not include the effect of inertia as the rate of change of skyrmion diameter is independent of R_{init}. We also notice that the rate of change of the diameter behaviour differs significantly at smaller skyrmion sizes. This is due to the fact that at smaller sizes, the exchange interaction also plays a significant role. In Figure 4.11c, we plot the rate as a function of the inverse of the diameter (data for smaller diameters removed), showing a clear linear behaviour for large diameters, which is consistent with our model. To further confirm the validity of the model, we compared it to the results of the micromagnetic simulations shown in Figure 4.11a. To this end, we also plot the expected behaviour from the model using the function $R(t) = \sqrt{R_{init}^2 - Bt}$, assuming R_{ini} and B as free fitting parameters. The model nicely captures the skyrmion annihilation dynamics and corroborates well with simulations (see white dots in Figure 4.11a).

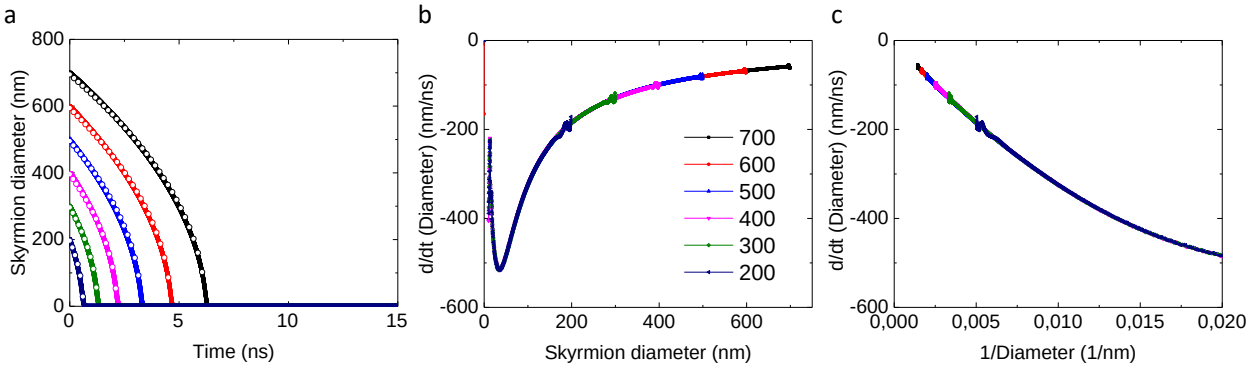

Fig. 4.11: Skyrmion relaxation in the absence of current | **a** Evolution of skyrmion diameter with time for different initial values. The dotted symbols are fits using Equation 4.24. Rate of change of the skyrmion diameter as a function of **b** the diameter and **c** its inverse. The color-code representing each initial diameter value is the same in the three graphs.

However, we observe that the fitting parameter B obtained from the micromagnetic simulations does not agree with the predictions of the model, namely $B = \frac{2A\gamma}{\alpha M_S}$. This is shown in Figure 4.12, which compares B extracted from the micromagnetic simulations data (red dots) and the one predicted by the analytical model (blue line) as a function of the skyrmion diameter. In our SAF we have Co and NiFe layers, so we computed the effective M_S and A in the following way:

$$A^{eff} = \frac{A_{Co}t_{Co} + A_{Py}t_{Py}}{t_{Co} + t_{Py}}, \tag{4.25}$$

$$M_S^{eff} = \frac{M_{Co}t_{Co} + M_{Py}t_{Py}}{t_{Co} + t_{Py}}. \tag{4.26}$$

One of the reasons behind the discrepancies can be attributed to the RKKY coupling. In the model, we implicitly considered infinite AF coupling, which is not true. I performed additional simulations for a given diameter value to observe the relaxation time dependence on the RKKY coupling. The stronger the coupling the faster the skyrmion annihilates.

I also compare in Figure 4.12 the fitting parameter B obtained from the time resolved experiments. One observes that B is significantly lower than the one obtained from the simulations. This discrepancy may be related to the temperature rise induced by the current injection, which can change the magnetic parameters. Heating would lead to a reduction of M_S that would accelerate the collapse. However, the role of A is to be analyzed. According to Moreno *et al.* [184,185], under temperature, A scales as $M_S^{1.8}$. Other works assumed the traditional M_S^2, or M_S^β, where β= 1.7 or 1.65 [186,187] depending on the temperature. In any case, it would mean that heating leads to a decrease of $B \propto A/Ms$, and thus an enhancement of the relaxation time. Also note that, contra-intuitively, the skyrmion collapses faster for smaller damping. We note that a larger damping could also explain the results, which would be surprising, given the large value already used in the micromagnetic simulations ($\alpha = 0.3$).

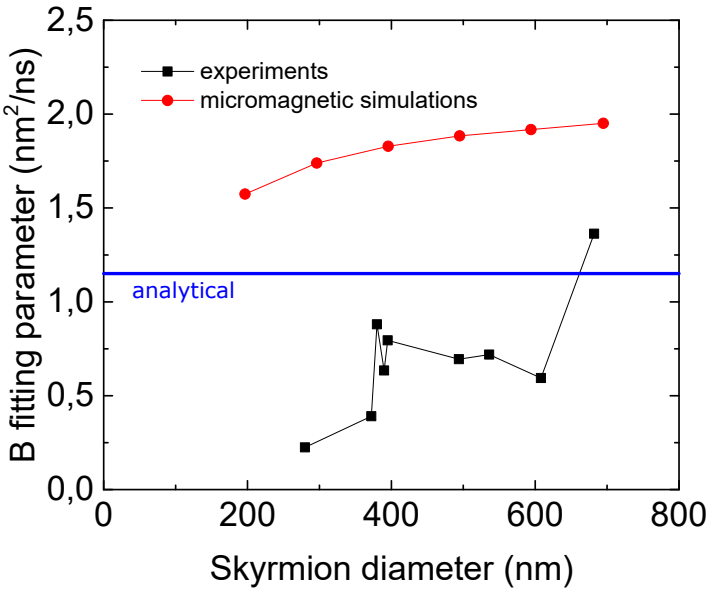

Fig. 4.12: Comparison of the experimental, simulations and analytical data | Fitting parameter values from experiments (black) and simulations (blue) for different skyrmion diameters. In red, the analytical value of the fitting parameter with $A^{eff} = 10.1$ pJ/m, $M_S^{eff} = 1.14$ MA/m and $\alpha = 0.3$.

4.4 Discussion and conclusions

In this chapter, we have demonstrated the reproducible current-induced nucleation and annihilation of magnetic skyrmions in fully compensated SAF and the real time observation of the nucleation dynamics. The experiments showed that the process occurs via the nucleation of a small nucleus below the metallic tip, followed by a fast expansion during the pulse injection and a slower relaxation when the pulse is turned off. Considering the directional injection of the current density, the reversal of the first magnetic layer may trigger a fast chain reaction on the other layers due to the RKKY interaction. The subsequent expansion can be understood as an out-of-plane field resulting from the spin orbit torques and heat gradient that moves the domain walls. After the current pulse goes off, the system dissipates the energy. Given the high anisotropy of our SAF, the skyrmion is not stable and therefore gradually collapses until the uniform state is recovered. To better understand the experimental results, we performed micromagnetic simulations using experimental parameters as well as analytical modelling. Taking into account the non-uniform current induced spin orbit torque under the tip, micromagnetic simulations reproduce qualitatively the current induced nucleation and annihilation processes. However, a current density much larger than in experiments is needed, suggesting a significant role of heating in the nucleation process. Analytical modelling and simulations of the skyrmion collapse after switching off the current were also performed and compared to the time resolved experiments. The model and simulations predict a collapse faster than in experiments, which can be attributed to a reduced magnetization and exchange interaction induced by local heating.

Chapter 5

Magnetic skyrmions in exchange-biased synthetic antiferromagnets

Contents

5.1 The exchange bias 70
5.2 Stabilization of magnetic skyrmions by exchange bias 72
5.3 X-ray induced skyrmions in exchange biased stacks 73
5.4 SAF skyrmions in exchange biased synthetic antiferromagnets 74
5.4.1 Optimization of the magnetic stack 74
5.4.2 X-ray induced reversing of the AF order 76
5.4.3 Nucleation of SAF skyrmions exchanged biased to IrMn 76
5.4.4 Skyrmion imprint using x-ray beam 77
5.4.5 Current-induced dynamics of SAF skyrmions exchanged biased to IrMn 78
5.5 Conclusions 79

This chapter details the work carried out mainly in the first and second year of my PhD thesis. The material system chosen were synthetic antiferromagnets exchange biased to an antiferromagnet. All the optimization process and the experimental results regarding the nucleation and observation of skyrmions will be explained.

The skyrmion nucleation techniques we have presented in the previous chapter suffer from limitations for the study of the skyrmion current-induced dynamics. Indeed, the thick metallic tip used to nucleate the SAF skyrmions locally shunts the current flowing in the track, such that the nucleated skyrmions can be hardly detached from the metallic tip when injecting an in-plane current. This issue may be solved by considering point contact current injection, or using an ultrathin tunneling barrier between the magnetic track and the nucleation electrode.

In this chapter, we present an innovative solution to nucleate skyrmions in SAF based on exchange biased systems. In FM systems, skyrmions can be easily nucleated from a stripe domain state by applying an external magnetic field along the easy axis. This strategy cannot be applied to SAF owing to their vanishing magnetic moment. An alternative approach is to couple one of the layers to an antiferromagnet. This leads to an internal effective magnetic field via the exchange bias effect, which allows the spontaneous nucleation of the skyrmions in the SAF. An additional advantage of a coupling to an antiferromagnet lies in their lower sensitivity to external fields and field perturbations, providing additional thermal stability to the skyrmions. In the next lines we will introduce the exchange bias effect and see how it can be helpful for the stabilization of skyrmions and more particularly SAF skyrmions.

5.1 The exchange bias

The exchange bias phenomenon arises in FM/AFM thin film heterostructures. It is characterized by a shift in the hysteresis loop as illustrated in Figure 5.1a for a Pt/Co/IrMn thin film. Thus, the exchange bias acts on the magnetization as an additional bias field. To achieve exchange bias, the FM/AFM is annealed above a so-called blocking temperature, which is related to the ordering temperature (T_N) of the AF, under a magnetic field aligned along the FM easy axis. The process is followed by a cooling under the same magnetic field. The basic principle of the exchange bias is the following: the ferromagnetic film will have its spins at the interface pinned by the exchange coupling with the AFM interfacial spins (see Figure 5.1b). Therefore the field-driven reversal of the ferromagnet will have an added energetic cost. The assumptions behind most of the models are that the interface plane is homogeneous and that the AFM spins at the interface are uncompensated [188].

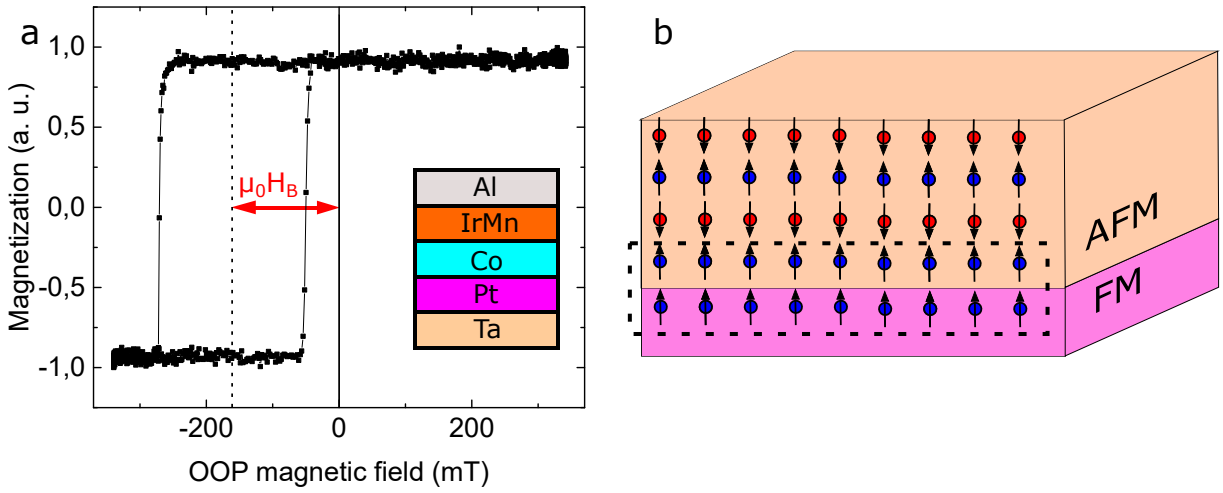

Fig. 5.1: Exchange bias interaction | **a** Schematic magnetic structure of an ideal FM/AFM bilayer. The exchange interaction that couples the FM and the AFM in the interface is represented by the dashed square. **b** Magnetic hysteresis loop of a sputtered Pt/Co/IrMn sample annealed at 250°C under an out-of-plane magnetic field (600 mT) during 30 minutes. The shift in the hysteresis loop denotes the presence of the exchange bias field $\mu_0 H_B$ arising from the Co/IrMn interface.

The exchange bias field was first explained by introducing a so called "uniaxial anisotropy". If we want to express this with a simple model, let us consider a particle with uniaxial anisotropy under a magnetic field $\mu_0 H$, aligned along the easy axis in a direction anti-parallel to the particle's magnetization [189–191]. The energy density of the system would read as:

$$\varepsilon = \mu_0 H M_S \cos\theta - K_u \cos\theta + K_1 \sin^2\theta, \tag{5.1}$$

where θ stands for the angle between the magnetization and the easy axis. K_u and K_1 are the unidirectional and uniaxial anisotropy energy constants. Thus, the magnetization is subject to an effective field of the form $\mu_0 H_{eff} = \mu_0 H - K_u/M_S$. This means that a solution for this system displaces the hysteresis loop by K_u/M_S and we can conclude that the explanation of the shift can be considered due to an additional unidirectional anisotropy term.

The studies showed that the effect is highly material dependent, i.e. materials with smaller M_S have more exchange bias (Co vs Py, for instance) following Equation 5.1. In addition, the strength of the exchange bias can also be controlled by the thicknesses of both the FM and AFM materials. A larger thickness of the FM will mitigate the effect while the thicker AFM will favour it up to a saturation point. Figure 5.2 summarizes the impact of the FM (Co) and AFM (IrMn) thicknesses on the exchange bias field in a Pt/Co/IrMn stack. We analyzed three independent Pt/Co/IrMn stacks with different Co thickness (1.4 nm, 1.5 nm and 1.6 nm) and IrMn deposited as a wedge. An annealing step under out-of-plane external magnetic field (600 mT) was performed at 250°C. We can see how the exchange bias effect does not appear for IrMn thickness values below 2.8 nm. This is independent from the FM thickness. For thicker IrMn, the shift in the hysteresis loop increases and it saturates above 4 nm (not shown). Regarding the impact of the FM thickness, the effect is stronger with thinner Co. This can be explained by the fact that the exchange bias effect is interfacial. This relation however becomes invalid if the FM layer is too thin, which could originate from the loss of homogeneity in the interface when the FM becomes too thin [192].

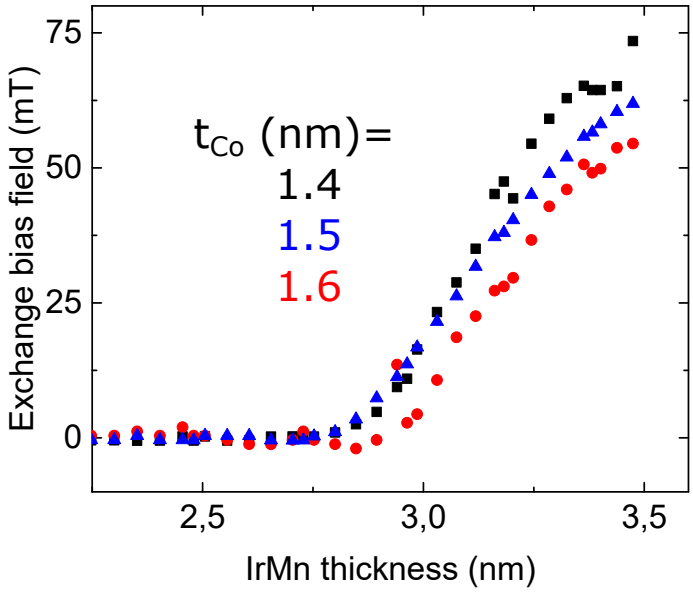

Fig. 5.2: Thickness dependence of the exchange bias interaction | FM and AFM thickness dependence of the exchange bias field.

This material engineering will also have a direct consequence on other parameters such as the effective anisotropy. This is why a fine tuning is necessary to obtain all the requirements to host skyrmions. In particular, we have already mentioned that low PMA stacks are appropriate for the stabilization of magnetic skyrmions. We studied in Chapter 2 that a magnetic field along the easy axis is needed to stabilize FM skyrmions from a stripe domain state. The key here is that the exchange bias effect can be used to mimic the effect of an external magnetic field. This way the stabilization of the skyrmions would be achieved at zero field.

5.2 Stabilization of magnetic skyrmions by exchange bias

In previous studies, it has been demonstrated that skyrmions with diameters of around 60 nm can be stabilized at room temperature without any external magnetic field in optimized Pt/Co/Py/IrMn multilayer stacks [193]. They showed that the exchange bias provides the skyrmions a stability against moderate field perturbations (dozens of mT) (see Figure 5.3a and 5.3b). This stability is associated to the strong coupling between the FM and AFM at the interface. The FM spin texture can also be influencing the AF order of the IrMn. Further studies by the author reported exploiting the exchange bias effect in antiferromagnets [194]. In this study, they demonstrated the imprint of ferromagnetic skyrmions into a thin film of an IrMn antiferromagnet at room temperature and in the absence of an external magnetic field. XMCD-PEEM allowed them to probe the uncompensated Mn spins at the interface, observing some spin textures in the AF thin film (see Figure 5.3c).

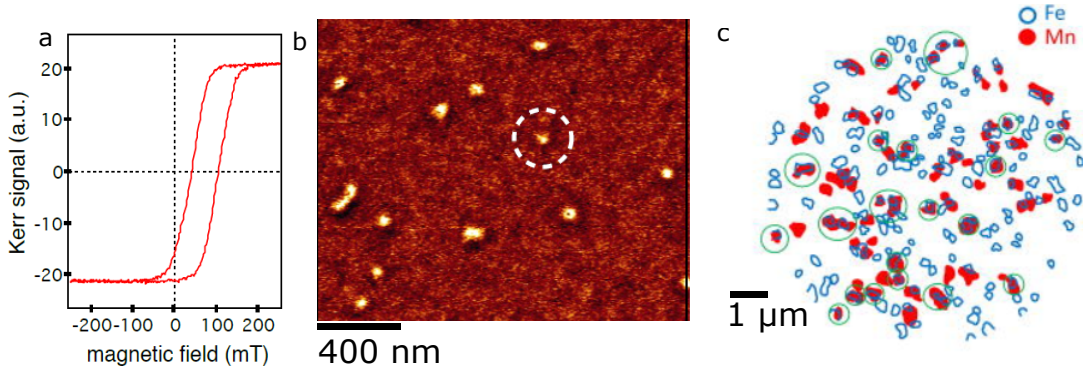

Fig. 5.3: Room temperature skyrmions in exchange biased multilayers | **a** Out-of-plane MOKE hysteresis loop for a Pt(3)/Co(0.3)/Py(2.1)/IrMn(4.2) (thickness in nm), showing a shift of the hysteresis loop. Py stands for $Ni_{80}Fe_{20}$. From [193]. **b** MFM images recorded at zero external field of the stack in **a**. From [193]. **c** Superposition of contours of textures obtained from XMCD-PEEM images measured at the Fe and Mn L_3 absorption edges at RT and zero field with a partial overlap. From [194].

In our case, the recipe to host skyrmions also requires the use of PMA stacks with DMI. We characterized similar thin films using magnetic force microscopy (MFM) and demonstrated that skyrmions in IrMn exchange biased stacks can be nucleated at zero field. A multilayer stack of Ta(3)/$[$Pt(3)/Co(0.3)/Py(t)/IrMn(4)$]_{x5}$/ Pt(1.5) (thickness in nm) was deposited by magnetron sputtering. The Py ($Ni_{80}Fe_{20}$) layer was deposited using a wedge deposition such that its thickness varies linearly along the 100 mm wafer between 1 and 2.6 nm. The samples were then annealed at 250°C for 30 minutes under a perpendicular magnetic field of 600 mT to achieve exchange bias.

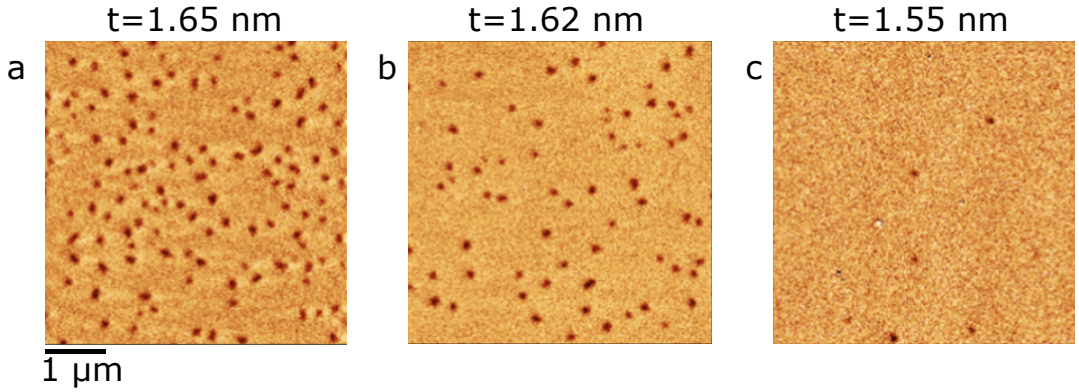

Fig. 5.4: Magnetic Force Microscopy experiments | **a-c** MFM images at different positions along the wafer, i.e different Py thicknesses, showing different skyrmion densities. The thinner area represents larger exchange bias effect, which gets closer from saturation, in line with the lower density of skyrmions.

MFM experiments showed that isolated skyrmions are observed at zero magnetic field. A Py thickness dependence study revealed that the thicker the Py layer, the larger the skyrmion density (see Figure 5.4a-c). Indeed, an increase in the FM thickness leads to a decrease in the bias magnetic field, and thus an increased skyrmion density.

5.3 X-ray induced skyrmions in exchange biased stacks

We deposited the same stack in Si_3N_4 membranes for STXM observations. As expected, STXM images also revealed skyrmion lattices at zero magnetic field. However, successive STXM images of the sample at zero field at different magnifications showed that the density of skyrmions depends both on the size of the observation area and on the number of observations. This revealed that the x-ray leads to the nucleation of skyrmions (see Figure 5.5).

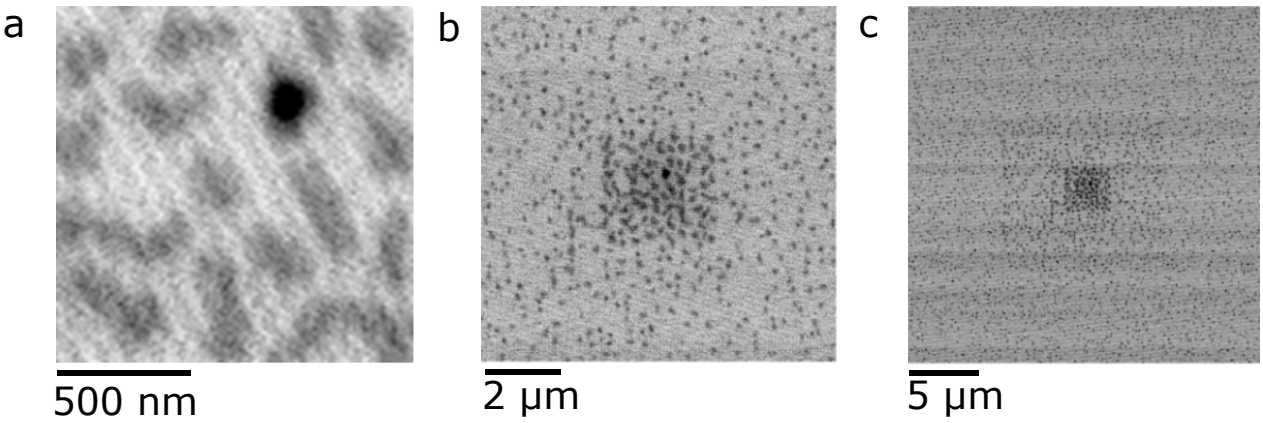

Fig. 5.5: STXM experiments for skyrmion nucleation | **a-c** XMCD-STXM images of skyrmion at zero field and room temperature. Their density depends on the size of the observation area and the number of observations performed.

More studies in similar IrMn exchange biased stacks (see Figure 5.6) have been also carried out, in which the influence of x-rays was analyzed [195]. They demonstrated "the creation of individual skyrmions at zero-field in an exchange-biased magnetic multilayer with exposure to soft x-rays". This was explained by a modification of the antiferromagnetic order of the IrMn by the focused x-ray beam leading to a reorientation of the exchange bias field. They also reported the creation of artificial skyrmion lattices. These results mean that the manipulation of the exchange bias is possible via x-rays to stabilize skyrmions in ferromagnets.

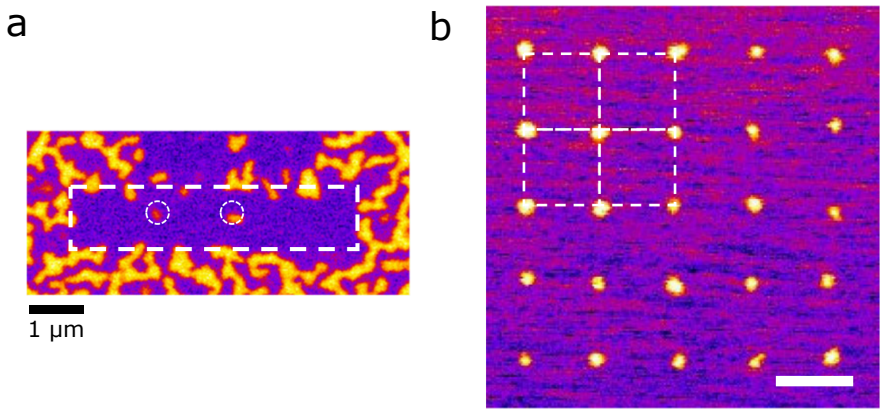

Fig. 5.6: Room temperature skyrmions in multilayer stacks exchange biased to IrMn | Artificial skyrmions created **a** individually and **b** in a lattice by x-ray illumination. Adapted from ref. [195].

Regarding SAF systems, SAF skyrmions were shown to be spontaneously nucleated in exchange biased SAF stacks [161]. In this study, one of the layer of the SAF was exchange coupled to a ferromagnetic bias layer, leading to an internal bias field favouring the nucleation of skyrmions close to the in-plane/out-of-plane spin reorientation transition. However, this stack leads potential drawbacks for applications. On the one hand, the bias layer remains sensitive to the external magnetic field effects. On the other hand, the thick layer also leads to large current shunting effects. This is an issue to keep in mind, for instance, if experiments of current-induced skyrmion motion are in sight to study.

5.4 SAF skyrmions in exchange biased synthetic antiferromagnets

Given the well known issues with ferromagnetic skyrmions and considering the advantages of the exchange bias phenomena, an alternative approach that tries to go beyond these works was to consider the insertion of IrMn as a bias layer. Here we take advantage of the antiferromagnetic properties: being insensitive to the external magnetic field and providing additional thermal stability to the skyrmions. Moreover, antiferromagnets can be highly resistive or even insulating, which would prevent current shunting effects. In the following sections we will show the optimization of such stack as well as the nucleation of skyrmions by an x-ray beam in sputtered ultrathin SAF multilayers exchange biased to IrMn.

5.4.1 Optimization of the magnetic stack

The stack that was used during the experiments was deposited by magnetron sputtering and has the following composition: Ta(3)/Pt(3)/FM_1/Ru(0.85)/Pt(0.5)/FM_2/Ru(0.85)/Pt(0.5)/FM_1/Ru(0.85)/Pt(0.5)/FM_2/IrMn(4.8)/Pt(2), where FM1 = Co(9.5)/Co(t_{Co}) and FM2 = Co(t_{Co})/Py(0.9)/Co(0.5) (all thicknesses are in nm).

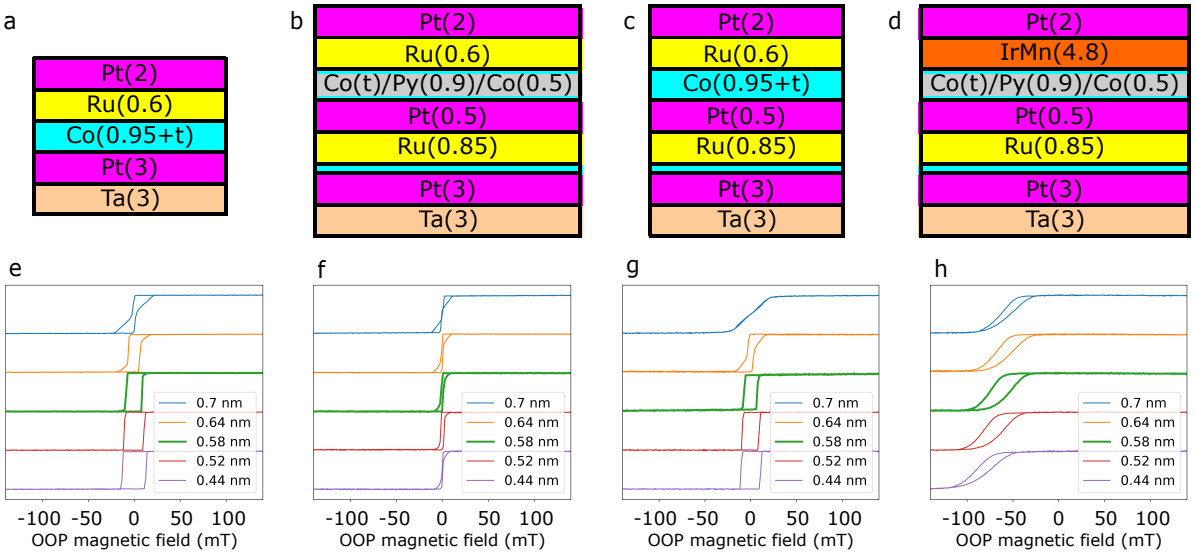

Fig. 5.7: Optimization of the magnetic layers | **a-d** Material stacks for the constituent FM layers, **a** Pt/FM_1/Ru, **b** Pt/Ru/Pt/FM_2/Ru, **c** Pt/Ru/Pt/FM_1 and **d** Pt/Ru/Pt/FM_2/IrMn, with FM_1=Co(0.95+t) and FM_2=Co(t)/Py(0.9)/Co(0.5). The Co layer in all the stacks is deposited as a wedge. **e-h** Out-of-plane MOKE hysteresis loops measured to each stack above. In green, the hysteresis loop of the desired thickness is highlighted.

The material stacks of the individual constituent FM layers deposited for the optimization of the exchange-biased SAF are presented in Figure 5.7a-d. The thickness of Ru (0.85 nm) was chosen to get the maximum AF coupling between all the FM layers. The objective during the optimization of these different individual layers was to get a fully magnetically compensated stack with both FM layers close to out-of-plane/in-plane spin reorientation transition. Figures 5.7e-h display the hysteresis loops measured by MOKE of the stacks in 5.7a-d. As a remark, note the difference of the FM_1= Co stack when it is directly deposited on the Ta/Pt buffer (Figure 5.8a,e) and when it is deposited above an additional Ru/Pt layer (Figure 5.7c,g) in order to mimic its growth and properties on the full stack. This is a clear sign that the anisotropy of the inner Pt/FM_1 layer is not the same as the bottom one due to the slight difference of the Pt layer below. Regarding the top FM_2 layer, it is exchange biased to IrMn. The stack was annealed at 250°C during 30 minutes under an external magnetic field of 600 mT in the out-of-plane direction to exploit the exchange bias effect with the neighbouring ferromagnet. As explained above, we see a shift in the hysteresis loops in Figure 5.8h, which varies with the thickness.

Lastly, the compensated stack with optimized material thicknesses and the corresponding out-of-plane hysteresis loop measured by VSM is shown in Figure 5.8. In red, the hysteresis loop of the full stack is

represented while the blue curve shows the hysteresis loop of a single bilayer[1] (removing both inner FM layers). Regarding the single bilayer graph, we see a vanishing magnetization at zero field, confirming the compensation point. The increase of the field leads to a reversal that comes at an RKKY field around 200 mT. The hysteresis loop is not symmetrical though. It is slightly shifted in field, around 30 mT, as expected from the exchange bias effect. The lower value of the shift compared to the Figure 5.7h can relate to the effect of the bottom Co layer.

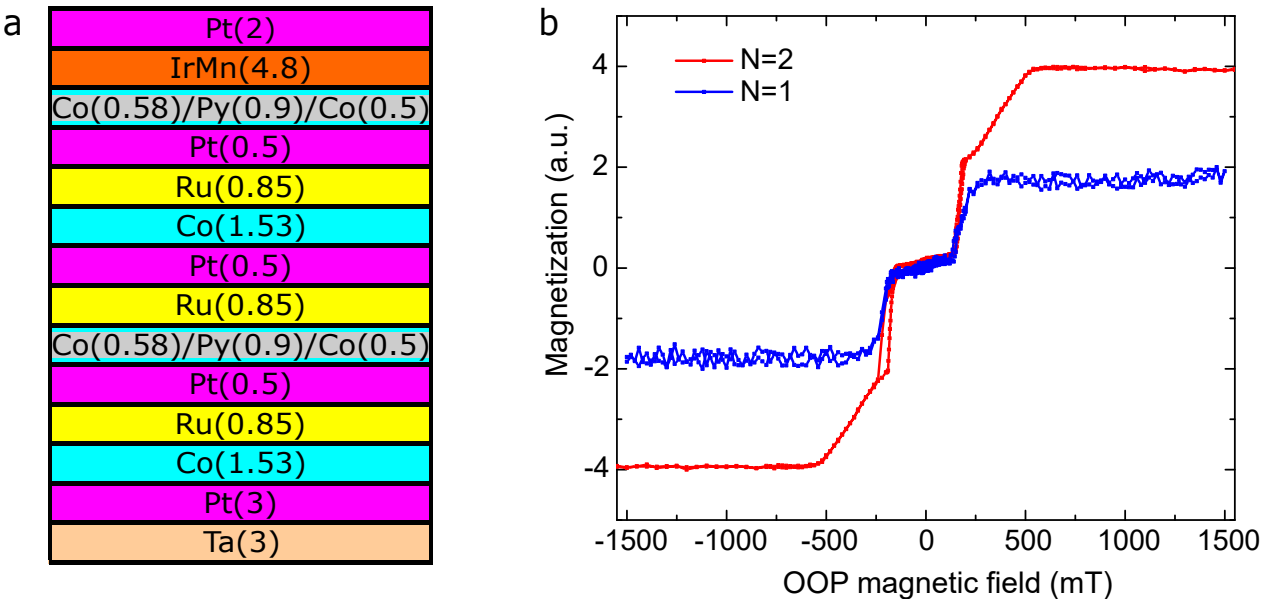

Fig. 5.8: Optimization of compensated exchanged biased SAF multilayers | **a** Material stack for the multi-layered SAF exchange-biased to IrMn with $t_{Co} = 0.58$ nm. **b** Out-of-plane VSM hysteresis loops measured for the multi-layered SAF exchange-biased to IrMn in **a** for $N = 2$ double bilayer and $N = 1$ single bilayer stacks. The signal is multiplied by the number of constituent FM layers after normalization.

For the $N = 2$ stack (red curve), we also notice a vanishing magnetization at zero field with a weak susceptibility due to the targeted out-of-plane/in-plane spin reorientation transition. Here, every individual FM layer is in an AF coupled configuration with the adjacent FM. When we start to increase the external magnetic field, we first note a relatively sharp reversal that indicates the switching of the bottom layer. This layer is the one that has the largest perpendicular magnetic anisotropy and the first reversal defines the interlayer exchange coupling field or the RKKY field, $\mu_0|H_{RKKY}|$. Its amplitude is the same as for the $N = 1$ stack. After this, more field is required to overcome the RKKY couplings from adjacent layers to gradually switch the remaining FM. Overall, these stacks fulfill the requirements needed to host skyrmions, that are PMA and strong DMI, in the same way we have presented in previous Pt/Co/Ru based stacks. The PMA and DMI originate from the Pt/Co interface and the Co/Ru interfaces reinforce them. The Ta buffer is needed for the proper growth of the Pt with the desired (111) texture, giving rise to the PMA. All the Co layers were deposited off axis (as a wedge) with a linear thickness variation along the wafer diameter in order to keep the stack fully compensated no matter the position on the wafer. The wedged thickness of Co varies from 0.3 nm to 0.7 nm.

[1] Ta(3)/Pt(3)/FM_1/Ru(0.85)/Pt(0.5)/FM_2/IrMn(4.8)/Pt(2).

5.4.2 X-ray induced reversing of the AF order

The STXM microscopy technique was used to image the double SAF + IrMn stack presented above at room temperature. The STXM experiments were performed at the Maxymus beamline in Bessy synchrotron, as well as at the Hermes beamline in Soleil synchrotron. For this, the compensated full stack was sputtered on 200 nm thick Si_3N_4 membranes. The great advantage of using Co and Py in the AF coupled layers composing the SAF is that even if the magnetization is compensated, the magnetic textures can be observed in one or the other layers by tuning the x-ray energy at the Co or Fe L3 edge.

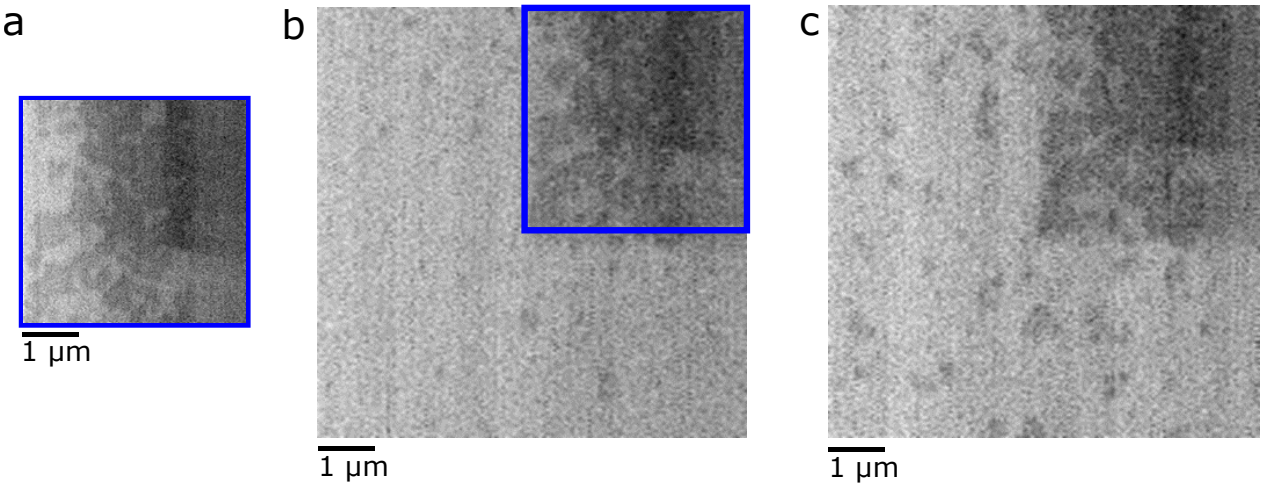

Fig. 5.9: Influence of the x-ray beam on the magnetization reversal | Sequence of successive STXM imaging (Fe L_3 edge) to study the effect of the x-ray beam on the domain nucleation for an external applied field of 150 mT. **a** STXM image after 3 consecutive images. **b** Same but on a larger area. The blue area corresponds to the previous acquisition. **c** Repeated once again in the same area.

At the beginning, the first images without any external magnetic field showed a monodomain state. In order to facilitate the skyrmion nucleation, we applied a positive magnetic field (150 mT) close to the magnetization reversal of the Co/Py/Co layer in contact with the IrMn. STXM imaging revealed that the x-ray beam had a significant influence on the domain nucleation in this field range. We show in Figure 5.9 successive STXM images taken at the Co L_3 edge. Figure 5.9a shows reversed domains in a 4x4 μm^2 area. Note that this image was obtained after 3 successive scans at the same position. Figure 5.9b shows an image for a larger 8x8 μm^2 scans including the previous area (in blue). One sees the difference in the domain pattern in the virgin areas compared to the one that had been already scanned. Repeating the same scanning led to more domain nucleation. It is important to emphasize that this experiment was performed close to the magnetization reversal of the Co/Py/Co layer in contact with the IrMn. Thus, we see that the x-ray beam favors the domain nucleation by reversing the antiferromagnetic order.

5.4.3 Nucleation of SAF skyrmions exchanged biased to IrMn

Those nucleated domains can be shrink to stabilize AF worm domains and skyrmions by decreasing the amplitude of the magnetic field. We show in Figure 5.10 worm domains and skyrmions for an applied perpendicular magnetic field of 115 mT. In order to confirm the antiferromagnetic alignment of the individual FM, we tuned the x-ray energy to independently probe the Co and Fe (from Py) to their respective L_3 absorption edges. The dichroic signal at the Fe L_3 edge probes only the FM_2 layer. However, the dichroic contrast at the Co L_3 edge probes both FM_1 and FM_2, given its Co content. This is far from being a problem because the difference in the Co magnetic volume (or thickness) between both layers makes the contribution of the pure Co FM_1 layer about 50% larger. An opposite magnetic contrast is observed at the Co L_3 edge (Figure 5.10a) and Fe L_3 (5.10b) which demonstrates the AF alignment of the Pt/Co and Pt/Co/NiFe/Co layer magnetization.

In Figure 5.10a one can notice the presence of a bright white contrast surrounded by black contrast in a grey background. This strong white contrast corresponds to the Co FM layers, while the black one is representing the Co from the Co/Py/Co FM layers. Furthermore, looking in more detail, one can notice that both black contrasts in Figure 5.10 are overlapping, which further confirms we are probing the same layers. The magnetic parameters of FM_1 and FM_2 are not identical. In addition to using different materials, the accumulation in the stacking makes crucial properties such as PMA and DMI to vary. This is why

the domains pattern in both layers does not exactly overlap. In particular, FM_2 has a lower perpendicular magnetic anisotropy, resulting in larger domains compared to the Co layer.

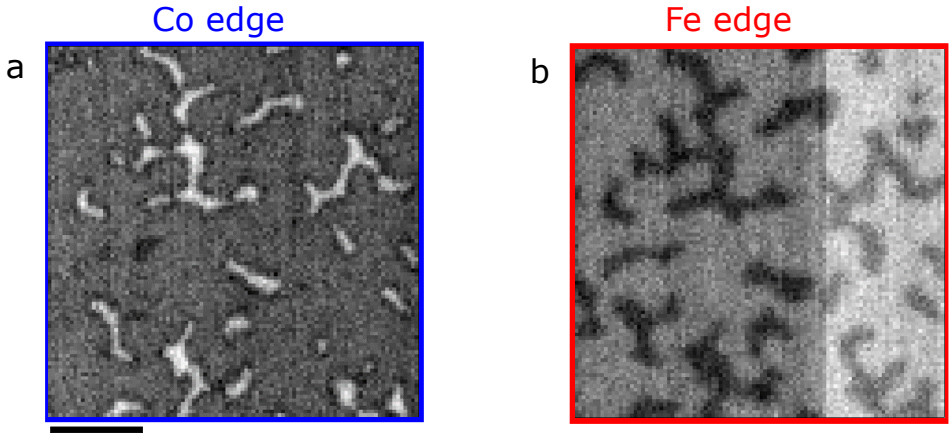

Fig. 5.10: Observation of SAF domain structure exchange biased to IrMn | XMCD-STXM images showing the domain pattern measured at **a** the Co L_3 edge and **b** the Fe L_3 edge, for an applied perpendicular magnetic field of 115 mT. The scale bar is 1 µm.

The observation of isolated SAF skyrmions was also demonstrated in exchange biased SAF system even without any external magnetic field (see Figure 5.11a,b). Again, the contrasts at both material edges demonstrate the opposite alignment of each sublattice. Diameter values of 182 ± 4 nm for the Co layers and 175 ± 3 nm for Co/Py/Co layers were extracted from the Full Width at Half Maximum (FWHM) after a Gaussian fitting of the linescans, as represented in Figure 5.11c. An overlap of the skyrmions is clearly observed from the linescans and the fittings. These experiments showed that isolated SAF skyrmions can be stabilized in SAF exchange biased to an IrMn antiferromagnet.

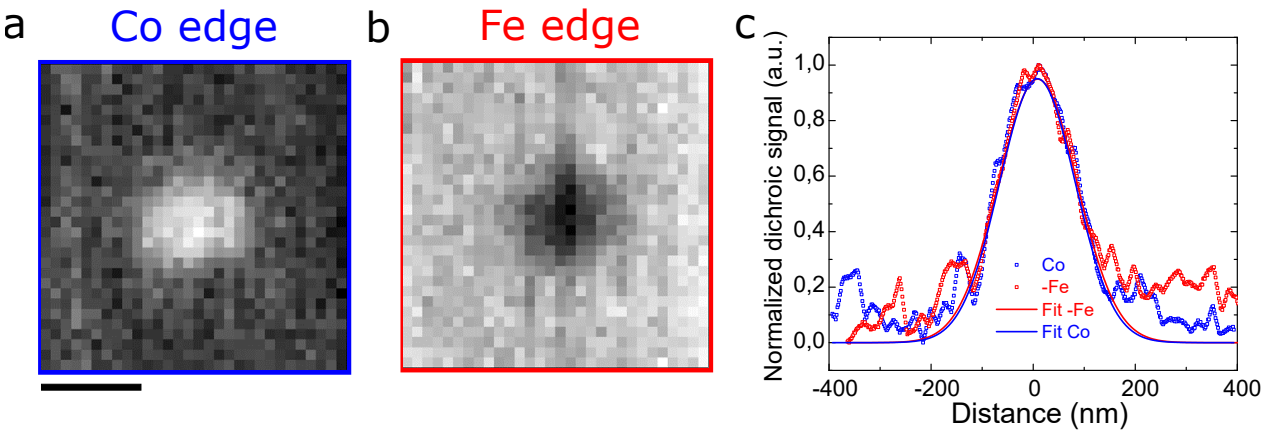

Fig. 5.11: Observation of a SAF skyrmion exchange biased to IrMn | **a,b** XMCD-STXM images measured at the Co L_3 edge of an isolated magnetic skyrmion at the Co and Fe edges (the material absorption edge is represented by the color code) at zero external magnetic field. **c** Line-scan along the skyrmion diameter at the Co **a** and Fe **b** edges. The scale bar is 200 nm. Continuous lines are fits using a Gaussian function and fixing the offset to zero. The average extracted FWHM is 178 ± 4 nm. The Co and Fe edge line-scans are comparable because the dichroic signal has been normalized and the Fe edge signal was multiplied by -1.

5.4.4 Skyrmion imprint using x-ray beam

Experiments also showed that illuminating the sample by the x-ray beam allows to imprint and erase the SAF skyrmion spin texture in the material as illustrated in Figure 5.12. In this experiment, a perpendicular magnetic field (120 mT after saturation at 180 mT) was first applied where skyrmions are known to be stable, and the sample was scanned by the x-ray beam. As expected, magnetic skyrmions can be observed (Figure 5.12a). Then, successive large positive or negative magnetic fields (180 mT) were applied, where skyrmions are expected to be unstable, without scanning the sample with the x-ray beam. A magnetic field close to the

initial magnetic field where skyrmions were initially observed (105 mT) was then applied, and the sample imaged (see Figure 5.12b). Surprisingly, most of the skyrmions initially present are observed, meaning that the skyrmion spin texture was not erased when applying the large magnetic field and seems imprinted.

We then removed the magnetic field. In this condition, skyrmions are expected to be less stable and Figure 5.12c shows the monodomain state without skyrmions. To confirm that we had erased the skyrmion texture, we then again applied successively larger positive and negative fields and imaged at the magnetic field value where skyrmions were initially observed (120 mT). We did not see any skyrmions this time (Figure 5.12d). This experiment showed that the skyrmion spin texture seems to be erased after imaging the sample at a magnetic field where skyrmions are not stable. It means that a re-initialization of the monodomain magnetic texture is possible when the sample is imaged at a magnetic field at which the skyrmions are not stable.

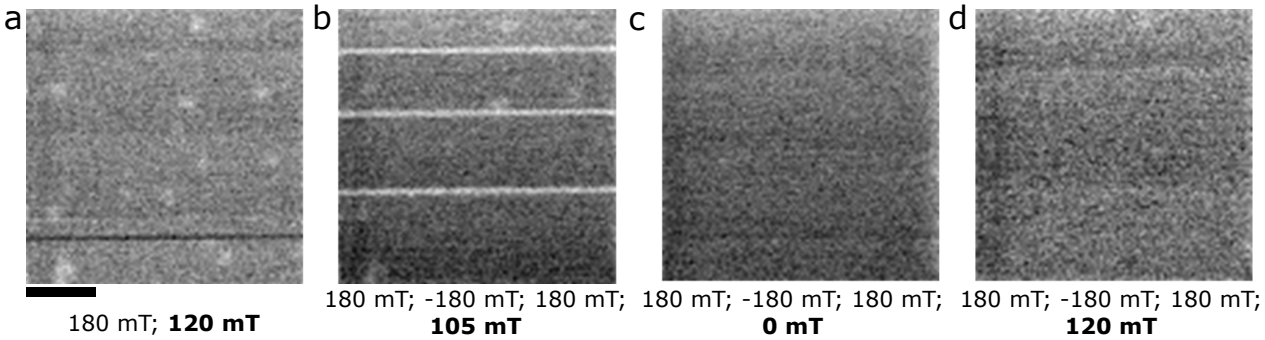

Fig. 5.12: Erasing and nucleating SAF skyrmions with x-rays | Sequence of successive STXM imaging (Fe L_3 edge) to study the effect of the x-ray beam on the skyrmion stabilization. **a** STXM image for a perpendicular magnetic field of 120 mT (after applying a field of 180 mT) showing magnetic skyrmions. **b** STXM image after a field sequence of 180 mT; -180 mT; 180 mT; 105 mT. No image was acquired during the field sweep sequence. The white lines are experimental errors. **c** Same at zero field where no skyrmions are observed. **d** Same after a field sequence 180 mT; -180 mT; 180 mT; 120 mT, having erased the skyrmions. The numbers in bold are the field applied at the imaging moment. The scale bar is 1 µm.

This experiment in SAF stacks can be explained in the light of our previous experiments as well as previous works [194,195] showing that the AF order in exchange bias IrMn can be manipulated using x-ray beam. However, this effect is different from a laser illumination [196], given the low increase of temperature (0.3 K) during the x-ray illumination [195]. It is therefore not related to heating. Other explanations may be the photon-induced magnetic anisotropy change [197,198] or the photon-induced reorientation of the AF order [199]. When illuminating the sample with the x-ray beam, the AF order of the IrMn spins at the Co/IrMn interface aligns with the spin texture of the Co layer due to the exchange interaction, leading to an imprint of the skyrmion spin texture in the IrMn local exchange bias. Under perpendicular magnetic field conditions where skyrmions are stable, this will favor the local skyrmion nucleation. This imprinted spin texture can be erased by illuminating the sample under field conditions where the skyrmions are unstable, for instance at zero field in our case.

5.4.5 Current-induced dynamics of SAF skyrmions exchanged biased to IrMn

The promising results obtained beforehand opened a direct path towards the electrical manipulation of SAF skyrmions in exchange biased SAF structures. Over 1000 m/s velocities without skyrmion Hall effect are expected in current-induced motions of SAF skyrmions due to the cancellation of the gyrotropic force. Having a control of the nucleation via the x-ray and magnetic fields is then a useful tool to study the dynamics in exchange biased SAF.

To study the current induced SAF skyrmion dynamics, µm tracks were patterned in the exchange biased SAF stack and contacted to gold electrodes for current injections. We systematically carried out current-induced motion experiments for different pulse widths and current densities. However, only small displacements and deformations were observed. Figure 5.13 displays an example of successive STXM images after positive and negative current pulse injections (1.8 ns and $J = 1.4 \cdot 10^{12}$ A/m^2). A significant deformation can be observed but so far no large displacements were detected. The lack of motion could be explained by two main reasons. On the one hand, the SAF skyrmions could be imprinted on the antiferromagnetic layer, giving as a result a large pinning due to the exchange interaction between the adjacent Co/Py/Co and IrMn

layers that prevents them from moving. On the other hand, the driving force of the skyrmion motion is the SOT that comes from the bottom Pt layer and the torque gets diluted when the number of FM layers is increased. Our sample has four FM layers; therefore, a stack with two FM layers is expected to show larger skyrmion mobility due to an enhancement of the SOT.

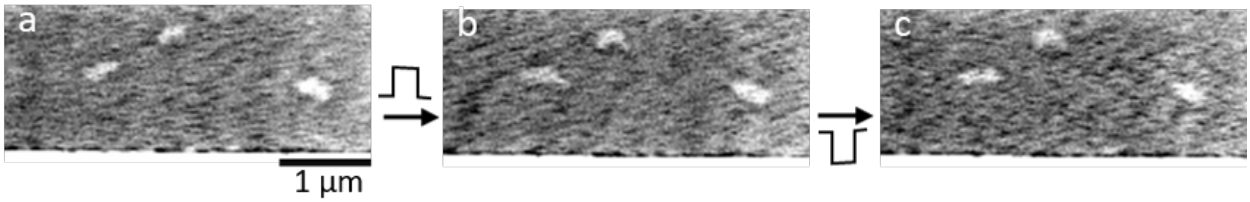

Fig. 5.13: Current-induced experiments in SAF exchange biased to IrMn | **a** STXM images at L_3 Co edge of SAF skyrmions before any pulse. **b** Same image after after the injection of a positive current pulse. **c** Same after a successive negative current pulse. The pulse width is 1.8 ns and the current density is $J = 1.4 \cdot 10^{12}$ A/m^2.

5.5 Conclusions

In this chapter we have presented a new approach to nucleate and stabilize SAF skyrmions using the exchange bias effect. Following the effect of the bias in FM skyrmions, we optimized a SAF stack. We have shown through XMCD-STXM observations that isolated SAF skyrmions can be stabilized in SAF exchange biased to an IrMn antiferromagnet. The x-ray beam leads to a local manipulation of the exchange bias, which is used to nucleate the SAF skyrmions. Layer resolved magnetic microscopy demonstrated the AF alignment within the different magnetic layers. Using the x-ray beam under different magnetic field conditions, the SAF skyrmions can be imprinted or erased by manipulating the exchange bias. These results were a first step towards the manipulation of SAF skyrmions by electrical current. However, the strong exchange interaction in the AF/FM interface makes the ultra-stable skyrmions to be pinned against current-induced torques. It means that there are still some limitations to study their current-induced dynamics.

Chapter 6

Magnetic skyrmions in magnetic tunnel junctions

Contents

6.1 Introduction 82
6.2 Optimization of the magnetic tunnel junction thin film stack 82
6.2.1 Transport characterization of MTJ fabricated on SiN membrane 83
6.3 Operando STXM magnetic microscopy of MTJ 84
6.4 Nucleation of skyrmions in 500 nm diameter MTJ using voltage 85
6.4.1 Manipulation of the skyrmion by external magnetic field and gate voltage 86
6.5 Nucleation of magnetic skyrmions in large pillars 87
6.5.1 DC voltage dependence on large pillars 88
6.5.2 Voltage pulse dependence on large pillars 88
6.5.3 Time resolved STXM experiments 89
6.6 Voltage control magnetic anisotropy experiments 90
6.6.1 Hard axis magnetotransport measurements 91
6.7 Characterization of the magnetic properties in thin film level 92
6.7.1 Magnetic moment, saturation magnetization and magnetic anisotropy 92
6.7.2 Measurement of the Dzyaloshinskii-Moriya interaction by Brillouin Light Scattering experiments 93
6.7.3 Domain wall dynamics experiments 94
6.7.4 Ferromagnetic resonance measurements 95
6.8 Lorentz Transmission Electron Microscopy observations 96
6.9 Micromagnetic simulations 98
6.9.1 Simulations for 500 nm dots 100
6.9.2 Simulations for 2 µm dots 101
6.10 Conclusion 102

This last chapter englobes the results obtained during the second half of my PhD research. Skyrmion-based devices require the low power electrical nucleation and electrical detection of skyrmions with large signals. This can be typically achieved in a magnetic tunnel junction, a device currently used in MRAM magnetic memory. Here, we demonstrate the electrical detection as well as the voltage induced nucleation and annihilation of a single skyrmion in an MTJ via *operando* magnetic microscopy experiments. The manipulation of the skyrmions with voltage and external magnetic field is also studied. Experiments are supported by micromagnetic simulations, which shed light on the voltage induced nucleation process. These results demonstrate the readout and voltage controlled writing operations for low power skyrmion-based technologies.

6.1 Introduction

Recent advancements have brought the spintronic community closer to practical skyrmion-based devices, with successful demonstrations of room-temperature skyrmions in ultrathin films [103,106,108,109], along with their rapid manipulation using electrical currents in tracks [119–121,123,200]. Despite these encouraging developments, challenges persist in achieving low-power electrical detection and controlled nucleation, which are essential for reliable read and write operations in these devices. Pioneering works have presented electrical detection of skyrmions at cryogenic temperatures in certain chiral magnets [130–132,201,202] using the topological Hall effect, as well as in ultrathin films using spin-polarized tunnel electron microscopy [105,139,203]. Single skyrmions have also been electrically detected at room temperature in ultrathin films using the anomalous Hall effect [140,141] or anomalous Nernst effect [143,204]. However, the relatively low electrical signals obtained using these methods hinder their practical implementation in real devices. An alternative approach is to use the tunnelling magnetoresistance (TMR) effect in magnetic tunnel junctions (MTJs) to achieve a much larger readout signal. Recent studies have observed distinct electrical signals in MTJs, induced by magnetic fields [205–207], gate voltages [208,209], or spin transfer torque [205], which were associated with the nucleation of magnetic skyrmions [205–209]. Their experimental findings provided compelling evidence of deterministic electrical switching in a MTJ free layer, transitioning from a ferromagnetic state to a non-trivial spin texture. Micromagnetic simulations suggested the formation of a single skyrmion within the free layer [205]. This skyrmion creation was facilitated by the stray field from the reference layer, promoting spins at the pillar edge to deviate from the bulk magnetization and was sufficient in order to create an intermediate resistance state with a %10 resistance change (enough for electrical detection). The electrical detection, nucleation and annihilation of intermediate resistance states in MTJ combined with VCMA effect was followed by [208], where they showed how the voltage modulates the interface anisotropy, claiming that the skyrmion could be created from an uniform state the bias voltage could control its stability. However, the lack of in-situ magnetic microscopy experiments has so far prevented a direct correlation between the measured electrical signals and the underlying spin textures. More recently, in-situ observation of single skyrmions in MTJs has been achieved using MFM (Magnetic Force Microscopy) [210], although the use of a thick skyrmion layer for the MFM observation has hindered the electrical manipulation of skyrmions, which is crucial for the write operation.

In this chapter, we will go through the work where we used x-ray magnetic microscopy experiments combined with *in-situ* electrical measurement to demonstrate unambiguously the electrical detection of a single magnetic skyrmion within a MTJ. We show that they can be manipulated using external magnetic field, and more importantly, that VCMA [211,212] enables a low energy nucleation/annihilation control of skyrmions in such MTJ. Our demonstration of the readout and write operations of a skyrmion in a MTJ are important steps toward the implementation of skyrmion-based devices. It also opens a promising outlook for the use of skyrmions non-conventional computing devices.

6.2 Optimization of the magnetic tunnel junction thin film stack

In order to stabilise skyrmions in MTJ, our film had the following composition: Si/Si_3N_4/Ta/[Co/Pt]x6 /Ru/[Co/Pt]x3/Co/W/FeCoB/Mg-Ox/FeCoB/W/Pt (see Figure 6.1a). The reference layer is composed of a FeCoB layer coupled to a [Co/Pt]/Ru/[Co/Pt] synthetic antiferromagnetic (SAF) structure through a thin W interlayer. The W interlayer allows the breaking of the (111) texture of the Co/Pt multilayers, the growth of the FeCoB/MgO with (001) texture and the absorption of the Boron (B) after the annealing process. A thick MgO insulator barrier was chosen to enhance the TMR as well as to allow the VCMA, with limited STT. The free layer was composed of a FeCoB, deposited as a wedge, such that its thickness is varying linearly along the 100 mm wafer. Here, we targeted the out-of-plane/in-plane spin reorientation transition to reduce the domain wall energy and allow an easier nucleation of skyrmions. The stack was annealed at 300°C under high vacuum during 10 minutes.

Figure 6.1b shows the out-of-plane hysteresis loops measured by MOKE for different thicknesses of the FeCoB free layer ranging between 1.57 nm - 1.61 nm, which corresponds to the region of interest for the following experiments. The hysteresis loops display the typical bended and butterfly hysteresis loops associated with stripe domain configurations, which are expected close to the in-plane to out-of-plane reorientation transition. The nominal thickness of the FeCoB free layer in the results presented in the next subsections is 1.59 nm.

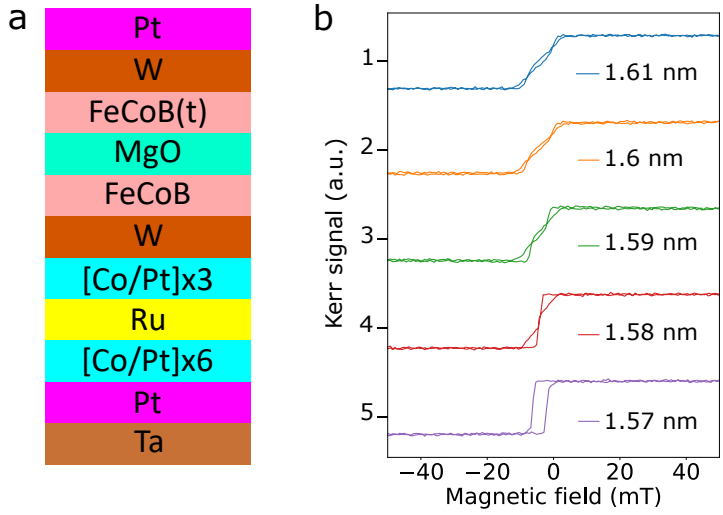

Fig. 6.1: Stack optimization of the MTJ | **a** Schematic representation of the MTJ stack composition and **b** Magneto-optical Kerr effect (MOKE) hysteresis loops of the FeCoB free layer for different thickness. The magnetic field is applied perpendicularly to the sample plane. The represented hysteresis loops correspond to the region of interest on the wafer. The curves are offset for clarity.

6.2.1 Transport characterization of MTJ fabricated on SiN membrane

Patterning of the MTJ pillars was carried out in the PTA facilities at Spintec with different diameters of the nanopillars ranging from 500 nm to 2 µm. A sketch of the device is displayed in Figure 6.2a. Figure 6.2b shows the resistance vs perpendicular magnetic field measurement of the 500 nm diameter MTJ pillar fabricated on Si_3N_4 membranes. TMR value above 53% with sharp reversal and a resistance area product around 700 $\Omega{\cdot}\mu m^2$ is measured. The lower TMR ratio compared to samples fabricated on Si wafer (see Section 6.6) is explained by the thinner Pt seed layer (5 nm) used to limit the x-ray absorption. As a result, the bottom electrode resistance after the nanofabrication process is more resistive (around 1.22 kΩ) and contributes more to the total MTJ resistance. After correcting for the bottom electrode resistance, a TMR of 75 % is found.

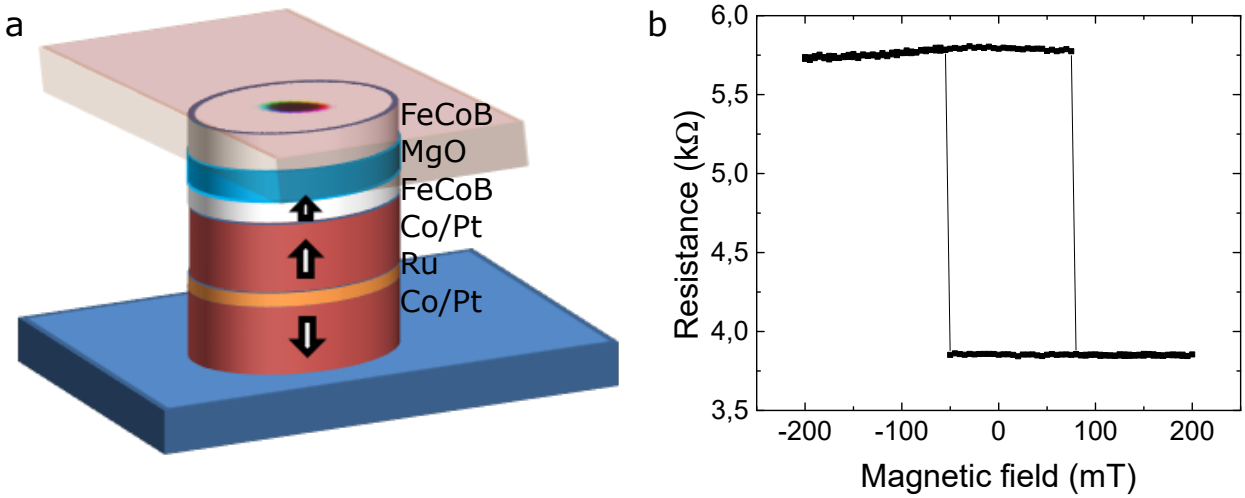

Fig. 6.2: Device level transport properties of 500 nm diameter MTJ on membrane | **a** Sketch of the MTJ pillar and **b** resistance vs perpendicular magnetic field hysteresis loop of a 500 nm diameter MTJ device fabricated on Si_3N_4 membranes.

6.3 Operando STXM magnetic microscopy of MTJ

To demonstrate the skyrmion electrical detection and nucleation in the MTJ unambiguously, it is essential to be able to simultaneously observe the free layer magnetization and measure the MTJ resistance. It is a challenging task since it requires the detection of spin textures in an ultrathin film buried far from the sample surface with high spatial resolution. This cannot be achieved using usual table-top magnetic microscopy techniques such as the MOKE, which can probe layers only a few nm away from the surface for metallic stacks, or MFM, with a limited sensitivity and spatial resolution for nm thick films far from the probe. In contrast, the long penetration depth of soft x-rays in the materials commonly used in MTJ stacks makes STXM relevant for operando magnetic imaging in MTJs [213,214]. To this end, the MTJ stack was grown on a 100 mm Si wafer where ultrathin (75 nm) Si_3N_4 membrane were locally defined on 50x50 μm^2 windows. Sub-micronic pillars were then fabricated on the membranes using standard MRAM nanofabrication process (see Figure 6.3a,b). To allow for the x-ray transmission, only light elements, such as Ti and Al were used to contact electrically the pillar.

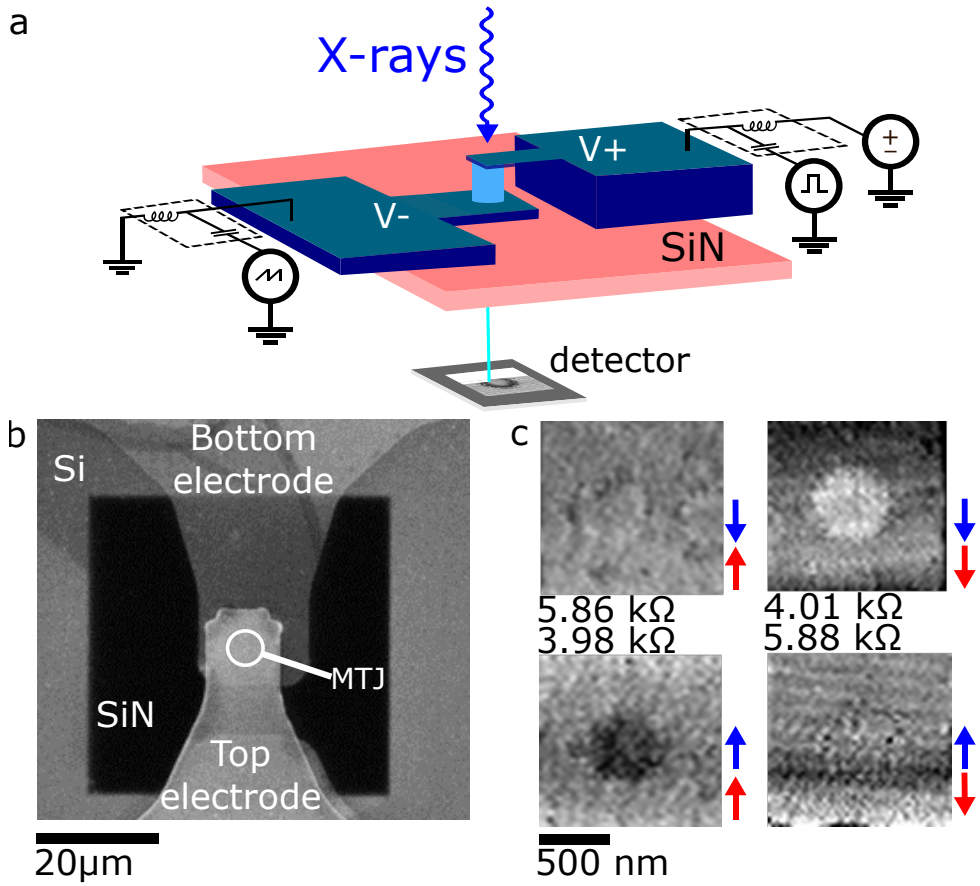

Fig. 6.3: MTJ nanopillar for operando STXM magnetic microscopy | **a** Schematic representation of the sample for STXM imaging. **b** SEM image of the sample. **c** XMCD-STXM images of the four possible single domain magnetization configurations of the FeCoB layers in a 500 nm diameter MTJ (top left AP configurations measured at an out-of-plane magnetic field of 29.5 mT, top right P configuration measured at 250 mT, bottom left P configurations measured at -250 mT, bottom right AP configuration measured at -50 mT). The blue and red arrows stand for the magnetization of the FeCoB free and reference layers respectively. Here the anti-parallel (AP) configurations appear as a grey contrast while the parallel (P) configurations appear as white or black contrast.

XMCD-STXM imaging combined with in-situ magnetotransport measurements confirmed the detection of both FeCoB layer magnetizations at the Fe L_3 edge and the simultaneous measurement of the MTJ resistance. As an example, we show in Figure 6.3c monodomain state images of the four possible configurations of the FeCoB magnetizations in a 500 nm diameter MTJ with their associated resistance values. Only monodomain states were observed when sweeping the magnetic field, in agreement with the measured square TMR hysteresis loops with sharp reversal. The corresponding RH hysteresis loop to this exact device was shown in Figure 6.2b.

6.4 Nucleation of skyrmions in 500 nm diameter MTJ using voltage

To nucleate magnetic skyrmions, we exploited the VCMA effect. Starting from an initial monodomain state with parallel magnetization configuration (R = 3.63 kΩ in Figure 6.4a), the application of a 10 ns voltage pulse leads to the nucleation of a skyrmion in the FeCoB free layer (see Figure 6.4b). The nucleation is associated with an increase of the resistance of 467 Ω, which is a quarter of the total TMR (1.92 kΩ difference and 51 % of TMR).

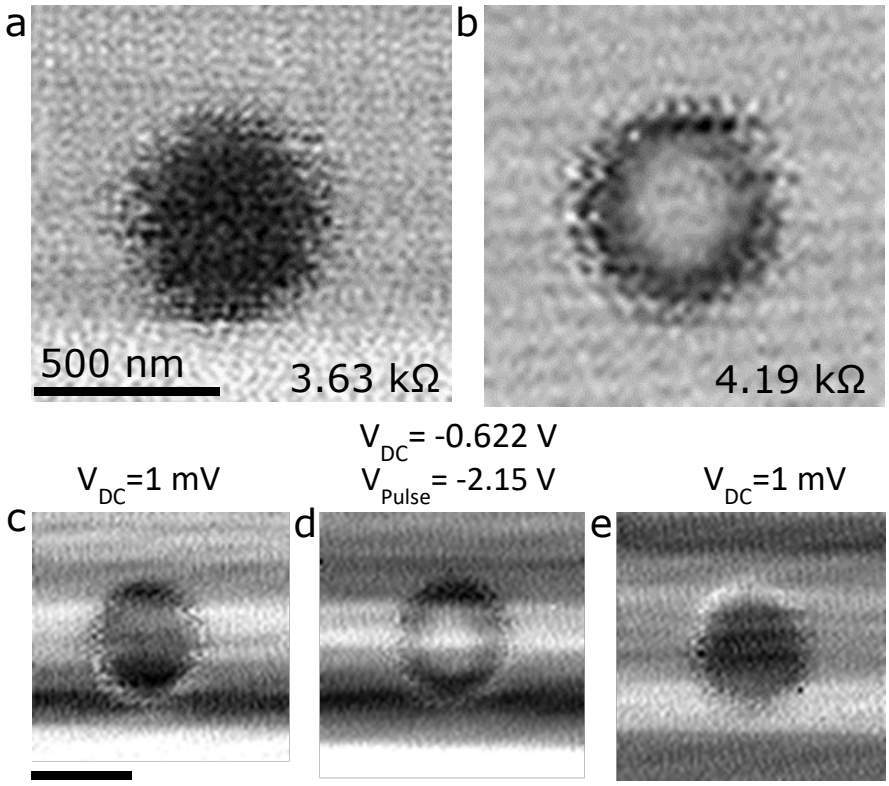

Fig. 6.4: Electrical detection of a skyrmion in an MTJ and its nucleation/annihilation using voltage | **a** XMCD-STXM images of a monodomain state measured at the Fe L_3 edge in 500 nm diameter MTJ and its associated resistance state (parallel magnetization configuration). An external perpendicular magnetic field of -2.75 mT is applied. **b** Same after the application of a 10 ns voltage 2.15 V pulse **c-e** STXM images **c** before, **d** after the application of a 10 ns voltage pulse of 2.15 V in the presence of a DC voltage of -622 mV and **e** after setting the DC voltage amplitude back to 1 mV. In **c-e**, the external perpendicular magnetic field has an amplitude of -2 mT. The black (grey) contrast shows that both FeCoB layers are in parallel (antiparallel) direction. The scale bar in d is also 500 nm.

Note that this intermediate resistance is not observed in the hysteresis loop when sweeping the external magnetic field. This change in resistance is in agreement with the one expected from the diameter of the skyrmion (240 nm) assuming parallel conduction channel for the P and AP resistance states. Due to the large R·A product, a low current density (around $7 \cdot 10^9$ A/m^2) is injected when applying the voltage pulse. As a result, the STT effect is expected to be negligible and the nucleation can be explained by the sole effect of the VCMA. A nucleation energy of around 30 pJ is estimated, which is large compared to the write energy in optimized STT-MRAM (around 100 fJ) [215]. This is explained by the larger area of the MTJ dots, compared to the tens of nm diameter MTJ pillars in STT-MRAM. However, a much lower energy could be achieved by increasing further the R·A product and/or reducing the MTJ size. The obtained skyrmionic state is found to be stable against subsequent pulse voltage excitations, either positive or negative. The range of magnetic fields in which the skyrmion remains stable is quite narrow (few mT) with a small dependence of the skyrmion diameter on the external magnetic fields (see Section 6.6). This suggests that the stray field from the edges and the SAF layers plays a significant role in the stabilization of the skyrmion, in line with previous experiments on geometrically confined skyrmions in ultrathin films [103,216]. As a result, subsequent annihilation of the skyrmion was not observed using voltage pulses. Yet, full electrical nucleation and annihilation could be achieved by modulating the skyrmion energy using a small DC voltage in the

presence of a small magnetic field which destabilizes the skyrmion state (see Figure 6.4c-e). Starting from a monodomain state (Figure 6.4c), a skyrmion is nucleated by applying a 10 ns voltage pulse in the presence of a DC voltage (Figure 6.4d), which further stabilizes the skyrmion. When releasing the DC voltage, the skyrmionic state is destabilized by the magnetic field and the initial monodomain state is again observed. This sequence demonstrates the full electrical nucleation/annihilation of a skyrmion in the MTJ.

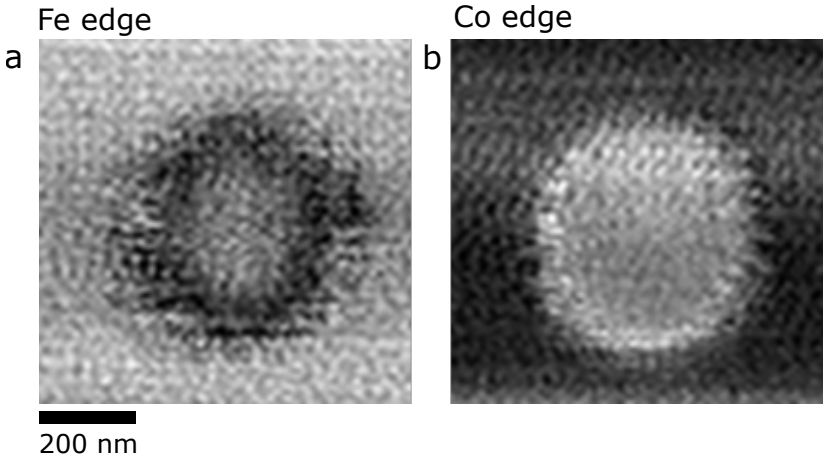

Fig. 6.5: Observation of the SAF structure in the MTJ with a skyrmionic state | **a** XMCD-STXM image of a skyrmion state measured at the Fe L_3 edge in the 500 nm diameter pillar. **b** XMCD-STXM image of a monodomain state measured at the Co L_3 edge at the same conditions. An external perpendicular magnetic field of -2 mT is applied. The white contrast in **b** shows the orientation of the thicker Pt/Co multilayer magnetization.

STXM imaging was also performed at the Co L_3 absorption edge to study the behaviour of the SAF layer during the switching. This is made possible by the non-compensation of the Co magnetization in the SAF due to the larger thickness of the bottom Pt/Co multilayers. Figure 6.5a shows a XMCD-STXM image of a skyrmion nucleated by a voltage pulse. The corresponding image in the Co L_3 absorption edge is displayed in Figure 6.5b. Here, the contrast we see is governed by the x6 repetition of the Pt/Co multilayers. The white contrast observed in the Co confirms both its uniformity in the presence of the skyrmion and its opposite alignment with respect to the fixed FeCoB layer. This observation is in agreement with the parallel magnetization configuration resistance value measured before the skyrmion nucleation.

6.4.1 Manipulation of the skyrmion by external magnetic field and gate voltage

We show in this section additional data on the manipulation of the skyrmion using external magnetic field and gate voltage.

Figure 6.6a shows the dependence on the external out-of-plane magnetic field of the skyrmion diameter in a 500 nm MTJ dot (black dots) and the corresponding change in resistance (blue curve). The diameter decreases from 250 nm to 170 nm over 1.5 mT. Here, the diameter was deduced from the sample conductance G assuming parallel conduction channels (black dots) with the following relation:

$$G = x \cdot G_P + (1 - x) \cdot G_{AP}, \tag{6.1}$$

where G_P (G_{AP}) are the conductance of the parallel (antiparallel) magnetization state. The prefactors, x and (1-x), represent the fractions of the area with P and the AP (skyrmionic) magnetization state, respectively. Note that for the skyrmion in Figure 6.4b we showed before (R = 4.19 kΩ), we measured a diameter of 240 nm and the conductance formula provides us with a resistance value of 4.02 kΩ, in line with the transport measurement values (see Section 6.6).

Figure 6.6b shows the field dependence of the skyrmion diameter measured in another sample for a DC voltage of -670 mV, using the area of the skyrmion measured by STXM (black curve) and the resistance value (red curve). A lower susceptibility is observed. The diameter decreases from 340 nm to 250 nm when increasing the magnetic field from 1 mT to 6.5 mT, where it annihilates. The small discrepancy between the two methods may arise from the domain wall width and the pillar size itself, which may be slightly different from the nominal 500 nm. Lastly, the dependence of the skyrmion diameter on the DC bias voltage for a

constant magnetic field of 3 mT, when increasing the DC voltage from -0.4 V to 0 V, is shown in Figure 6.6c. A small decrease of the diameter is noted upon the removal of the DC voltage, as expected from the increase of the DW energy induced by VCMA.

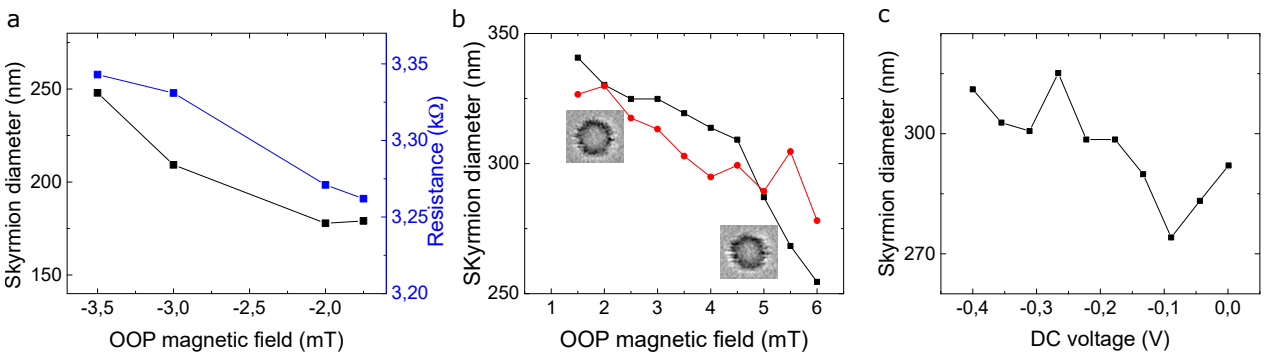

Fig. 6.6: Evolution of the magnetic skyrmion size in 500 nm dots in response to external magnetic field and applied DC voltage | **a** Dependence of the skyrmion diameter on external out-of-plane magnetic field for a DC voltage of -622 mV (sample A). **b** Dependence of skyrmion diameter on external out-of-plane magnetic field for a DC voltage of -670 mV (sample B). The diameter was measured by increasing the magnetic field from 2 mT up to 6.5 mT, where the skyrmion annihilates. The diameter values are extracted from the area of the skyrmion (red dots) and from the resistance of the junction assuming parallel conduction channels (black dots). The insets shows examples of the textures during this sequence (corresponding to 2 mT and 5 mT respectively), demonstrating a reduction in the skyrmion size. **c** Dependence of skyrmion diameter on DC voltage, showing a reduction with the bias removal.

6.5 Nucleation of magnetic skyrmions in large pillars

Larger diameter pillars (2 µm diameter) were also studied. In this case, the application of a negative DC voltage led to a drastic change of the hysteresis loop. While at low voltage a square hysteresis loop with sharp reversal was observed, at larger voltage ($V_{DC} = -0.52$ V) a continuous decrease of the resistance from the AP to the P state is measured (Figure 6.7a). XMCD-STXM measurements revealed that this decrease in resistance was associated to the creation of a skyrmion in the pillar, which nucleates on the edges, then gradually decreases in size and eventually annihilates when increasing the magnetic field (see Figure 6.7b).

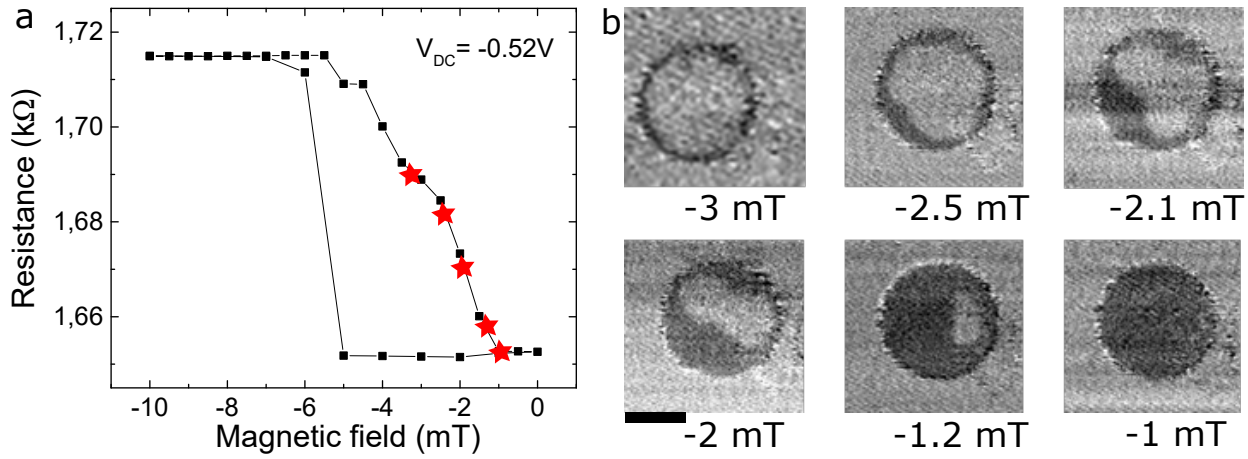

Fig. 6.7: Magnetic field dependence of the skyrmion in a 2µm MTJ pillar | **a** Resistance vs perpendicular magnetic field hysteresis loop for a DC voltage $V_{DC} = -0.52$ V. The red stars show the resistance values corresponding to the images shown in **b**. **b** STXM images of the MTJ free layer (Fe L_3 edge) for different magnetic field for $V_{DC} = -0.52$ V. The scale bar is 1 µm.

6.5.1 DC voltage dependence on large pillars

We show in Figure 6.8 that the nucleated bubbles are sensitive to the gate voltage amplitude. Figure 6.8a and 6.8b display a decrease (increase) in the bubble size when increasing (decreasing) the gate voltage, which is explained by the modulation of the DW energy via VCMA. Those skyrmions were nucleated at different magnetic field conditions. Compared to smaller pillars, the larger susceptibility of the bubbles to external magnetic fields and gate voltages in larger dots can be explained by the shallower stray field energy potential when increasing the dot size [103,216]. However, there were occasional instances of unexpected behaviour. Here, some events with opposite voltage dependence were also detected suggesting a stochastic response to gate voltage. An example is shown in Figure 6.8c, where an increase of the DC voltage, i.e an increase of the PMA, leads to an increase of the skyrmion size. These events may be attributed to jumps enabled by voltage excitations over the energy barrier between local energy minima defined by the pillar geometry and local pinning sites. The irregular shapes of the skyrmions also evidence the influence of pinning.

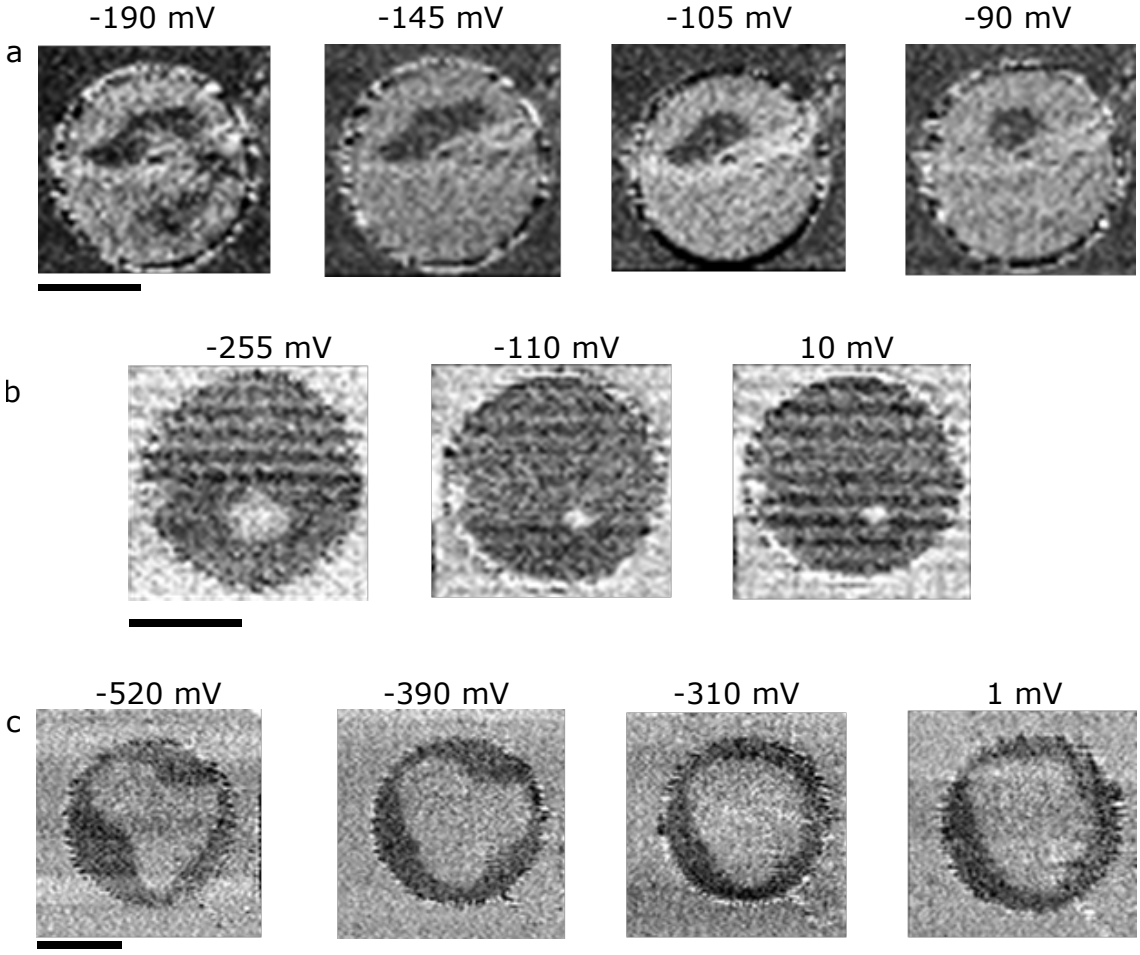

Fig. 6.8: DC voltage dependencies for different magnetic textures in a 2µm MTJ pillar | **a** Sequence of STXM images showing voltage dependence of the magnetic texture in the MTJ at -2.3 mT. **b** Another sequence of successive STXM images showing isolated skyrmions for different DC voltages and an out-of-plane external magnetic field of 4 mT. **c** Skyrmions also showing a variation in size with the DC voltage at an external out-of-plane field of -2.3 mT. The scale bar in every sequence is 1 µm. The images in are normalized with respect to an STXM image of the dot in the AP resistance state at a field of -20 mT.

6.5.2 Voltage pulse dependence on large pillars

The bubble shape can also be manipulated using ns width voltage pulses (see Figure 6.9). Voltage pulses also induced stochastic deformation as shown in Figure 6.9 (see sequence 6.9a-c). Here, the application of a 10 ns voltage pulse with positive polarity leads to a decrease of the skyrmion size through a small jump of the skyrmion's DW from one pinning site to another. The DW can be moved back to its initial position through applying a second pulse with the same polarity. Applying another pulse with negative polarity allows another switching of the DW configuration associated with a smaller skyrmion size (Figure 6.9d). This experiment

shows that the skyrmion's DW can be moved back and forth between two stable pinned configurations by the voltage pulses, independently of the voltage polarity.

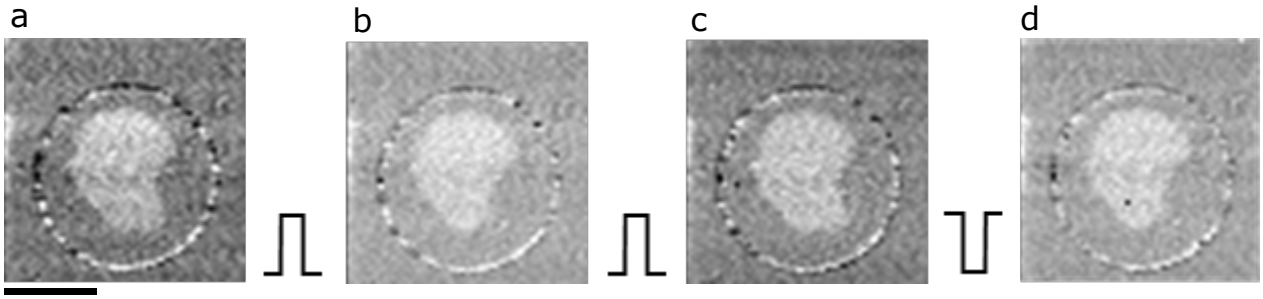

Fig. 6.9: Manipulation of a skyrmion by voltage pulse in a 2 µm dot | Successive STXM images of a skyrmion. **a** Initial configuration, **b** after the application of a positive voltage pulse, **c** after the application of a second positive voltage pulse and **d** after the application of a negative voltage pulse. The images are acquired after applying different voltage pulse polarities of 10 ns. The amplitude of the voltage pulses is ±150 mV and the applied DC bias is -70 mV under a magnetic field of 6 mT. The scale bar is 1 µm.

A better control of these skyrmions using voltage pulses would open interesting new functionalities for devices based on skyrmions in MTJ. For instance, if voltage pulses are able to create and annihilate multiple skyrmion state, this could be exploited as a multilevel memory. However, a fine tuning of the external excitations is required for such operations.

6.5.3 Time resolved STXM experiments

We also performed time resolved observations using pump probe measurements. Both monodomain configuration and the skyrmionic state were analysed. To this end, systematic measurements of the time dependent response of a fully saturated state to sine excitations with various amplitudes and frequencies were performed. This allows us to identify a dynamical mode with a resonance frequency around 117.8 MHz with a small line-width, typically a few MHz.

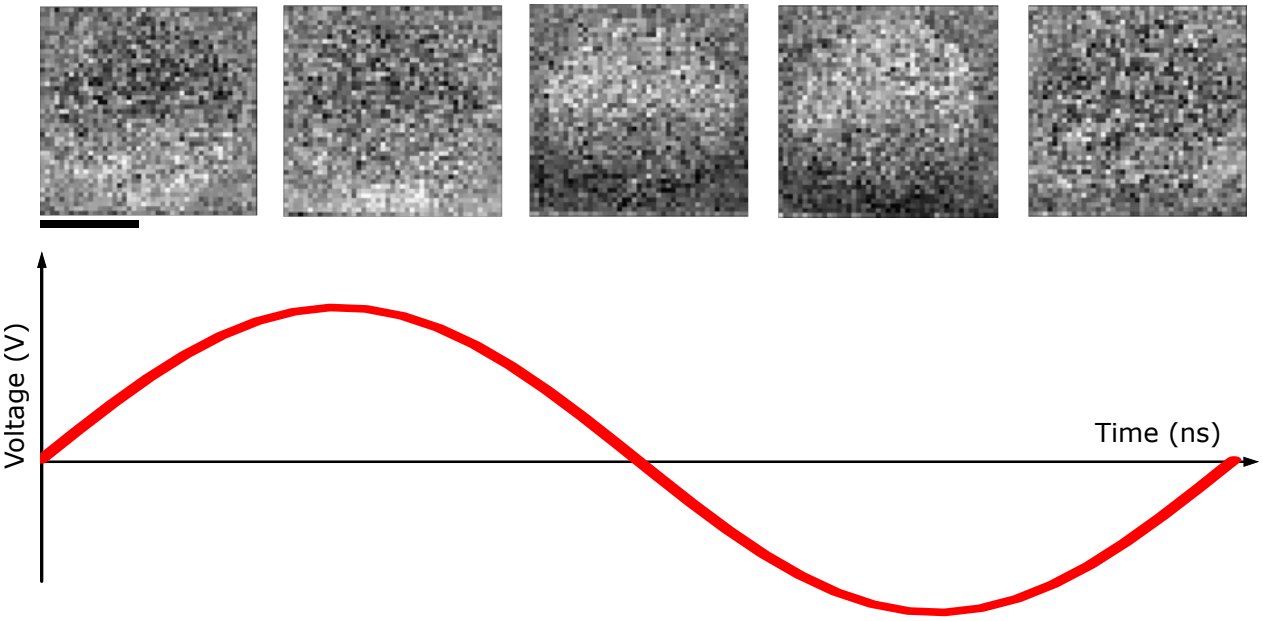

Fig. 6.10: Time resolved STXM observations of the MTJ | Equally spaced frames covering a full excitation period from the time resolved STXM observation of the MTJ. It was excited under a sine voltage with 117.8 MHz frequency and 0.11 V amplitude. An out-of-plane field of 2.4 mT and a 10 mV bias were applied. The white contrast represents the beating of the magnetization due to switching. The scale bar is 1 µm.

Figure 6.10 is displaying equally spaced frames in time that cover a full excitation period. This beating represents the back and forth excitation of the free layer.

6.6 Voltage control magnetic anisotropy experiments

Applying a DC voltage across the MTJ affects the electronic structure and magnetic properties of the system [217,218]. As expected, a decrease of the TMR is expected with the applied voltage. Figure 6.11 shows an example of the measurements we performed during the characterization of the magnetic properties of the MTJ pillars nanofabricated on a Si wafer. The standard MRAM process without modifications was followed. This way, we defined a Ta hard mask by etching (instead of Ti by lift-off for STXM experiments).

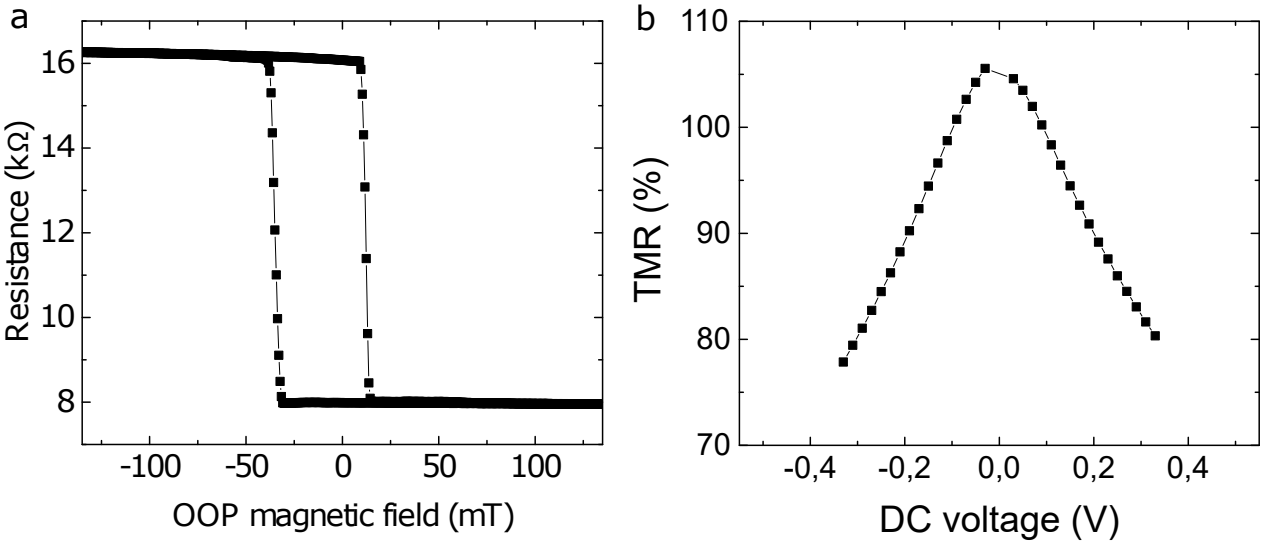

Fig. 6.11: Magnetotransport measurements of MTJ patterned on Si wafer | **a** Resistance vs out-of-plane magnetic field hysteresis loop of a 150 nm diameter MTJ pillar. **b** Average of 18 hysteresis cycles are shown. A typical bell-shaped curve is displaying the TMR behaviour against the applied DC voltage for the same device.

The VCMA effect in the MTJ was characterized using two different experiments. Firstly, from the voltage dependence of the magnetic field switching probability (see Figure 6.12a) [219,220]. The VCMA leads to a variation of the coercive field when applying the DC bias voltage. The anisotropy field can be estimated from the distribution of the switching field using the following formula:

$$P_{SW}(H_Z) = 1 - \exp\left(-\frac{H_{Keff} f_0 \sqrt{\pi}}{2R\sqrt{\Delta}} \mathrm{erfc}\left[\sqrt{\Delta}\left(1 - \frac{H_Z - H_f}{H_{Keff}}\right)\right]\right), \tag{6.2}$$

where f_0 is the attempt frequency, R is the external magnetic field sweep rate and H_f is the stray field from the fixed FeCoB and SAF layers. The probability curves measured for different voltages were fitted with the distribution which allowed us to extract the magnetic anisotropy field $\mu_0 H_{Keff}$ and thermal stability factor Δ as a function of the voltage.

The quantification of the VCMA coefficient requires the dependence of the anisotropy on the DC voltage. For this, we summarized our pillars global behavior in Figure 6.12a, where the probability curves for different voltages are plotted. In the same line, anisotropy and coercive field dependencies are shown in Figure 6.12b. A linear fit leads to a variation of the anisotropy of 17 mT/V, that we can inject in the field-estimated VCMA coefficient, ϵ_H, given by:

$$\epsilon_H = \frac{1}{2}\mu_0 M_{S,FL} t_{FL} t_{MgO} \frac{dH_{Keff}}{dV}, \tag{6.3}$$

where $M_{S,FL}$ and t_{FL} refer to the saturation magnetization and the thickness of the free layer. t_{MgO} is the barrier thickness. Here we use $t_{MgO} = 3.03$ nm, $t_{FL} = 1.04$ nm and $M_{S,FL} = 1.63$ MA/m to get a value of $\epsilon_H = 44$ fJ/Vm, in line with the literature [219,221–223].

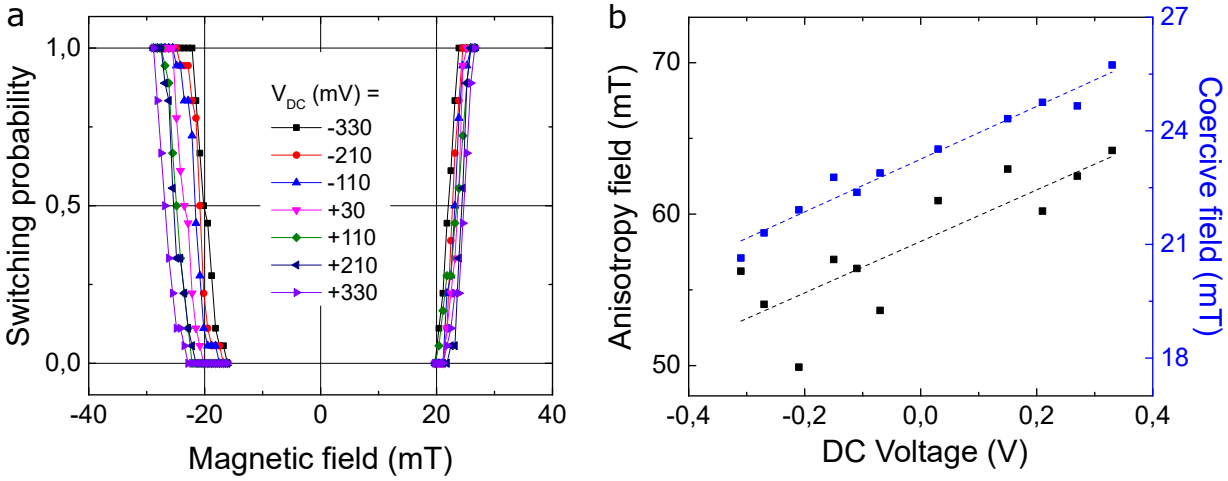

Fig. 6.12: Voltage control of magnetic anisotropy | **a** Switching probability vs external magnetic field for different voltages applied. Negative field show the switching from the P to AP configuration and positive field the switching from AP to P configurations. An offset field of 12 mT is subtracted. **b** Coercive field (blue dots) and anisotropy field (black dots) vs DC voltage. The dotted lines are linear fits. The nominal thickness of FeCoB is 1.55 nm.

6.6.1 Hard axis magnetotransport measurements

To confirm these results, we also performed hard axis measurement to extract the anisotropy field under various applied gate voltages. To this end, we considered MTJs stacks with a slightly thicker FeCoB free layer ($t = 1.64$ nm), such that the FeCoB free layer is in-plane magnetized, while the reference layer remains out-of-plane magnetized. The sketch in Figure 6.13 explains the geometry of the system at zero field. When a small external out-of-plane magnetic field is applied, the magnetization of the free layer gets also oriented out-of-plane towards either P or the AP configuration depending on the field direction. The reference layer magnetization remains fixed and unaffected for these magnetic field values.

In the scenario where an external in-plane field is applied, the magnetic layers being affected are the fixed FeCoB layer and the SAF. Figure 6.13a shows the resistance vs magnetic field hysteresis loops performed in this configuration for a 1 µm diameter dot. Due to the fact that we do not have an in-plane pinned layer, it is not possible to reach the AP relative orientation of the layers. The highest possible resistance value hence corresponds to the orthogonal orientation of the layers at zero field, which is the midpoint resistance value between the P and the AP. This measurement confirms the in-plane configuration of the free layer. For large field values, the system will tend to align both layers in-plane and the resistance value will converge towards the parallel resistance value. In principle, this will be the case for any in-plane oriented external field given the cylindrical symmetry. However, the asymmetric RH loop observed could give the information that the free layer magnetization has some preferred orientation.

Resistance vs magnetic field hysteresis loops are shown in Figure 6.13b for out-of-plane external field in the same device. Here, a fast variation of the resistance is observed in a short magnetic field range (-20 mT and 20 mT). These resistance values correspond to the P and AP states. Performing the measurements for different applied voltages, the slopes vary significantly. This is explained by the tilting of the free layer magnetization towards out-of-plane direction by the magnetic field, whose saturation field depends on the applied voltage due to the VCMA effect. Linear fits of the slopes allow us to extract the anisotropy field for various gate voltages (see Figure 6.13c). A value of 15.6 mV/T is extracted, in line with the value obtained from easy axis measurements.

The hard axis magnetotransport measurements were performed with the help of Aurélie Kandazoglou.

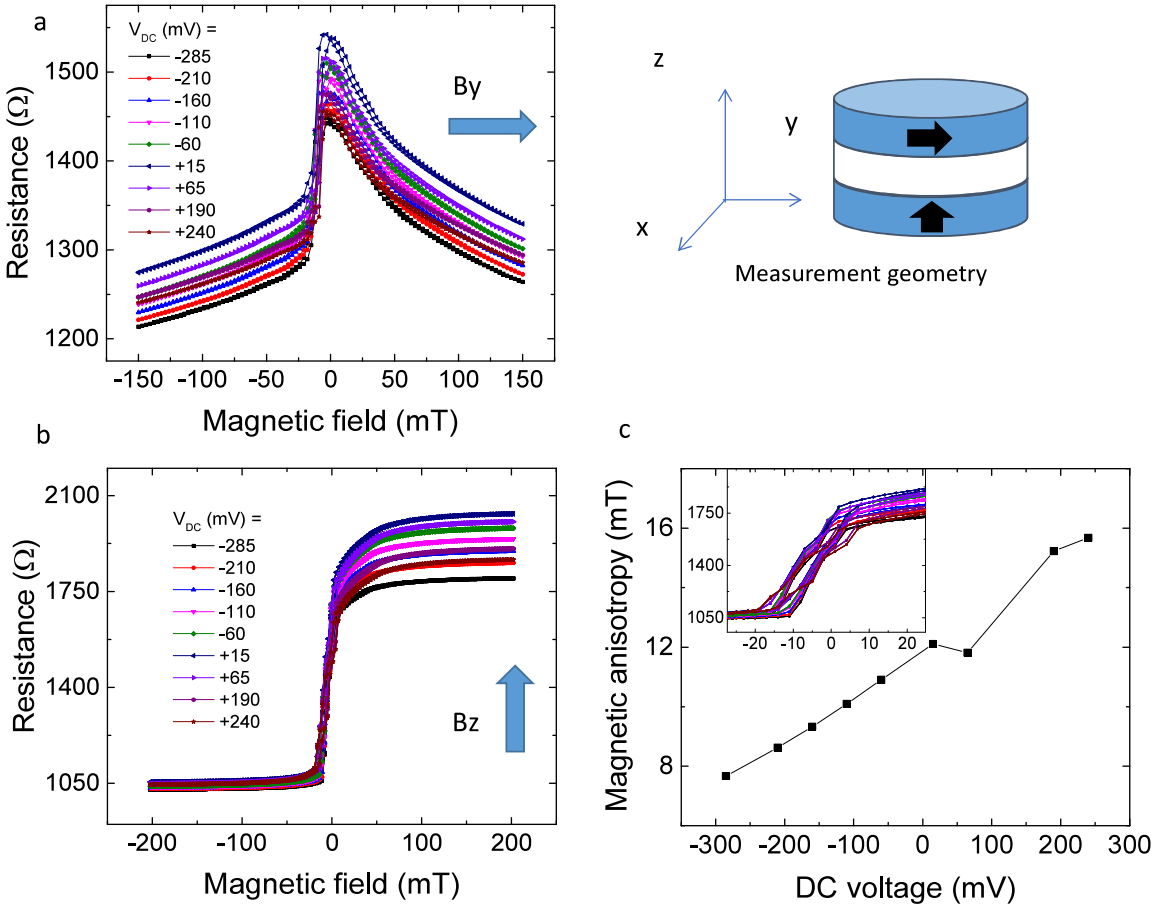

Fig. 6.13: Voltage dependence measurements on the magnetoresistance hysteresis loops for an in-plane free layer configuration | **a** External in-plane and **b** out-of-plane magnetic field measurements. **c** Anisotropy dependence on voltage extracted from the slope of the curves in **b** (see inset). The inset is the zoom of **b** at low field values showing the change in the slope due to the voltage. The device has a 1 µm diameter and 1.64 nm of nominal free layer thickness.

6.7 Characterization of the magnetic properties in thin film level

To characterize the magnetic properties of the free FeCoB layer, a stack similar to the MTJ was deposited, in which only the free FeCoB layer was magnetically active. This was achieved by substituting the Co layers in the SAF with Pt and replacing the fixed FeCoB thickness with a magnetically dead FeCoB layer of 0.3 nm. This sample was used to characterize the magnetic parameters of the FeCoB free layer, namely, the magnetic moment, magnetic anisotropy, Dzyaloshinskii-Moriya interaction (DMI) and magnetic damping. These measurements are described in the following subsections.

6.7.1 Magnetic moment, saturation magnetization and magnetic anisotropy

The magnetic moment per unit area μ_S of the free layer was measured using SQUID magnetometry leading $\mu_S = 1.760 \pm 0.029$ mA (Figure 6.14a). To measure the saturation magnetization, the magnetically active thickness of the FeCoB free layer was estimated from the dependence of the Kerr signal amplitude on the thickness of the FeCoB layer (see Figure 6.14b). The Kerr amplitude decreases linearly with the ferromagnetic thickness and a linear fit allows us to extract a magnetic dead layer thickness $t_d = 0.51$ nm. This leads to a saturation magnetization $M_S = 1.63 \pm 0.19$ MA/m. The perpendicular magnetic anisotropy field $\mu_0 H_K$ was measured from hard axis SQUID magnetometry leading to $\mu_0 H_K = 35 \pm 5$ mT.

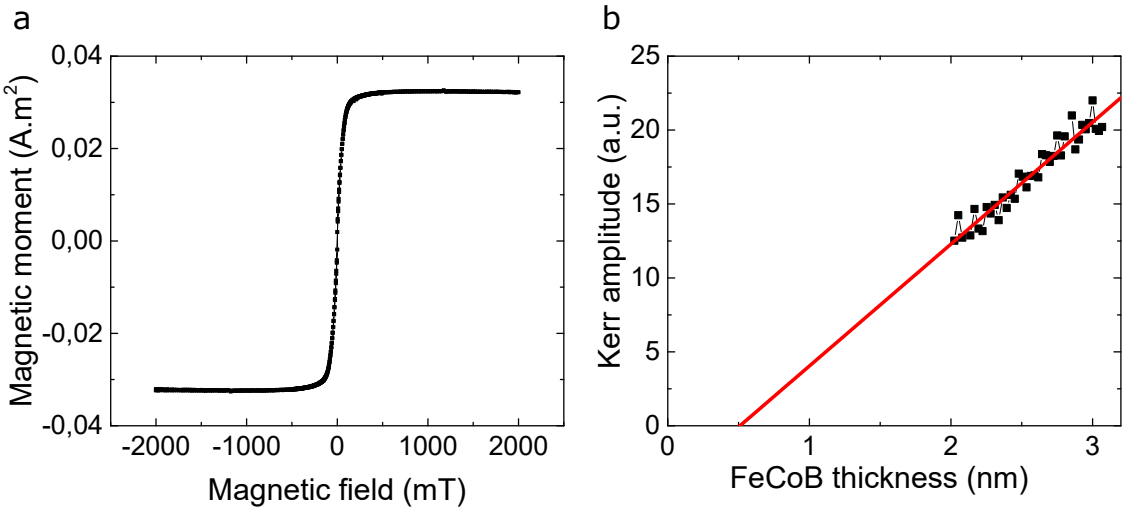

Fig. 6.14: Thin film characterization of the magnetic properties | **a** In-plane hysteresis loop to extract the saturation magnetization and the perpendicular magnetic anisotropy. **b** Kerr amplitude vs thickness of the FeCoB free layer. The red line is a linear fit. The extrapolation does not intersect in the origin, meaning there is a presence of a dead layer, which does not contribute to the amplitude of the signal.

6.7.2 Measurement of the Dzyaloshinskii-Moriya interaction by Brillouin Light Scattering experiments

Brillouin light scattering (BLS) experiments were carried out in order to extract the Dzyaloshinskii-Moriya interaction (DMI) of the free layer [224]. This measurement required a slightly thinner FeCoB layer thickness (nominal 1.52 nm instead of 1.59 nm).

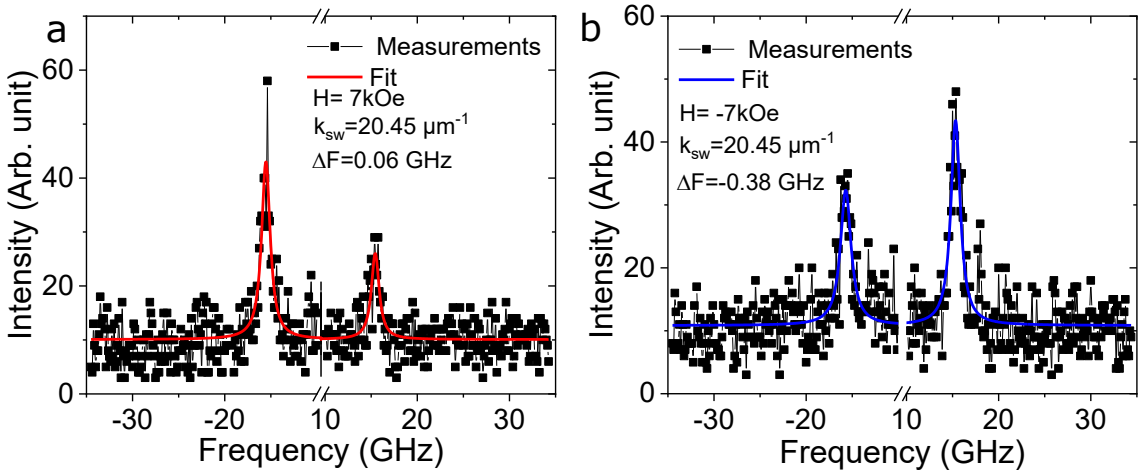

Fig. 6.15: Brillouin light scattering measurements | BLS frequency spectrum for a given k vector of 20.45 µm^{-1} for **a** positive and **b** negative magnetic fields. An average frequency shift $\Delta f = -0.22$ GHz is found.

The principle of the measurement is the following: an external in-plane magnetic field is applied to saturate the thin film in the plane and a laser with a certain wave vector probes the spin waves (SW) that propagate perpendicularly to the field (Damon-Eshbar geometry). The DMI induces a preferred chirality of the spin wave and leads to an energy difference between SW propagating with opposite wave vectors. The corresponding shift in the SW frequencies is directly related to the interfacial DMI amplitude through the following relation:

$$\Delta f(k) = \frac{2\gamma k D_S}{\pi M_S t}, \tag{6.4}$$

with $\gamma = g\mu_B/\hbar$ the gyromagnetic ratio, M_S the saturation magnetization and g the gyromagnetic factor. The DMI amplitude can be extracted either for a given k vector or from the slope of the curve when k is

varied. In our case, a measurable signal could only be achieved for the largest possible wave vector. Furthermore positive and negative field measurements were performed to overcome the non-zero frequency position that could occur. The corresponding frequency spectrums are displayed in Figure 6.15a (positive fields) and 6.15b (negative fields). Averaging both frequency shift values leads to $D_S = -0.15 \pm 0.07$ pJ/m.

The BLS measurements were performed by Mohamed Belmeguenai at the LSPM laboratory in Villetaneuse, France.

6.7.3 Domain wall dynamics experiments

We performed additional field induced domain wall dynamics experiments in order to estimate the magnetic damping and to confirm the small DMI measured using BLS. To characterize the DW dynamics, wide field magneto-optical Kerr microscopy experiments were performed. The DW velocity was deduced from the expansion of bubble domains driven by out-of-plane magnetic field pulses of strength up to 600 mT, generated using microcoils associated to pulsed current generators [225].

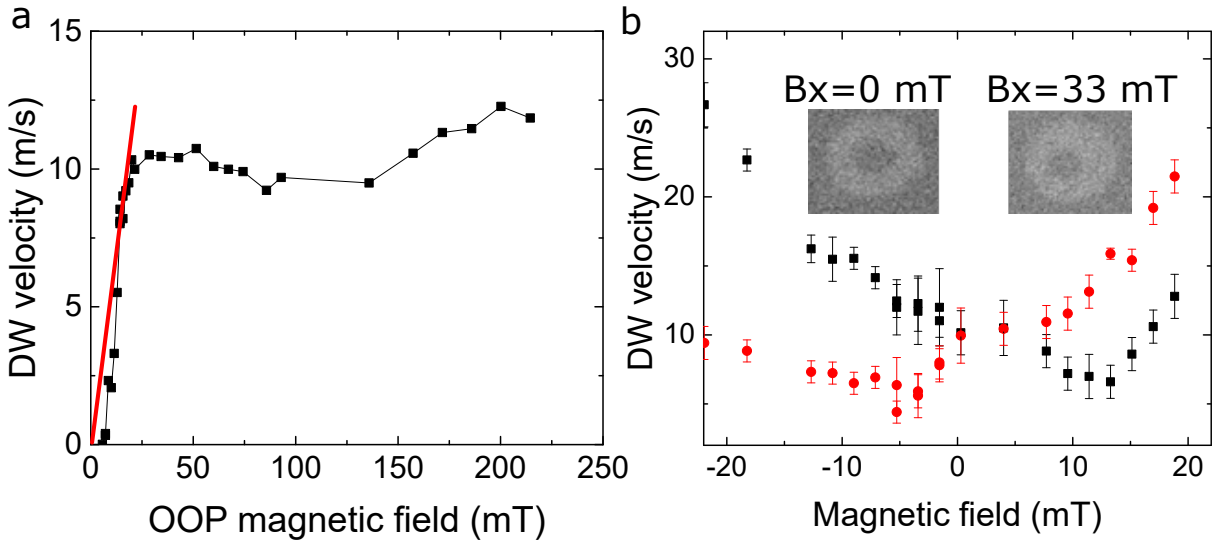

Fig. 6.16: Field-induced bubble expansion measurements for DMI measurements | **a** DW velocity vs out-of-plane magnetic field at room temperature. The black points are data with standard deviation error bars. The red line was used to estimate the mobility in the flow regime. **b** DW velocity vs in-plane field for a perpendicular field-pulse of $B_Z = 33$ mT and 5 pulses of 50 ns width. The curve has a minimum when the DMI field compensated the external in-plane magnetic field. The red and black curves show the dynamics of up/down and down/up domain walls. The insets display differential pMOKE images showing the expansion of the circular domain (white contrast) induced by a magnetic field pulse of 33 mT for a constant in-plane field $B_X = 0$ (left) and $B_X = 3.3$ mT (right).

In this sample, the FeCoB free layer had a nominal thickness slightly thinner ($t = 1.49$ nm) such that sufficiently large domains are stabilized to achieve the bubble expansion. Figure 6.16a displays the average velocity of the DW as a function of the perpendicular magnetic field pulse. Assuming that the large mobility at low field (red line) corresponds to the flow dynamical regime, the damping can be estimated from the mobility using $v_{DW} = \gamma \Delta \mu_0 H / \alpha$ (see Section 1.2 in Chapter 1). Using $\mu_0 H_{Keff} = 95 \pm 5$ mT measured via in-plane SQUID magnetometry and $A = 12 \pm 6$ pJ/m [226], $\Delta = 12.4 \pm 3.1$ nm is estimated. Using $\gamma/2\pi = 29.6 \pm 1.0$ GHz/T, measured by FMR, we obtain $\alpha = 4 \pm 2$, which is unrealistically high. This suggests that the large mobility regime at low field corresponds actually to a thermally activated regime which hides the flow regime and the Walker breakdown [227].

For the DMI measurements, field induced bubble expansion measurements were performed [225]. Under the presence of an external static in-plane magnetic field, out-of-plane magnetic field pulses expand the circular magnetic domains. With DMI, different velocities are observed for DW propagating along or opposite to the in-plane field direction and for up/down and down/up DWs. Here, the DMI acts as an effective in-plane magnetic field $\mu_0 H_{DMI} = D_S/(M_S t \Delta)$ with opposite directions for up/down and down/up domain walls. As a result, the DMI shifts the minimum of the velocity by $\pm H_{DMI}$. Thus, the DMI field can be

measured from the dependence of the DW velocities on the in-plane external fields. Figure 6.16b shows the domain wall velocity vs in-plane magnetic field for up/down (red dots) and down/up (black dots) domains. From the average of the minima of both curves, a DMI field $\mu_0 H_{DMI} = 9 \pm 1$ mT is extracted which gives $D_S = 0.27 \pm 0.06$ pJ/m. Although the value is larger than the one measured by BLS, both values fit within error bars.

The DW dynamics measurements were performed by Van Tuong Pham at the Institut Néel in Grenoble, France.

6.7.4 Ferromagnetic resonance measurements

The magnetic damping was measured by ferromagnetic resonance (FMR) for different thickness of the FeCoB free layer (see Figure 6.17). Samples in in-plane configurations were required for such measurements and a linear fit was performed to extrapolate the damping for the relevant thickness value, namely, $\alpha = (1.6 \pm 0.1) \cdot 10^{-2}$, in line with the results from DW dynamics. The intercept at zero gives the bulk damping value $\alpha_0 = 1.14 \cdot 10^{-2}$.

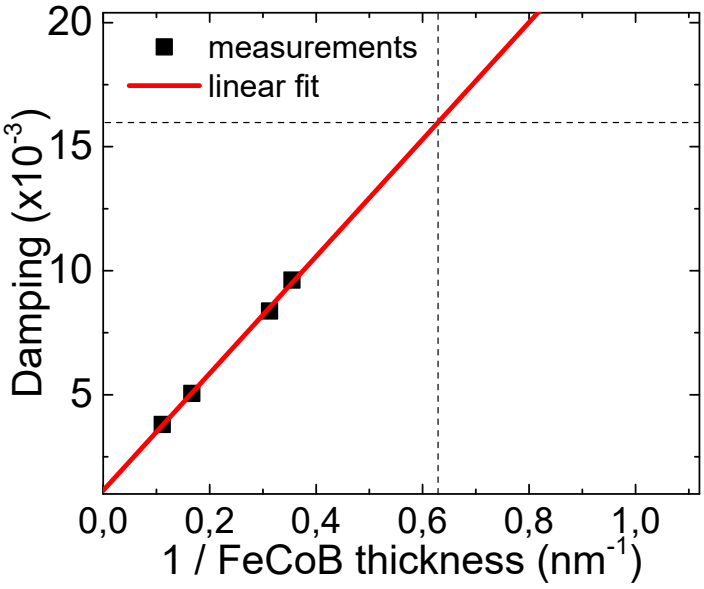

Fig. 6.17: Ferromagnetic resonance measurements | Magnetic damping measurements for different FeCoB thickness measured by FMR showing a linear dependence of the damping with respect to the inverse of the film thickness.

The FMR measurements were performed by Mohamed Belmeguenai at the LSPM laboratory in Villetaneuse, France.

6.8 Lorentz Transmission Electron Microscopy observations

To characterize the chirality of the domain walls in the stack, we performed Fresnel mode Lorentz transmission electron microscopy imaging. The stack was the same as the one used for characterization, namely a stack similar to the MTJ, in which only the free FeCoB layer was magnetically active and was deposited onto homemade 30-nm thick SiN membranes. Experiments were carried out on a Titan Ultimate microscope operated around 200 kV. The imaging was made with a Lorentz lens, the objective lens was fully characterized with a Hall probe chips mounted onto a multi-contact holder and the acquisition was realized with a OneView Gatan camera. Acquisition time has been extended to 1 min for each image with the help of image stabilization [228] to increase Signal-to-Noise Ratio (SNR).

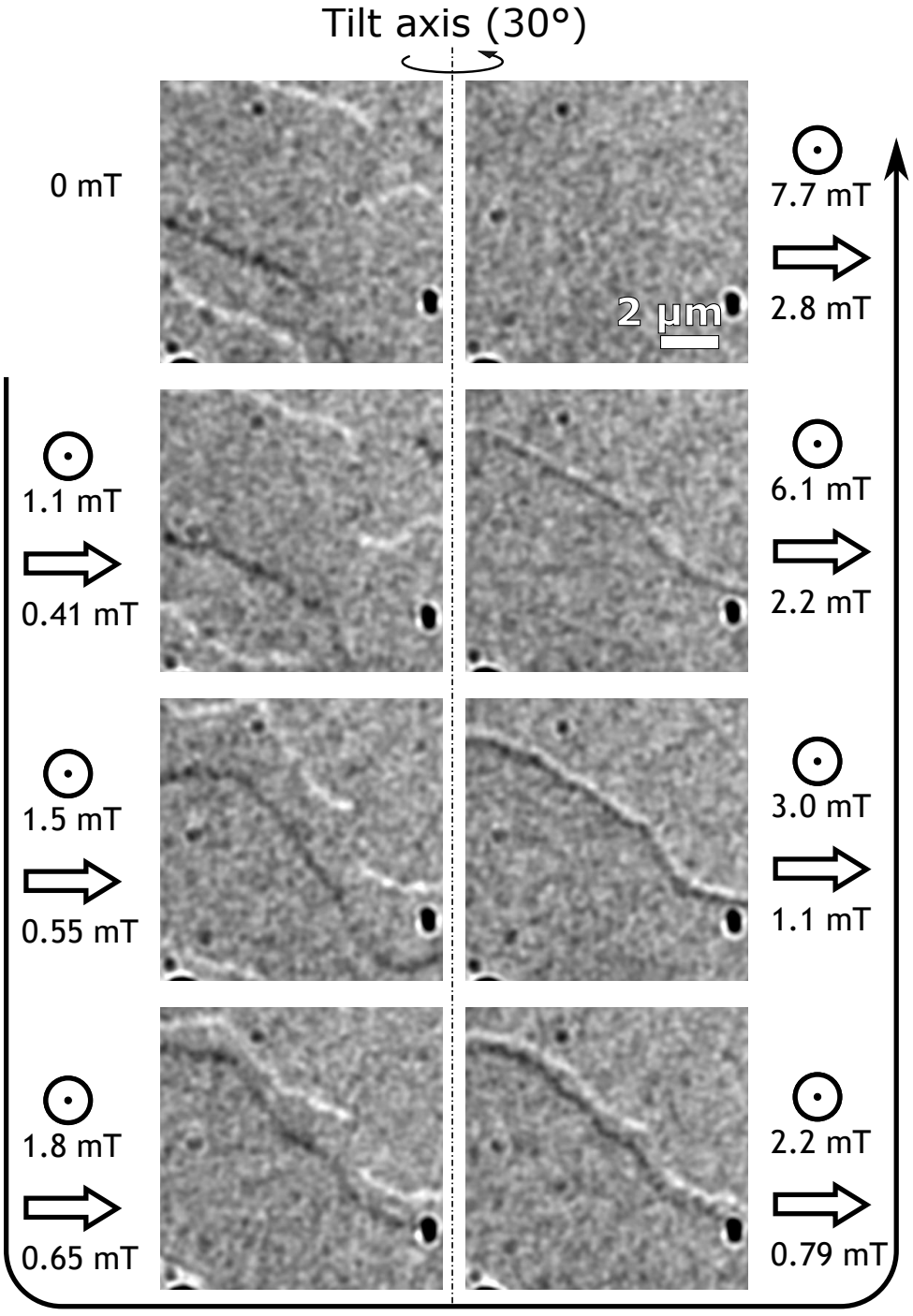

Fig. 6.18: Magnetic field series observation in TEM | Fresnel magnetic field series of the saturation of the stack. Defocus has been measured at 33 mm. Values of magnetic field both in- and out-of-plane are given according to the measured tilt of 30°. Images are 10x10 µm^2 in size.

Figure 6.18 displays a serie of Fresnel mode images of magnetic domains for increasing field applied using the microscope objective lens and realized with a tilt of the sample around 30° and a defocus measured at 33 mm. The sample tilt allows us to provide Fresnel contrast from the projection of domains magnetization perpendicular to the electron wave propagation vector and thus detect the domain walls, independently of their chirality. A multidomain state is observed at remanence with a typical domain size of several µm. When increasing the magnetic field, a gradual narrowing of the domain in the center of the image is noticed, which eventually annihilates for a perpendicular field of 7.7 mT.

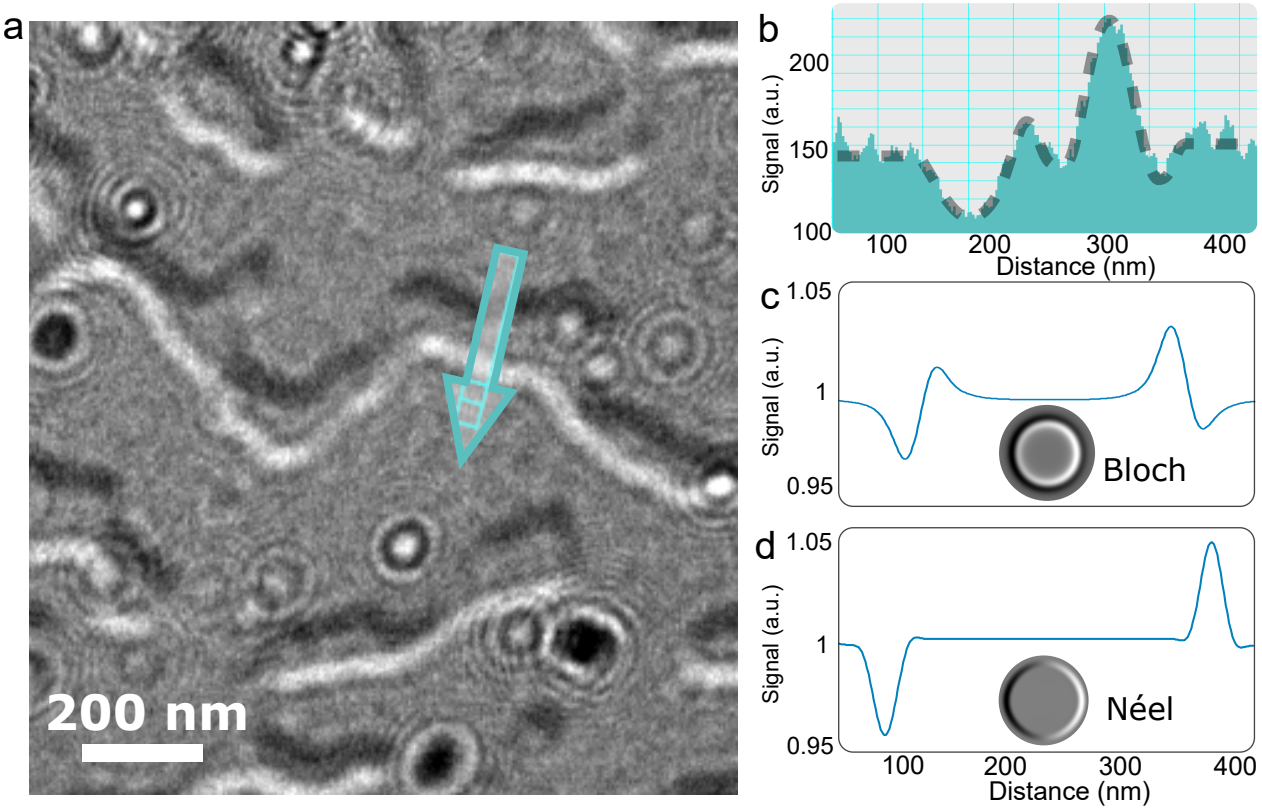

Fig. 6.19: Micromagnetic simulations for TEM analysis | Fresnel contrast obtain at 30° of tilt with a defocus of 85 mm (inset is the same image obtained at 0° of tilt). The experimental contrast profile of the dashed area is shown on top of the right column and compared to the profiles simulated for Néel and Bloch magnetic bubble configuration below (2D contrast displayed as inset under the curves).

At first sight, no Fresnel contrast can be seen at 0° of sample tilt thus leading to a Néel wall configuration [229]. However, knowing that 1.04 nm of Co layer would lead to a phase shift slope of less than 10 mrad/nm, it would be rather impossible to detect such low phase shift for a few nm-width wall (overestimating with a Bloch core perpendicular to the electron wave over the full thickness). Furthermore, we noticed a potential asymmetry in the Fresnel contrast of the domain wall at 20° of tilt that could only be explained by the presence of a Bloch component inside the wall.

We performed simulations of the Néel and Bloch configuration Fresnel contrast based on the simple assumption of a pure phase object obtained from micromagnetic simulation. We compare such contrast with our experimental profile in Figure 6.19. The asymmetry in the conventional contrast obtained with high sample tilt (due to projection of domains magnetization perpendicular to the electron wave propagation vector) is only observable when a Bloch wall is inserted inside the micromagnetic model. Still such evidence has to be considered with precaution as one has to consider also the Fresnel fringes associated to the beam overlap that could be associated to an asymmetry in such small SNR contrast.

To confirm our finding we proceeded to a careful analysis of the contrast around 0° of tilt by removing the background contrast obtained in our case with a full saturation of the layer. The sub-pixel alignment of the two images was eventually preformed manually. Despite the poor SNR even with our long time exposure, we were eventually able to observe a pure Bloch wall signal [230] as seen in Figure 6.20. It is worth noticing that the contrast level of such wall is just above the noise range. Such double analysis seems to confirm the presence of Bloch walls in our stack.

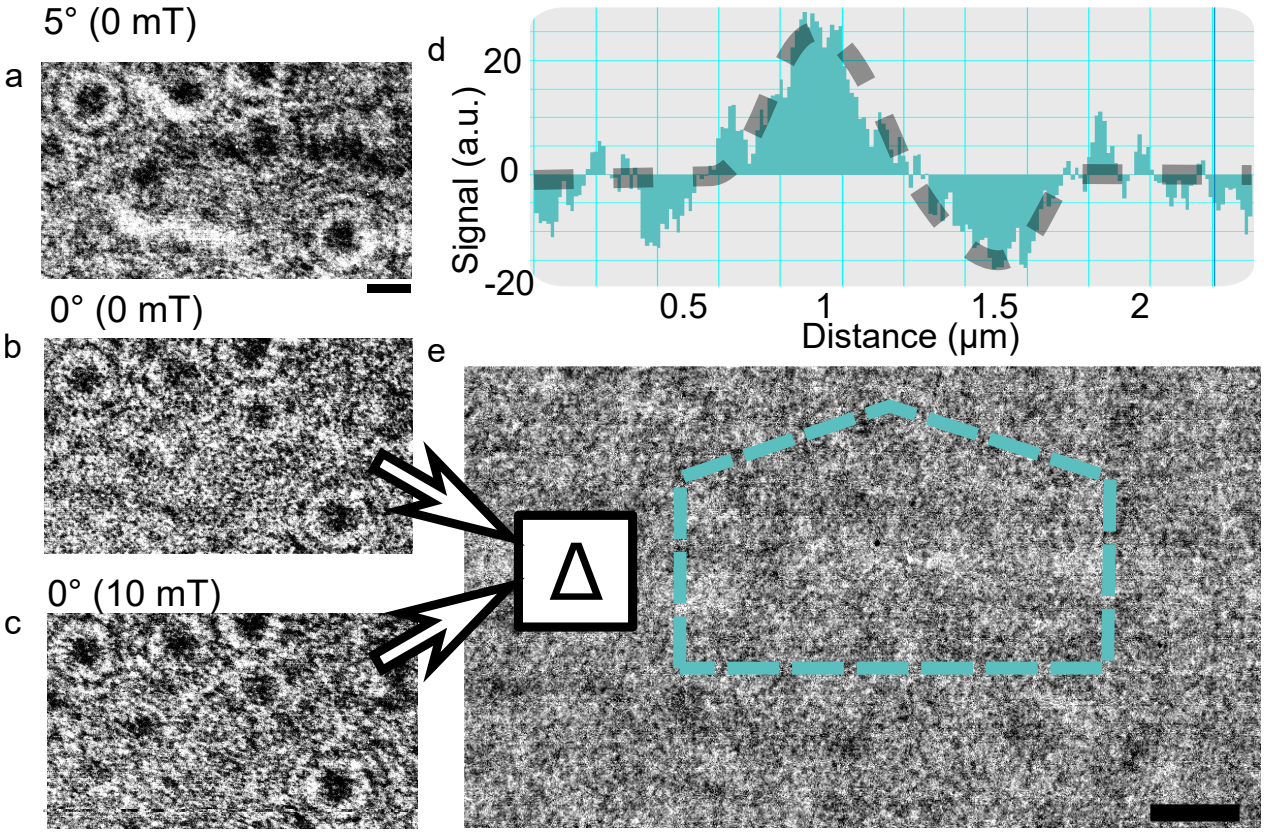

Fig. 6.20: TEM observation with background subtraction | Left column displays (from up to down respectively) the Fresnel contrast at 5° with a defocus of 20 mm, the same area with 0° of tilt, the same area with 0° of tilt and under 10 mT out-of-plane. Defects in the layer act as guide to the eye for location and defocus adjustment. Right column displays (from bottom to top respectively) the difference of the two images acquired at 0° of tilt with and without magnetic field, the profile took at the same location of the wall observed with 5° of tilt and averaged over the length of the wall. The Bloch wall signature is emphasised with a guide to the eye on the profile.

The LTEM experiments were performed by Aurélien Masseboeuf in Plate-Forme de Nano-Caractérisation (PFNC) laboratory in Grenoble, France.

6.9 Micromagnetic simulations

To better understand the physics behind our experiments, we carried out micromagnetic simulations using Mumax3 [231,232] software. Regarding the geometry of the micromagnetic system, we chose a 256 × 256 × 1 u^3 field with cell sizes of 1.95 × 1.95 × 1.05 nm^3, having as a result a 500 × 500 nm^2 field in which a cylindrical geometry was defined (see Figure 6.21).

The magnetic parameters chosen for this study are M_S = 1.63 MA/m, $\mu_0 H_K$ = 30 mT, D = −0.148 mJ/m^2 and VCMA slope = 16.2 mT/V (also shown in Table 6.1). These parameters were derived experimentally as explained in Section 6.7. The exchange interaction parameter A = 12 pJ/m was used [233]. In order to mimic the VCMA effect, the applied voltage is assumed to decrease the PMA. The STT is neglected, due to the low current density injected (maximum $7 \cdot 10^9$ A/m^2) owing to the large R·A product in our system. Finally, in order to make these simulations more realistic, we also considered the stray field that is originated from both the Pt/Co repetitions in the SAF and the fixed FeCoB layer. This was simulated independently using the experimental parameters and assuming that the different layers composing the SAF have opposite magnetization aligned along z.

As observed experimentally, we see that the simulations reproduce the nucleation of the skyrmion induced by the voltage in a MTJ. This sheds light on the reversal mechanism. Figure 6.21 shows different snapshots of the magnetization in a 500 nm dot during the application of a 10 ns voltage pulse. The nucleation proceeds by the creation of a transient curling state due to the decrease of the magnetic anisotropy (t = 4 ns), followed

by the nucleation of a ring with reversed perpendicular magnetization, a configuration which is favored by the stray field energy. When the pulse is turned off, the ring increases in size and leads to a single bubble, which eventually grows to its final size. Micromagnetic simulations predict a Bloch skyrmion chirality owing to the low DMI in the stack, in agreement with Lorentz TEM measurements (Section 6.8).

t_{FeCoB} (nm)	1.59
t_{dead} (nm)	0.51
$\gamma/(2\pi)$ (GHz T^{-1})	29.6
M_S (MA m^{-1})	1.63 ± 0.19
$\mu_0 H_K$ (mT)	35 ± 5
α_{FMR}	0.016 ± 0.001
D^{BLS} (mJ m^{-2})	-0.139 ± 0.069
A (pJ m^{-1})	12
dH/dV (mT V^{-1})	16.2

Table 6.1: Summary of the parameters for the MTJ stack | Sample thickness t_{FeCoB}, dead layer t_d, gyromagnetic ratio γ, saturation magnetization M_S, anisotropy field $\mu_0 H_K$, magnetic damping parameter α, DMI constant D, exchange constant A and the VCMA slope.

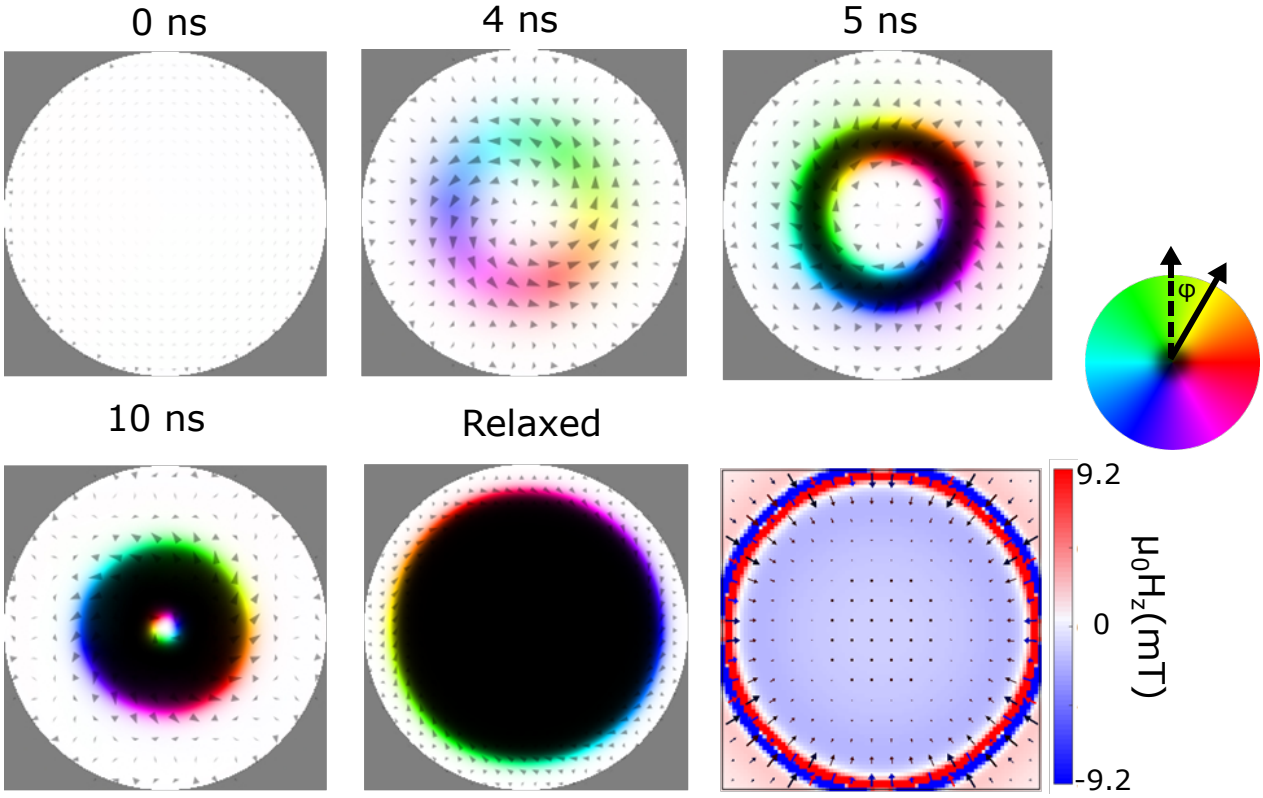

Fig. 6.21: Micromagnetic simulation of the skyrmion nucleation | Spatial distribution of the spin texture at different time in a 500 nm diameter dot. A voltage pulse of -2.15 V is applied at $t = 0$ and is switched off at 10 ns. Black/white is for the magnetization pointing downward/upward. The color wheel illustrates the in-plane color map. The bottom right panel shows the calculated stray field from the SAF layer, with the reference layer magnetization being parallel to the free layer one.

6.9.1 Simulations for 500 nm dots

We also studied the dependence on the external out-of-plane magnetic field for different bias voltage values. Figure 6.22a displays the evolution of the skyrmion size with a varying magnetic field. At large magnetic fields, the skyrmion diameters are exceeding 400 nm and they show a small susceptibility to the magnetic field. This can be related to the proximity of the pillar edge. Conversely, smaller skyrmions exhibit a more notable susceptibility to both the magnetic field and bias voltage (see Figure 6.22a and inset).

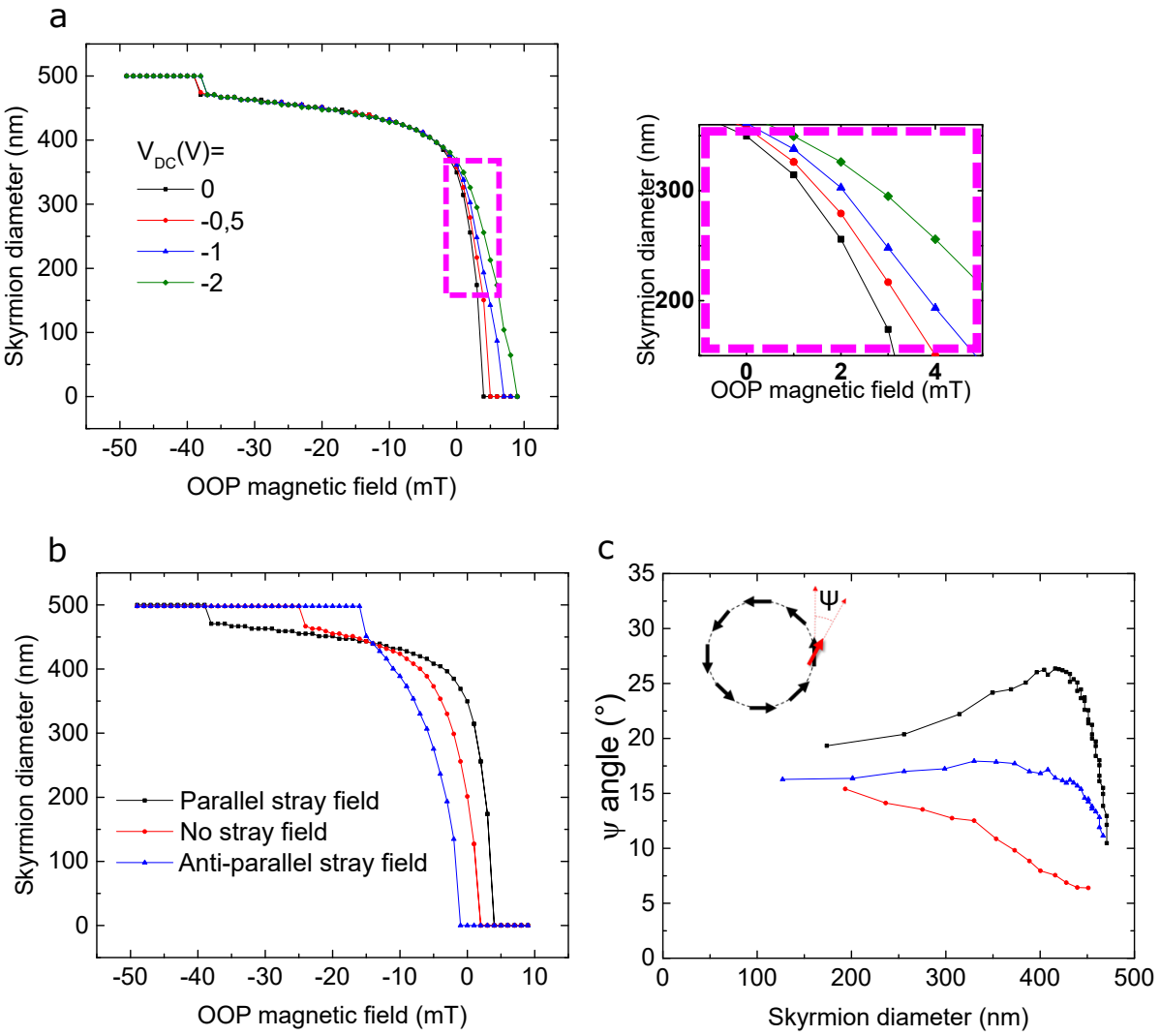

Fig. 6.22: Micromagnetic simulation of skyrmion manipulation by external magnetic field and DC voltage in a 500 nm diameter dot | **a** Skyrmion diameter vs out-of-plane magnetic field for different bias voltage. **b** Skyrmion diameter vs out-of-plane magnetic field without stray field from the SAF (red curve), with stray field from the SAF, the FeCoB layer magnetization being aligned antiparallel to the skyrmion core magnetization (black curve, labelled "Parallel stray field") and parallel to the skyrmion core magnetization (blue curve, labelled as "Anti-parallel stray field"). **c** Domain wall angle of the skyrmion vs skyrmion diameter for different stray field configuration. The angle is measured with respect to the Bloch DW configuration (see inset).

The simulations also reveal that the stray field from the SAF has a large impact on the range of magnetic field where the skyrmion is stable. This range increases (decreases) when the SAF stray field is in P (AP) configuration, corresponding to the fixed layer magnetization aligned AP (P) to the skyrmion core magnetization respectively (see Figure 6.22b).

Finally, the tilt of the DW magnetization was also studied as a function of the skyrmion diameter for different stray field configurations (Figure 6.22c). A small dependence of the DW magnetization angle is observed on the skyrmion diameter and on the SAF orientation, which can be explained by the impact of the stray field from the edges and from the SAF.

6.9.2 Simulations for 2 µm dots

As mentioned earlier, 2 µm diameter dots exhibit larger susceptibility to the external magnetic field than smaller ones, which can be attributed to the shallower potential resulting from the edge stray field as the dimensions increase. In addition, a significant susceptibility to gate voltage is observed as depicted in Figure 6.7. Figure 6.23 shows corresponding micromagnetic simulations using experimental parameters to study these external excitations. The dependence of the diameter on the external out-of-plane magnetic field for different bias voltage values is shown in Figure 6.23a. For large skyrmions, little diameter variation against the external magnetic field is noticed (for negative fields), whereas there is a significant dependence for smaller skyrmions and they eventually collapse for small increase of positive field. Similarly to the findings for the 500 nm diameter dots, the stray field from the SAF has a large impact on the range of magnetic field where the skyrmion is stable. The range of stability expands (contracts) when including the SAF stray field in the P (resp. AP) configuration (see Figure 6.23b), illustrating the impact of the stray field presence and orientation for a given voltage value (0 V in this case). A small dependence of the DW magnetization angle on the skyrmion diameter is also observed, which depends on the stray field orientation (see Figure 6.23c).

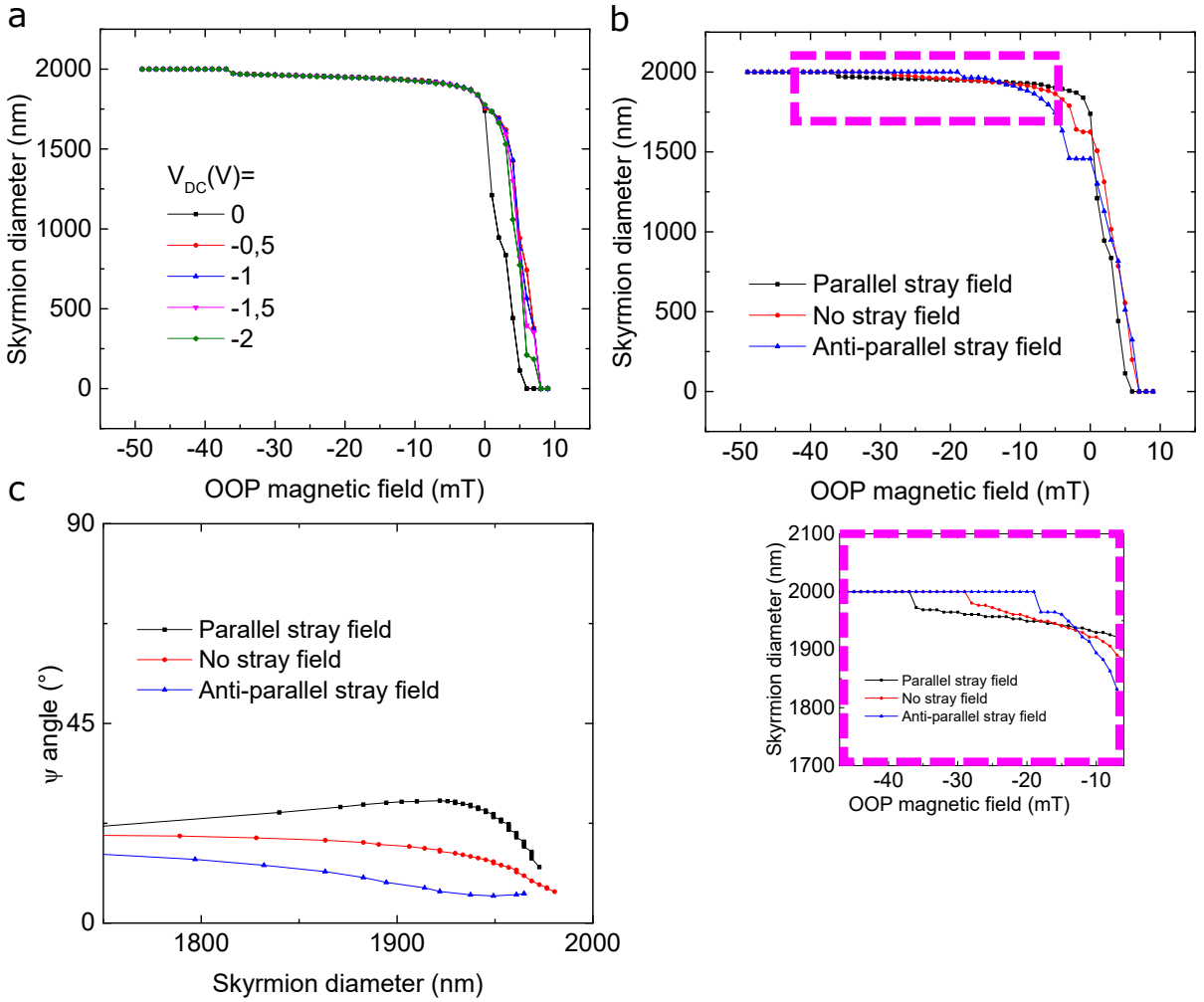

Fig. 6.23: Micromagnetic simulation of skyrmion manipulation by external magnetic field and DC voltage in a 2 µm diameter dot | **a** Skyrmion diameter vs out-of-plane magnetic field for different bias voltages. **b** Skyrmion diameter vs out-of-plane magnetic field without stray field from the SAF (red curve), with stray field from the SAF, the FeCoB layer magnetization being aligned antiparallel to the skyrmion core magnetization (black curve, labeled "parallel stray field") and parallel to the skyrmion core magnetization (blue curve, labeled as "anti-parallel stray field"). For clarity, the inset is added to see the different magnetic field values at which the skyrmion collapses. **c** Domain wall angle of the skyrmion vs skyrmion diameter in the presence of stray field in parallel configuration (black curve), without stray field (red curve) and stray field in anti-parallel configuration (blue curve). The angle is measured with respect to the Bloch DW configuration, as earlier mentioned.

6.10 Conclusion

To conclude, we have demonstrated the electrical detection and electrical nucleation and annihilation of a single skyrmion in a MTJ using operando magnetic microscopy experiments. The nucleation of the skyrmion was enabled by voltage excitations exploiting the VCMA effect and leads to a large variation of the MTJ resistance (467 Ω) owing to the large TMR of the junction. Micromagnetic simulations using experimental parameters reproduce the nucleation process well and show that the nucleation proceeds via the transient creation of a curling state. The skyrmion can be manipulated using voltage excitations and the external magnetic field, which leads to tunable intermediate resistance states. Our results mark major milestones for skyrmion-based devices, demonstrating unambiguously the readout and low power write operations in a single device. Furthermore, they open promising pathways for low power multilevel memory and neuromorphic skyrmionic devices, leveraging the tunable manipulation of the skyrmion state hosted in the MTJ using low power voltage excitation.

Chapter 7

Summary and perspectives

7.1 Summary

The following lines are meant to provide a comprehensive summary of the work done during the last three years. We insisted on the relevance of the magnetic skyrmions and the skyrmionic research field for the next generation spintronic devices. Important steps towards the practical implementation of skyrmion-based technologies were performed recently with the demonstration of room temperature magnetic skyrmions and their current induced manipulation. However, several important challenges still remain regarding their stabilization, low-power nucleation, current-induced dynamics, as well as electrical detection.

One challenge is related to the limited skyrmion minimal size and maximal velocity resulting from their magnetic moment and topological charge. Antiferromagnetic skyrmions allow to lift these limitations owing to their vanishing magnetization and net zero topological charge, leading to small skyrmions with fast (> 1 km/s) motion without skyrmion Hall effect. However, one drawback of the AF skyrmions is their vanishing magnetic moment, which makes their nucleation and detection challenging. To address this challenge, we considered synthetic antiferromagnets (SAF), which combine important advantages to stabilize AF skyrmions, including tunable properties and compatibility with spintronic devices.

A first objective of this thesis was to reliably nucleate SAF skyrmions with current and to shed light on the nucleation and annihilation dynamics. To this end, we optimized a Pt/Co based multilayer structure fulfilling all the requirements to host SAF skyrmions. Using local current injection via a metallic tip, we were able to demonstrate the reproducible nucleation/annihilation of SAF skyrmions using scanning transmission x-ray microscopy (STXM). We exploited the high reproducibility of the process to perform pump-probe time-resolved STXM experiments. It allowed us to observe the nucleation and relaxation process with very high time (125 ps) and spatial resolution (50 nm). The experiments showed that the nucleation occurs via the formation of a small nucleus below the metallic tip, followed by a fast expansion during the pulse injection and a slower relaxation when the pulse is turned off. The maximal diameter is found to be proportional to the current pulse amplitude.

To better understand the experimental results, we performed micromagnetic simulations using experimental parameters as well as analytical modelling. Taking into account the non-uniform current induced spin orbit torque under the tip, micromagnetic simulations reproduce qualitatively the current induced nucleation and annihilation processes. However, a current density much larger than in experiments is needed, suggesting a significant role of heating in the nucleation process. Analytical modelling and simulations of the skyrmion collapse after the current injection were also performed and compared to the time resolved experiments. The model and simulations predict a collapse faster than in experiments, which can be attributed to a reduced magnetization and exchange interaction induced by local heating.

Still involving SAF structures, the second part of this thesis focused on a new approach for the skyrmion nucleation and stabilization. In FM systems, skyrmions can be easily nucleated from a stripe domain state by applying an external magnetic field along the easy axis. This strategy cannot be applied to SAF owing to their vanishing magnetic moment. An alternative approach is to couple one of the layers to an antiferromagnet. This leads to an internal effective magnetic field via the exchange bias effect, which allows the spontaneous nucleation of the skyrmions in the SAF. An additional advantage of a coupling to an antiferromagnet lies in their lower sensitivity to external fields and field perturbations, providing additional thermal stability to the skyrmions.

In this study, SAF stacks exchanged coupled to an antiferromagnet layer were optimized to stabilize

magnetic skyrmions and achieve their observation via STXM microscopy. First STXM experiments showed that, surprisingly, the exchange bias can be manipulated using the x-ray beam. We leveraged this property to nucleate skyrmions in exchange biased SAF using the x-ray beam. Layer resolved XMCD-STXM observations allowed us to demonstrate the antiferromagnetic alignment of such stacks, and further confirm the stabilization of SAF skyrmions exchange biased to IrMn. Using the x-ray beam under different magnetic field conditions, the SAF skyrmions can be imprinted or erased by manipulating the exchange bias. Our results demonstrate the stabilization of SAF skyrmions at zero field and room temperature in exchange biased SAF. The possibility to manipulate the exchange bias field using x-rays opens a new path to write spin textures in antiferromagnetic stacks.

Another important challenge I addressed during the second half of my thesis is the electrical detection and nucleation of skyrmions in a magnetoresistive device, which is a crucial step for skyrmions based applications. At the beginning of my thesis, the electrical detection of a single magnetic skyrmion had only been demonstrated using anomalous Hall effect. However, the output signal, a few mω/skyrmion, was too low for applications. A much larger readout signal is expected by exploiting the tunnelling magnetoresistance (TMR) effect in a magnetic tunnel junction (MTJ).

In this work, we employed x-ray magnetic microscopy experiments combined with in-situ electrical magneto-transport measurements to unambiguously demonstrate the electrical detection of a single magnetic skyrmion in an MTJ, as well as its low energy nucleation/annihilation using a gate voltage. This was made possible through the fabrication of electrically contacted MTJs on an ultrathin Si_3N_4 membrane, enabling their observation using STXM. The nucleation was driven by the voltage control of the magnetic anisotropy (VCMA) in the MTJ and led to a large variation of the MTJ resistance (470 Ω), owing to the large TMR of the junction.

To better understand the experimental observations, we performed a full characterization of the magnetic and transport properties of the devices as well as micromagnetic simulations. The later reproduced the experimental results well and showed that the nucleation occurs via a transient curling state. Furthermore, we showed that the skyrmion can be manipulated using both external magnetic field and gate voltage. The VCMA effect allowed us to achieve a nucleation energy down to 30 pJ, a value which could be easily lowered by engineering the MTJ tunneling barrier. Our results mark major milestones for skyrmion-based devices, demonstrating unambiguously the readout and low power write operations in a single device.

7.2 Perspectives

7.2.1 Manipulation of the antiferromagnetic order using light

There are intriguing paths to explore regarding the manipulation of IrMn using light. Firstly, there is the need to further investigate the mechanisms behind the exchange bias manipulation. This means understanding the role of heat and angular momentum transfer in FM/AFM interfaces and disentangling those effects. Additionally, employing atomistic spin calculations would definitely provide valuable insights. In particular, understanding the imprint of skyrmions through exchange bias [234]. It is plausible that atomistic spin calculations enable the reproduction of this imprint, incorporating local thermal excitations. Secondly, the effect of light on the antiferromagnetic order offers opportunities to write spin textures into thin films. Such advancements hold potential for applications in fields like logic and magnonics.

7.2.2 Skyrmion racetrack memory

During the thesis, we worked on the individual functionalities of the skyrmion racetrack memory, exploring their nucleation, the distinct readout and manipulation processes in skyrmions. The ultimate goal is to gather these varied capabilities into a unified device that could kick-start the skyrmion nucleation, guide their motion through currents and flawlessly execute readout operations. This calls for the creation of three-terminal devices, featuring the magnetic tunnel junction (MTJ) fabricated and integrated on top of the magnetic nanotrack. Nevertheless, this technical step also presents challenges, as the nanofabrication process can impact on the magnetic properties of the layer that would host the skyrmions [235]. An additional problem to address is also pinning, as detected in our experiments with MTJs.

7.2.3 Fast motion of SAF skyrmions

The fast dynamics of SAF skyrmions has been a pending subject since their proposal. Predicted to exceed the 1 km/s barrier, the material engineering for the optimization of the magnetic parameters namely PMA, DMI, SOT, the RKKY coupling and full magnetic compensation is crucial. During my PhD thesis, we have

made solid progress on this. We targeted Pt/Co/Ru stacks with low PMA and characterized the SOT and DMI. The key here has been to achieve full compensation. This can be seen in Figure 7.1a, where we displayed how the velocity gets enhanced when we reach the compensation point with respect to the FM coupling. The dependance on the size of SAF skyrmions and their enhancement on the velocity is also notable. Even if small skyrmions have been predicted in SAF, their stabilization adds additional challenges to optimize the stack.

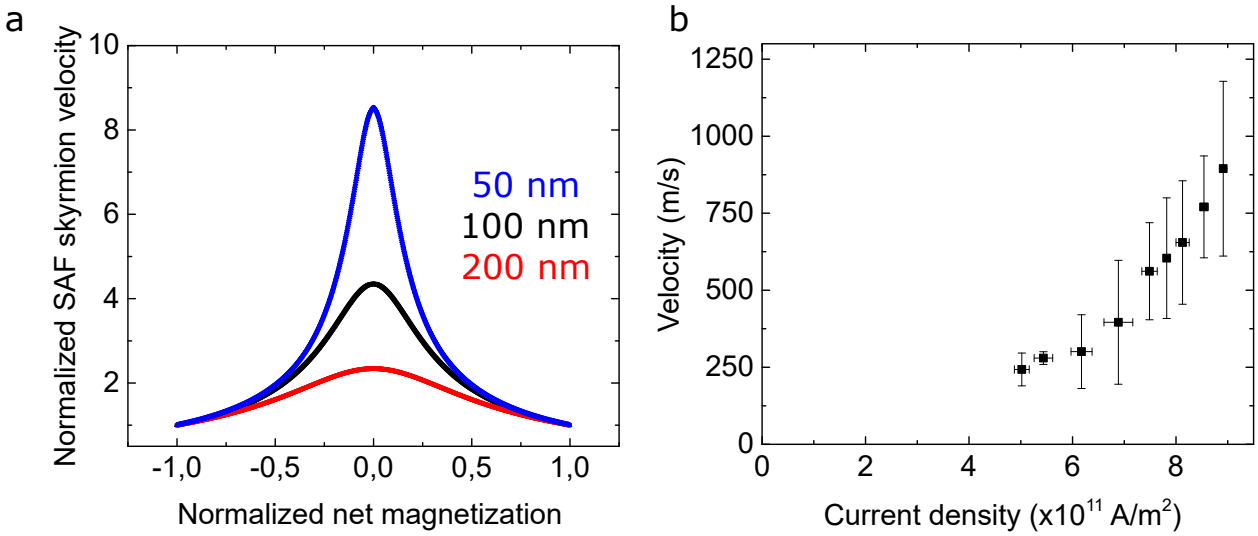

Fig. 7.1: Dynamics of SAF skyrmions | **a** Enhancement of velocity depending on the magnetic compensation for different SAF skyrmion radius. The free parameters for such enhancement are: $M_S = 1.43$ MA/m, $\alpha = 0.1$, $\Delta = 21$ nm. **b** SAF skyrmion velocity with respect to the applied current density.

In our group we succeeded in moving the SAF skyrmions driven by SOT at high speed without skyrmion Hall effect using MFM (see Figure 7.1b). I did not perform the MFM experiments that showed their fast dynamics. This work was done by Van Pham Tuong, who worked as a post-doc in our group. I contributed to optimize the stack, in the synchrotron observations and in the characterization of some magnetic parameters. The typical skyrmion diameters were around 200 nm, which means that regarding scalability there is potential to even improve the complex SAF dynamics. The large pinning related to the Co layers could also be improved choosing other amorphous materials such as CoFeB.

7.2.4 Skyrmion-based logic gates

The information technology (IT) industry is currently facing significant difficulties regarding power dissipation and energy consumption. In addition, the historical trend of the Metal-Oxide-Semiconductor technologies towards miniaturizing the transistors is now becoming rather a problem than a solution. Furthermore, volatile on-chip memory modules contribute to a static power consumption. In such scenario, logic-in-memory architectures, fusing non-volatile memories and logic circuits, offer potential solutions, promising ultra-low power and shorter interconnection delays.

Magnetic skyrmions hold promise as building blocks for these technologies. In particular, Sisodia *et al.* proposed a programmable skyrmion-based logic-in-memory device controlling their confinement and channeling by anisotropy energy barriers in SAF [149]. This device is based on the mutual repulsion between skyrmions. The demonstration of the controlled nucleation of skyrmions in SAF and their fast manipulation using electrical current, combined with the possibility to pattern locally the magnetic properties, using for instance light ion irradiation as shown in Spintec [236], opens a door for the experimental demonstration of such skyrmion-based logic-in-memory concept.

7.2.5 Non-conventional computing based on magnetic skyrmions

The essential building blocks of our digital world rely on high performance integrated circuits. One of the limiting factors is the Von Neumann bottleneck, i.e the 'traffic jam' in our computers. The memory elements and the processing units need a permanent data exchange, consuming a large amount of energy. This issue is particularly relevant when solving artificial intelligence tasks based on artificial neural networks where the

constant shuffle of data between the artificial synapses (i.e memory) and neurons (computing units) leads to a dramatic rise in energy and delay. To solve this issue, we ideally are looking forward to integrating artificial neurons and synapses close together, mimicking our energy-efficient brains. In addition, the training algorithms of high-performance integrated circuits are complex and demand powerful data centers.

In this scenario, reservoir computing (RC) emerges as a promising paradigm to address these challenges [237]. In particular for spintronics, there exist different spin systems as candidates for RC. A major breakthrough arrived with the work of Torrejon *et al.* with nanoscale spintronic oscillators [238]. Other spin systems like skyrmions are potential candidates for small and low-power reservoir devices. Skyrmions were recognized as potential storage systems to achieve efficient and fast cognitive computing with ultra-low consumption [152]. Using skyrmions in MTJs is beneficial due to the advantages of spintronic devices and materials. They are compatible with CMOS technology, their properties can be fine-tuned and we proved their unambiguous electrical detection in Chapter 6.

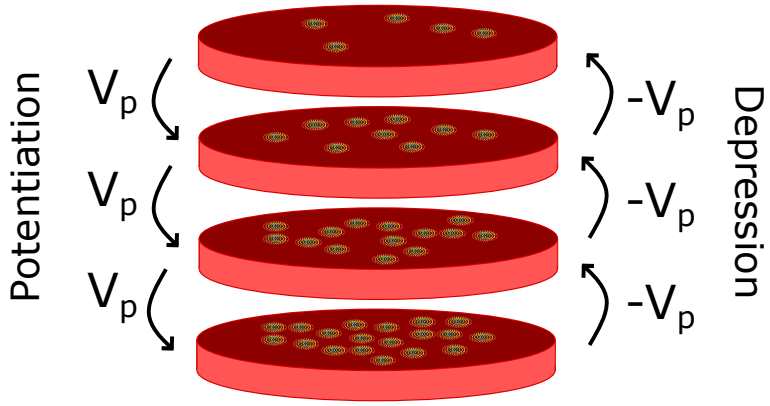

Fig. 7.2: Magnetic skyrmion-based artificial synapses in MTJ | Schematic representation of a free layer in a MTJ with a lattice of skyrmions. In such a synapse, the weights are proportional to the number of skyrmions and can be tuned by external excitations such as voltage pulses or currents. In the image, the number of skyrmions is augmented (potentiation) or reduced (depression) with voltage pulses of opposite polarity. The resistance state of the MTJ would vary accordingly.

Other topological spin textures like skyrmions lattices would be ideal candidates for skyrmion-based artificial synapses (see Figure 7.2). In this case, the number of skyrmions would act as synaptic weights. The tuning of these weights could be performed by applying voltage pulses. Expanding this to arrays of MTJs is also possible. The reading is done by TMR and the resistance contribution of each skyrmion would be equivalent.

Appendix

Contents

A.1 Skyrmion number 108
A.1.1 From LLG to Thiele equation 110
A.1.2 Thiele equation 112
A.2 Thiele equation with the force due to the DL-SOT 113

The appendix is wrote in order to provide a more explicit skyrmion number calculation. Starting from the LLG equation, we also derive the Thiele equation. Lastly, we include the SOT term in the Thiele equation to compute the different terms that appear in the Thiele equation.

A.1 Skyrmion number

The skyrmion number is defined as:

$$N_{Sk} = \frac{1}{4\pi} \iint \vec{m} \cdot \left(\frac{\partial \vec{m}}{\partial x} \times \frac{\partial \vec{m}}{\partial y} \right) dxdy. \tag{A.1}$$

Here, $\vec{m}$ is the reduced magnetization vector and the integration is performed along all the 2-D space [87,239]. In the saturated FM state, note that all the spins are parallel, consequently having $(\partial \vec{m}/\partial y) = (\partial \vec{m}/\partial y) = 0$ and $N_{Sk} = 0$. For the computation of the skyrmion number in an FM environment, we will conveniently use polar coordinates (r, φ), such that $x = r\cos\varphi$ and $y = r\sin\varphi$ where the value of r goes from 0 to ∞ and φ is varying from 0 to 2π. A unit sphere contains the reduced magnetization vector $\vec{m}$ described by the unitary spherical coordinates $(1, \Phi(\varphi), \theta(r))$, so that $\vec{m}$ can be written as $\vec{m} = (\cos\Phi\sin\theta, \sin\Phi\sin\theta, \cos\theta)$. The angles are defined in Figure A.3.

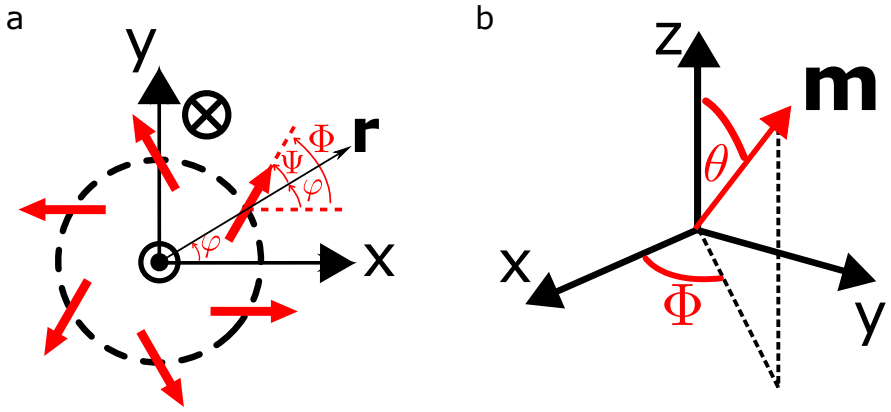

Fig. A.3: Scheme of angles for skyrmion number calculation | **a** Definition of magnetisation angles with respect to the radial direction. **b** Polar angles.

θ is defined as the angle between the vertical z axis and the magnetization vector. This means that it only depends on the coordinate r and not on φ due to the cylindrical symmetry of the skyrmion. Note that when $r \to \infty$, $\theta \to \pi$. Furthermore, the in-plane magnetic variable Φ does not depend on r, but only on φ. For skyrmionic bubbles this is not strictly true due to their big core, but since it does not contribute to the skyrmion number[1], we will go on with this assumption. The present calculation requires some tedious algebra in case one computes explicitly term by term the components of $\vec{m} \cdot (\partial \vec{m}/\partial x \times \partial \vec{m}/\partial y)$. In order to make it less tedious the partial derivatives of x and y can be converted into polar coordinates using the chain rule:

$$\frac{\partial}{\partial x_i} = \frac{\partial r}{\partial x_i}\frac{\partial}{\partial r} + \frac{\partial \varphi}{\partial x_i}\frac{\partial}{\partial \varphi}. \tag{A.2}$$

After a computation, we obtain the following components that can be plugged in the skyrmion number integral: $\partial r/\partial x = \cos\varphi$, $\partial r/\partial y = \sin\varphi$, $\partial\varphi/\partial x = -(\sin\varphi)/r$ and $\partial\varphi/\partial y = (\cos\varphi)/r$.

Let us check this step: we know from the polar units that $r = \sqrt{x^2+y^2}$ and $\tan\varphi = y/x$. So this way we can obtain the following relations:

$$\frac{\partial r}{\partial x} = \frac{1}{2}\frac{2x}{\sqrt{x^2+y^2}} = \frac{x}{r} = \cos\varphi, \tag{A.3}$$

$$\frac{\partial r}{\partial y} = \frac{1}{2}\frac{2y}{\sqrt{x^2+y^2}} = \frac{y}{r} = \sin\varphi, \tag{A.4}$$

$$\frac{\partial \varphi}{\partial x} = -\frac{y}{x^2}\frac{1}{(y/x)^2+1} = -\frac{y}{x^2+y^2} = -\frac{y}{r^2} = -\frac{\sin\varphi}{r}, \tag{A.5}$$

$$\frac{\partial \varphi}{\partial y} = \frac{1}{x}\frac{1}{(y/x)^2+1} = \frac{x}{x^2+y^2} = \frac{x}{r^2} = \frac{\cos\varphi}{r}. \tag{A.6}$$

[1] If the spin distribution does not contain singularities.

So that:

$$\frac{\partial}{\partial x} = \frac{\partial r}{\partial x}\frac{\partial}{\partial r} + \frac{\partial \varphi}{\partial x}\frac{\partial}{\partial \varphi} = \cos\varphi \frac{\partial}{\partial r} - \frac{\sin\varphi}{r}\frac{\partial}{\partial \varphi}, \tag{A.7}$$

$$\frac{\partial}{\partial y} = \frac{\partial r}{\partial y}\frac{\partial}{\partial r} + \frac{\partial \varphi}{\partial y}\frac{\partial}{\partial \varphi} = \sin\varphi \frac{\partial}{\partial r} + \frac{\cos\varphi}{r}\frac{\partial}{\partial \varphi}. \tag{A.8}$$

It is possible to do a similar chain rule procedure with the unitary magnetization vector $\vec{m}$, such that, $\frac{\partial \vec{m}}{\partial r} = \frac{\partial \theta}{\partial r}\frac{\partial \vec{m}}{\partial \theta}$ and $\frac{\partial \vec{m}}{\partial \varphi} = \frac{\partial \Phi}{\partial \varphi}\frac{\partial \vec{m}}{\partial \Phi}$. So, we convert the partial derivatives of x and y into θ and Φ. Altogether:

$$\frac{\partial \vec{m}}{\partial x} = \frac{\partial r}{\partial x}\frac{\partial \vec{m}}{\partial r} + \frac{\partial \varphi}{\partial x}\frac{\partial \vec{m}}{\partial \varphi} = \frac{\partial r}{\partial x}\frac{\partial \theta}{\partial r}\frac{\partial \vec{m}}{\partial \theta} + \frac{\partial \varphi}{\partial x}\frac{\partial \Phi}{\partial \varphi}\frac{\partial \vec{m}}{\partial \Phi} \tag{A.9}$$

$$\frac{\partial \vec{m}}{\partial y} = \frac{\partial r}{\partial y}\frac{\partial \vec{m}}{\partial r} + \frac{\partial \varphi}{\partial y}\frac{\partial \vec{m}}{\partial \varphi} = \frac{\partial r}{\partial y}\frac{\partial \theta}{\partial r}\frac{\partial \vec{m}}{\partial \theta} + \frac{\partial \varphi}{\partial y}\frac{\partial \Phi}{\partial \varphi}\frac{\partial \vec{m}}{\partial \Phi} \tag{A.10}$$

For the skyrmion number integral, one has to compute the cross product of both terms. The only remaining term is $\frac{\partial \vec{m}}{\partial \theta} \times \frac{\partial \vec{m}}{\partial \Phi} = \vec{m}\sin\theta$.

$$\begin{aligned}
\frac{\partial \vec{m}}{\partial x} \times \frac{\partial \vec{m}}{\partial y} &= \left(\frac{\partial r}{\partial x}\frac{\partial \theta}{\partial r}\frac{\partial \varphi}{\partial y}\frac{\partial \Phi}{\partial \varphi} - \frac{\partial \varphi}{\partial x}\frac{\partial \Phi}{\partial \varphi}\frac{\partial r}{\partial y}\frac{\partial \theta}{\partial r}\right)\vec{m}\sin\theta \\
&= \left(\frac{\partial r}{\partial x}\frac{\partial \varphi}{\partial y} - \frac{\partial \varphi}{\partial x}\frac{\partial r}{\partial y}\right)\frac{\partial \theta}{\partial r}\frac{\partial \Phi}{\partial \varphi}\vec{m}\sin\theta \\
&= \left(\cos\varphi\frac{\cos\varphi}{r} + \frac{\sin\varphi}{r}\sin\varphi\right)\frac{\partial \theta}{\partial r}\frac{\partial \Phi}{\partial \varphi}\vec{m}\sin\theta \\
&= \frac{1}{r}\frac{\partial \theta}{\partial r}\frac{\partial \Phi}{\partial \varphi}\vec{m}\sin\theta.
\end{aligned} \tag{A.11}$$

We are now able to come back to the integration taking into account, firstly that $\vec{m}\cdot\vec{m} = 1$, the Jacobian when we change from x and y to r and φ, $dxdy \to rdrd\varphi$; and also the limits of integration:

$$\begin{aligned}
N_{Sk} &= \frac{1}{4\pi}\iint \vec{m}\cdot\left(\frac{\partial \vec{m}}{\partial x}\times\frac{\partial \vec{m}}{\partial y}\right)dxdy \\
&= \frac{1}{4\pi}\int_0^{2\pi}\int_0^{\infty}\frac{\partial \theta}{\partial r}\frac{\partial \Phi}{\partial \varphi}\sin\theta dr d\varphi \\
&= \frac{1}{4\pi}\int_0^{2\pi} d\varphi\frac{\partial \Phi}{\partial \varphi}\int_0^{\infty}\sin\theta\frac{\partial \theta}{\partial r}dr \\
&= \frac{1}{4\pi}\left[\Phi(\varphi)\right]_0^{2\pi}\left[-\cos\theta(r)\right]_0^{\infty} = W\cdot p,
\end{aligned} \tag{A.12}$$

with p the skyrmion core polarity number and W the Winding number. Note that $m_z = \cos\theta(r)$. So we end up with the definition of these two numbers:

$$p = \frac{1}{2}\left[-\cos\theta(r)\right]_0^{\infty} = \frac{1}{2}\left[m_z(0) - m_z(\infty)\right] = \pm 1, \tag{A.13}$$

$$W = \frac{1}{2\pi}\left[\Phi(\varphi)\right]_0^{2\pi}. \tag{A.14}$$

A.1.1 From LLG to Thiele equation

In this section we derive explicitly the Thiele equation from the LLG equation including the DL-SOT term. The LLG reads:

$$\frac{\partial \vec{m}}{\partial t} = -\gamma_0 \left(\vec{m} \times \vec{H}_{eff}\right) + \alpha \left(\vec{m} \times \frac{\partial \vec{m}}{\partial t}\right) - \gamma_0 \left(\vec{m} \times \vec{H}_{DL}\right). \tag{A.15}$$

Here, $H_{eff} = H_{ex} + H_K + H_d + H_{DMI} + H_{ext}$ (exchange, anisotropy, dipolar, DMI and external fields). In order to derive the Thiele equation we have to manipulate this one. Let us first factorize the right hand side of the equation into a total magnetic field, $\vec{H}_{tot}$.

$$\frac{\partial \vec{m}}{\partial t} = -\gamma_0 \vec{m} \times \vec{H}_{tot} = -\gamma_0 \vec{m} \times \left(\vec{H}_{eff} - \frac{\alpha}{\gamma_0}\frac{\partial \vec{m}}{\partial t} + \vec{H}_{DL}\right). \tag{A.16}$$

We then have to cross multiply both sides of the equation with $\vec{m}$:

$$\frac{\partial \vec{m}}{\partial t} \times \vec{m} = -\gamma_0 \left(\vec{m} \times \vec{H}_{tot}\right) \times \vec{m}. \tag{A.17}$$

Following the properties of the cross product multiplication, the next step reads:

$$\frac{\partial \vec{m}}{\partial t} \times \vec{m} = -\gamma_0 \left[\vec{H}_{tot} - \left(\vec{m} \cdot \vec{H}_{tot}\right)\vec{m}\right]. \tag{A.18}$$

Defining the following parameter $\lambda = \vec{m} \cdot \vec{H}_{tot}$, we can rewrite the equation:

$$-\frac{1}{\gamma_0}\frac{\partial \vec{m}}{\partial t} \times \vec{m} = \vec{H}_{eff} - \frac{\alpha}{\gamma_0}\frac{\partial \vec{m}}{\partial t} + \vec{H}_{DL} - \lambda \vec{m}. \tag{A.19}$$

We now isolate the effective field $\vec{H}_{eff}$ and we get:

$$\vec{H}_{eff} = \lambda \vec{m} - \frac{1}{\gamma_0}\frac{\partial \vec{m}}{\partial t} \times \vec{m} - \vec{H}_{DL} + \frac{\alpha}{\gamma_0}\frac{\partial \vec{m}}{\partial t}. \tag{A.20}$$

The total force due to the effective field $\vec{H}_{eff}$ acting on a rigid magnetization texture is:

$$\begin{aligned} \vec{F} &= \begin{pmatrix} F_x \\ F_y \\ F_z \end{pmatrix}, \\ F_i &= -\mu_0 M_S \iiint dV \vec{H}_{eff} \cdot \frac{\partial \vec{m}}{\partial x_i}. \end{aligned} \tag{A.21}$$

A strong consideration in Thiele's formalism is the rigid motion of the magnetization texture, which can be written as $\vec{m}(\vec{r}, t) = \vec{m}(\vec{r} - \vec{v}t)$. Performing calculations in time derivatives is easier and this allows us to change the derivative parameter from space to time following the well known chain rule (repeated indices mean summation in Einstein's notation):

$$\frac{\partial \vec{m}}{\partial t} = -\frac{\partial x_i}{\partial t}\frac{\partial \vec{m}}{\partial x_i} = v_i \frac{\partial \vec{m}}{\partial x_i}. \tag{A.22}$$

Let us continue the calculation ignoring first the DL-SOT term ($\vec{H}_{DL} = 0$) and substituting the rest in the effective field $\vec{H}_{eff}$:

$$\begin{aligned} F_i &= -\mu_0 M_S \iiint dV \left[\lambda \vec{m} - \frac{1}{\gamma_0}\frac{\partial \vec{m}}{\partial t} \times \vec{m} + \frac{\alpha}{\gamma_0}\frac{\partial \vec{m}}{\partial t}\right] \cdot \frac{\partial \vec{m}}{\partial x_i} \\ &= -\mu_0 M_S \iiint dV \left[\lambda \vec{m} - \frac{1}{\gamma_0} v_j \frac{\partial \vec{m}}{\partial x_j} \times \vec{m} + \frac{\alpha}{\gamma_0} v_j \frac{\partial \vec{m}}{\partial x_j}\right] \cdot \frac{\partial \vec{m}}{\partial x_i} \\ &= -\frac{\mu_0 M_S}{\gamma_0} \iiint dV \left[\gamma_0 \lambda \vec{m} - v_j \frac{\partial \vec{m}}{\partial x_j} \times \vec{m} + \alpha v_j \frac{\partial \vec{m}}{\partial x_j}\right] \cdot \frac{\partial \vec{m}}{\partial x_i}. \end{aligned} \tag{A.23}$$

If the magnetization of the film is homogeneous across its thickness, we can integrate the z variable of the volume $\iiint dxdydz = t \iint dxdy$. Also, the magnetization direction and its spatial derivative vector's direction

are orthogonal, which cancels the λ term. Lastly, $\vec{H}_{eff}$ does not generate any force on the skyrmion, so $F_i = 0$.

$$\begin{aligned} F_i &= -\frac{\mu_0 M_S t}{\gamma_0} \iint dxdy \left[\gamma_0 \lambda \vec{m} - v_j \frac{\partial \vec{m}}{\partial x_j} \times \vec{m} + \alpha v_j \frac{\partial \vec{m}}{\partial x_j}\right] \cdot \frac{\partial \vec{m}}{\partial x_i} \\ &= -\frac{\mu_0 M_S t}{\gamma_0} \iint dxdy \left[-v_j \frac{\partial \vec{m}}{\partial x_j} \times \vec{m} + \alpha v_j \frac{\partial \vec{m}}{\partial x_j}\right] \cdot \frac{\partial \vec{m}}{\partial x_i} \\ &= -\frac{\mu_0 M_S t}{\gamma_0} \iint dxdy \left[-\frac{\partial \vec{m}}{\partial x_j} \times \vec{m} + \alpha \frac{\partial \vec{m}}{\partial x_j}\right] \cdot \frac{\partial \vec{m}}{\partial x_i} v_j = 0. \end{aligned} \tag{A.24}$$

We therefore have two components in this equation. Let us separate them:

$$0 = -\frac{\mu_0 M_S t}{\gamma_0} \iint dxdy \left[-\frac{\partial \vec{m}}{\partial x_j} \times \vec{m}\right] \cdot \frac{\partial \vec{m}}{\partial x_i} v_j - \frac{\mu_0 M_S t}{\gamma_0} \iint dxdy \left[\alpha \frac{\partial \vec{m}}{\partial x_j}\right] \cdot \frac{\partial \vec{m}}{\partial x_i} v_j. \tag{A.25}$$

We can clean the expression using also $\gamma_0 = \mu_0 \gamma$:

$$0 = -\frac{M_S t}{\gamma} \iint dxdy \left[\vec{m} \times \frac{\partial \vec{m}}{\partial x_j}\right] \cdot \frac{\partial \vec{m}}{\partial x_i} v_j - \alpha \frac{M_S t}{\gamma} \iint dxdy \frac{\partial \vec{m}}{\partial x_j} \cdot \frac{\partial \vec{m}}{\partial x_i} v_j. \tag{A.26}$$

Cross product properties change the first part[2]

$$0 = -\frac{M_S t}{\gamma} \iint dxdy \left[\frac{\partial \vec{m}}{\partial x_j} \times \frac{\partial \vec{m}}{\partial x_i}\right] \cdot \vec{m} v_j - \alpha \frac{M_S t}{\gamma} \iint dxdy \frac{\partial \vec{m}}{\partial x_j} \cdot \frac{\partial \vec{m}}{\partial x_i} v_j, \tag{A.27}$$

and finally a vectorial form can be developed for this expression:

$$\vec{G} \times \vec{v} - \alpha \mathbf{D} \cdot \vec{v} = 0, \tag{A.28}$$

$$\vec{G} \times \begin{pmatrix} v_x \\ v_y \\ v_z \end{pmatrix} - \alpha \mathbf{D} \cdot \begin{pmatrix} v_x \\ v_y \\ v_z \end{pmatrix} = 0. \tag{A.29}$$

Note that the z direction motion does not exist. If we focus only in $\vec{G} = (0, 0, G)$ then we obtain the following expressions:

$$\vec{G} = \begin{pmatrix} 0 \\ 0 \\ G \end{pmatrix}, G = -\frac{M_S t}{\gamma} \iint dxdy \vec{m} \cdot \left(\frac{\partial \vec{m}}{\partial x} \times \frac{\partial \vec{m}}{\partial y}\right), \tag{A.30}$$

$$\mathbf{D} = \begin{pmatrix} D_{xx} & D_{xy} & 0 \\ D_{yx} & D_{yy} & 0 \\ 0 & 0 & 0 \end{pmatrix}, D_{ij} = \frac{M_S t}{\gamma} \iint dxdy \left(\frac{\partial \vec{m}}{\partial x_i} \cdot \frac{\partial \vec{m}}{\partial x_j}\right), \tag{A.31}$$

$$\vec{v} = \begin{pmatrix} v_x \\ v_y \\ 0 \end{pmatrix}. \tag{A.32}$$

[2] $(a \times b) \cdot c = a \cdot (b \times c) = (b \times c) \cdot a$.

A.1.2 Thiele equation

In Thiele's formalism the skyrmion is assumed to be a rigid spin texture so that we consider it point-like, only paying attention to the motion of its centre of mass. Under this assumption, the steady state velocity of the skyrmion $\vec{v}$ results from an equilibrium of different forces, as discussed just before:

$$\vec{F}_{DL} + \vec{G} \times \vec{v} - \alpha \mathbf{D} \vec{v} = 0 \tag{A.33}$$

where $\vec{F}_{DL}$ is the force due to the DL-SOT, $\vec{G}$ is the gyrotropic vector and D the dissipative tensor. They are respectively given by:

$$\begin{aligned}
\vec{F}_{DL} &= \begin{pmatrix} F_{DL,x} \\ F_{DL,y} \\ 0 \end{pmatrix} \\
F_{DL,i} &= -\mu_0 M_S t H^0_{DL} \iint dxdy \left(m_x \frac{\partial m_z}{\partial x_i} - m_z \frac{\partial m_x}{\partial x_i} \right) \qquad \text{(A.34)} \\
\vec{G} &= \begin{pmatrix} 0 \\ 0 \\ G \end{pmatrix} \\
G &= -\frac{M_S t}{\gamma} \iint dxdy \vec{m} \cdot \left(\frac{\partial \vec{m}}{\partial x} \times \frac{\partial \vec{m}}{\partial y} \right) \qquad \text{(A.35)} \\
\mathbf{D} &= \begin{pmatrix} D_{xx} & D_{xy} \\ D_{yx} & D_{yy} \end{pmatrix} \\
D_{ij} &= \frac{M_S t}{\gamma} \iint dxdy \left(\frac{\partial \vec{m}}{\partial x_i} \cdot \frac{\partial \vec{m}}{\partial x_j} \right) \qquad \text{(A.36)}
\end{aligned}$$

where $i = x, y$ and t is the FM thickness. Note that the FL-SOT does not generate a force on a rigid skyrmion because its action is equivalent to that of a homogeneous external magnetic field transverse to the current direction. Assuming further that the skyrmion exhibits a rotational symmetry, one has $(\partial \vec{m}/\partial y) \perp (\partial \vec{m}/\partial y)$. This means that $D_{xx} = D_{yy} = D$ and $D_{xy} = D_{yx} = 0$. Then notice that $G = -(M_S t/\gamma) \cdot 4\pi N_{Sk}$ and the equations become:

$$\begin{aligned}
\vec{F}_{DL} &= \begin{pmatrix} F_{DL,x} \\ F_{DL,y} \\ 0 \end{pmatrix}, F_{DL,i} = -\mu_0 M_S t H^0_{DL} \iint dxdy \left(m_x \frac{\partial m_z}{\partial x_i} - m_z \frac{\partial m_x}{\partial x_i} \right) \qquad \text{(A.37)} \\
\vec{G} &= \begin{pmatrix} 0 \\ 0 \\ G \end{pmatrix}, G = -4\pi \frac{M_S t}{\gamma} N_{Sk} \qquad \text{(A.38)} \\
\mathbf{D} &= \begin{pmatrix} D & 0 \\ 0 & D \end{pmatrix}, D = \frac{M_S t}{\gamma} \iint dxdy \left(\frac{\partial \vec{m}}{\partial x} \right)^2 \qquad \text{(A.39)}
\end{aligned}$$

Going back to the Thiele's equation and plugging in these terms, we arrive to the following expression after a couple of simplifications:

$$\begin{pmatrix} F_{DL,x} \\ F_{DL,y} \\ 0 \end{pmatrix} + G \begin{pmatrix} -v_y \\ v_x \\ 0 \end{pmatrix} - \alpha D \begin{pmatrix} v_x \\ v_y \\ 0 \end{pmatrix} = 0 \tag{A.40}$$

After some algebra (just obtain a component of velocity and substitute), one arrives to the following expressions for longitudinal (v_x) and transverse (v_y) skyrmion velocities:

$$v_x = \frac{\alpha D F_{DL,x} - G F_{DL,y}}{G^2 + \alpha^2 D^2} \tag{A.41}$$

$$v_y = \frac{\alpha D F_{DL,y} + G F_{DL,x}}{G^2 + \alpha^2 D^2} \tag{A.42}$$

Finally, the skyrmion Hall angle (SkHA) Θ_{SkH}, i.e. the angle between $\vec{F}_{DL}$ and $\vec{v}$, can be calculated:

$$\tan \Theta_{SkH} = \frac{G}{\alpha D} \tag{A.43}$$

A.2 Thiele equation with the force due to the DL-SOT

Following the procedure of the previous lines, we can now compute the force due to the DL-SOT. The effective field associated with the DL-SOT can be written as $\vec{H}_{DL} = H^0_{DL}\left(\vec{m}\times\left(\hat{j}\times\hat{z}\right)\right)$ where $\vec{J} = J\hat{j}$ is the charge current (opposite to the electron flow). We assume $H_{DL} > 0$ and furthermore the effective magnetic field can be written as as $\mu_0 H^0_{DL} = C_{DL}J$, where C_{DL} is the effective magnetic field per unit current density (in T $\mathrm{A}^{-1}\mathrm{m}^2$). Choosing $\hat{j} = \hat{x}$ leads to ($\hat{m}\times(\hat{x}\times\hat{z}) = -\hat{m}\times\hat{y} = \hat{y}\times\hat{m}$):

$$\vec{H}_{DL} = H^0_{DL}\left(\hat{y}\times\vec{m}\right) \tag{A.44}$$

The Thiele equation with the DL-SOT force is:

$$\vec{F}_{DL} + \vec{G}\times\vec{v} - \alpha\mathbf{D}\cdot\vec{v} = 0 \tag{A.45}$$

Replacing $\vec{H}_{eff}$ by $-\vec{H}_{DL}$ in the expression of the total force (see Equation A.21) on the rigid magnetization texture:

$$\vec{F} =, F_i = -\mu_0 M_S \iiint dV\,\vec{H}_{eff}\cdot\frac{\partial\vec{m}}{\partial x_i} \tag{A.46}$$

$$= \mu_0 M_S \iiint dV\,\vec{H}_{DL}\cdot\frac{\partial\vec{m}}{\partial x_i} \tag{A.47}$$

$$= \mu_0 M_S H^0_{DL} \iiint dV\,\left(\hat{y}\times\vec{m}\right)\cdot\frac{\partial\vec{m}}{\partial x_i}. \tag{A.48}$$

Remember the expression of the magnetization vector $\vec{m} = (m_x, m_y, m_z)$ and consider the integration in the $\hat{z}$ direction $\int dz = t$. As a result, we obtain:

$$F_i = \mu_0 M_S t H^0_{DL} \iint dxdy\,\left(\hat{y}\times\vec{m}\right)\cdot\frac{\partial\vec{m}}{\partial x_i} \tag{A.49}$$

$$= \mu_0 M_S t H^0_{DL} \iint dxdy\,\begin{pmatrix}0 & 1 & 0\end{pmatrix}\times\begin{pmatrix}m_x & m_y & m_z\end{pmatrix}\cdot\begin{pmatrix}\frac{\partial m_x}{\partial x_i}\\ \frac{\partial m_y}{\partial x_i}\\ \frac{\partial m_z}{\partial x_i}\end{pmatrix} \tag{A.50}$$

$$= \mu_0 M_S t H^0_{DL} \iint dxdy\,\begin{pmatrix}m_z & 0 & -m_x\end{pmatrix}\cdot\begin{pmatrix}\frac{\partial m_x}{\partial x_i}\\ \frac{\partial m_y}{\partial x_i}\\ \frac{\partial m_z}{\partial x_i}\end{pmatrix} \tag{A.51}$$

$$= \mu_0 M_S t H^0_{DL} \iint dxdy\left(m_z\frac{\partial m_x}{\partial x_i} - m_x\frac{\partial m_z}{\partial x_i}\right). \tag{A.52}$$

After all this, we can compute the force terms. We need again to get the polar coordinates for this. Remember that the magnetization can be written as $\vec{m} = (m_x, m_y, m_z) = (\cos\Phi\sin\theta, \sin\Phi\sin\theta, \cos\theta)$ and it is unitary ($|\vec{m}|^2 = 1$). Furthermore, we can identify in spherical coordinates $m_r(r) = \sin\theta(r)$ and $m_z(r) = \cos\theta(r)$. Now we consider a Néel skyrmion ($W = 1$ and $\Psi = 0$) and therefore $\Phi(\varphi) = W\varphi + \Psi = \varphi$:

$$\vec{m} = (m_r(r)\cos\varphi, m_r(r)\sin\varphi, m_z(r)) \tag{A.53}$$

Consider also that there is not a DL-SOT force component in y direction. So $F_{DL,y} = 0$ and $F_{DL,x} = F_{DL}$:

$$\begin{aligned}
F_{DL} &= \mu_0 M_S t H^0_{DL} \iint dxdy\left(m_z\frac{\partial m_x}{\partial x} - m_x\frac{\partial m_z}{\partial x}\right)\\
&= \mu_0 M_S t H^0_{DL} \iint rdrd\varphi\left(\sin\theta\cos\varphi\frac{\partial\cos\theta}{\partial x} - \cos\theta\frac{\partial\left(\sin\theta\cos\varphi\right)}{\partial x}\right)\\
&= \mu_0 M_S t H^0_{DL} \int_0^{2\pi}\int_0^{\infty} rdrd\varphi\left(\sin\theta\cos\varphi\frac{\partial r}{\partial x}\frac{\partial\cos\theta}{\partial r} - \cos\theta\frac{\partial r}{\partial x}\frac{\partial\left(\sin\theta\cos\varphi\right)}{\partial r}\right)\\
&= \mu_0 M_S t H^0_{DL} \int_0^{2\pi}\int_0^{\infty} rdrd\varphi\left(-\sin^2\theta\cos^2\varphi\frac{d\theta}{dr} - \cos^2\theta\cos^2\varphi\frac{d\theta}{dr}\right)\\
&= -\mu_0 M_S t H^0_{DL} \int_0^{2\pi}\int_0^{\infty} rdrd\varphi\cos^2\varphi\frac{d\theta}{dr}.
\end{aligned} \tag{A.54}$$

We can perform the integral of φ, $\int_0^{2\pi} d\varphi \cos^2\varphi = \pi$. So we have:

$$F_{DL} = -\mu_0 M_S t H_{DL}^0 \pi \int_0^\infty r dr \frac{d\theta}{dr}. \tag{A.55}$$

In order to evaluate the integral of the DL-SOT force we need to remember the assumption of the skyrmion radial 180 Bloch DW profile:

$$\theta(r) = -2\arctan\left(\exp\left(\frac{r-R}{\Delta}\right)\right). \tag{A.56}$$

The relation that a 180° Bloch DW profile[3] holds as: $\sin\theta = \Delta\frac{d\theta}{dr}$. So the force reads:

$$F_{DL} = -\mu_0 M_S t H_{DL}^0 \frac{\pi}{\Delta} \int_0^\infty r dr \sin\theta \tag{A.57}$$

If the skyrmion radious is much larger than the domain wall width ($R >> \Delta$), we can substitute in the integral $r = R$ and then perform the integration of the $\sin\theta$:

$$\begin{aligned} F_{DL} &\approx -\mu_0 M_S t H_{DL}^0 \pi \int_0^\infty dr \frac{R}{\Delta}\sin\theta \\ &\approx -\mu_0 M_S t H_{DL}^0 \pi \frac{R}{\Delta}\int_0^\infty dr \sin\theta \\ &\approx -\mu_0 M_S t H_{DL}^0 \pi \frac{R}{\Delta}\left[-2\Delta\arctan\left(\exp\left(\frac{r-R}{\Delta}\right)\right)\right]_0^\infty \\ &\approx \mu_0 M_S t H_{DL}^0 2\pi\Delta\frac{R}{\Delta}\left[\pi/2 - \arctan\left(\exp\left(-R/\Delta\right)\right)\right]. \end{aligned} \tag{A.58}$$

And finally:

$$F_{DL} \approx \mu_0 M_S t H_{DL}^0 \pi^2 R. \tag{A.59}$$

Regarding the dissipation factor, we have:

$$D = \frac{M_S t}{\gamma}\iint dxdy\left(\frac{\partial\vec{m}}{\partial x}\right)^2. \tag{A.60}$$

Again with the polar and spherical coordinates we have to compute the $\left(\frac{\partial\vec{m}}{\partial x}\right)^2 = \left(\frac{\partial\vec{m}}{\partial y}\right)^2$ term. Let us have a look at it remembering the relations for the chain rule and also that $\Phi(\varphi) = \varphi$ for Néel skyrmions in our case:

$$\frac{\partial\vec{m}}{\partial x} = \frac{\partial r}{\partial x}\frac{\partial\vec{m}}{\partial r} + \frac{\partial\varphi}{\partial x}\frac{\partial\vec{m}}{\partial\varphi} = \cos\varphi\frac{\partial\vec{m}}{\partial r} - \frac{\sin\varphi}{r}\frac{\partial\vec{m}}{\partial\varphi}. \tag{A.61}$$

We previously computed the magnetization vector in spherical coordinates, so that we can perform the derivatives of r and φ:

$$\vec{m} = \left(m_r(r)\cos\varphi, m_r(r)\sin\varphi, m_z(r)\right). \tag{A.62}$$

And the derivative is:

$$\frac{\partial\vec{m}}{\partial x} = \begin{pmatrix}\frac{\partial m_x}{\partial x}\\ \frac{\partial m_y}{\partial x}\\ \frac{\partial m_z}{\partial x}\end{pmatrix} = \begin{pmatrix}\cos\varphi\frac{\partial(m_r(r)\cos\varphi)}{\partial r} - \frac{\sin\varphi}{r}\frac{\partial(m_r(r)\cos\varphi)}{\partial\varphi}\\ \cos\varphi\frac{\partial(m_r(r)\sin\varphi)}{\partial r} - \frac{\sin\varphi}{r}\frac{\partial(m_r(r)\sin\varphi)}{\partial\varphi}\\ \cos\varphi\frac{\partial(m_z(r))}{\partial r} - \frac{\sin\varphi}{r}\frac{\partial(m_z(r))}{\partial\varphi}\end{pmatrix} = \begin{pmatrix}\cos^2\varphi\frac{dm_r(r)}{dr} + \frac{\sin^2\varphi}{r}m_r(r)\\ \sin\varphi\cos\varphi\frac{dm_r(r)}{dr} - \frac{\sin\varphi\cos\varphi}{r}m_r(r)\\ \cos\varphi\frac{dm_z(r)}{dr}\end{pmatrix} \tag{A.63}$$

Let us compute the square of it. The coefficients of $\frac{dm_r(r)}{dr}\frac{m_r(r)}{r}$ cancel out and one arrives to:

$$\left(\frac{\partial\vec{m}}{\partial x}\right)^2 = \frac{\partial\vec{m}}{\partial x}\cdot\frac{\partial\vec{m}}{\partial x} = \left(\frac{dm_r(r)}{dr}\right)^2\cos^2\varphi + \left(\frac{m_r(r)}{r}\right)^2\sin^2\varphi + \left(\frac{dm_z(r)}{dr}\right)^2\cos^2\varphi. \tag{A.64}$$

[3] $\frac{d\theta}{dr} = \frac{1}{\Delta}\mathrm{sech}\left(\frac{r-R}{\Delta}\right)$. Also: $\sin\theta(r) = \mathrm{sech}\left(\frac{r-R}{\Delta}\right)$.

To continue with the dissipation integral, consider again the Jacobian for polar coordinates and then note that it is possible to perform the integral of φ obtaining a common factor π[4].

$$\begin{aligned} D &= \frac{M_S t}{\gamma} \iint dxdy \left(\frac{\partial \vec{m}}{\partial x}\right)^2 \\ &= \frac{M_S t}{\gamma} \int_0^\infty \int_0^{2\pi} rdrd\varphi \left(\left(\frac{dm_r(r)}{dr}\right)^2 \cos^2\varphi + \left(\frac{m_r(r)}{r}\right)^2 \sin^2\varphi + \left(\frac{dm_z(r)}{dr}\right)^2 \cos^2\varphi \right) \\ &= \frac{M_S t\pi}{\gamma} \int_0^\infty rdr \left[\left(\frac{dm_r(r)}{dr}\right)^2 + \left(\frac{m_r(r)}{r}\right)^2 + \left(\frac{dm_z(r)}{dr}\right)^2 \right]. \end{aligned} \tag{A.65}$$

Substituting as before $m_z = \cos\theta$ and $m_r = \sin\theta$:

$$\begin{aligned} D &= \frac{M_S t\pi}{\gamma} \int_0^\infty rdr \left[\left(\frac{d(\sin\theta)}{dr}\right)^2 + \left(\frac{\sin\theta}{r}\right)^2 + \left(\frac{d(\cos\theta)}{dr}\right)^2 \right] \\ &= \frac{M_S t\pi}{\gamma} \int_0^\infty rdr \left[\cos^2\theta \left(\frac{d\theta}{dr}\right)^2 + \left(\frac{\sin\theta}{r}\right)^2 + \sin^2\theta \left(\frac{d\theta}{dr}\right)^2 \right] \\ &= \frac{M_S t\pi}{\gamma} \int_0^\infty rdr \left[\left(\frac{\sin\theta}{r}\right)^2 + \left(\frac{d\theta}{dr}\right)^2 \right]. \end{aligned} \tag{A.66}$$

Using the $\sin\theta = \Delta\frac{d\theta}{dr}$ relation and considering again that the radious is much larger than the DW width, we can substitute $r = R$ and perform the integration of $\sin^2\theta$:

$$\begin{aligned} D &= \frac{M_S t\pi}{\gamma} \int_0^\infty rdr \left[\left(\frac{\sin\theta}{r}\right)^2 + \left(\frac{\sin\theta}{\Delta}\right)^2 \right] = \frac{M_S t\pi}{\gamma} \int_0^\infty rdr \sin^2\theta \left[\frac{1}{r^2} + \frac{1}{\Delta^2}\right] \\ &\approx \frac{M_S t\pi}{\gamma} \left(\frac{1}{R} + \frac{R}{\Delta^2}\right) \int_0^\infty dr \sin^2\theta \\ &\approx \frac{M_S t\pi}{\gamma} \left(\frac{1}{R} + \frac{R}{\Delta^2}\right) \left[-2\Delta \frac{\exp(2R/\Delta)}{\exp(2R/\Delta) + \exp(2x/\Delta)} \right]_0^\infty \\ &\approx \frac{M_S t\pi}{\gamma} \left(\frac{1}{R} + \frac{R}{\Delta^2}\right) \left[0 + 2\Delta \frac{\exp(2R/\Delta)}{\exp(2R/\Delta) + 1} \right] \\ &\approx \frac{M_S t\pi}{\gamma} \left(\frac{1}{R} + \frac{R}{\Delta^2}\right) 2\Delta \\ &\approx \frac{M_S t}{\gamma} 2\pi \left(\frac{\Delta}{R} + \frac{R}{\Delta}\right) \approx \frac{M_S t}{\gamma} 2\pi \frac{R}{\Delta}. \end{aligned} \tag{A.67}$$

To finish with, we have the expression for G:

$$G = -4\pi \frac{M_S t}{\gamma}. \tag{A.68}$$

And now the last thing is to inject all three equations (G, D and F_{DL}) in the skyrmion velocity equation as well as in the skyrmion Hall angle:

$$v = \sqrt{v_x^2 + v_y^2} = \sqrt{\left(\frac{\alpha D F_{DL,x} - G F_{DL,y}}{G^2 + \alpha^2 D^2}\right)^2 + \left(\frac{\alpha D F_{DL,y} + G F_{DL,x}}{G^2 + \alpha^2 D^2}\right)^2} \tag{A.69}$$

[4] $\int_0^{2\pi} d\varphi cos^2\varphi = \int_0^{2\pi} d\varphi sin^2\varphi = \pi$.

Remember that we said the y component of the force was zero, and we computed only the x component:

$$\begin{aligned} v &= \sqrt{\left(\frac{\alpha D F_{DL}}{G^2+\alpha^2 D^2}\right)^2 + \left(\frac{G F_{DL}}{G^2+\alpha^2 D^2}\right)^2} = \frac{1}{G^2+\alpha^2 D^2}\sqrt{\alpha^2 D^2 F_{DL}^2 + G^2 F_{DL}^2} \\ &= \frac{F_{DL}}{\sqrt{G^2+\alpha^2 D^2}} = \frac{\mu_0 M_S t H_{DL}^0 \pi^2 R}{\sqrt{\left(4\pi\frac{M_S t}{\gamma}\right)^2 + \alpha^2\left(\frac{M_S t}{\gamma} 2\pi\frac{R}{\Delta}\right)^2}} = \frac{\gamma\pi R}{4\sqrt{1+\left(\frac{\alpha R}{2\Delta}\right)^2}}\mu_0 H_{DL}^0 \\ &= \frac{\gamma\pi R}{4\sqrt{1+\left(\frac{\alpha R}{2\Delta}\right)^2}} C_{DL} J \end{aligned} \tag{A.70}$$

$$\tan\Theta_{SkH} = \frac{G}{\alpha D} = \frac{-4\pi\frac{M_S t}{\gamma}}{\alpha 2\pi\frac{M_S t}{\gamma}\frac{R}{\Delta}} = \frac{-2\Delta}{\alpha R}. \tag{A.71}$$

References

[1] M. N. Baibich, J. M. Broto, A. Fert, F. Nguyen Van Dau, F. Petroff, P. Etienne, G. Creuzet, A. Friederich, and J. Chazelas. Giant Magnetoresistance of (001)Fe/(001)Cr Magnetic Superlattices. *Phys. Rev. Lett.*, 61:2472, 1988. [p. 1]

[2] G. Binasch, P. Grünberg, F. Saurenbach, and W. Zinn. Enhanced magnetoresistance in layered magnetic structures with antiferromagnetic interlayer exchange. *Phys. Rev. B*, 39:4828, 1989. [p. 1]

[3] M. Julliere. Tunneling between ferromagnetic films. *Phys. Lett. A*, 54:225, 1975. [pp. 1, 20]

[4] J. S. Moodera, Lisa R. Kinder, Terrilyn M. Wong, and R. Meservey. Large magnetoresistance at room temperature in ferromagnetic thin film tunnel junctions. *Physical Review Letters*, 74(16):3273–3276, 1995. [pp. 1, 20, 21]

[5] J. C. Slonczewski. Current-driven excitation of magnetic multilayers. *J. Magn. Magn. Mater.*, 159:L1, 1996. [pp. 1, 17]

[6] E. B. Myers, D. C. Ralph, J. A. Katine, R. N. Louie, and R. A. Buhrman. Current-Induced Switching of Domains in Magnetic Multilayer Devices. *Science*, 285:867, 1999. [p. 1]

[7] A. Manchon, J. Železný, I. M. Miron, T. Jungwirth, J. Sinova, A. Thiaville, K. Garello, and P. Gambardella. Current-induced spin-orbit torques in ferromagnetic and antiferromagnetic systems. *Rev. Mod. Phys.*, 91:035004, 2019. [pp. 1, 17]

[8] Ioan Mihai Miron, Thomas Moore, Helga Szambolics, Liliana Daniela Buda-Prejbeanu, Stéphane Auffret, Bernard Rodmacq, Stefania Pizzini, Jan Vogel, Marlio Bonfim, Alain Schuhl, and Gilles Gaudin. Fast current-induced domain-wall motion controlled by the Rashba effect. *Nat. Mater.*, 10:419, 2011. [pp. 1, 17]

[9] Stuart S. P. Parkin, Masamitsu Hayashi, and Luc Thomas. Magnetic Domain-Wall Racetrack Memory. *Science*, 320(5873):190–194, 2008. Publisher: American Association for the Advancement of Science Section: Review. [p. 1]

[10] J. Grollier, D. Querlioz, K. Y. Camsari, K. Everschor-Sitte, S. Fukami, and M. D. Stiles. Neuromorphic spintronics. *Nature Electronics*, 3(7):360–370, March 2020. [p. 1]

[11] William Fuller Brown. *Micromagnetics*. Interscience Publishers, 1963. [p. 6]

[12] C L Dennis, R P Borges, L D Buda, U Ebels, J F Gregg, M Hehn, E Jouguelet, K Ounadjela, I Petej, I L Prejbeanu, and M J Thornton. The defining length scales of mesomagnetism: a review. *Journal of Physics: Condensed Matter*, 14(49):R1175–R1262, November 2002. [p. 6]

[13] R Skomski. Nanomagnetics. *Journal of Physics: Condensed Matter*, 15(20):R841–R896, May 2003. [p. 6]

[14] A. Hubert and R. Schafer. *Magnetic Domains*. Springer Berlin Heidelberg, 1998. [p. 6]

[15] Alberto P. Guimarães. *Principles of Nanomagnetism*. Springer International Publishing, 2017. [p. 6]

[16] A. E. LaBonte. Two-dimensional bloch-type domain walls in ferromagnetic films. *Journal of Applied Physics*, 40(6):2450–2458, May 1969. [p. 6]

[17] M. Schabes and A. Aharoni. Magnetostatic interaction fields for a three-dimensional array of ferromagnetic cubes. *IEEE Transactions on Magnetics*, 23(6):3882–3888, November 1987. [p. 6]

[18] Amikam Aharoni. Demagnetizing factors for rectangular ferromagnetic prisms. *J. Appl. Phys.*, 83:3432, 1998. [p. 7]

[19] Louis Néel. Anisotropie magnétique superficielle et surstructures d'orientation. *J. Phys. Radium*, 15:225, 1954. [p. 8]

[20] P. Bruno and C. Chappert. Ruderman-Kittel theory of oscillatory interlayer exchange coupling. *Phys. Rev. B*, 46:261, 1992. [p. 9]

[21] Tadao Kasuya. A theory of metallic ferro- and antiferromagnetism on zener model. *Progress of Theoretical Physics*, 16(1):45–57, July 1956. [p. 9]

[22] Kei Yosida. Magnetic properties of cu-mn alloys. *Physical Review*, 106(5):893–898, June 1957. [p. 9]

[23] S. S. P. Parkin, N. More, and K. P. Roche. Oscillations in exchange coupling and magnetoresistance in metallic superlattice structures: Co/Ru, Co/Cr, and Fe/Cr. *Phys. Rev. Lett.*, 64:2304, 1990. [p. 9]

[24] S. S. P. Parkin and D. Mauri. Spin engineering: Direct determination of the Ruderman-Kittel-Kasuya-Yosida far-field range function in ruthenium. *Phys. Rev. B*, 44:7131, 1991. [p. 9]

[25] I. Dzyaloshinsky. A thermodynamic theory of "weak" ferromagnetism of antiferromagnetics. *Journal of Physics and Chemistry of Solids*, 4(4):241–255, 1958. [p. 10]

[26] Tôru Moriya. Anisotropic Superexchange Interaction and Weak Ferromagnetism. *Physical Review*, 120(1):91–98, 1960. Publisher: American Physical Society. [p. 10]

[27] Tôru Moriya. New Mechanism of Anisotropic Superexchange Interaction. *Phys. Rev. Lett.*, 4:228, 1960. [p. 10]

[28] L Ludgren, O Beckman, V Attia, S P Bhattacheriee, and M Richardson. Helical spin arrangement in cubic FeGe. *Physica Scripta*, 1(1):69–72, 1970. [p. 10]

[29] Y. Ishikawa, K. Tajima, D. Bloch, and M. Roth. Helical spin structure in manganese silicide MnSi. *Solid State Communications*, 19(6):525–528, 1976. [p. 10]

[30] P Bak and M H Jensen. Theory of helical magnetic structures and phase transitions in MnSi and FeGe. *Journal of Physics C: Solid State Physics*, 13(31):L881–L885, 1980. [p. 10]

[31] A. Fert and Peter M. Levy. Role of Anisotropic Exchange Interactions in Determining the Properties of Spin-Glasses. *Physical Review Letters*, 44(23):1538–1541, 1980. Publisher: American Physical Society. [p. 10]

[32] A.R. Fert. Magnetic and transport properties of metallic multilayers. *Materials Science Forum*, 59-60:439–480, 1991. [p. 10]

[33] A. Crépieux and C. Lacroix. Dzyaloshinsky–Moriya interactions induced by symmetry breaking at a surface. *J. Magn. Magn. Mater.*, 182:341, 1998. [p. 10]

[34] André Thiaville, Stanislas Rohart, Émilie Jué, Vincent Cros, and Albert Fert. Dynamics of Dzyaloshinskii domain walls in ultrathin magnetic films. *Europhys. Lett.*, 100:57002, 2012. [pp. 13, 17, 19, 61]

[35] Lev Davidovich Landau and E. Lifshitz. *On the Theory of the Dispersion of Magnetic Permeability in Ferromagnetic Bodies*. Elsevier, 1935. [p. 14]

[36] T. L. Gilbert. A phenomenological theory of damping in ferromagnetic materials. *IEEE Trans. Magn.*, 40:3443, 2004. [p. 14]

[37] S. Azzawi, A. T. Hindmarch, and D. Atkinson. Magnetic damping phenomena in ferromagnetic thin-films and multilayers. *J. Phys. D: Appl. Phys.*, 50:473001, 2017. [p. 14]

[38] N. L. Schryer and L. R. Walker. The motion of 180° domain walls in uniform dc magnetic fields. *J. Appl. Phys.*, 45:5406, 1974. [pp. 15, 16]

[39] A. Mougin, M. Cormier, J. P. Adam, P. J. Metaxas, and J. Ferré. Domain wall mobility, stability and Walker breakdown in magnetic nanowires. *Europhys. Lett.*, 78:57007, 2007. [pp. 15, 16]

[40] Thai Ha Pham, J. Vogel, J. Sampaio, M. Vaňatka, J.-C. Rojas-Sánchez, M. Bonfim, D. S. Chaves, F. Choueikani, P. Ohresser, E. Otero, A. Thiaville, and S. Pizzini. Very large domain wall velocities in Pt/Co/GdO_x and Pt/Co/Gd trilayers with Dzyaloshinskii-Moriya interaction. *Europhys. Lett.*, 113:67001, 2016. [p. 17]

[41] Arne Brataas, Andrew D. Kent, and Hideo Ohno. Current-induced torques in magnetic materials. *Nat. Mater.*, 11:372, 2012. [p. 17]

[42] J. Sampaio, V. Cros, S. Rohart, A. Thiaville, and A. Fert. Nucleation, stability and current-induced motion of isolated magnetic skyrmions in nanostructures. *Nature Nanotechnology*, 8(11):839–844, 2013. [pp. 17, 30, 32, 37]

[43] R. Tomasello, E. Martinez, R. Zivieri, L. Torres, M. Carpentieri, and G. Finocchio. A strategy for the design of skyrmion racetrack memories. *Sci. Rep.*, 4:6784, 2014. [pp. 17, 37]

[44] L. Berger. Emission of spin waves by a magnetic multilayer traversed by a current. *Physical Review B*, 54(13):9353–9358, October 1996. [p. 17]

[45] O. Boulle, G. Malinowski, and M. Kläui. Current-induced domain wall motion in nanoscale ferromagnetic elements. *Mater. Sci. Eng. R*, 72:159, 2011. [p. 18]

[46] S. Zhang and Z. Li. Roles of Nonequilibrium Conduction Electrons on the Magnetization Dynamics of Ferromagnets. *Phys. Rev. Lett.*, 93:127204, 2004. [p. 18]

[47] Jianwei Zhang, Peter M. Levy, Shufeng Zhang, and Vladimir Antropov. Identification of Transverse Spin Currents in Noncollinear Magnetic Structures. *Phys. Rev. Lett.*, 93:256602, 2004. [p. 18]

[48] A. Thiaville, Y. Nakatani, J. Miltat, and N. Vernier. Domain wall motion by spin-polarized current: A micromagnetic study. *J. Appl. Phys.*, 95:7049, 2004. [p. 18]

[49] A Thiaville, Y Nakatani, J Miltat, and Y Suzuki. Micromagnetic understanding of current-driven domain wall motion in patterned nanowires. *Europhysics Letters (EPL)*, 69(6):990–996, March 2005. [pp. 18, 34]

[50] J. E. Hirsch. Spin Hall Effect. *Phys. Rev. Lett.*, 83:1834, 1999. [p. 18]

[51] Jairo Sinova, Dimitrie Culcer, Q. Niu, N. A. Sinitsyn, T. Jungwirth, and A. H. MacDonald. Universal Intrinsic Spin Hall Effect. *Phys. Rev. Lett.*, 92:126603, 2004. [p. 18]

[52] M. I. Dyakonov and V. I. Perel. Current-induced spin orientation of electrons in semiconductors. *Phys. Lett. A*, 35:459, 1971. [p. 18]

[53] V. M. Edelstein. Spin polarization of conduction electrons induced by electric current in two-dimensional asymmetric electron systems. *Solid State Comm.*, 73:233, 1990. [p. 18]

[54] Pietro Gambardella and Ioan Mihai Miron. Current-induced spin–orbit torques. *Phil. Trans. R. Soc. A*, 369:3175, 2011. [p. 18]

[55] A. V. Khvalkovskiy, V. Cros, D. Apalkov, V. Nikitin, M. Krounbi, K. A. Zvezdin, A. Anane, J. Grollier, and A. Fert. Matching domain-wall configuration and spin-orbit torques for efficient domain-wall motion. *Phys. Rev. B*, 87:020402, 2013. [p. 18]

[56] H. L. Wang, C. H. Du, Y. Pu, R. Adur, P. C. Hammel, and F. Y. Yang. Scaling of spin hall angle in 3d, 4d, and 5d metals from y3fe5o12/metal spin pumping. *Physical Review Letters*, 112(19), may 2014. [p. 18]

[57] Luqiao Liu, O. J. Lee, T. J. Gudmundsen, D. C. Ralph, and R. A. Buhrman. Current-Induced Switching of Perpendicularly Magnetized Magnetic Layers Using Spin Torque from the Spin Hall Effect. *Phys. Rev. Lett.*, 109:096602, 2012. [p. 18]

[58] Kevin Garello, Ioan Mihai Miron, Can Onur Avci, Frank Freimuth, Yuriy Mokrousov, Stefan Blügel, Stéphane Auffret, Olivier Boulle, Gilles Gaudin, and Pietro Gambardella. Symmetry and magnitude of spin-orbit torques in ferromagnetic heterostructures. *Nat. Nanotech.*, 8:587, 2013. [p. 18]

[59] Satoru Emori, Uwe Bauer, Sung-Min Ahn, Eduardo Martinez, and Geoffrey S. D. Beach. Current-driven dynamics of chiral ferromagnetic domain walls. *Nat. Mater.*, 12:611, 2013. [p. 18]

[60] Luqiao Liu, Chi-Feng Pai, Y. Li, H. W. Tseng, D. C. Ralph, and R. A. Buhrman. Spin-Torque Switching with the Giant Spin Hall Effect of Tantalum. *Science*, 336:555, 2012. [p. 18]

[61] Chi-Feng Pai, Luqiao Liu, Y. Li, H. W. Tseng, D. C. Ralph, and R. A. Buhrman. Spin transfer torque devices utilizing the giant spin Hall effect of tungsten. *Appl. Phys. Lett.*, 101:122404, 2012. [p. 18]

[62] Bernard Dieny, Ronald B. Goldfarb, and Kyung&xJin Lee, editors. *Introduction to Magnetic Random Access Memory*. John Wiley & Sons, Inc., 2017. [p. 20]

[63] T. Miyazaki and N. Tezuka. Giant magnetic tunneling effect in fe/al2o3/fe junction. *Journal of Magnetism and Magnetic Materials*, 139(3):L231–L234, 1995. [pp. 20, 21]

[64] Chang He Shang, Janusz Nowak, Ronnie Jansen, and Jagadeesh S. Moodera. Temperature dependence of magnetoresistance and surface magnetization in ferromagnetic tunnel junctions. *Physical Review B*, 58(6):R2917–R2920, 1998. [p. 20]

[65] S Yuasa, T Sato, E Tamura, Y Suzuki, H Yamamori, K Ando, and T Katayama. Magnetic tunnel junctions with single-crystal electrodes: A crystal anisotropy of tunnel magneto-resistance. *Europhysics Letters (EPL)*, 52(3):344–350, 2000. [p. 20]

[66] Jose Maria De Teresa, Agnes Barthelemy, Albert Fert, Jean Pierre Contour, Francois Montaigne, and Pierre Seneor. Role of metal-oxide interface in determining the spin polarization of magnetic tunnel junctions. *Science*, 286(5439):507–509, 1999. [p. 20]

[67] David D. Djayaprawira, Koji Tsunekawa, Motonobu Nagai, Hiroki Maehara, Shinji Yamagata, Naoki Watanabe, Shinji Yuasa, Yoshishige Suzuki, and Koji Ando. 230% room-temperature magnetoresistance in CoFeB/MgO/CoFeB magnetic tunnel junctions. *Applied Physics Letters*, 86(9), 2005. [p. 21]

[68] S. Ikeda, J. Hayakawa, Y. Ashizawa, Y. M. Lee, K. Miura, H. Hasegawa, M. Tsunoda, F. Matsukura, and H. Ohno. Tunnel magnetoresistance of 604% at 300k by suppression of ta diffusion in CoFeB/MgO/CoFeB pseudo-spin-valves annealed at high temperature. *Applied Physics Letters*, 93(8), 2008. [p. 21]

[69] B. Dieny and M. Chshiev. Perpendicular magnetic anisotropy at transition metal/oxide interfaces and applications. *Rev. Mod. Phys.*, 89:025008, 2017. [p. 21]

[70] Titiksha Srivastava. *Engineering and Dynamical Control of Interfacial Properties in Ultra-Thin Films to Tune Magnetic Spin Textures*. PhD thesis,, Univ. Grenoble Alpes, 2019. [p. 21]

[71] Charles-Elie Fillion. *Electric control of skyrmions for spintronic applications*. Theses, Université Grenoble Alpes [2020-....], January 2023. [p. 21]

[72] Charles-Elie Fillion, Johanna Fischer, Raj Kumar, Aymen Fassatoui, Stefania Pizzini, Laurent Ranno, Djoudi Ourdani, Mohamed Belmeguenai, Yves Roussigné, Salim-Mourad Chérif, Stéphane Auffret, Isabelle Joumard, Olivier Boulle, Gilles Gaudin, Liliana Buda-Prejbeanu, Claire Baraduc, and Hélène Béa. Gate-controlled skyrmion and domain wall chirality. *Nature Communications*, 13(1), sep 2022. [p. 21]

[73] Chong Bi, Yaohua Liu, T. Newhouse-Illige, M. Xu, M. Rosales, J. W. Freeland, Oleg Mryasov, Shufeng Zhang, S. G. E. te Velthuis, and W. G. Wang. Reversible control of co magnetism by voltage-induced oxidation. *Physical Review Letters*, 113(26), dec 2014. [p. 21]

[74] Uwe Bauer, Lide Yao, Aik Jun Tan, Parnika Agrawal, Satoru Emori, Harry L. Tuller, Sebastiaan van Dijken, and Geoffrey S. D. Beach. Magneto-ionic control of interfacial magnetism. *Nature Materials*, 14(2):174–181, nov 2014. [p. 21]

[75] Aymen Fassatoui, Jose Peña Garcia, Laurent Ranno, Jan Vogel, Anne Bernand-Mantel, Hélène Béa, Sergio Pizzini, and Stefania Pizzini. Reversible and irreversible voltage manipulation of interfacial magnetic anisotropy in ptcooxide multilayers. *Physical Review Applied*, 14(6), dec 2020. [p. 21]

[76] Chun-Gang Duan, S. S. Jaswal, and E. Y. Tsymbal. Predicted magnetoelectric effect in febatio3 multilayers: Ferroelectric control of magnetism. *Physical Review Letters*, 97(4), jul 2006. [p. 22]

[77] James M. Rondinelli, Massimiliano Stengel, and Nicola A. Spaldin. Carrier-mediated magnetoelectricity in complex oxide heterostructures. *Nature Nanotechnology*, 3(1):46–50, 2007. [p. 22]

[78] Martin Weisheit, Sebastian Fahler, Alain Marty, Yves Souche, Christiane Poinsignon, and Dominique Givord. Electric field-induced modification of magnetism in thin-film ferromagnets. *Science*, 315(5810):349–351, 2007. [p. 22]

[79] T. Maruyama, Y. Shiota, T. Nozaki, K. Ohta, N. Toda, M. Mizuguchi, A. A. Tulapurkar, T. Shinjo, M. Shiraishi, S. Mizukami, Y. Ando, and Y. Suzuki. Large voltage-induced magnetic anisotropy change in a few atomic layers of iron. *Nature Nanotechnology*, 4(3):158–161, 2009. [p. 22]

[80] Wei-Gang Wang, Mingen Li, Stephen Hageman, and C. L. Chien. Electric-field-assisted switching in magnetic tunnel junctions. *Nature Materials*, 11(1):64–68, 2011. [p. 22]

[81] Yoichi Shiota, Takayuki Nozaki, Frédéric Bonell, Shinichi Murakami, Teruya Shinjo, and Yoshishige Suzuki. Induction of coherent magnetization switching in a few atomic layers of feco using voltage pulses. *Nature Materials*, 11(1):39–43, 2011. [p. 22]

[82] M. Endo, S. Kanai, S. Ikeda, F. Matsukura, and H. Ohno. Electric-field effects on thickness dependent magnetic anisotropy of sputtered MgO/co40fe40b20/ta structures. *Applied Physics Letters*, 96(21), 2010. [p. 22]

[83] T. H. R. Skyrme. A unified field theory of mesons and baryons. *Nucl. Phys.*, 31:556, 1962. [pp. 26, 37]

[84] Karin Everschor. *Current-induced dynamics of chiral magnetic structures: skyrmions, emergent electrodynamics and spin-transfer torques*. Phd thesis, Universitat zu Koln, Koln, Germany, 2012. https://kups.ub.uni-koeln.de/4811/1/Thesis_zum_Veroeffentlichen.pdf. [p. 26]

[85] A. Bogdanov and D. Yablonskiui. Thermodynamically stable "vortices" in magnetically ordered crystals. the mixed state of magnets. *Sov. Phys. JETP*, 68:101, 01 1989. [pp. 26, 27]

[86] A. Bogdanov and A. Hubert. Thermodynamically stable magnetic vortex states in magnetic crystals. *J. Magn. Magn. Mater.*, 138:255, 1994. [p. 26]

[87] Naoto Nagaosa and Yoshinori Tokura. Topological properties and dynamics of magnetic skyrmions. *Nature Nanotechnology*, 8(12):899–911, 2013. Number: 12 Publisher: Nature Publishing Group. [pp. 27, 36, 108]

[88] Hans-Benjamin Braun. Topological effects in nanomagnetism: from superparamagnetism to chiral quantum solitons. *Advances in Physics*, 61(1):1–116, 2012. [p. 27]

[89] Felix Büttner, Ivan Lemesh, and Geoffrey S. D. Beach. Theory of isolated magnetic skyrmions: From fundamentals to room temperature applications. *Sci. Rep.*, 8:4464, 2018. [pp. 27, 38]

[90] T. H. R. Skyrme. A non-linear theory of strong interactions. *Proceedings of the Royal Society of London. Series A. Mathematical and Physical Sciences*, 247(1249):260–278, September 1958. [p. 27]

[91] A O Leonov, T L Monchesky, N Romming, A Kubetzka, A N Bogdanov, and R Wiesendanger. The properties of isolated chiral skyrmions in thin magnetic films. *New Journal of Physics*, 18(6):065003, May 2016. [p. 27]

[92] Xichao Zhang, Jing Xia, Yan Zhou, Daowei Wang, Xiaoxi Liu, Weisheng Zhao, and Motohiko Ezawa. Control and manipulation of a magnetic skyrmionium in nanostructures. *Phys. Rev. B*, 94:094420, 2016. [p. 27]

[93] Shilei Zhang, Florian Kronast, Gerrit van der Laan, and Thorsten Hesjedal. Real-space observation of skyrmionium in a ferromagnet-magnetic topological insulator heterostructure. *Nano Letters*, 18(2):1057–1063, 2018. [p. 27]

[94] Gong Chen, Sang Pyo Kang, Colin Ophus, Alpha T. N'Diaye, Hee Young Kwon, Ryan T. Qiu, Changyeon Won, Kai Liu, Yizheng Wu, and Andreas K. Schmid. Out-of-plane chiral domain wall spin-structures in ultrathin in-plane magnets. *Nature Communications*, 8(1), 2017. [p. 27]

[95] S. A. Meynell, M. N. Wilson, K. L. Krycka, B. J. Kirby, H. Fritzsche, and T. L. Monchesky. Neutron study of in-plane skyrmions in MnSi thin films. *Physical Review B*, 96(5), 2017. [p. 27]

[96] Kyoung-Woong Moon, Jungbum Yoon, Changsoo Kim, and Chanyong Hwang. Existence of in-plane magnetic skyrmion and its motion under current flow. *Physical Review Applied*, 12(6), December 2019. [p. 27]

[97] Anne Bernand-Mantel, Lorenzo Camosi, Alexis Wartelle, Nicolas Rougemaille, Michaël Darques, and Laurent Ranno. The skyrmion-bubble transition in a ferromagnetic thin film. *SciPost Phys.*, 4:027, 2018. [pp. 27, 38]

[98] A. Bocdanov and A. Hubert. The properties of isolated magnetic vortices. *physica status solidi (b)*, 186(2):527–543, 1994. [pp. 27, 37]

[99] N S Kiselev, A N Bogdanov, R Schäfer, and U K Rößler. Chiral skyrmions in thin magnetic films: new objects for magnetic storage technologies? *Journal of Physics D: Applied Physics*, 44(39):392001, September 2011. [p. 27]

[100] S. Rohart and A. Thiaville. Skyrmion confinement in ultrathin film nanostructures in the presence of dzyaloshinskii-moriya interaction. *Physical Review B*, 88(18), November 2013. [p. 27]

[101] A. A. Thiele. Theory of the static stability of cylindrical domains in uniaxial platelets. *Journal of Applied Physics*, 41(3):1139–1145, March 1970. [p. 28]

[102] X. Z. Yu, Y. Onose, N. Kanazawa, J. H. Park, J. H. Han, Y. Matsui, N. Nagaosa, and Y. Tokura. Real-space observation of a two-dimensional skyrmion crystal. *Nature*, 465(7300):901–904, 2010. [pp. 30, 31]

[103] Olivier Boulle, Jan Vogel, Hongxin Yang, Stefania Pizzini, Dayane de Souza Chaves, Andrea Locatelli, Tevfik Onur Menteş, Alessandro Sala, Liliana D. Buda-Prejbeanu, Olivier Klein, Mohamed Belmeguenai, Yves Roussigné, Andrey Stashkevich, Salim Mourad Chérif, Lucia Aballe, Michael Foerster, Mairbek Chshiev, Stéphane Auffret, Ioan Mihai Miron, and Gilles Gaudin. Room-temperature chiral magnetic skyrmions in ultrathin magnetic nanostructures. *Nature Nanotechnology*, 11(5):449–454, 2016. [pp. 30, 31, 53, 82, 85, 88]

[104] Niklas Romming, André Kubetzka, Christian Hanneken, Kirsten von Bergmann, and Roland Wiesendanger. Field-Dependent Size and Shape of Single Magnetic Skyrmions. *Phys. Rev. Lett.*, 114:177203, 2015. [p. 31]

[105] Niklas Romming, Christian Hanneken, Matthias Menzel, Jessica E. Bickel, Boris Wolter, Kirsten von Bergmann, André Kubetzka, and Roland Wiesendanger. Writing and Deleting Single Magnetic Skyrmions. *Science*, 341:636, 2013. [pp. 30, 31, 82]

[106] Wanjun Jiang, Pramey Upadhyaya, Wei Zhang, Guoqiang Yu, M. Benjamin Jungfleisch, Frank Y. Fradin, John E. Pearson, Yaroslav Tserkovnyak, Kang L. Wang, Olle Heinonen, Suzanne G. E. te Velthuis, and Axel Hoffmann. Blowing magnetic skyrmion bubbles. *Science*, 349(6245):283–286, 2015. [pp. 30, 31, 33, 82]

[107] Gong Chen, Arantzazu Mascaraque, Alpha T. N'Diaye, and Andreas K. Schmid. Room temperature skyrmion ground state stabilized through interlayer exchange coupling. *Appl. Phys. Lett.*, 106:242404, 2015. [p. 31]

[108] C. Moreau-Luchaire, C. Moutafis, N. Reyren, J. Sampaio, C. a. F. Vaz, N. Van Horne, K. Bouzehouane, K. Garcia, C. Deranlot, P. Warnicke, P. Wohlhüter, J.-M. George, M. Weigand, J. Raabe, V. Cros, and A. Fert. Additive interfacial chiral interaction in multilayers for stabilization of small individual skyrmions at room temperature. *Nat. Nanotech.*, 11:444, 2016. [pp. 31, 38, 82]

[109] Seonghoon Woo, Kai Litzius, Benjamin Krüger, Mi-Young Im, Lucas Caretta, Kornel Richter, Maxwell Mann, Andrea Krone, Robert M. Reeve, Markus Weigand, Parnika Agrawal, Ivan Lemesh, Mohamad-Assaad Mawass, Peter Fischer, Mathias Kläui, and Geoffrey S. D. Beach. Observation of room-temperature magnetic skyrmions and their current-driven dynamics in ultrathin metallic ferromagnets. *Nat. Mater.*, 15:501, 2016. [pp. 30, 31, 32, 33, 38, 82]

[110] S. Mühlbauer, B. Binz, F. Jonietz, C. Pfleiderer, A. Rosch, A. Neubauer, R. Georgii, and P. Böni. Skyrmion Lattice in a Chiral Magnet. *Science*, 323:915, 2009. [p. 30]

[111] X. Z. Yu, N. Kanazawa, Y. Onose, K. Kimoto, W. Z. Zhang, S. Ishiwata, Y. Matsui, and Y. Tokura. Near room-temperature formation of a skyrmion crystal in thin-films of the helimagnet FeGe. *Nat. Mater.*, 10:106, 2011. [p. 30]

[112] M. Bode, M. Heide, K. von Bergmann, P. Ferriani, S. Heinze, G. Bihlmayer, A. Kubetzka, O. Pietzsch, S. Blügel, and R. Wiesendanger. Chiral magnetic order at surfaces driven by inversion asymmetry. *Nature*, 447:190, 2007. [p. 30]

[113] Jeremy M. Higgins, Ruihua Ding, John P. DeGrave, and Song Jin. Signature of helimagnetic ordering in single-crystal MnSi nanowires. *Nano Letters*, 10(5):1605–1610, 2010. [p. 30]

[114] Stefan Heinze, Kirsten von Bergmann, Matthias Menzel, Jens Brede, André Kubetzka, Roland Wiesendanger, Gustav Bihlmayer, and Stefan Blügel. Spontaneous atomic-scale magnetic skyrmion lattice in two dimensions. *Nat. Phys.*, 7:713, 2011. [pp. 30, 36]

[115] Anjan Soumyanarayanan, M. Raju, A. L. Gonzalez Oyarce, Anthony K. C. Tan, Mi-Young Im, A. P. Petrović, Pin Ho, K. H. Khoo, M. Tran, C. K. Gan, F. Ernult, and C. Panagopoulos. Tunable room-temperature magnetic skyrmions in Ir/Fe/Co/Pt multilayers. *Nat. Mater.*, 16:898, 2017. [p. 30]

[116] F. Jonietz, S. Mühlbauer, C. Pfleiderer, A. Neubauer, W. Münzer, A. Bauer, T. Adams, R. Georgii, P. Böni, R. A. Duine, K. Everschor, M. Garst, and A. Rosch. Spin Transfer Torques in MnSi at Ultralow Current Densities. *Science*, 330:1648, 2010. [p. 32]

[117] Junichi Iwasaki, Masahito Mochizuki, and Naoto Nagaosa. Universal current-velocity relation of skyrmion motion in chiral magnets. *Nat. Comm.*, 4:1463, 2013. [p. 32]

[118] X. Z. Yu, N. Kanazawa, W. Z. Zhang, T. Nagai, T. Hara, K. Kimoto, Y. Matsui, Y. Onose, and Y. Tokura. Skyrmion flow near room temperature in an ultralow current density. *Nat. Comm.*, 3:988, 2012. [p. 32]

[119] Kai Litzius, Ivan Lemesh, Benjamin Krüger, Pedram Bassirian, Lucas Caretta, Kornel Richter, Felix Büttner, Koji Sato, Oleg A. Tretiakov, Johannes Förster, Robert M. Reeve, Markus Weigand, Iuliia Bykova, Hermann Stoll, Gisela Schütz, Geoffrey S. D. Beach, and Mathias Kläui. Skyrmion Hall effect revealed by direct time-resolved X-ray microscopy. *Nat. Phys.*, 13:170, 2017. [pp. 32, 33, 82]

[120] Roméo Juge, Soong-Geun Je, Dayane de Souza Chaves, Liliana D. Buda-Prejbeanu, José Peña-Garcia, Jayshankar Nath, Ioan Mihai Miron, Kumari Gaurav Rana, Lucia Aballe, Michael Foerster, Francesca Genuzio, Tevfik Onur Menteş, Andrea Locatelli, Francesco Maccherozzi, Sarnjeet S. Dhesi, Mohamed Belmeguenai, Yves Roussigné, Stéphane Auffret, Stefania Pizzini, Gilles Gaudin, Jan Vogel, and Olivier Boulle. Current-Driven Skyrmion Dynamics and Drive-Dependent Skyrmion Hall Effect in an Ultrathin Film. *Phys. Rev. Appl.*, 12:044007, 2019. [pp. 32, 33, 35, 82]

[121] Wanjun Jiang, Xichao Zhang, Guoqiang Yu, Wei Zhang, Xiao Wang, M. Benjamin Jungfleisch, John E. Pearson, Xuemei Cheng, Olle Heinonen, Kang L. Wang, Yan Zhou, Axel Hoffmann, and Suzanne G. E. te Velthuis. Direct observation of the skyrmion Hall effect. *Nat. Phys.*, 13:162, 2017. [pp. 32, 33, 82]

[122] William Legrand, Davide Maccariello, Nicolas Reyren, Karin Garcia, Christoforos Moutafis, Constance Moreau-Luchaire, Sophie Collin, Karim Bouzehouane, Vincent Cros, and Albert Fert. Room-Temperature Current-Induced Generation and Motion of sub-100 nm Skyrmions. *Nano Lett.*, 17:2703, 2017. [p. 33]

[123] Seonghoon Woo, Kyung Mee Song, Xichao Zhang, Yan Zhou, Motohiko Ezawa, Xiaoxi Liu, S. Finizio, J. Raabe, Nyun Jong Lee, Sang-Il Kim, Seung-Young Park, Younghak Kim, Jae-Young Kim, Dongjoon Lee, OukJae Lee, Jun Woo Choi, Byoung-Chul Min, Hyun Cheol Koo, and Joonyeon Chang. Current-driven dynamics and inhibition of the skyrmion Hall effect of ferrimagnetic skyrmions in GdFeCo films. *Nat. Comm.*, 9:959, 2018. [pp. 33, 82]

[124] A. A. Thiele. Steady-State Motion of Magnetic Domains. *Physical Review Letters*, 30(6):230–233, 1973. [p. 34]

[125] T. Ono. *Spin-transfer torque in nonuniform magnetic structures*. Oxford University Press, December 2017. [p. 34]

[126] Albert Fert, Vincent Cros, and João Sampaio. Skyrmions on the track. *Nature Nanotechnology*, 8(3):152–156, 2013. Number: 3 Publisher: Nature Publishing Group. [pp. 34, 37]

[127] A. Hrabec, J. Sampaio, M. Belmeguenai, I. Gross, R. Weil, S. M. Chérif, A. Stashkevich, V. Jacques, A. Thiaville, and S. Rohart. Current-induced skyrmion generation and dynamics in symmetric bilayers. *Nat. Comm.*, 8:15765, 2017. [p. 35]

[128] Xichao Zhang, Yan Zhou, and Motohiko Ezawa. Magnetic bilayer-skyrmions without skyrmion hall effect. *Nature Communications*, 7(1):10293, 2016. [pp. 35, 38]

[129] Joseph Barker and Oleg A. Tretiakov. Static and Dynamical Properties of Antiferromagnetic Skyrmions in the Presence of Applied Current and Temperature. *Physical Review Letters*, 116(14):147203, 2016. arXiv: 1505.06156 version: 2. [p. 35]

[130] N. Kanazawa, Y. Onose, T. Arima, D. Okuyama, K. Ohoyama, S. Wakimoto, K. Kakurai, S. Ishiwata, and Y. Tokura. Large topological hall effect in a short-period helimagnet MnGe. *Physical Review Letters*, 106(15), 2011. [pp. 36, 82]

[131] T. Schulz, R. Ritz, A. Bauer, M. Halder, M. Wagner, C. Franz, C. Pfleiderer, K. Everschor, M. Garst, and A. Rosch. Emergent electrodynamics of skyrmions in a chiral magnet. *Nat. Phys.*, 8:301, 2012. [pp. 36, 82]

[132] A. Neubauer, C. Pfleiderer, B. Binz, A. Rosch, R. Ritz, P. G. Niklowitz, and P. Böni. Topological hall effect in the a phase of mnsi. *Physical Review Letters*, 102(18), 2009. [pp. 36, 82]

[133] R. Ritz, M. Halder, C. Franz, A. Bauer, M. Wagner, R. Bamler, A. Rosch, and C. Pfleiderer. Giant generic topological hall resistivity of MnSi under pressure. *Physical Review B*, 87(13), 2013. [p. 36]

[134] S. X. Huang and C. L. Chien. Extended skyrmion phase in epitaxial fege(111) thin films. *Physical Review Letters*, 108(26), 2012. [p. 36]

[135] Yufan Li, N. Kanazawa, X. Z. Yu, A. Tsukazaki, M. Kawasaki, M. Ichikawa, X. F. Jin, F. Kagawa, and Y. Tokura. Robust formation of skyrmions and topological hall effect anomaly in epitaxial thin films of MnSi. *Physical Review Letters*, 110(11), 2013. [p. 36]

[136] Haifeng Du, Dong Liang, Chiming Jin, Lingyao Kong, Matthew J. Stolt, Wei Ning, Jiyong Yang, Ying Xing, Jian Wang, Renchao Che, Jiadong Zang, Song Jin, Yuheng Zhang, and Mingliang Tian. Electrical probing of field-driven cascading quantized transitions of skyrmion cluster states in MnSi nanowires. *Nature Communications*, 6(1), 2015. [p. 36]

[137] N. Kanazawa, M. Kubota, A. Tsukazaki, Y. Kozuka, K. S. Takahashi, M. Kawasaki, M. Ichikawa, F. Kagawa, and Y. Tokura. Discretized topological hall effect emerging from skyrmions in constricted geometry. *Physical Review B*, 91(4), 2015. [p. 36]

[138] Dong Liang, John P. DeGrave, Matthew J. Stolt, Yoshinori Tokura, and Song Jin. Current-driven dynamics of skyrmions stabilized in MnSi nanowires revealed by topological hall effect. *Nature Communications*, 6(1), 2015. [p. 36]

[139] Christian Hanneken, Fabian Otte, André Kubetzka, Bertrand Dupé, Niklas Romming, Kirsten von Bergmann, Roland Wiesendanger, and Stefan Heinze. Electrical detection of magnetic skyrmions by tunnelling non-collinear magnetoresistance. *Nat. Nanotech.*, 10:1039, 2015. [pp. 36, 82]

[140] Davide Maccariello, William Legrand, Nicolas Reyren, Karin Garcia, Karim Bouzehouane, Sophie Collin, Vincent Cros, and Albert Fert. Electrical detection of single magnetic skyrmions in metallic multilayers at room temperature. *Nat. Nanotech.*, 13:233, 2018. [pp. 36, 82]

[141] Katharina Zeissler, Simone Finizio, Kowsar Shahbazi, Jamie Massey, Fatma Al Ma'Mari, David M. Bracher, Armin Kleibert, Mark C. Rosamond, Edmund H. Linfield, Thomas A. Moore, Jörg Raabe, Gavin Burnell, and Christopher H. Marrows. Discrete hall resistivity contribution from néel skyrmions in multilayer nanodiscs. *Nature Nanotechnology*, 13(12):1161–1166, 2018. [pp. 36, 82]

[142] Zidong Wang, Minghua Guo, Heng-An Zhou, Le Zhao, Teng Xu, Riccardo Tomasello, Hao Bai, Yiqing Dong, Soong-Geun Je, Weilun Chao, Hee-Sung Han, Sooseok Lee, Ki-Suk Lee, Yunyan Yao, Wei Han, Cheng Song, Huaqiang Wu, Mario Carpentieri, Giovanni Finocchio, Mi-Young Im, Shi-Zeng Lin, and Wanjun Jiang. Thermal generation, manipulation and thermoelectric detection of skyrmions. *Nature Electronics*, 3(11):672–679, 2020. [p. 36]

[143] Alexander Fernández Scarioni, Craig Barton, Héctor Corte-León, Sibylle Sievers, Xiukun Hu, Fernando Ajejas, William Legrand, Nicolas Reyren, Vincent Cros, Olga Kazakova, and Hans W. Schumacher. Thermoelectric signature of individual skyrmions. *Physical Review Letters*, 126(7), 2021. [pp. 36, 82]

[144] Xichao Zhang, Motohiko Ezawa, and Yan Zhou. Magnetic skyrmion logic gates: Conversion, duplication and merging of skyrmions. *Sci. Rep.*, 5:9400, 2015. [p. 37]

[145] Wang Kang, Yangqi Huang, Chentian Zheng, Weifeng Lv, Na Lei, Youguang Zhang, Xichao Zhang, Yan Zhou, and Weisheng Zhao. Voltage Controlled Magnetic Skyrmion Motion for Racetrack Memory. *Sci. Rep.*, 6:23164, 2016. [p. 37]

[146] Hamed Vakili, Jun-Wen Xu, Wei Zhou, Mohammad Nazmus Sakib, Md Golam Morshed, Timothy Hartnett, Yassine Quessab, Kai Litzius, Chung T. Ma, Samiran Ganguly, Mircea R. Stan, Prasanna V. Balachandran, Geoffrey S. D. Beach, S. Joseph Poon, Andrew D. Kent, and Avik W. Ghosh. Skyrmionics—computing and memory technologies based on topological excitations in magnets. *Journal of Applied Physics*, 130(7), 2021. [p. 37]

[147] Cros V., Fert A., Sampaio J., and Seneor P. Dispositif memoire avec skyrmions magnetiques et procede associe, 2022. [p. 37]

[148] Naveen Sisodia, Johan Pelloux-Prayer, Liliana D. Buda-Prejbeanu, Lorena Anghel, Gilles Gaudin, and Olivier Boulle. Robust and programmable logic-in-memory devices exploiting skyrmion confinement and channeling using local energy barriers. *Physical Review Applied*, 18(1), 2022. [p. 37]

[149] Naveen Sisodia, Johan Pelloux-Prayer, Liliana D. Buda-Prejbeanu, Lorena Anghel, Gilles Gaudin, and Olivier Boulle. Programmable skyrmion logic gates based on skyrmion tunneling. *Physical Review Applied*, 17(6), 2022. [pp. 37, 105]

[150] Kyung Mee Song, Jae-Seung Jeong, Biao Pan, Xichao Zhang, Jing Xia, Sunkyung Cha, Tae-Eon Park, Kwangsu Kim, Simone Finizio, Jörg Raabe, Joonyeon Chang, Yan Zhou, Weisheng Zhao, Wang Kang, Hyunsu Ju, and Seonghoon Woo. Skyrmion-based artificial synapses for neuromorphic computing. *Nature Electronics*, 3(3):148–155, 2020. [p. 37]

[151] Yangqi Huang, Wang Kang, Xichao Zhang, Yan Zhou, and Weisheng Zhao. Magnetic skyrmion-based synaptic devices. *Nanotechnology*, 28:08LT02, 2017. [p. 37]

[152] D. Pinna, G. Bourianoff, and K. Everschor-Sitte. Reservoir computing with random skyrmion textures. *Physical Review Applied*, 14(5), 2020. [pp. 37, 38, 106]

[153] Matteo Cucchi, Steven Abreu, Giuseppe Ciccone, Daniel Brunner, and Hans Kleemann. Hands-on reservoir computing: a tutorial for practical implementation. *Neuromorphic Computing and Engineering*, 2(3):032002, August 2022. [p. 37]

[154] Senfu Zhang, Jianbo Wang, Qi Zheng, Qiyuan Zhu, Xianyin Liu, Shujun Chen, Chendong Jin, Qingfang Liu, Chenglong Jia, and Desheng Xue. Current-induced magnetic skyrmions oscillator. *New Journal of Physics*, 17(2):023061, 2015. [p. 38]

[155] Xichao Zhang, Yan Zhou, and Motohiko Ezawa. Antiferromagnetic skyrmion: Stability, creation and manipulation. *Scientific Reports*, 6(1), April 2016. [p. 38]

[156] Rodrigo Jaeschke-Ubiergo and Alvaro S. Nunez. Stability of atomic-sized skyrmions in antiferromagnetic bilayers. *Annals of Physics*, 405:29–37, June 2019. [p. 38]

[157] Chendong Jin, Chengkun Song, Jianbo Wang, and Qingfang Liu. Dynamics of antiferromagnetic skyrmion driven by the spin hall effect. *Applied Physics Letters*, 109(18), October 2016. [p. 38]

[158] R Tomasello, V Puliafito, E Martinez, A Manchon, M Ricci, M Carpentieri, and G Finocchio. Performance of synthetic antiferromagnetic racetrack memory: domain wall versus skyrmion. *Journal of Physics D: Applied Physics*, 50(32):325302, 2017. [p. 38]

[159] S. S. P. Parkin, A. Mansour, and G. P. Felcher. Antiferromagnetic interlayer exchange coupling in sputtered Fe/Cr multilayers: Dependence on number of Fe layers. *Appl. Phys. Lett.*, 58:1473, 1991. [p. 39]

[160] Takaaki Dohi, Samik DuttaGupta, Shunsuke Fukami, and Hideo Ohno. Formation and current-induced motion of synthetic antiferromagnetic skyrmion bubbles. *Nature Communications*, 10(1), nov 2019. [p. 39]

[161] William Legrand, Davide Maccariello, Fernando Ajejas, Sophie Collin, Aymeric Vecchiola, Karim Bouzehouane, Nicolas Reyren, Vincent Cros, and Albert Fert. Room-temperature stabilization of antiferromagnetic skyrmions in synthetic antiferromagnets. *Nature Materials*, 19(1):34–42, 2020. Number: 1 Publisher: Nature Publishing Group. [pp. 39, 73]

[162] Roméo Juge, Naveen Sisodia, Joseba Urrestarazu Larrañaga, Qiang Zhang, Van Tuong Pham, Kumari Gaurav Rana, Brice Sarpi, Nicolas Mille, Stefan Stanescu, Rachid Belkhou, Mohamad-Assaad Mawass, Nina Novakovic-Marinkovic, Florian Kronast, Markus Weigand, Joachim Gräfe, Sebastian Wintz, Simone Finizio, Jörg Raabe, Lucia Aballe, Michael Foerster, Mohamed Belmeguenai, Liliana D. Buda-Prejbeanu, Johan Pelloux-Prayer, Justin M. Shaw, Hans T. Nembach, Laurent Ranno, Gilles Gaudin, and Olivier Boulle. Skyrmions in synthetic antiferromagnets and their nucleation via electrical current and ultra-fast laser illumination. *Nature Communications*, 13(1), August 2022. [pp. 39, 40, 58, 60, 64]

[163] M. R. Parker. The Kerr magneto-optic effect (1876–1976). *Physica B+C*, 86-88:1171, 1977. [p. 45]

[164] B.L. Henke, E.M. Gullikson, and J.C. Davis. X-ray interactions: Photoabsorption, scattering, transmission, and reflection at e = 50-30, 000 eV, z = 1-92. *Atomic Data and Nuclear Data Tables*, 54(2):181–342, July 1993. [p. 47]

[165] J. Stöhr, H. A. Padmore, S. Anders, T. Stammler, and M. R. Scheinfein. Principles of x-ray magnetic dichroism spectromicroscopy. *Surface Review and Letters*, 05(06):1297–1308, dec 1998. [p. 51]

[166] C. T. Chen, Y. U. Idzerda, H.-J. Lin, N. V. Smith, G. Meigs, E. Chaban, G. H. Ho, E. Pellegrin, and F. Sette. Experimental confirmation of the x-ray magnetic circular dichroism sum rules for iron and cobalt. *Physical Review Letters*, 75(1):152–155, 1995. [p. 51]

[167] E. Beaurepaire, J.-C. Merle, A. Daunois, and J.-Y. Bigot. Ultrafast spin dynamics in ferromagnetic nickel. *Physical Review Letters*, 76(22):4250–4253, may 1996. [p. 54]

[168] Hermann Stoll, Aleksander Puzic, Bartel van Waeyenberge, Peter Fischer, Joerg Raabe, Matthias Buess, Thomas Haug, Rainer Höllinger, Christian Back, Dieter Weiss, and Gregory Denbeaux. High-resolution imaging of fast magnetization dynamics in magnetic nanostructures. *Applied Physics Letters*, 84(17):3328–3330, apr 2004. [p. 54]

[169] J. Vogel, W. Kuch, M. Bonfim, J. Camarero, Y. Pennec, F. Offi, K. Fukumoto, J. Kirschner, A. Fontaine, and S. Pizzini. Time-resolved magnetic domain imaging by x-ray photoemission electron microscopy. *Applied Physics Letters*, 82(14):2299–2301, apr 2003. [p. 54]

[170] M. Bonfim, G. Ghiringhelli, F. Montaigne, S. Pizzini, N. B. Brookes, F. Petroff, J. Vogel, J. Camarero, and A. Fontaine. Element-selective nanosecond magnetization dynamics in magnetic heterostructures. *Physical Review Letters*, 86(16):3646–3649, apr 2001. [p. 54]

[171] Falk-Ulrich Stein, Lars Bocklage, Markus Weigand, and Guido Meier. Time-resolved imaging of nonlinear magnetic domain-wall dynamics in ferromagnetic nanowires. *Scientific Reports*, 3(1), apr 2013. [p. 54]

[172] Claire Donnelly, Simone Finizio, Sebastian Gliga, Mirko Holler, Aleš Hrabec, Michal Odstrčil, Sina Mayr, Valerio Scagnoli, Laura J. Heyderman, Manuel Guizar-Sicairos, and Jörg Raabe. Time-resolved imaging of three-dimensional nanoscale magnetization dynamics. *Nature Nanotechnology*, 15(5):356–360, feb 2020. [p. 54]

[173] Markus Weigand, Sebastian Wintz, Joachim Gräfe, Matthias Noske, Hermann Stoll, Bartel Van Waeyenberge, and Gisela Schütz. TimeMaxyne: A shot-noise limited, time-resolved pump-and-probe acquisition system capable of 50 GHz frequencies for synchrotron-based x-ray microscopy. *Crystals*, 12(8):1029, July 2022. [p. 54]

[174] Roméo Juge. *Exploring different facets of magnetic skyrmion nucleation and dynamics in ultrathin films*. PhD thesis, UGA, 2020. [p. 59]

[175] Hongxin Yang, Gong Chen, Alexandre A. C. Cotta, Alpha T. N'Diaye, Sergey A. Nikolaev, Edmar A. Soares, Waldemar A. A. Macedo, Kai Liu, Andreas K. Schmid, Albert Fert, and Mairbek Chshiev. Significant Dzyaloshinskii–Moriya interaction at graphene–ferromagnet interfaces due to the Rashba effect. *Nat. Mater.*, 17:605, 2018. [p. 59]

[176] Durga Khadka, Sabit Karayev, and S. X. Huang. Dzyaloshinskii–Moriya interaction in Pt/Co/Ir and Pt/Co/Ru multilayer films. *J. Appl. Phys.*, 123:123905, 2018. [p. 59]

[177] Simone Finizio, Katharina Zeissler, Sebastian Wintz, Sina Mayr, Teresa Weßels, Alexandra J. Huxtable, Gavin Burnell, Christopher H. Marrows, and Jörg Raabe. Deterministic Field-Free Skyrmion Nucleation at a Nanoengineered Injector Device. *Nano Lett.*, 19:7246, 2019. [pp. 62, 63]

[178] Manuel Baumgartner, Kevin Garello, Johannes Mendil, Can Onur Avci, Eva Grimaldi, Christoph Murer, Junxiao Feng, Mihai Gabureac, Christian Stamm, Yves Acremann, Simone Finizio, Sebastian Wintz, Jörg Raabe, and Pietro Gambardella. Spatially and time-resolved magnetization dynamics driven by spin–orbit torques. *Nature Nanotechnology*, 12(10):980–986, August 2017. [p. 62]

[179] Soong-Geun Je, Pierre Vallobra, Titiksha Srivastava, Juan-Carlos Rojas-Sánchez, Thai Ha Pham, Michel Hehn, Gregory Malinowski, Claire Baraduc, Stéphane Auffret, Gilles Gaudin, Stéphane Mangin, Hélène Béa, and Olivier Boulle. Creation of Magnetic Skyrmion Bubble Lattices by Ultrafast Laser in Ultrathin Films. *Nano Lett.*, 18:7362, 2018. [p. 63]

[180] E. Iacocca, T.-M. Liu, A. H. Reid, Z. Fu, S. Ruta, P. W. Granitzka, E. Jal, S. Bonetti, A. X. Gray, C. E. Graves, R. Kukreja, Z. Chen, D. J. Higley, T. Chase, L. Le Guyader, K. Hirsch, H. Ohldag, W. F. Schlotter, G. L. Dakovski, G. Coslovich, M. C. Hoffmann, S. Carron, A. Tsukamoto, A. Kirilyuk, A. V. Kimel, Th. Rasing, J. Stöhr, R. F. L. Evans, T. Ostler, R. W. Chantrell, M. A. Hoefer, T. J. Silva, and H. A. Dürr. Spin-current-mediated rapid magnon localisation and coalescence after ultrafast optical pumping of ferrimagnetic alloys. *Nature Communications*, 10(1), April 2019. [p. 63]

[181] A.P. Malozemoff and J.C. Slonczewski. *Magnetic Domain Walls in Bubble Materials*. Applied solid state science. Academic Press, 1979. [pp. 65, 66]

[182] Eloi Haltz, Sachin Krishnia, Léo Berges, Alexandra Mougin, and João Sampaio. Domain wall dynamics in antiferromagnetically coupled double-lattice systems. *Physical Review B*, 103(1), January 2021. [p. 66]

[183] O. Boulle, S. Rohart, L. D. Buda-Prejbeanu, E. Jué, I. M. Miron, S. Pizzini, J. Vogel, G. Gaudin, and A. Thiaville. Domain wall tilting in the presence of the dzyaloshinskii-moriya interaction in out-of-plane magnetized magnetic nanotracks. *Physical Review Letters*, 111(21), November 2013. [p. 66]

[184] R. Moreno, R. F. L. Evans, S. Khmelevskyi, M. C. Muñoz, R. W. Chantrell, and O. Chubykalo-Fesenko. Temperature-dependent exchange stiffness and domain wall width in co. *Physical Review B*, 94(10), September 2016. [p. 67]

[185] Sarah Schlotter, Parnika Agrawal, and Geoffrey S. D. Beach. Temperature dependence of the dzyaloshinskii-moriya interaction in pt/co/cu thin film heterostructures. *Applied Physics Letters*, 113(9), August 2018. [p. 67]

[186] Franz Heider and Wyn Williams. Note on temperature dependence of exchange constant in magnetite. *Geophysical Research Letters*, 15(2):184–187, February 1988. [p. 67]

[187] L. de Brouckere and J. Vennik. The temperature dependence of magnetic bubble parameters. *Physica Status Solidi (a)*, 61(2):455–461, October 1980. [p. 67]

[188] J Nogués and Ivan K Schuller. Exchange bias. *Journal of Magnetism and Magnetic Materials*, 192(2):203–232, February 1999. [p. 70]

[189] W. H. Meiklejohn and C. P. Bean. New magnetic anisotropy. *Physical Review*, 102(5):1413–1414, June 1956. [p. 70]

[190] W. H. Meiklejohn and C. P. Bean. New magnetic anisotropy. *Physical Review*, 105(3):904–913, February 1957. [p. 70]

[191] A.E. Berkowitz and Kentaro Takano. Exchange anisotropy — a review. *Journal of Magnetism and Magnetic Materials*, 200(1-3):552–570, October 1999. [p. 70]

[192] L.M. Falicov, F. Mejía-Lira, and J.L. Morán-López. *Magnetic Properties of Low-dimensional Systems II*. Lecture Notes in Computer Science. Springer-Verlag, 1990. [p. 71]

[193] K. Gaurav Rana, A. Finco, F. Fabre, S. Chouaieb, A. Haykal, L. D. Buda-Prejbeanu, O. Fruchart, S. Le Denmat, P. David, M. Belmeguenai, T. Denneulin, R. E. Dunin-Borkowski, G. Gaudin, V. Jacques, and O. Boulle. Room-temperature skyrmions at zero field in exchange-biased ultrathin films. *Phys. Rev. Applied*, 13(4):044079, 2020. [p. 72]

[194] Kumari Gaurav Rana, Rafael Lopes Seeger, Sandra Ruiz-Gómez, Roméo Juge, Qiang Zhang, Kaushik Bairagi, Van Tuong Pham, Mohamed Belmeguenai, Stéphane Auffret, Michael Foerster, Lucia Aballe, Gilles Gaudin, Vincent Baltz, and Olivier Boulle. Imprint from ferromagnetic skyrmions in an antiferromagnet via exchange bias. *Appl. Phys. Lett.*, 119(19):192407, 2021. [pp. 72, 78]

[195] Yao Guang, Iuliia Bykova, Yizhou Liu, Guoqiang Yu, Eberhard Goering, Markus Weigand, Joachim Gräfe, Se Kwon Kim, Junwei Zhang, Hong Zhang, Zhengren Yan, Caihua Wan, Jiafeng Feng, Xiao Wang, Chenyang Guo, Hongxiang Wei, Yong Peng, Yaroslav Tserkovnyak, Xiufeng Han, and Gisela Schütz. Creating zero-field skyrmions in exchange-biased multilayers through x-ray illumination. *Nat Commun*, 11(1):949, 2020. Number: 1 Publisher: Nature Publishing Group. [pp. 73, 78]

[196] M. C. Weber, H. Nembach, B. Hillebrands, and J. Fassbender. Modified gilbert damping due to exchange bias in NiFe/FeMn bilayers. *Journal of Applied Physics*, 97(10), April 2005. [p. 78]

[197] N. P. Duong, T. Satoh, and M. Fiebig. Ultrafast manipulation of antiferromagnetism of NiO. *Physical Review Letters*, 93(11), September 2004. [p. 78]

[198] X. Ma, F. Fang, Q. Li, J. Zhu, Y. Yang, Y. Z. Wu, H. B. Zhao, and G. Lüpke. Ultrafast spin exchange-coupling torque via photo-excited charge-transfer processes. *Nature Communications*, 6(1), October 2015. [p. 78]

[199] H. Ehrke, R. I. Tobey, S. Wall, S. A. Cavill, M. Först, V. Khanna, Th. Garl, N. Stojanovic, D. Prabhakaran, A. T. Boothroyd, M. Gensch, A. Mirone, P. Reutler, A. Revcolevschi, S. S. Dhesi, and A. Cavalleri. Photoinduced melting of antiferromagnetic order in lasrmno4 measured using ultrafast resonant soft x-ray diffraction. *Physical Review Letters*, 106(21), May 2011. [p. 78]

[200] Kai Litzius, Jonathan Leliaert, Pedram Bassirian, Davi Rodrigues, Sascha Kromin, Ivan Lemesh, Jakub Zazvorka, Kyu-Joon Lee, Jeroen Mulkers, Nico Kerber, Daniel Heinze, Niklas Keil, Robert M. Reeve, Markus Weigand, Bartel Van Waeyenberge, Gisela Schütz, Karin Everschor-Sitte, Geoffrey S. D. Beach, and Mathias Kläui. The role of temperature and drive current in skyrmion dynamics. *Nature Electronics*, 3(1):30–36, 2020. [p. 82]

[201] Gen Yin, Yizhou Liu, Yafis Barlas, Jiadong Zang, and Roger K. Lake. Topological spin hall effect resulting from magnetic skyrmions. *Physical Review B*, 92(2), 2015. [p. 82]

[202] N. A. Porter, J. C. Gartside, and C. H. Marrows. Scattering mechanisms in textured FeGe thin films: Magnetoresistance and the anomalous hall effect. *Physical Review B*, 90(2), 2014. [p. 82]

[203] Marco Perini, Sebastian Meyer, André Kubetzka, Roland Wiesendanger, Stefan Heinze, and Kirsten von Bergmann. Electrical detection of domain walls and skyrmions in co films using noncollinear magnetoresistance. *Physical Review Letters*, 123(23), 2019. [p. 82]

[204] Zidong Wang, Minghua Guo, Heng-An Zhou, Le Zhao, Teng Xu, Riccardo Tomasello, Hao Bai, Yiqing Dong, Soong-Geun Je, Weilun Chao, Hee-Sung Han, Sooseok Lee, Ki-Suk Lee, Yunyan Yao, Wei Han, Cheng Song, Huaqiang Wu, Mario Carpentieri, Giovanni Finocchio, Mi-Young Im, Shi-Zeng Lin, and Wanjun Jiang. Thermal generation, manipulation and thermoelectric detection of skyrmions. *Nature Electronics*, 3(11):672–679, 2020. [p. 82]

[205] N. E. Penthorn, X. Hao, Z. Wang, Y. Huai, and H. W. Jiang. Experimental observation of single skyrmion signatures in a magnetic tunnel junction. *Physical Review Letters*, 122(25), 2019. [p. 82]

[206] Bin He, Yue Hu, Chenbo Zhao, Jinwu Wei, Junwei Zhang, Yu Zhang, Chen Cheng, Jiahui Li, Zhuyang Nie, Yanxiang Luo, Yan Zhou, Shilei Zhang, Zhongming Zeng, Yong Peng, John Michael David Coey, Xiufeng Han, and Guoqiang Yu. Realization of zero-field skyrmions in a magnetic tunnel junction. *Advanced Electronic Materials*, 9(4), 2023. [p. 82]

[207] Sai Li, Ao Du, Yadong Wang, Xinran Wang, Xueying Zhang, Houyi Cheng, Wenlong Cai, Shiyang Lu, Kaihua Cao, Biao Pan, Na Lei, Wang Kang, Junming Liu, Albert Fert, Zhipeng Hou, and Weisheng Zhao. Experimental demonstration of skyrmionic magnetic tunnel junction at room temperature. *Science Bulletin*, 67(7):691–699, 2022. [p. 82]

[208] Shinya Kasai, Satoshi Sugimoto, Yoshinobu Nakatani, Ryo Ishikawa, and Yukiko K. Takahashi. Voltage-controlled magnetic skyrmions in magnetic tunnel junctions. *Applied Physics Express*, 12(8):083001, 2019. [p. 82]

[209] Shaohai Chen, Pin Ho, James Lourembam, Alexander K. J. Toh, Jifei Huang, Xiaoye Chen, Hang Khume Tan, Sherry K. L. Yap, Royston J. J. Lim, Hui Ru Tan, T. S. Suraj, Yeow Teck Toh, Idayu Lim, Jing Zhou, Hong Jing Chung, Sze Ter Lim, and Anjan Soumyanarayanan. All-electrical skyrmionic bits in a chiral magnetic tunnel junction, 2023. [p. 82]

[210] Yao Guang, Like Zhang, Junwei Zhang, Yadong Wang, Yuelei Zhao, Riccardo Tomasello, Senfu Zhang, Bin He, Jiahui Li, Yizhou Liu, Jiafeng Feng, Hongxiang Wei, Mario Carpentieri, Zhipeng Hou, Junming Liu, Yong Peng, Zhongming Zeng, Giovanni Finocchio, Xixiang Zhang, John Michael David Coey, Xiufeng Han, and Guoqiang Yu. Electrical detection of magnetic skyrmions in a magnetic tunnel junction. *Advanced Electronic Materials*, 9(1), 2022. [p. 82]

[211] Tatsuya Yamamoto, Rie Matsumoto, Takayuki Nozaki, Hiroshi Imamura, and Shinji Yuasa. Developments in voltage-controlled subnanosecond magnetization switching. *Journal of Magnetism and Magnetic Materials*, 560:169637, 2022. [p. 82]

[212] S. Kanai, M. Yamanouchi, S. Ikeda, Y. Nakatani, F. Matsukura, and H. Ohno. Electric field-induced magnetization reversal in a perpendicular-anisotropy CoFeB-MgO magnetic tunnel junction. *Applied Physics Letters*, 101(12), 2012. [p. 82]

[213] X. W. Yu, V. S. Pribiag, Y. Acremann, A. A. Tulapurkar, T. Tyliszczak, K. W. Chou, B. Bräuer, Z.-P. Li, O. J. Lee, P. G. Gowtham, D. C. Ralph, R. A. Buhrman, and J. Stöhr. Images of a spin-torque-driven magnetic nano-oscillator. *Physical Review Letters*, 106(16), 2011. [p. 84]

[214] David P. Bernstein, Björn Bräuer, Roopali Kukreja, Joachim Stöhr, Thomas Hauet, Julien Cucchiara, Stéphane Mangin, Jordan A. Katine, Tolek Tyliszczak, Kang W. Chou, and Yves Acremann. Nonuniform switching of the perpendicular magnetization in a spin-torque-driven magnetic nanopillar. *Physical Review B*, 83(18), 2011. [p. 84]

[215] B. Dieny, I. L. Prejbeanu, K. Garello, P. Gambardella, P. Freitas, R. Lehndorff, W. Raberg, U. Ebels, S. O. Demokritov, J. Akerman, A. Deac, P. Pirro, C. Adelmann, A. Anane, A. V. Chumak, A. Hirohata, S. Mangin, Sergio O. Valenzuela, M. Cengiz Onbaşlı, M. d'Aquino, G. Prenat, G. Finocchio, L. Lopez-Diaz, R. Chantrell, O. Chubykalo-Fesenko, and P. Bortolotti. Opportunities and challenges for spintronics in the microelectronics industry. *Nature Electronics*, 3(8):446–459, 2020. [p. 85]

[216] Roméo Juge, Soong-Geun Je, Dayane de Souza Chaves, Stefania Pizzini, Liliana D. Buda-Prejbeanu, Lucia Aballe, Michael Foerster, Andrea Locatelli, Tevfik Onur Menteş, Alessandro Sala, Francesco Maccherozzi, Sarnjeet S. Dhesi, Stéphane Auffret, Eric Gautier, Gilles Gaudin, Jan Vogel, and Olivier Boulle. Magnetic skyrmions in confined geometries: Effect of the magnetic field and the disorder. *Journal of Magnetism and Magnetic Materials*, 455:3–8, 2018. [pp. 85, 88]

[217] Evgeny Y Tsymbal, Oleg N Mryasov, and Patrick R LeClair. Spin-dependent tunnelling in magnetic tunnel junctions. *Journal of Physics: Condensed Matter*, 15(4):R109–R142, January 2003. [p. 90]

[218] LeClair, PR (Patrick). Fundamental aspects of spin polarized tunneling : magnetic tunnel junctions and spin filters, 2002. [p. 90]

[219] Y.C. Wu, K. Garello, W. Kim, M. Gupta, M. Perumkunnil, V. Kateel, S. Couet, R. Carpenter, S. Rao, S. Van Beek, K.K. Vudya Sethu, F. Yasin, D. Crotti, and G.S. Kar. Voltage-gate-assisted spin-orbit-torque magnetic random-access memory for high-density and low-power embedded applications. *Physical Review Applied*, 15(6), 2021. [p. 90]

[220] Luc Thomas, Guenole Jan, Jian Zhu, Huanlong Liu, Yuan-Jen Lee, Son Le, Ru-Ying Tong, Keyu Pi, Yu-Jen Wang, Dongna Shen, Renren He, Jesmin Haq, Jeffrey Teng, Vinh Lam, Kenlin Huang, Tom Zhong, Terry Torng, and Po-Kang Wang. Perpendicular spin transfer torque magnetic random access memories with high spin torque efficiency and thermal stability for embedded applications (invited). *Journal of Applied Physics*, 115(17):172615, 2014. [p. 90]

[221] Takayuki Nozaki, Tatsuya Yamamoto, Shinji Miwa, Masahito Tsujikawa, Masafumi Shirai, Shinji Yuasa, and Yoshishige Suzuki. Recent progress in the voltage-controlled magnetic anisotropy effect and the challenges faced in developing voltage-torque MRAM. *Micromachines*, 10(5):327, 2019. [p. 90]

[222] B. Dieny and M. Chshiev. Perpendicular magnetic anisotropy at transition metal/oxide interfaces and applications. *Rev. Mod. Phys.*, 89:025008, 2017. [p. 90]

[223] Pedram Khalili Amiri, Juan G. Alzate, Xue Qing Cai, Farbod Ebrahimi, Qi Hu, Kin Wong, Cecile Grezes, Hochul Lee, Guoqiang Yu, Xiang Li, Mustafa Akyol, Qiming Shao, Jordan A. Katine, Jurgen Langer, Berthold Ocker, and Kang L. Wang. Electric-field-controlled magnetoelectric RAM: Progress, challenges, and scaling. *IEEE Transactions on Magnetics*, 51(11):1–7, 2015. [p. 90]

[224] Mohamed Belmeguenai, Jean-Paul Adam, Yves Roussigné, Sylvain Eimer, Thibaut Devolder, Joo-Von Kim, Salim Mourad Cherif, Andrey Stashkevich, and André Thiaville. Interfacial Dzyaloshinskii-Moriya interaction in perpendicularly magnetized Pt/Co/AlO_x ultrathin films measured by Brillouin light spectroscopy. *Phys. Rev. B*, 91:180405, 2015. [p. 93]

[225] M Vaňatka, J-C Rojas-Sánchez, J Vogel, M Bonfim, M Belmeguenai, Y Roussigné, A Stashkevich, A Thiaville, and S Pizzini. Velocity asymmetry of dzyaloshinskii domain walls in the creep and flow regimes. *Journal of Physics: Condensed Matter*, 27(32):326002, 2015. [p. 94]

[226] Titiksha Srivastava, Willy Lim, Isabelle Joumard, Stéphane Auffret, Claire Baraduc, and Hélène Béa. Mapping different skyrmion phases in double wedges of ta/FeCoB/TaOx trilayers. *Physical Review B*, 100(22), 2019. [p. 94]

[227] P. J. Metaxas, J. P. Jamet, A. Mougin, M. Cormier, J. Ferré, V. Baltz, B. Rodmacq, B. Dieny, and R. L. Stamps. Creep and Flow Regimes of Magnetic Domain-Wall Motion in Ultrathin Pt/Co/Pt Films with Perpendicular Anisotropy. *Phys. Rev. Lett.*, 99:217208, 2007. [p. 94]

[228] C. Gatel, J. Dupuy, F. Houdellier, and M. J. Hÿtch. Unlimited acquisition time in electron holography by automated feedback control of transmission electron microscope. *Applied Physics Letters*, 113(13), 2018. [p. 96]

[229] M. J. Benitez, A. Hrabec, A. P. Mihai, T. A. Moore, G. Burnell, D. McGrouther, C. H. Marrows, and S. McVitie. Magnetic microscopy and topological stability of homochiral néel domain walls in a pt/co/AlOx trilayer. *Nature Communications*, 6(1), 2015. [p. 97]

[230] A Masseboeuf, C Gatel, A Marty, Jean-Christophe Toussaint, and P Bayle-Guillemaud. Lorentz microscopy mapping during magnetization process of l10 fepd thin films. *Journal of Physics: Conference Series*, 126:012055, 2008. [p. 97]

[231] Arne Vansteenkiste, Jonathan Leliaert, Mykola Dvornik, Mathias Helsen, Felipe Garcia-Sanchez, and Bartel Van Waeyenberge. The design and verification of MuMax3. *AIP Advances*, 4(10), 2014. [p. 98]

[232] A. Vansteenkiste and B. Van de Wiele. MuMax: A new high-performance micromagnetic simulation tool. *Journal of Magnetism and Magnetic Materials*, 323(21):2585–2591, 2011. [p. 98]

[233] Titiksha Srivastava, Marine Schott, Roméo Juge, Viola Křižáková, Mohamed Belmeguenai, Yves Roussigné, Anne Bernand-Mantel, Laurent Ranno, Stefania Pizzini, Salim-Mourad Chérif, Andrey Stashkevich, Stéphane Auffret, Olivier Boulle, Gilles Gaudin, Mairbek Chshiev, Claire Baraduc, and Hélène Béa. Large-Voltage Tuning of Dzyaloshinskii–Moriya Interactions: A Route toward Dynamic Control of Skyrmion Chirality. *Nano Lett.*, 18:4871, 2018. [p. 98]

[234] Miina Leiviskä, Sarah Jenkins, Richard F. L. Evans, Daria Gusakova, and Vincent Baltz. Dynamic imprinting of nanoscale topological phases into an antiferromagnet, 2023. [p. 104]

[235] E. Raymenants, O. Bultynck, D. Wan, T. Devolder, K. Garello, L. Souriau, A. Thiam, D. Tsvetanova, Y. Canvel, D. E. Nikonov, I. A. Young, M. Heyns, B. Soree, I. Asselberghs, I. Radu, S. Couet, and V. D. Nguyen. Nanoscale domain wall devices with magnetic tunnel junction read and write. *Nature Electronics*, 4(6):392–398, June 2021. [p. 104]

[236] Roméo Juge, Kaushik Bairagi, Kumari Gaurav Rana, Jan Vogel, Mamour Sall, Dominique Mailly, Van Tuong Pham, Qiang Zhang, Naveen Sisodia, Michael Foerster, Lucia Aballe, Mohamed Belmeguenai, Yves Roussigné, Stéphane Auffret, Liliana D. Buda-Prejbeanu, Gilles Gaudin, Dafiné Ravelosona, and Olivier Boulle. Helium ions put magnetic skyrmions on the track. *Nano Letters*, 21(7):2989–2996, March 2021. [p. 105]

[237] Gouhei Tanaka, Toshiyuki Yamane, Jean Benoit Héroux, Ryosho Nakane, Naoki Kanazawa, Seiji Takeda, Hidetoshi Numata, Daiju Nakano, and Akira Hirose. Recent advances in physical reservoir computing: A review. *Neural Networks*, 115:100–123, July 2019. [p. 106]

[238] Jacob Torrejon, Mathieu Riou, Flavio Abreu Araujo, Sumito Tsunegi, Guru Khalsa, Damien Querlioz, Paolo Bortolotti, Vincent Cros, Kay Yakushiji, Akio Fukushima, Hitoshi Kubota, Shinji Yuasa, Mark D. Stiles, and Julie Grollier. Neuromorphic computing with nanoscale spintronic oscillators. *Nature*, 547(7664):428–431, July 2017. [p. 106]

[239] Hans-Benjamin Braun. Topological effects in nanomagnetism: From superparamagnetism to chiral quantum solitons. *Adv. Phy.*, 61:1, 2012. [p. 108]